

# Cantilever Dynamic Analysis in Tapping Mode Atomic Force Microscopy

Wenqi Deng

A thesis submitted in partial fulfilment of the requirements of  
Liverpool John Moores University for the degree of Doctor of  
Philosophy

April 2015

**Abstract:** Tapping mode atomic force microscopy (AFM) is becoming popular in the area of biology, as well as for polymer and semiconductor materials science. Unlike other AFM techniques, it only makes intermittent contact with the sample, which largely reduces any potential surface damage to soft materials, like cells and polymer. Moreover, phase image can also be obtained from tapping mode AFM besides height and amplitude image. Phase images provide extra information on the test sample in comparison with height and amplitude images.

Studies have been carried out to investigate the contributions to phase shifts in tapping mode AFM using point-mass model. Results showed that the phase shift is independent of the Young's modulus of the material; the phase shift only changes when energy dissipation occurs, such as the case with adhesion hysteresis and viscosity. However, the simple point mass model can only study the first order vibration mode of the AFM cantilever. Moreover, it does not take into account geometrical effects of the tip and the cantilever.

However, correct interpretation of phase images still poses a significant challenge to the AFM community. In this study, the cantilever's dynamic behaviour in tapping mode AFM is studied through a three dimensional finite element method. A rectangular silicon cantilever with the dimensions 240  $\mu\text{m}$  length, 30  $\mu\text{m}$  width, 2.7  $\mu\text{m}$  thick and with a silicon tip radius of 9nm, are used in the simulation. The cantilever dimensions are the same as those of the Olympus model AC240TS cantilevers used in AFM experiments. The material properties of the silicon cantilever as used in the simulation again match those of the real cantilevers and are defined as: Young's modulus of 170 GPa and a Poisson's ratio of 0.28. A piezo actuator is attached to the cantilever. A sinusoidal voltage is subsequently applied to the piezo actuator in order to vibrate the cantilever.

The cantilever's dynamic displacement responses are firstly obtained via simulation under different tip-sample separations and for different tip-sample interaction forces, such as elastic force, adhesion force, viscosity force and the van der Waals force, which correspond to the cantilever's action upon various different representative computer-generated test samples. Simulated results show that the dynamic cantilever displacement response consists of three states: free vibration, a transition state and a stable state. Phase shift, transition time, stable amplitude and frequency changes are then analysed from the dynamic displacement responses that are obtained. The phase shift of free vibration is  $90^\circ$ . It is found that under pure repulsive force, the phase shifts are above  $90^\circ$ , while the phase shifts are below  $90^\circ$  under pure attractive force. Also, attractive forces have the ability to decrease the phase shifts. When different interaction forces are coupled together, depending on the strength of the attractive forces, the phase shifts may suddenly drop below  $90^\circ$ .

Finally, experiments are carried out on a real AFM system to support the findings of the simulations. Olympus model AC240TS cantilever is used in the experiment, while polyurethane (PU), polyvinyl chloride (PVC) and parafilm are used as test sample. Phase shifts were recorded by changing the setpoint ratio (setpoint ratio = setpoint amplitude/free amplitude). The phase shifts were recorded from set-point amplitudes varying from 43.6nm to 4.36nm, which have the similar trend as simulation results.

## Table of Contents

Chapter 1 Introduction .....	14
1.1 Background to Project.....	14
1.1.1 Non-contact mode AFM.....	16
1.1.2 Contact mode AFM .....	20
1.1.3 Tapping mode AFM.....	23
1.2 Aims and Objectives.....	25
1.3 Motivation and Contribution to knowledge .....	26
1.4 Structure of the thesis .....	29
Chapter 2 Background of Atomic Force Microscope .....	32
2.1 Evolution of the atomic force microscope.....	32
2.2 Vibration Modes of the Cantilever.....	39
2.3 Variants of AFM Imaging techniques .....	40
2.3.1 Static mode AFM techniques .....	41
2.3.2 Dynamic mode AFM techniques .....	41
2.4 Key Components of tapping mode AFM .....	44
2.4.1 AFM System .....	44
2.4.2 Feedback system.....	45
2.4.3 Optical beam deflection method .....	46
2.4.3 Piezo-electric actuators.....	48
2.4.4 Cantilever and tip.....	49
2.5 Calibration of the cantilever .....	52
2.5.1 Optical sensitivity .....	52
2.5.2 Determination of the spring constant .....	53
2.5.3 Damping of AFM system .....	55
2.6 Summary and Discussions.....	55
Chapter 3 Numerical Modelling of Atomic Force Microscope .....	58
3.1 Point Mass Analytical Model.....	58
3.1.1 The Basic Point Mass Model .....	58
3.1.2 The Wang Model.....	62
3.1.3 The Energy Conservation Model.....	64
3.2 1D beam analytical model .....	65
3.3 3D numerical model.....	68
3.4 Summary and Discussions.....	70

Chapter 4 Tip-Sample Interaction Force .....	74
4.1 Van der Waals force .....	74
4.2 Capillary force .....	75
4.3 Contact force.....	77
4.3.1 Hertz model.....	77
4.3.2 DMT model.....	78
4.3.3 JKR model.....	78
4.4 Non-conservative forces .....	79
4.5 Summary and Discussions.....	80
Chapter 5 Phase Imaging .....	82
5.1 General description.....	82
5.2 Theory of Phase imaging.....	86
5.2.1 Resonance frequency shift theory .....	86
5.2.2 Energy dissipation theory .....	89
5.2.3 Analytical models for phase shift.....	91
5.3 Interpretation of phase imaging .....	96
5.4 Summary and Discussions.....	98
Chapter 6 A Real Contact Model Based on Finite Element Modelling of Tapping Mode AFM .....	100
6.1 A Real Contact Model .....	100
6.2 Preliminary Results .....	102
6.3 Summary and Discussions.....	104
Chapter 7 A Simplified 3D Model Based Finite Element Modelling of Tapping Mode AFM.....	106
7.1 The geometric model and material properties.....	106
7.2 Boundary conditions .....	107
7.3 Difference between the finite element model and the real tapping mode AFM system .....	109
7.4 Mesh .....	110
7.5 Study types of the simulation .....	111
7.5.1 Eigenfrequency study.....	111
7.5.2 Frequency domain study.....	112
7.5.3 Stationary study .....	113
7.5.4 Time-dependent study.....	113
7.6 Discussions of the FEA model .....	116
7.7 Modal analysis of the cantilever .....	119
7.8 Damping analysis of the cantilever .....	123

7.9 Summary and Discussions.....	125
Chapter 8 Dynamic Behaviour Analysis of Tapping Mode AFM .....	127
8.1 Dynamic Behaviour of the Cantilever under Free Vibration.....	127
8.1.1 Simulation setup .....	127
8.1.2 Simulation results .....	127
8.2 Dynamic Behaviour Analysis of the cantilever under tip-sample interaction .....	129
8.2.1 Simulation setup .....	129
8.2.2 Dynamic displacement response of a cantilever .....	129
8.3 Phase shift analysis .....	131
8.3.1 Phase shift extraction from the dynamic displacement response of the cantilever .....	131
8.3.2 Phase shift analysis .....	133
8.4 Transition time analysis .....	140
8.5 Stable amplitude analysis .....	141
8.8 Instantaneous frequency .....	145
8.9 Summary and Discussions.....	146
Chapter 9 AFM Experimentation .....	148
9.1 Equipment.....	148
9.2 Preparation of samples .....	149
9.3 Cantilever calibration.....	150
9.4 Force curve analysis .....	153
9.5 AFM imaging .....	156
9.6 Measurement of phase shift.....	159
9.6.1 Indirect phase shift measurement.....	159
9.6.2 Direct phase shift measurement.....	161
9.7 Summary and Discussions.....	162
Chapter 10 Conclusions .....	165
10.1 Conclusions .....	165
10.2 Further work .....	167
References .....	169
Appendix .....	176

## **ACKNOWLEDGEMENTS**

I would like to express my sincere gratitude and thanks to everyone who provided guidance, support and guidance, support, advice and invaluable expertise throughout this project.

In particular, I would like to thank Dr. Guangming Zhang who recruited me to GERI for his continuous support and guidance in research. I would like to thank Professor David R Burton for providing the full scholarship for my PhD study and also the idea to carry out this project. I would like to thank Professor David M Harvey and Dr. Francis Lilley for their continuous guidance and expertise in their respected fields throughout this thesis. I would like to thank Dr. Mark F Murphy, also for providing continuous guidance and support in the AFM experiments. Also, I would like to thank Dr. Frederic Bezombe for helping some experiment work. Moreover, I would like to thank our lovely administrator Helen Pottle for helping me with all the administrative stuffs.

I would like to thank Dr. Jonathan Moffat from Asylum Research and Atomic Force for his help in AFM system. I would like to also thank all the staffs of the technical support team in COMSOL Multiphysics during my early stage of the PhD study.

Finally, I would like to thank my parents, family, friends and my girlfriend for their continuous support throughout my PhD study.

## Glossary

### Miller index

Miller index is used to define the plane in crystal lattices. Generally, the Miller index is represented by three integers  $h, k, \ell$ . The plane defined by the Miller indices is orthogonal to the lattice plane  $(h\mathbf{a}_1, k\mathbf{a}_2, \ell\mathbf{a}_3)$ , where  $(\mathbf{a}_1, \mathbf{a}_2, \mathbf{a}_3)$  are the vectors in  $x, y, z$  directions.

### Adatom

Adatom is contracted from "adsorbed atom". It can be considered as an atom which lies on a crystal surface, and can also be regarded as the opposite of a surface vacancy.

### Extracellular polymeric substances (EPS)

The extracellular polymeric substances (EPS) is created by bacterial species, which can be considered a combination of different materials, such as lipopolysaccharides, proteins, peptides, nucleic acids, especially the polysaccharides.

### Salmonella typhimurium (S. typhimurium)

Salmonella typhimurium is one kind of pathogenic bacteria which usually found when consuming some contaminated food or water. Salmonella typhimurium can be used to produce extracellular polymers, which has lots of different pathogenic antigens.

## List of abbreviations

AFM	Atomic force microscope
$A_0$	Free amplitude
$A_t$	Tapping amplitude
AFAM	Atomic force acoustic microscopy
EPS	Extracellular polymeric substances
FFM	Friction force microscopy
FMM	Force modulation mode
k	Spring constant
LE	Lateral excitation
LM-AFM	Lateral force modulation atomic force microscopy
NC-AFM	Non-contact AFM
PID	Proportional integral differential
STM	Scanning tunnelling microscope
<i>S. typhimurium</i>	Salmonella typhimurium
TM	Tapping mode
TR	Torsional resonance
UAFM	Ultrasonic atomic force microscopy

## List of figures

Figure 1.1 Force vs tip-sample separation .....	15
Figure 1.2 Schematic diagram of non-contact mode AFM .....	16
Figure 1.3 Topographic image of TiO <sub>2</sub> (110) which was captured using non-contact mode AFM. Scan size: 5.4nm by 5.4nm. The peak to peak vibration amplitude of cantilever was 30 nm. A cantilever with a spring constant of 28 N/m and resonant frequency of 280 kHz was used in the experiment. The frequency shift set for this experiment is 80 Hz. Adapted with permission to reproduce this figure from (Fukui et al., 1997) has been granted by Chemical Physics Letters.....	18
Figure 1.4 Topographic image of Si(111) surface which was captured using non-contact mode AFM. Scan size: 89 angstrom by 89 angstrom. The peak to peak vibration amplitude of cantilever was 16 nm. A cantilever with a spring constant of 36 N/m and resonant frequency of 169 kHz was used in the experiment. The frequency shift set for this experiment is -28 Hz. Adapted with permission to reproduce this figure from(Sugawara et al., 1997) has been granted by Applied Surface Science. ....	19
Figure 1.5 Schematic diagram of contact mode AFM.....	20
Figure 1.6 Deflection image of a living fibroblast cell which was captured using contact mode AFM. Scan size: 27um by 27um.....	22
Figure 1.7 Schematic diagram of tapping mode AFM.....	23
Figure 1.8 AFM images of a <i>S. typhimurium</i> cell covered with an EPS capsule. (a) height image; (b) height measurement of the black line indicated in (a); (c) phase image; (d) amplitude image. Adapted with permission to reproduce this figure from (Suo et al., 2006) has been granted by American Chemical Society. ....	25
Figure 2.1 Schematic view of a scanning tunnelling microscope (STM). Adapted from ( <a href="http://en.wikipedia.org/wiki/Scanning_tunneling_microscope">http://en.wikipedia.org/wiki/Scanning_tunneling_microscope</a> ) .....	33
Figure 2.2 SEM image of tungsten needle. Adapted from ( <a href="http://www.brukerafmprobes.com/p-3411-dtt10.aspx">http://www.brukerafmprobes.com/p-3411-dtt10.aspx</a> ).....	35
Figure 2.3 Schematic diagram of the mechanism of the earliest dynamic AFM .....	36
Figure 2.4 Topography image of purple membrane captured using tapping mode AFM. Setpoint amplitude: 11 mV. Scanned size: 180nm by 180nm. Adapted with permission to reproduce this figure from (Möller et al., 1999) has been granted by Biophysical Journal.....	37
Figure 2.5 Schematic diagram bimodal AFM .....	38
Figure 2.6 Phase shifts against materials with different Young's modulus. Q factor is 500, $A_t/A_0 = 0.6$ , $k=20$ N/m, resonant frequency is 200kHz. Adapted with permission to reproduce this figure from (Tamayo and García, 1997) has been granted by Applied Physics Letters. ....	39
Figure 2.7 Vibration modes of the cantilever .....	40
Figure 2.8 Torsion resonance mode and lateral excitation mode AFM.....	44
Figure 2.9 Schematic diagram of the key components of a tapping mode AFM system. Adapted with permission to reproduce this figure from (Garcia, October 2010) has been granted by Wiley Books	45
Figure 2.10 Schematic diagram of feedback system .....	46
Figure 2.11 Schematic diagram of the Optical Beam Deflection method .....	47
Figure 2.12 (a) acoustic excitation (b) magnetic excitation .....	48
Figure 2.13 SEM image of an AFM tip. Adapted from ( <a href="http://www.nanoandmore.com/AFM-Probe-PNP-TRS.html">http://www.nanoandmore.com/AFM-Probe-PNP-TRS.html</a> ).....	49

Figure 2.14 Rectangular and triangular cantilevers. ( <a href="http://www.brukerafmprobes.com/p-3693-snl-10.aspx">http://www.brukerafmprobes.com/p-3693-snl-10.aspx</a> ) .....	50
Figure 2.15 SEM image of a carbon nanotube with a length of 1000nm. Adapted from (Martinez et al., 2005) .....	51
Figure 2.16 force-distance curve .....	53
Figure 2.17 power spectrum .....	55
Figure 3.1 Point mass model.....	58
Figure 3.2 1D beam model, $\lambda$ indicates the location of the tip, $k_n$ , $k_t$ and $\eta_n$ , $\eta_t$ represent the spring constant and viscosity, respectively, in the normal and tangential directions. ....	65
Figure 3.3 Schematic diagram of a 3D finite element model .....	68
Figure 3.4 3D beam element.....	69
Figure 4.1 Schematic diagram shows how the water meniscus forms between tip and sample.....	75
Figure 5.1 Schematic diagram of height and phase measurement of regions A and B.....	83
Figure 5.2 AFM images of three buried cells: (a) Height image, (b) Phase image, (c) Amplitude image, the scale bar corresponds to 2 $\mu$ m. Adapted with permission to reproduce this figure from (Suo et al., 2006) has been granted by American Chemical Society.....	84
Figure 5.3 AFM images of hydrogenated diblock copolymer, scanned size: 500nm by 500nm. Adapted with permission to reproduce this figure from (Reiter et al., 2001) has been granted by Physical Review Letters.....	85
Figure 5.4 3D image of parafilm reconstructed with height and phase image .....	86
Figure 5.5 AFM experiments are performed on a polyethylene sample. Free vibration amplitude is 20 nm. Amplitude-frequency curve (solid) and phase shift-frequency curve (dash) are shown with different set-point ratios (a) setpoint ratio = 1, (b) setpoint ratio = 0.7, (c) setpoint ratio = 0.5, (d) setpoint ratio = 0.2. Adapted with permission to reproduce this figure from (Magonov et al., 1997b) has been granted by Surface Science. ....	87
Figure 5.6 Phase shift were recorded against different setpoint ratios with different free vibration amplitudes for materials with different Young's moduli. Adapted with permission to reproduce this figure from (Magonov et al., 1997b) has been granted by Surface Science.....	89
Figure 5.7 Q factor = 500, k = 20N/m, viscosity is 30 Pa*s. The open circle dash curve shows the phase shifts when only the elastic force is considered, while the open triangle dash curve shows the phase shifts when the viscosity force is coupled with the elastic force. Both phase shifts were obtained under a setpoint ratio = 0.6. Adapted with permission to reproduce this figure from (García et al., 1998) has been granted by Applied Physics A: Materials Science & Processing .....	90
Figure 5.8 Q factor = 500, k = 20N/m, approaching surface energy is 10 mJ/m <sup>2</sup> , retracting surface energy is 60 mJ/m <sup>2</sup> . The closed circle dash curve shows the phase shifts when only the elastic force is considered, while the closed triangle dash curve shows the phase shifts when adhesion hysteresis is coupled with the elastic force. Both phase shifts were obtained under a setpoint ratio = 0.6 Adapted with permission to reproduce this figure from (García et al., 1999) has been granted by Surface & Interface Analysis.....	91
Figure 6.1 Schematic diagram of the side view of the geometry of 3D real contact model. ....	100
Figure 6.2 Refined mesh on the sample surface, which is indicated as a blue circle. ....	101
Figure 6.3 Boundary conditions are shown on the side view of the schematic diagram of 3D geometry contact model.....	102
Figure 6.4 Dynamic displacement response of the cantilever for one cycle (1.22e <sup>-5</sup> s), unit of time: s. ....	103

Figure 6.5 Stress on the tip and sample, the unit of the colour bar is Pa.....	104
Figure 7.1 Geometric model .....	106
Figure 7.2 SEM image of cantilever and tip ( <a href="http://www.asylumresearch.com/Probe/AC240TS">http://www.asylumresearch.com/Probe/AC240TS</a> )....	107
Figure 7.3 Illustration of tip-sample contact area. I: the approaching contact region; II: the retracting contact region. ....	108
Figure 7.4 Mesh model .....	111
Figure 7.5 User interface of Eigenfrequency study.....	112
Figure 7.6 User interface of Frequency domain study.....	113
Figure 7.7 User interface of Time-dependent study.....	115
Figure 7.8 User interface of Time-dependent solver.....	116
Figure 7.9 Frequency response of the cantilever when $Q = 1$ , unit of frequency is Hz. ....	117
Figure 7.10 Displacement of the cantilever against different vibration frequencies. ....	118
Figure 7.11 Amplitude of the cantilever against different vibration frequencies .....	118
Figure 7.12 Flexural modes (a) first order, (b) second order, (c) third order, (d) fourth order.....	120
Figure 7.13 Torsion modes (a) first order, (b) second order, (c) third order, (d) fourth order .....	121
Figure 7.14 Lateral modes: (a) first order, (b) second order. ....	122
Figure 7.15 First order extension mode.....	122
Figure 7.16 Frequency response of the cantilever for different degrees of damping: (a) $Q = 1$ , (b) $Q = 100$ , unit of frequency is Hz. ....	124
Figure 8.1 Displacement of cantilever when $Q = 100$ .....	128
Figure 8.2 Displacement of cantilever when $Q = 1$ .....	128
Figure 8.3 The simulated dynamic displacement response of a cantilever during tapping mode imaging, when only considering the elastic force. Free vibration amplitude $Amp_{free} = 40nm$ , tip-sample separation $d_0 = 20nm$ , $Q = 100$ . Test sample material: Young's modulus of the test sample 1GPa, Poisson's ratio of the test sample 0.4. ....	129
Figure 8.4 The simulated dynamic displacement response of a cantilever during tapping mode imaging, when only considering the elastic force. Free vibration amplitude $Amp_{free} = 40nm$ , tip-sample separation $d_0 = 20nm$ , $Q = 1$ . Test sample material: Young's modulus of the test sample 1GPa, Poisson's ratio of the test sample 0.4.....	130
Figure 8.5 Power spectrum of the displacement signal.....	132
Figure 8.6 Phase versus frequency obtained by doing FFT to the displacement signal of the cantilever. ....	132
Figure 8.7 The trend of phase shifts when only elastic force (Square) or adhesion force (Circle) is applied to the cantilever tip.....	133
Figure 8.8 Phase shifts under elastic force and with different levels of adhesion energy hysteresis. The surface energy $\gamma_{approach}$ is $30mJ/m^2$ ; The $\gamma_{retract}$ is respectively, $35mJ/m^2$ (I), $60mJ/m^2$ (II), $90mJ/m^2$ (III), and $120mJ/m^2$ (IV). ....	134
Figure 8.9 Phase shifts under elastic force with a Young's modulus of 1GPa and Poisson's ratio of 0.4 coupled with I: adhesion hysteresis; II: adhesion hysteresis and van der Waals force. The $\gamma_{approach}$ surface energy is $30mJ/m^2$ , the $\gamma_{retract}$ is $90mJ/m^2$ , the Hamaker constant is $6e^{-20} J$ . ....	136
Figure 8.10 Phase shifts under elastic force and for different viscosity forces. I: elastic force only; II: elastic force + low viscosity force. III: low viscosity force only; IV: elastic force + high viscosity force. V: high viscosity force only.....	137
Figure 8.11 Phase shifts of I: only elastic force with a Young's modulus of 1GPa and Poisson's ratio of 0.4; II: only elastic force with a Young's modulus of 5GPa and Poisson's ratio of 0.4; III, IV are based	

on I and II, respectively, with the same adhesion hysteresis, where the $\gamma_{\text{approach}}$ surface energy is $30\text{mJ/m}^2$ and the $\gamma_{\text{retract}}$ is $90\text{mJ/m}^2$ .	139
Figure 8.12 Transition time: I. purely elastic force. II, III, IV. elastic force and different levels of adhesion hysteresis. For II, III and IV, the $\gamma_{\text{approach}}$ is $30\text{mJ/m}^2$ ; The $\gamma_{\text{retract}}$ is, $35\text{mJ/m}^2$ (II), $60\text{mJ/m}^2$ (III), $90\text{mJ/m}^2$ (IV) respectively.	140
Figure 8.13 Stable amplitude under I: purely elastic force, II: elastic force and adhesion hysteresis.	142
Figure 8.14 Dynamic displacement response of the cantilever during the steady state. $Q=100$ , free vibration amplitude $\text{Amp}_{\text{free}} = 40\text{nm}$ , tip sample separation $d_0 = 4\text{nm}$ . Young's modulus = $1\text{GPa}$ , Poisson's ratio = $0.4$ . $\gamma_{\text{approach}} = 30\text{mJ/m}^2$ , $\gamma_{\text{retract}}=90\text{mJ/m}^2$ . Elastic force has been coupled with adhesion hysteresis to produce this result.	143
Figure 8.15 Stable amplitudes of elastic force couples with I: $\gamma_{\text{approach}} = 100\text{mJ/m}^2$ , $\gamma_{\text{retract}}=150\text{mJ/m}^2$ , II: $\gamma_{\text{approach}} = 100\text{mJ/m}^2$ , $\gamma_{\text{retract}}=200\text{mJ/m}^2$	144
Figure 8.16 Stable amplitudes of elastic force couples with viscosity force I: $500\text{ Pa}\cdot\text{s}$ , II: $5000\text{ Pa}\cdot\text{s}$	145
Figure 8.17 Vibration periods, $Q=100$ , free vibration amplitude $\text{Amp}_{\text{free}} = 40\text{nm}$ , tip-sample separation $d_0= 20\text{nm}$ . Young's modulus = $1\text{GPa}$ , Poisson's ratio = $0.4$ . $\gamma_{\text{approach}} = 30\text{mJ/m}^2$ , $\gamma_{\text{retract}} = 90\text{mJ/m}^2$ . Elastic force has been coupled with adhesion hysteresis to produce this result.	146
Figure 9.1 The whole AFM system setup.	149
Figure 9.2 Top view of the AFM	150
Figure 9.3 Sum and deflection meter.	151
Figure 9.4 The tune tab in the master channel	151
Figure 9.5 Tune graph shows the resonant frequency of the cantilever and the phase shift at resonant frequency.	152
Figure 9.6 The user interface of calibration of the spring constant.	152
Figure 9.7 Force panel in the AFM software.	153
Figure 9.8 Force curve of a glass substrate	154
Figure 9.9 Force curve of PU	154
Figure 9.10 Force curve of parafilm	155
Figure 9.11 Force curve of PVC	155
Figure 9.12 Main panel in the AFM software	156
Figure 9.13 Phase image, amplitude image, height image for a PU sample in each row: (a) setpoint amplitude: $900\text{ mV}$ , (b) setpoint amplitude: $500\text{ mV}$ , (c) setpoint amplitude: $200\text{ mV}$ .	157
Figure 9.14 Phase image (left column), amplitude image (middle column), height image (right column) of a parafilm sample, with each row representing: (a) setpoint amplitude: $900\text{ mV}$ , (b) setpoint amplitude: $500\text{ mV}$ , (c) setpoint amplitude: $200\text{ mV}$ .	158
Figure 9.15 Phase image, amplitude image, height image of parafilm in each row: (a) setpoint amplitude: $900\text{ mV}$ , (b) setpoint amplitude: $500\text{ mV}$ , (c) setpoint amplitude: $200\text{ mV}$ . ( $1.5\mu\text{m}\cdot 1.5\mu\text{m}$ )	159
Figure 9.16 Deflection signal of cantilever captured using oscilloscope from the real AFM instrument during experimentation: setpoint amplitude of $500\text{mV}$ , $Q=134.8$ , resonant frequency= $74504\text{ Hz}$ .	160
Figure 9.17 Phase shifts which were obtained using an FFT of the deflection signals and from the sum and deflection meter.	161
Figure 9.18 Comparison of the phase shifts recorded against different setpoint ratios for PVC, PU and Parafilm with the simulation results.	162

## List of tables

Table 3.1 Advantage and disadvantage of different models .....	72
Table 7.1 Different orders of natural frequencies of flexural mode.....	119
Table 7.2 Different orders of natural frequencies of torsion mode .....	119
Table 7.3 Different orders of natural frequencies of lateral mode and extension mode.....	119

# Chapter 1

# Introduction

# Chapter 1 Introduction

## 1.1 Background to Project

The Atomic Force Microscope (AFM) was first invented in 1986 by Gerd Binnig and his co-workers (Binnig et al., 1986). Generally, there are three operational modes in AFM: non-contact mode, contact mode and tapping mode (Jalili and Laxminarayana, 2004). Non-contact mode is usually used to detect the electric, magnetic and atomic forces of a sample. Non-contact mode works by lifting the cantilever just above the surface of a sample. The cantilever is vibrated near its resonant frequency. Non-contact mode detects the resonant frequency shift caused by the attractive forces, which can be used to extract the topography of the sample. As for contact mode, it retains contact between the AFM tip and the sample during the scanning process. Tapping mode is a combination of both contact mode and non-contact mode, where in each vibration cycle, the tip only intermittently contacts the sample and this mode is thus sometimes alternatively referred to as intermittent contact mode. The force-distance curve shown in Figure 1.1 indicates how the interaction forces change when the tip is getting close to the sample's surface. Also, the region of each operational mode, namely 'contact', 'intermittent contact' and 'non-contact', are marked in the force-distance curve.

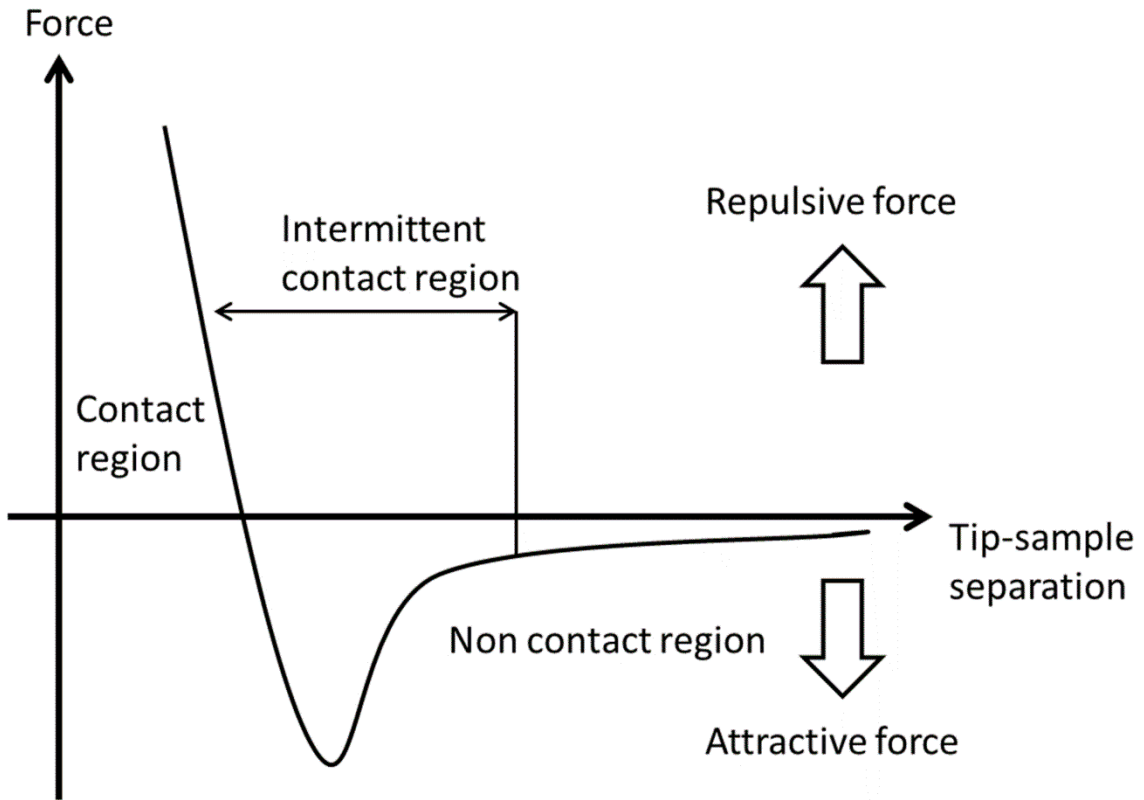
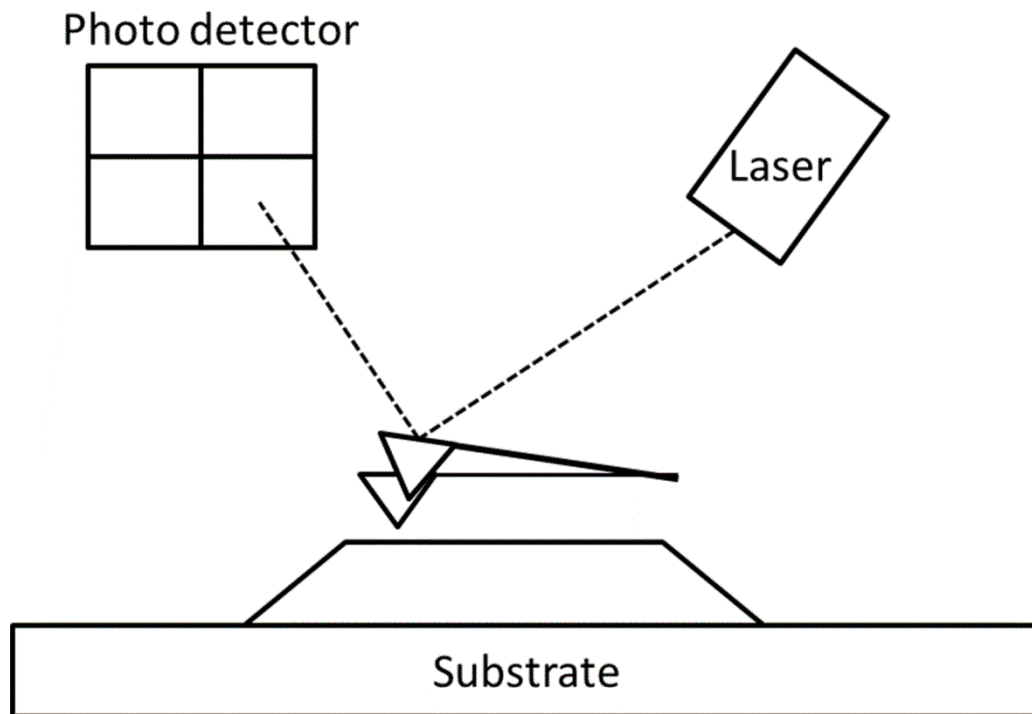


Figure 1.1 Force vs tip-sample separation

### 1.1.1 Non-contact mode AFM



**Figure 1.2 Schematic diagram of non-contact mode AFM**

Non-contact mode involves the AFM tip usually being vibrated at its resonant frequency at a distance of about 50 to 150 angstroms above the sample's surface. Figure 1.2 shows a schematic diagram for non-contact mode AFM. Nowadays, non-contact mode is applied within the range of the van der Waals forces. The topographic image is obtained by detecting the van der Waals forces between the AFM tip and the sample. Since the strength of the van der Waals force is relatively small compared with some of the repulsive forces, like the contact force, then in order to detect the variation in amplitude, phase, and frequency of the cantilever, it is necessary to make sure the tip vibration is smaller than 10nm. However, in reality when measuring in air, the sample is always contaminated by a surface fluid layer, caused by the humidity of the air. During the vibration process, the tip is dragged into this fluid layer, which significantly affects the detection of the van der Waals force, because the tip sample interaction force is no longer in the range of van der Waals force. Thus, the resolution of the topography image is limited by the contaminating fluid layer, which is one disadvantage of non-contact mode in air. The other is that non-contact mode cannot detect the tip-sample separation, which is considered to be an important

factor in improving the resolution of the topography image. Non-contact mode has been applied in different materials, such as metals, semi-conductors, polymers and biological samples, and it outperforms other techniques, like contact mode AFM and scanning tunnelling microscopy (STM), because non-contact mode can provide the topography image without contacting the sample. The attractive interaction force between the AFM tip and sample is in the range between 10 to 12 pN, which is good for imaging soft samples. Also, it would be useful for some samples like silicon wafers, which could be degraded during the tip sample contact using contact mode AFM. Without any contact between tip and sample the captured images would thus not be affected by the contamination and degradation of the tip under several consecutive experiments. Hence, non-contact mode AFM is usually performed in ultrahigh vacuum conditions. Under these particular circumstances, the quality factor of the cantilever is significantly increased, which can be larger than 10000. In other words, the sensitivity of the measurement is significantly enhanced. The frequency shift caused by the tip-sample interaction is therefore easier to detect (Jalili and Laxminarayana, 2004). Moreover, non-contact mode AFM is able to provide images with atomic scale resolution. Therefore, non-contact mode AFM has been applied in several different applications. Here, a sample surface of  $\text{TiO}_2(110)$  was imaged using non-contact mode AFM under ultra-high vacuum conditions, shown in Figure 1.3. The topographic image revealed a regular pattern of bright rows in the [001] direction with a thickness of 0.65 nm, while the corrugation along the bright row is 0.30 nm. It was found that the bright areas indicated the oxygen atoms of the  $\text{TiO}_2$  (Fukui et al., 1997). The surface of  $\text{Si}(111)$  was also investigated. It can be seen that in Figure 1.4 the adatoms were separately distributed on the  $\text{Si}(111)$  surface. It can also be noticed that the contrast changed in the middle part of the image, which could be due to a change of the atom position on the tip surface (Sugawara et al., 1997).

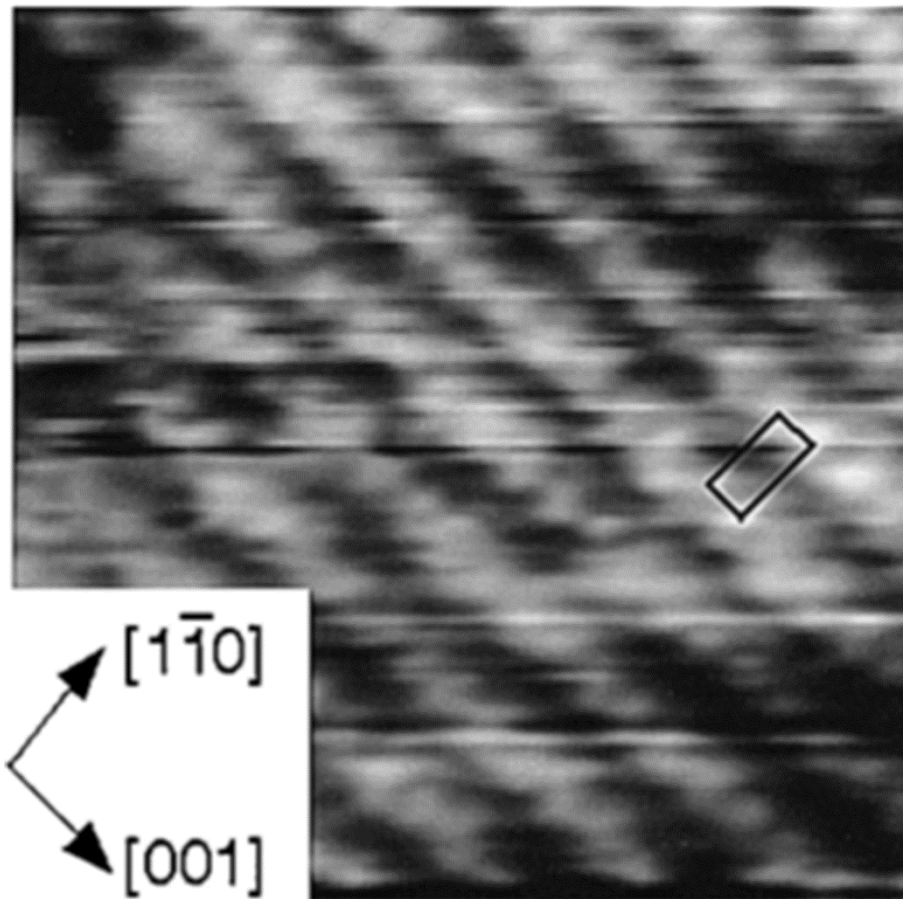


Figure 1.3 Topographic image of  $\text{TiO}_2(110)$  which was captured using non-contact mode AFM. Scan size: 5.4nm by 5.4nm. The peak to peak vibration amplitude of cantilever was 30 nm. A cantilever with a spring constant of 28 N/m and resonant frequency of 280 kHz was used in the experiment. The frequency shift set for this experiment is 80 Hz. Adapted with permission to reproduce this figure from (Fukui et al., 1997) has been granted by Chemical Physics Letters.

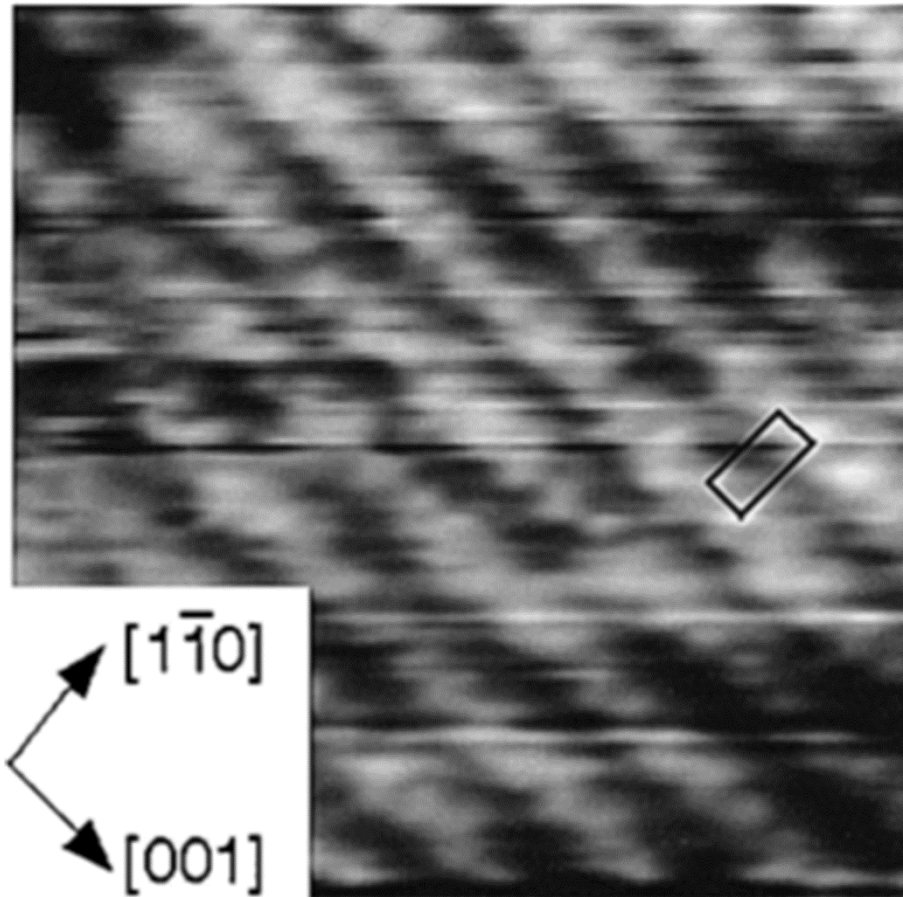
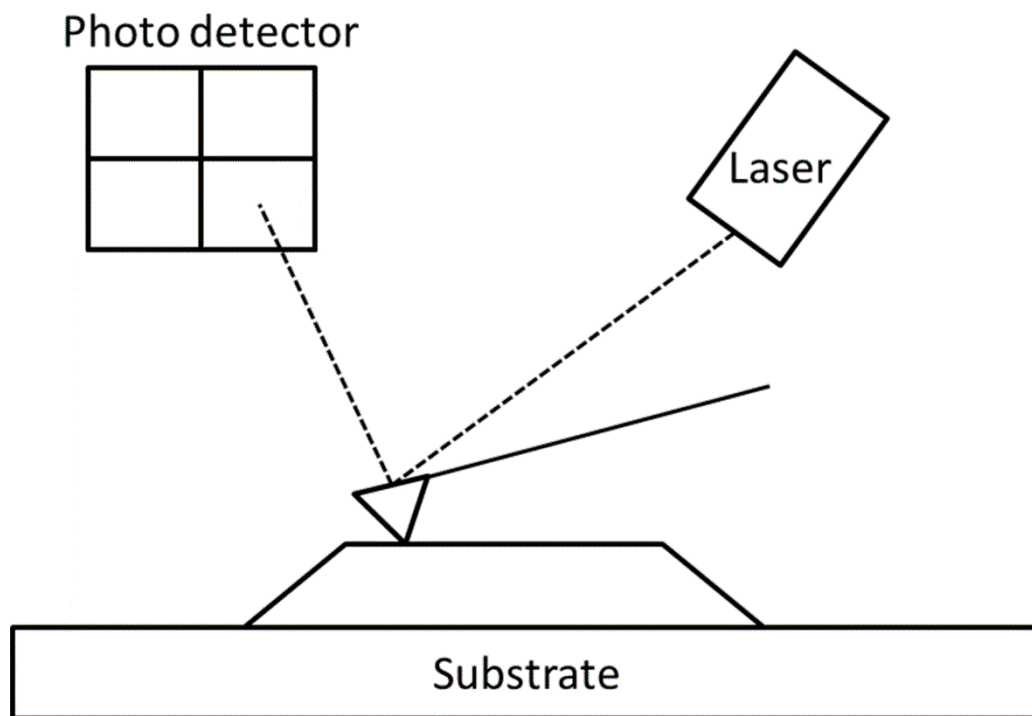


Figure 1.4 Topographic image of Si(111) surface which was captured using non-contact mode AFM. Scan size: 89 angstrom by 89 angstrom. The peak to peak vibration amplitude of cantilever was 16 nm. A cantilever with a spring constant of 36 N/m and resonant frequency of 169 kHz was used in the experiment. The frequency shift set for this experiment is -28 Hz. Adapted with permission to reproduce this figure from(Sugawara et al., 1997) has been granted by Applied Surface Science.

### 1.1.2 Contact mode AFM



**Figure 1.5 Schematic diagram of contact mode AFM**

During scanning, the tip remains in contact with the sample in contact mode AFM, as shown in Figure 1.5. In theory, the interaction force in the z direction is a repulsive force caused by the contact and the van der Waals force. Owing to the fact that the strength of the repulsive force is larger than that of the van der Waals force, the repulsive force is dominant. However, in an ambient environment, there is always a contaminating fluid layer caused by the humidity of atmospheric air. Thus, another attractive interaction force called the capillary force appears. In the lateral direction, a shear force occurs as the tip is dragged along the sample during scanning. There are two operational modes in contact mode AFM. One involves keeping the height constant, the other involves keeping the force constant. The 'constant height mode' works by moving the cantilever in the lateral direction to scan the sample. Movement in the vertical direction is not allowed. The interactions between the tip and sample cause a deflection of the cantilever, which is used to obtain the topography image. However, the disadvantage here is that the tip may easily damage, or even break, when it comes across some high features upon the sample's surface. On the other hand, 'constant force mode' is more popular in contact mode AFM. Here a feedback system is

adopted to maintain the tip sample interaction force so that it is constant in the z direction. Generally, the cantilever is firstly moved close to the sample until the cantilever deflection reaches a set value. During scanning the cantilever deflection is captured. If any difference between the cantilever deflection and the set value is found, the feedback system would set a voltage signal to the scanner to move the cantilever up or down, driving it so that the interaction force between tip and sample remains constant. Also, the voltage signal sent by the feedback system helps to provide the topography information. However, contact mode may damage softer samples, like polymers, or cells, due to the shear force coming from the lateral scanning process. Even if the topography image is obtained, it cannot reveal the true nature of the sample, because of the degradation caused by the tip. Thus, contact mode AFM is not recommended for use in imaging soft samples. However, contact mode AFM is still widely used in imaging living cells, because it is difficult to image living cells using tapping mode AFM as the tip becomes stuck to the sample surface during scanning. Experiments were performed by GERI cell mechanic group to image a living fibroblast cell. A silicon nitride triangular cantilever with a spring constant of 0.02 N/m and a resonant frequency of 11 kHz was used. During scanning, the force between the AFM tip and the sample was maintained at 2.8 nN. Figure 1.6 shows the deflection image of a living fibroblast cell.

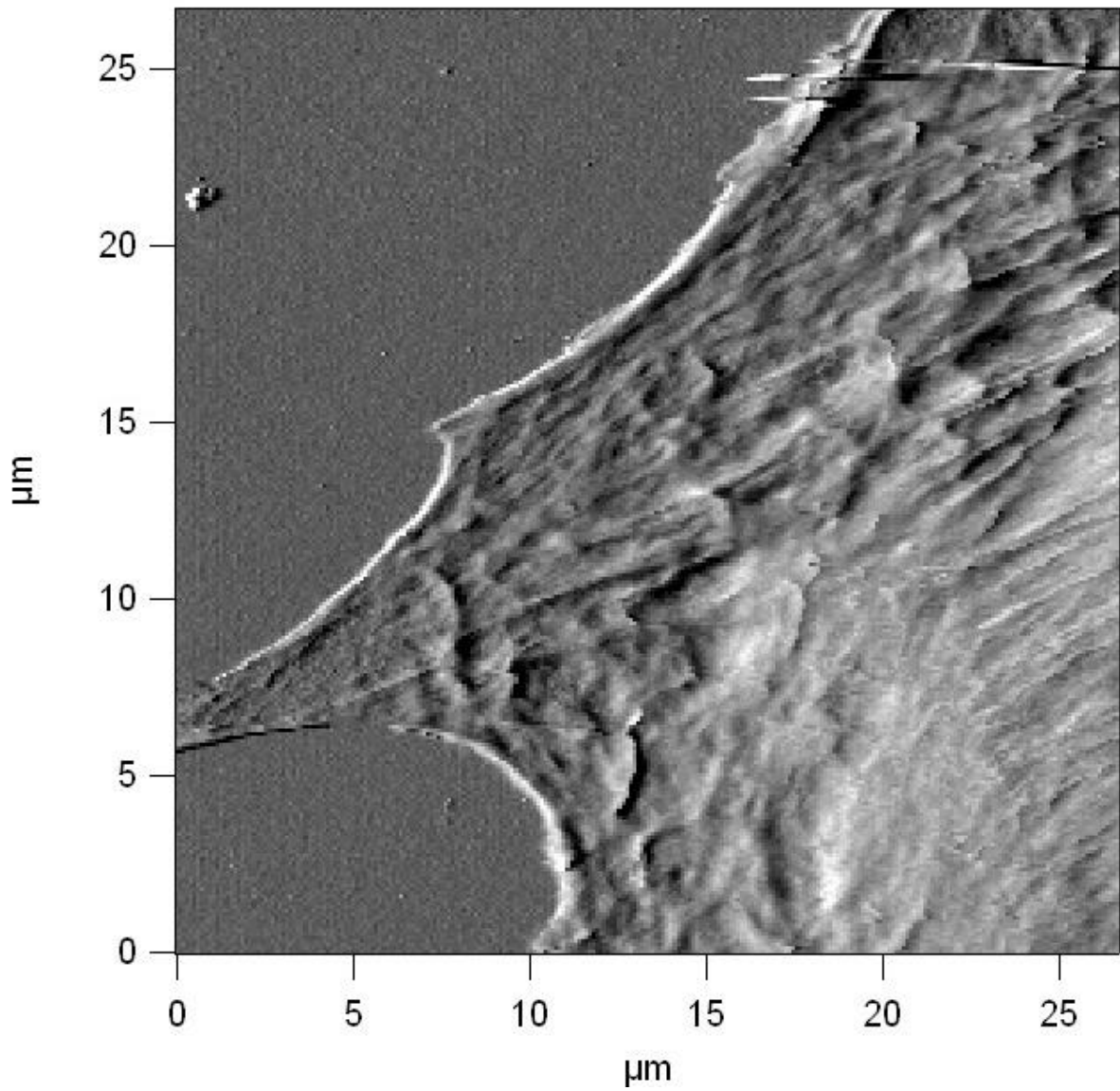


**Figure 1.6** Deflection image of a living fibroblast cell which was captured using contact mode AFM. Scan size: 27μm by 27μm.

### 1.1.3 Tapping mode AFM

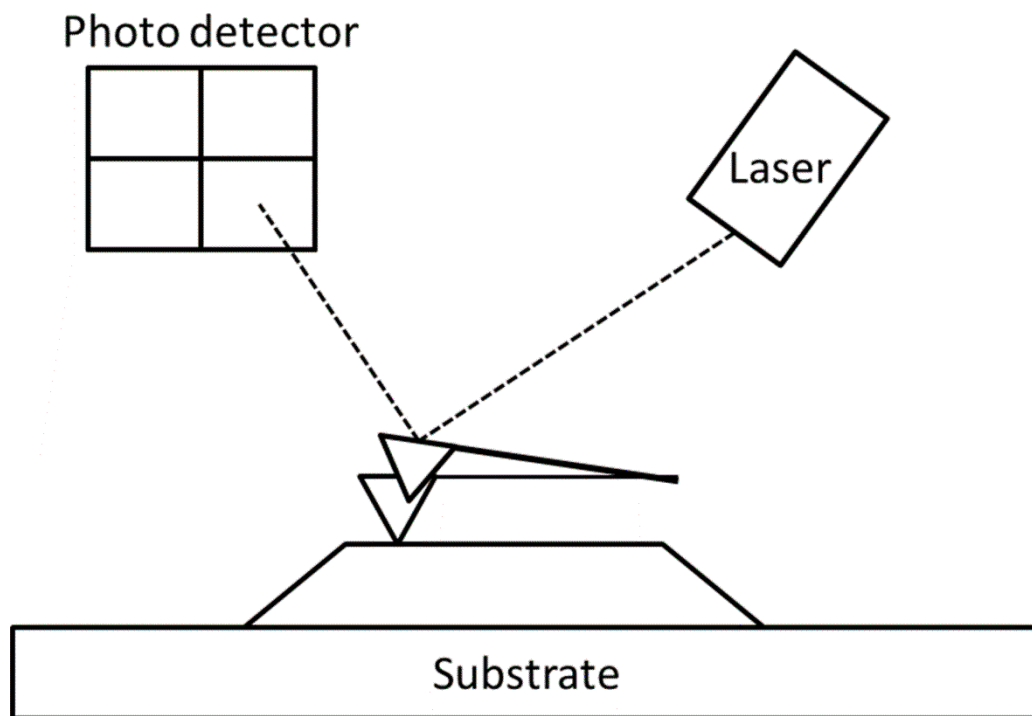


**Figure 1.7 Schematic diagram of tapping mode AFM**

Unlike contact mode AFM, in tapping mode the tip only contacts the sample intermittently in each vibration cycle, as shown in Figure 1.7. Thus, tapping mode will not easily damage the sample, which makes imaging soft material with high resolution possible. Moreover, tapping mode AFM can also provide an additional phase image, other than the standard topography image, which offers additional information compared to other AFM techniques. In tapping mode AFM, the cantilever is usually vibrated at, or near to, its resonant frequency (the first flexural mode) typically in the range from 50 kHz to 500 kHz. When the tip is far away from the sample, it almost feels no interaction forces, as the strength of the long range van der Waals force is in a magnitude of  $10^{-11}$  N and thus can be neglected. In this case, the cantilever is freely vibrated. The 'free' amplitude of the cantilever is usually in between 20 nm and 100 nm. As the tip comes close to the sample, the amplitude decreases for the tip becomes subject to the interaction forces between the tip and sample. During scanning, the optical system captures the amplitude of the cantilever and compares it to the setpoint amplitude. If amplitude difference is found, the feedback system will send a voltage to the z-piezo actuator so as to move the cantilever upwards, or downwards, in order to

maintain the amplitude constant. In other words, tapping mode keeps the amplitude of cantilever at the setpoint amplitude during the imaging process. Phase images and topography images are captured simultaneously. The difference between the actual amplitude and the setpoint amplitude is usually regarded as an error signal. This error signal, combined with the position of the x and y direction, form the amplitude image. The phase image is obtained by comparing the phase difference between the cantilever deflection and the drive signal, where the drive signal is that which is being used to vibrate the cantilever.

The use of tapping mode AFM may not be a good idea to measure living cells, but it is still widely applied in the area of biology and polymer materials surface science. Phase imaging is an extension of tapping mode AFM, which could provide better contrast compared with height images and amplitude images. Figure 1.8 shows the AFM images of a *S. typhimurium* cell covered with an EPS capsule using tapping mode AFM. The experiment was performed using a silicon rectangular cantilever with a spring constant of 40 N/m and resonant frequency of 40 kHz. The scanned size of the AFM images is 1 $\mu$ m by 1 $\mu$ m. The phase image in Figure 1.8(c) noticeably separates the *S. typhimurium* cell and its capsule cover in terms of bright and dark contrast. It can be seen that the phase image reveals the structure of the cell more clearly than height and amplitude images. Also, the phase image indicates that it has the ability to image the subsurface of the sample (Suo et al., 2006).

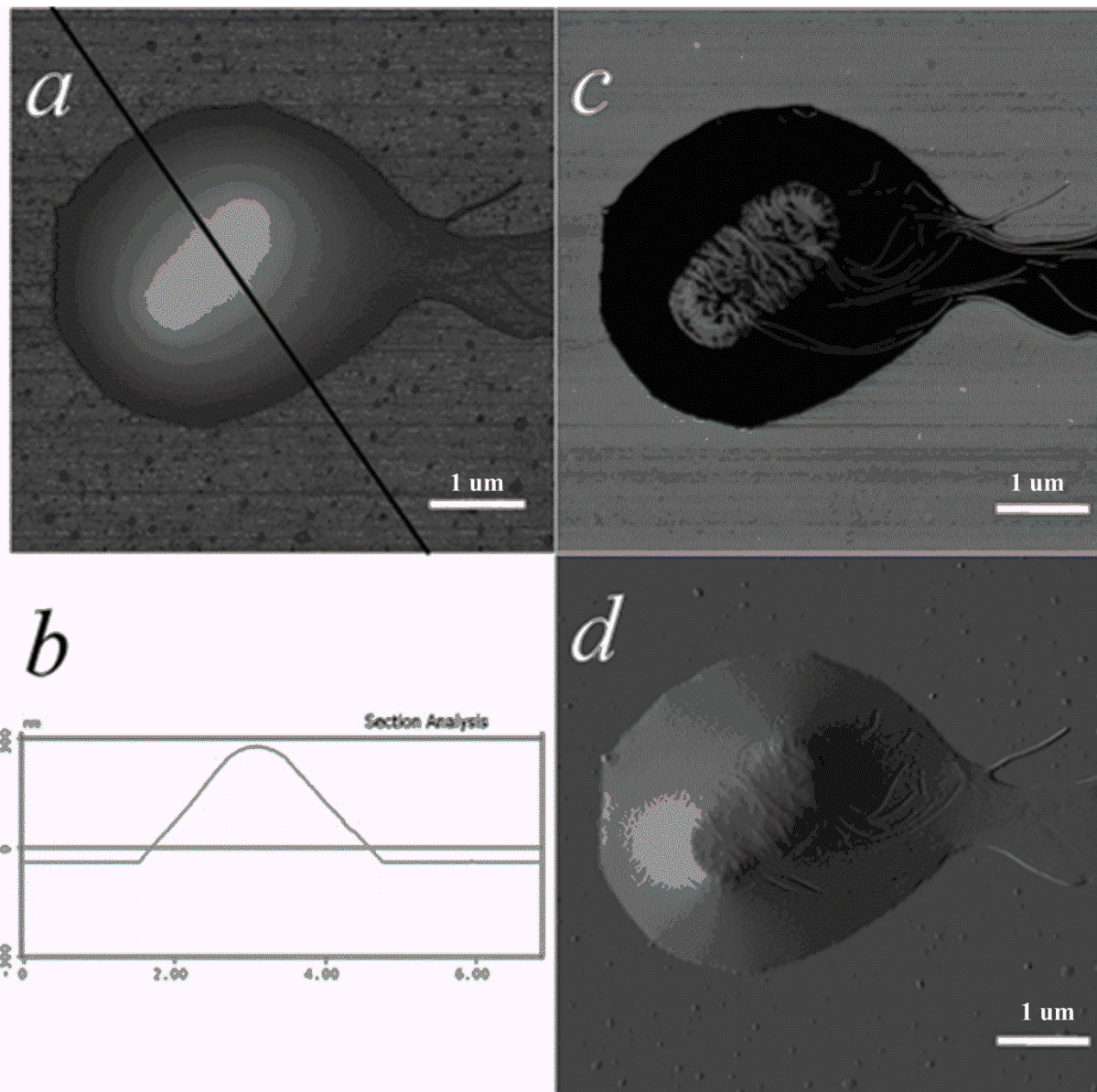


Figure 1.8 AFM images of a *S. typhimurium* cell covered with an EPS capsule. (a) height image; (b) height measurement of the black line indicated in (a); (c) phase image; (d) amplitude image. Adapted with permission to reproduce this figure from (Suo et al., 2006) has been granted by American Chemical Society.

## 1.2 Aims and Objectives

The aims and objectives of this thesis are given as follow:

- Investigate the dynamic behaviour of tapping mode AFM using 3D finite element method.
- Create a 3D contact model using commercial finite element software COMSOL Multiphysics.
- Also, create a 3D simplified model.

- Study the cantilever displacement responses under free vibration with different damping environment.
- Study the cantilever displacement responses under different tip-sample interaction forces, such as elastic force, adhesion force, viscosity force and van der Waals force.
- Phase shift, transition time, stable amplitude and instantaneous frequency are extracted from the cantilever displacement responses.
- Investigate how the interaction forces affect the phase shift.
- Provide guidance on how to select the setpoint amplitude for real experiment.
- Also, provide guidance on how to select the scanning speed corresponding to different sample.

### **1.3 Motivation and Contribution to knowledge**

Phase imaging could provide high resolution information about the sample surface and even the sub-surface structure, but it is still not well understood. Although AFM generates high quality images, it is often difficult to interpret these images physically in practical applications. A theoretical study of AFM imaging has therefore been carried out here. Although numerical modelling techniques were carried out to understand the fundamental physical mechanism of AFM imaging and to investigate the fundamental science behind the phase shifts (details will be reviewed in Chapter 3), full understanding and interpretation of the phase shifts is still elusive. In this thesis, the dynamic behaviour of tapping mode AFM has been studied through a combination of finite element analysis and experimentation.

In tapping mode AFM, the quality of the phase image is mainly affected by the dynamic behaviour of the cantilever during the tip-sample interaction. In this thesis, a 3D simulation contact model, consisting of a cantilever and a tip, and a test sample was firstly constructed to simulate the tapping mode imaging process of the real AFM system used in the experiments. Some preliminary results were obtained. However, the computation load was very large (about 20 hours to obtain one cycle vibration), and it was unrealistic to get the dynamic displacement response of the cantilever using this approach.

A simplified 3D geometrical model consisting of a piezo actuator, a cantilever and a tip was then built to investigate the cantilever behaviour during the tapping vibration process. The geometry of the cantilever and tip were based on a real cantilever that was used in the experiments and these modelled objects are then vibrated by the virtual piezo actuator. In

this simplified model the test sample was removed from the above 3D contact model. The test sample and tip-sample interaction was implemented by applying the tip-sample interaction forces, including elastic forces, adhesion forces, viscosity forces and the van der Waals forces. The tip-sample separation was implemented by adjusting the force loading time and loading directions during a tapping vibration period, so that these forces reflected the real tip-sample contact and interaction. This model facilitates the numerical studying of a variety of behaviours of the cantilever, such as the impact of the cantilever and tip geometry on the dynamic behaviours of the cantilever, the linear and nonlinear vibrations, and the vibration modes. This simplified model can not only significantly reduce the computational load, but also provides additional advantages. One major advantage is being able to study the impact of individual types of forces on the dynamic behaviour of the cantilever, and thus the phase shift.

Based on the aforementioned geometrical model simulations were subsequently carried out for mode analysis and frequency analysis to study the vibration modes, resonance frequencies and damping effects in different mediums, such as air and liquid, through finite element simulations.

The cantilever's dynamic behaviour was studied via simulation under different tip-sample separations and for different tip-sample interaction forces, such as elastic forces, adhesion forces, viscosity forces and the van der Waals forces, which correspond to the cantilever's action upon various different representative computer-generated test samples. The dynamic displacement response of the cantilever was obtained for the first time. Simulated results revealed that the dynamic cantilever displacement response consists of three states: a free vibration state, a transition state and finally the stable state. This finding enables further in-depth study of many phenomena. In the literature (Song and Bhushan, 2006a), numerical modelling normally directly leads to the phase shifts derived from the stable state, ignoring the transition state. Simulation results showed that the transition time is affected by many factors such as the geometry of the cantilever and tip, the tip-sample interaction forces (as a result of the sample materials, and surface conditions), the excitation voltage, and the tip-sample separation. The length of the transition time will determine the limit of the mechanical scanning speed of the cantilever during the AFM imaging process. If this

speed limit is exceeded, then the phase image quality will deteriorate. Moreover, the frequency changed in the transition state will help to elucidate the phase generation mechanism.

The phase shift is interpreted as the phase lag between the driving voltage signal and the actual displacement response of the cantilever in the stable state. The dynamic vibration of the cantilever is affected by different interaction forces, which are affected by many factors, including tip-sample separation, radius of the tip, Young's modulus, surface energy and the viscosity of the sample. In other words, all of these factors may make some contributions to the phase shifts that comprise the phase image. In order to be able to usefully interpret AFM phase images, the phase shifts caused by different interaction forces and for different test materials, under different tip-sample separations, were analysed from the dynamic displacement responses that were obtained. The findings not only help to understand the phase images, but also provide some theoretical guidance to potentially enhance the phase images themselves.

Transition times were analysed in this thesis from the dynamic displacement responses. The phase shifts in real tapping mode AFM are obtained from the stable state of the cantilever vibration. When the cantilever moves to an X-Y position during mechanical scanning, the cantilever needs to reach a new stable state due to the tip-sample separation changes that are caused by the surface topography of the test sample. The transition time taken to move from a free vibration state to a stable state limits the AFM's scanning speed. Therefore, an investigation of the transition times under different conditions, such as different tip-sample interaction forces and different tip-sample separations, can provide guidance on the selection of the optimal scanning speed to use in tapping mode AFM imaging.

The vibration amplitude in the stable state was investigated from the dynamic displacement responses. In the real AFM system, the stable amplitude is used to form the amplitude image. Simulation results showed that the amplitude image is not an exact reflection of the surface topography of the test sample in tapping mode imaging. Many other factors, such as the material of the test sample, will also contribute to the height image (Bar et al., 1997).

Frequency changes were analysed from the dynamic displacement responses in the thesis. The frequency variation analysis particularly in the transition state provides an efficient tool to study the generation mechanism of the phase shifts and for interpreting the phase images.

Finally, experiments were carried out on a real AFM system to support the findings of the computer simulations. Experiments were carried out using a Molecular Force Probe-3D (MFP-3D) atomic force microscope (Asylum Research, Santa Barbara, CA) with software written in IGOR pro (Wavemetrics, USA). The maximum scanning range in the x and y directions is 90  $\mu\text{m}$ , while the movement of the z-piezo is up to 16  $\mu\text{m}$ . In order to avoid problems due to external noise, the MFP-3D-IO was first mounted upon a TS-150 active vibration isolation table (HWL Scientific instruments GmbH, Germany), both of which were located inside an acoustic isolation enclosure (IGAM mbH, Germany).

The simulation methods and the data analysis techniques developed in this thesis provide an efficient way for dynamic analysis of tapping mode AFM and interpretation of phase images. This may lead to some new applications of tapping mode AFM, for example, detection of sub-surface defects of semiconductor device.

## **1.4 Structure of the thesis**

The thesis is divided into ten chapters and an appendix.

**Chapter 1** is the introduction illustrating background to the project, the motivation behind and contribution to knowledge of the research programme and also details the structure of the thesis.

**Chapter 2** describes the historical development of the atomic force microscope; it also provides an overview of different AFM techniques and introduces the mechanical system of a typical AFM.

**Chapter 3** reviews the theoretical models of AFMs, such as point mass models, 1D beam models and 3D numerical models.

**Chapter 4** introduces the typical interaction forces that occur in AFM systems

**Chapter 5** gives a general description of and discusses applications of phase imaging. Also, background theory and interpretation of phase images are presented.

**Chapter 6** proposes a real 3D contact model to simulate the behaviour of tapping mode AFM and discusses the difficulty in simulating the contact model.

**Chapter 7** describes the simplified simulation model used in this thesis in terms of its geometric model, boundary conditions and mesh parameters. Furthermore, here a model verification procedure is performed.

**Chapter 8** illustrates the simulation results. Different simulation studies are investigated, such as the modal analysis, damping analysis, free vibration analysis and contact vibration analysis. Also, results that have been post processed from the dynamic cantilever displacement are discussed, such as the phase shift, transition time, stable amplitude and instantaneous frequency.

**Chapter 9** shows the real AFM instrument based experiments that were conducted in this thesis and which are used as verification for the computer simulation results.

**Chapter 10** presents the conclusions and offers recommendations for further work.

# Chapter 2

## Background of Atomic Force Microscope

## **Chapter 2 Background of Atomic Force Microscope**

In Chapter 2, the evolution of the atomic force microscope is introduced. A brief description of variant AFM techniques is presented. The tapping mode AFM system is then described and illustrated through its various different components. Finally, the theory of cantilever calibration is demonstrated.

### **2.1 Evolution of the atomic force microscope**

In 1981, Gerd Binnig and Heinrich Rohrer invented the scanning tunnelling microscope (STM), which led them to be awarded with a Nobel Prize in 1986 (Binnig et al., 1982, Binnig and Rohrer, 1983). Figure 2.1 shows a schematic diagram of a scanning tunnelling microscope. In STM, a biased voltage is applied between the tip and the sample surface. When the tip approaches the sample surface, the electrons on the tip and the conductive sample surface begin to interact. STM detects the current between the tip and the sample surface when the tip moves very close to the surface. There are two mechanisms that can be used for imaging using STM. One is to keep the tip-sample separation constant during the scanning process in the x and y directions, whilst at the same time the changes of the current are detected. In this case, the captured image is called a current image. On the other hand, in STM it is more common to image the sample by maintaining the current constant, through a process of changing the tip-sample separation during scanning. Once the detected current is different from the user-set current, a voltage will be sent to the piezo actuator to change the tip-sample separation in order to drive it so as to meet the expected set-point current value. The voltage here can be regarded as an error signal which is used to form the STM image. The lateral resolution and vertical resolution of STM is 0.1 nm and 0.01 nm, respectively, which practically needs very good environmental vibration damping conditions and a very sharp tip. STM can be conducted in different conditions, such as ultra-high vacuum, air, water and so on. However, the disadvantage of STM is that it does not work well with non-conducting materials like biological samples and polymers. Hence, in order to deal with these disadvantages of STM, a few years later in 1986, Gerd Binnig and his co-workers invented the first atomic force microscope or AFM (Binnig et al., 1986), which has the great advantage over STM in that it can deal with most material types. The first AFM experiment was performed in contact mode by detecting the static deflection

of the cantilever. Another year later, Martin and his co-workers developed the first dynamic AFM (Martin et al., 1987). The cantilever was vibrated at its resonant frequency. During scanning, it was used to detect the long range attractive forces when the tip-sample separation was between 30 to 150 angstroms. In other words, the tip is not actually contacting the sample. The vibration amplitude of the cantilever was detected very accurately by using a laser heterodyne interferometer. Also, they suggested a method to image the profile of the sample by using the amplitude of the cantilever as a feedback signal to move the cantilever up or down so that the tip-sample separation could remain constant during scanning.

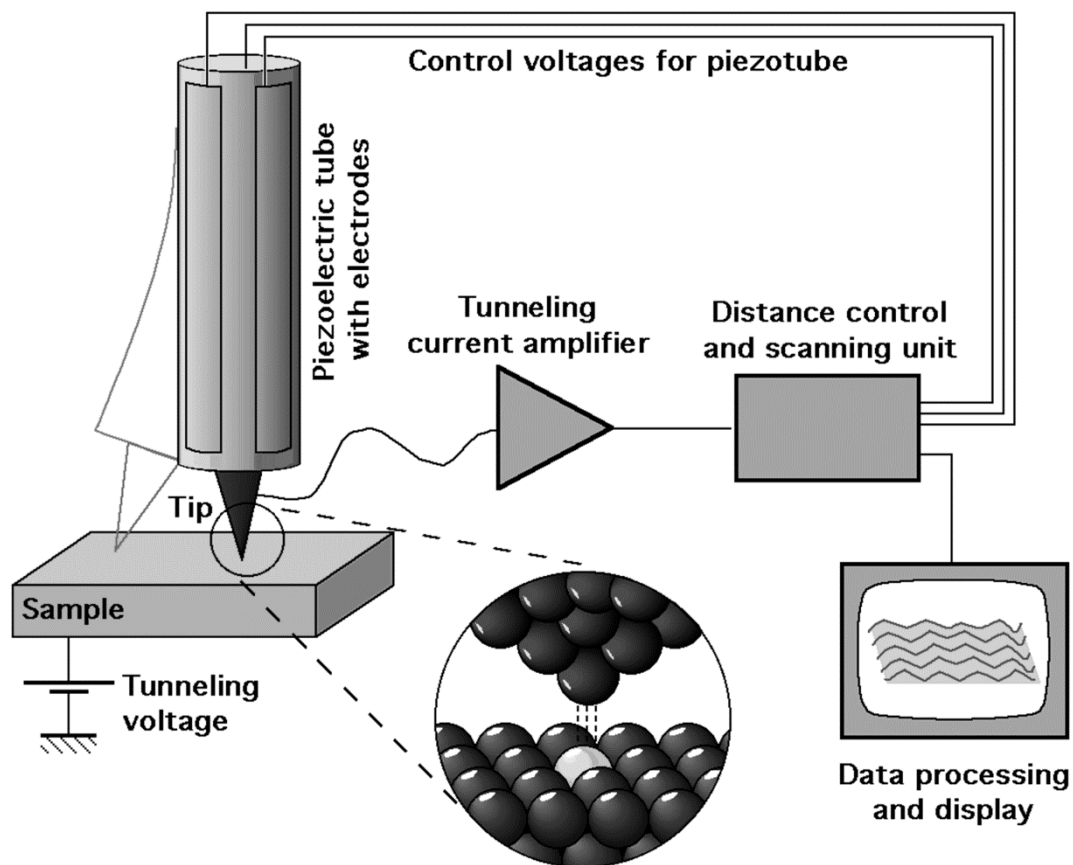


Figure 2.1 Schematic view of a scanning tunnelling microscope (STM). Adapted from ([http://en.wikipedia.org/wiki/Scanning\\_tunneling\\_microscope](http://en.wikipedia.org/wiki/Scanning_tunneling_microscope))

However, due to its complexity, there were only few dynamic atomic force microscopes in existence in these early years (Nonnenmacher et al., 1991, Martin et al., 1987). At that time, tungsten needles, shown in Figure 2.2, were used as cantilevers, while the cantilever

deflection was captured using an interferometer. The schematic diagram of the first dynamic AFM is shown in Figure 2.3. The advantage of this technique is that it could work with different devices to image the surface properties, such as the magnetic property and so on (Martin and Wickramasinghe, 1987, Nonnenmacher et al., 1991, Terris et al., 1989). In order to image the magnetic field of the sample, a soft cantilever with a spring constant less than 1 N/m, was vibrated at its resonant frequency while scanning across the sample. The amplitude of the cantilever changed due to the magnetic field of the sample, and would be detected by the laser probe, which was a device that was introduced into the AFM system. Dynamic AFM was not widespread until 1993. With a growing interest of imaging bio-sample surfaces, such as DNA, proteins, etc (Radmacher et al., 1994, Fritz et al., 1995, Leuba et al., 1994, Rivetti et al., 1996, Lyubchenko and Shlyakhtenko, 1997, Anselmetti et al., 1994) and polymers (Zhong et al., 1993, Spatz et al., 1996, Leclère et al., 1996, Magonov and Reneker, 1997, Bar et al., 1997, McLean and Sauer, 1997) at the nano-scale, dynamic AFM was subsequently widely explored and expanded. Improvements to the instrument were made. The cantilever deflection was captured by adopting the optical beam deflection method (Meyer and Amer, 1988, Alexander et al., 1989), while micro-machining techniques made it possible to produce a cantilever with a high resonant frequency, small spring constant and a sharp tip, which significantly improved the sensitivity of the measurement, resulting in an increasing reliability of the instrument (Albrecht et al., 1990, Wolter et al., 1991). The development of measuring the phase shift and topography of surfaces simultaneously was a significant milestone with the advent of tapping mode AFM, which made it possible to image the variation of the structure and the material property. Also, tapping mode AFM was able to be carried out in liquid, which helped to observe dynamic changes in biomolecules (Hansma et al., 1994, Putman et al., 1994). The short cantilevers fabricated by Paul Hansma and Virgil were proved to suppress thermal noise. Experiments were performed to investigate the thermal noise of different lengths of cantilever. The level of thermal noise could be measured through the thermal motion amplitude at the resonant frequency. It was found that the thermal motion amplitude could drop by about two orders of magnitude for short cantilevers, when compared with that of a long cantilever. Also, it was discovered that images could be captured at a scanning speed of 65  $\mu\text{m/s}$  without damaging the sample, which indicated that short cantilevers could make great contributions in the development of fast AFM imaging (Walters et al., 1996, Viani et al., 1999).



Figure 2.2 SEM image of tungsten needle. Adapted from (<http://www.brukerafmprobes.com/p-3411-dtt10.aspx>)

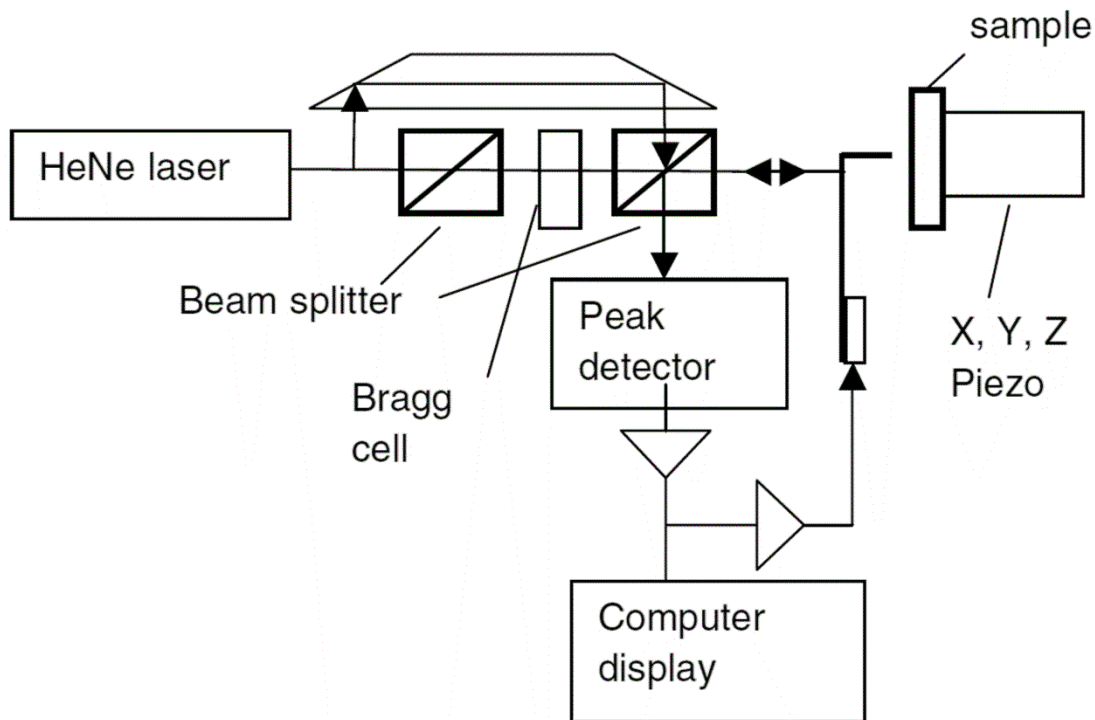


**Figure 2.3 Schematic diagram of the mechanism of the earliest dynamic AFM**

Although AFM techniques were able to image surface structure with nanoscale resolution, people still did not really understand why AFM techniques could provide such features. At that time, the reason why the amplitude decreases and what triggers the higher harmonics was not clear. In between 2000-2006, an increasing number of papers were published to study this technique in order to gain a better theoretical understanding of AFM, such as the nonlinear behaviour of cantilever dynamics (Nony et al., 1999, García and San Paulo, 2000, Sebastian et al., 2001) and the generation of higher harmonics (Stark and Heckl, 2000, Rodríguez and García, 2002). Stark and his co-workers managed to capture the time resolved interaction force through the integration of the cantilever vibration of higher harmonics (Stark et al., 2002). On the other hand, researchers used higher vibration modes to measure sample properties (Sahin et al., 2004, Stark et al., 2002, Rodríguez and García, 2004), where it was found that the elasticity of the material was very sensitive to the higher harmonics. Molecular resolution images were also captured. Muller and his co-workers obtained purple membrane images in tapping mode, shown in Figure 2.4, and in contact

mode AFM. Both of the images provided a lateral resolution of around 1.1 nm (Möller et al., 1999). The other finding was that molecular resolution could be achieved in air. Klinov and Magonov succeeded in imaging a polymer sample, which reached a resolution of about 0.4 nm (Klinov and Magonov, 2004).

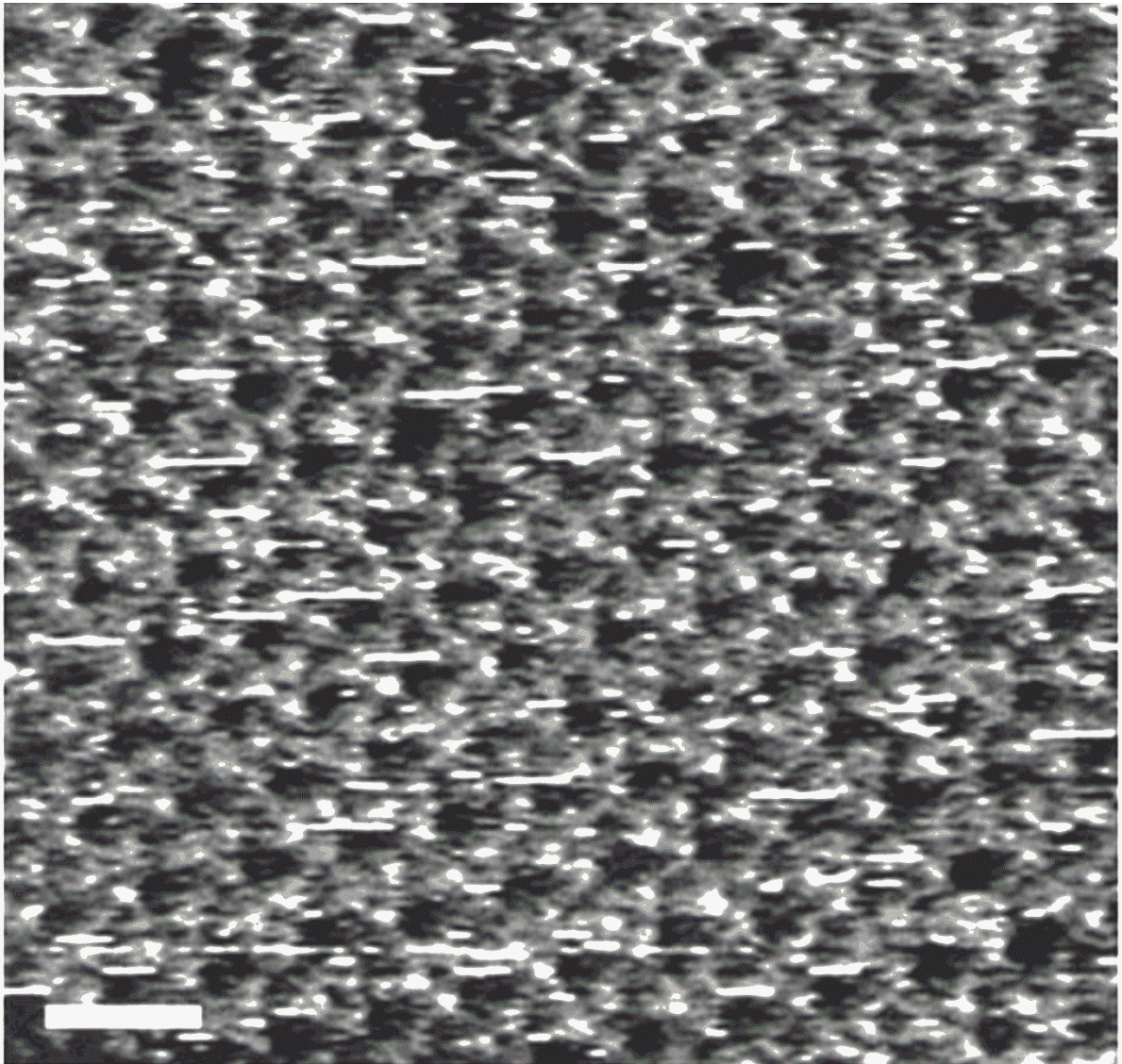


**Figure 2.4 Topography image of purple membrane captured using tapping mode AFM. Setpoint amplitude: 11 mV. Scanned size: 180nm by 180nm. Adapted with permission to reproduce this figure from (Möller et al., 1999) has been granted by Biophysical Journal.**

Later, a new AFM technique called bimodal AFM was established. Bimodal AFM (Martínez et al., 2008) works by activating the first and second flexural modes of the cantilever

simultaneously, as shown in Figure 2.5. The aim of this technique is to image the material properties of the sample with molecular spatial resolution.

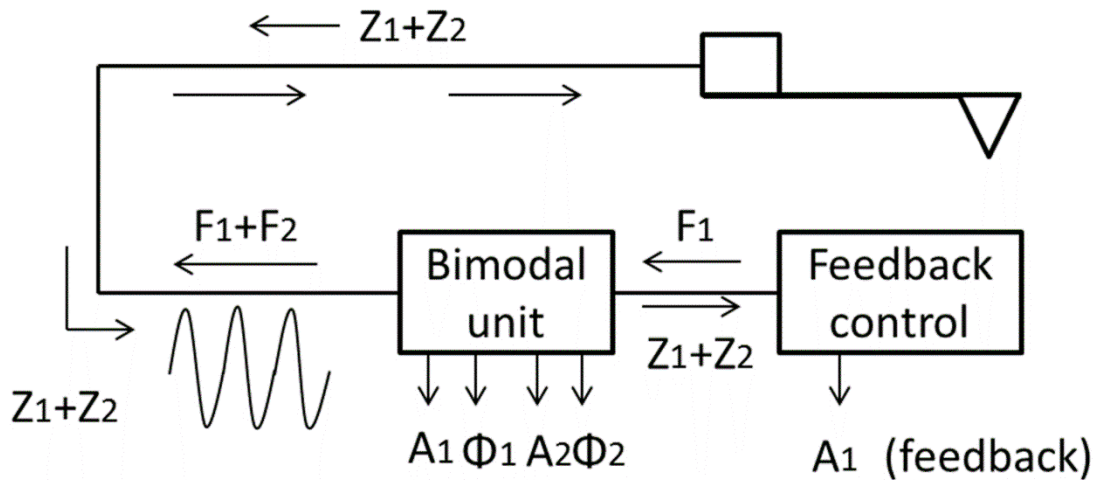


Figure 2.5 Schematic diagram bimodal AFM

Numerical modelling has also been used to investigate the cantilever dynamics of AFM. The sudden change in amplitude between the repulsive and attractive force regimes was able to be explained by (Kühle et al., 1997, García and San Paulo, 1999, Anczykowski et al., 1996). It was found that whether, or not, the change of amplitude from the attractive regime to the repulsive regime was smooth, largely relied upon the free vibration amplitude of the cantilever and the material properties of the sample. A sudden change in amplitude was usually shown when a hard material specimen and small free vibration amplitude were used. On the other hand, the transition between attractive and repulsive regimes was very smooth when a soft material specimen was used. Also, it was found that the phase shifts were related to the energy dissipation, as shown in Figure 2.6. This indicated that the phase shifts of different elastic moduli were almost the same when only elastic force was considered. However, when elastic force was coupled with energy dissipation, the phase shifts of compliant materials were significantly changed. On the other hand, the phase shifts of stiff materials seem not sensitive, compared with that of soft materials. Subsequently, an analytical expression between phase shift and energy dissipation was first developed by (Tamayo and García, 1997).

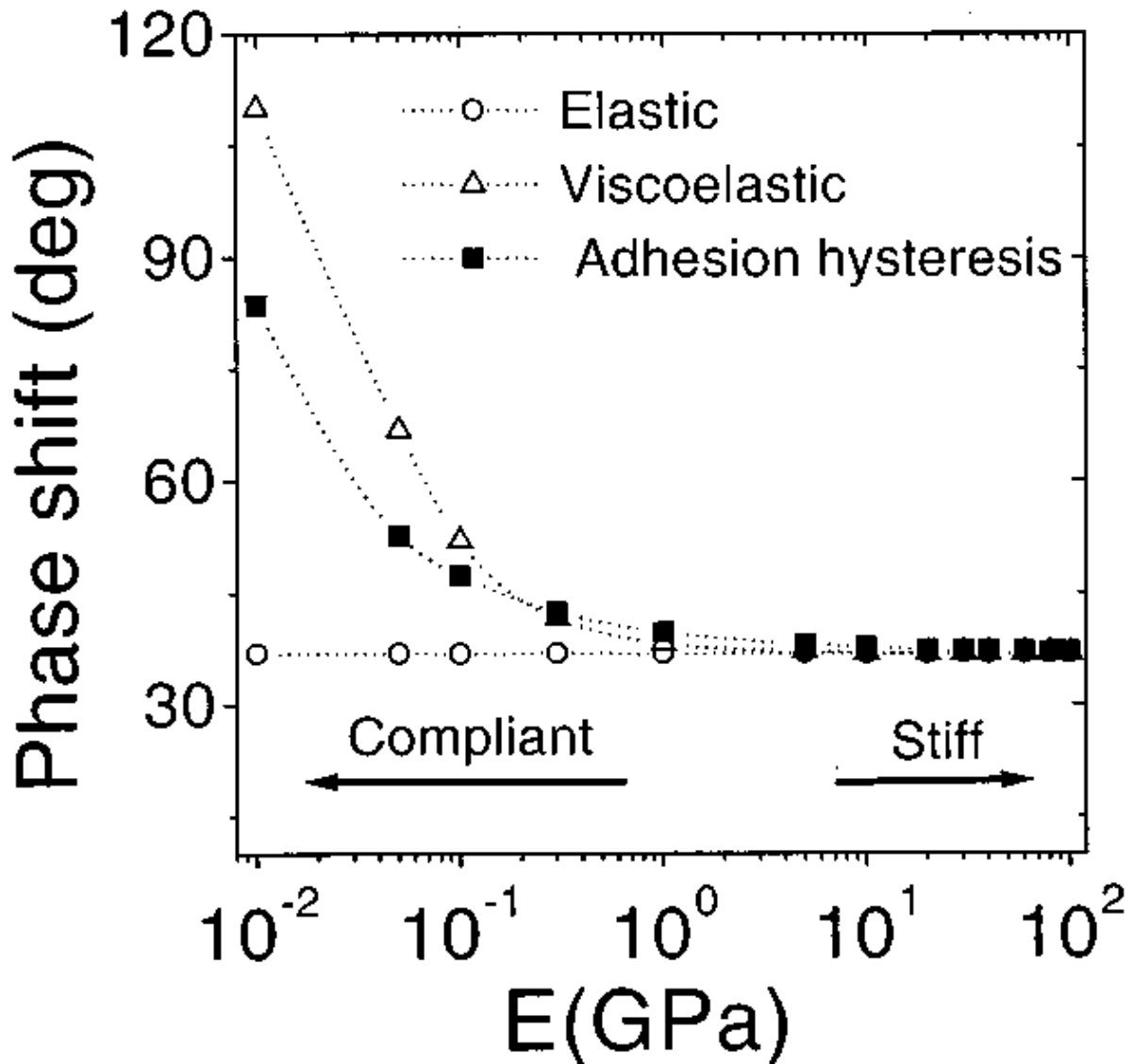


Figure 2.6 Phase shifts against materials with different Young's modulus. Q factor is 500,  $A_v/A_0 = 0.6$ ,  $k=20$  N/m, resonant frequency is 200kHz. Adapted with permission to reproduce this figure from (Tamayo and García, 1997) has been granted by Applied Physics Letters.

## 2.2 Vibration Modes of the Cantilever

Different AFM techniques have been developed since the invention of the atomic force microscope. In relation to the aspect of the various vibration modes, there are flexural modes, torsion modes, lateral bending modes and extension modes, which are shown in Figure 2.7. In flexural mode, the cantilever vibrates around the y axis, while the cantilever vibrates around x axis in torsion mode. In lateral bending mode, the cantilever vibrates around the z axis. The cantilever displacement is in the x direction in extension mode.

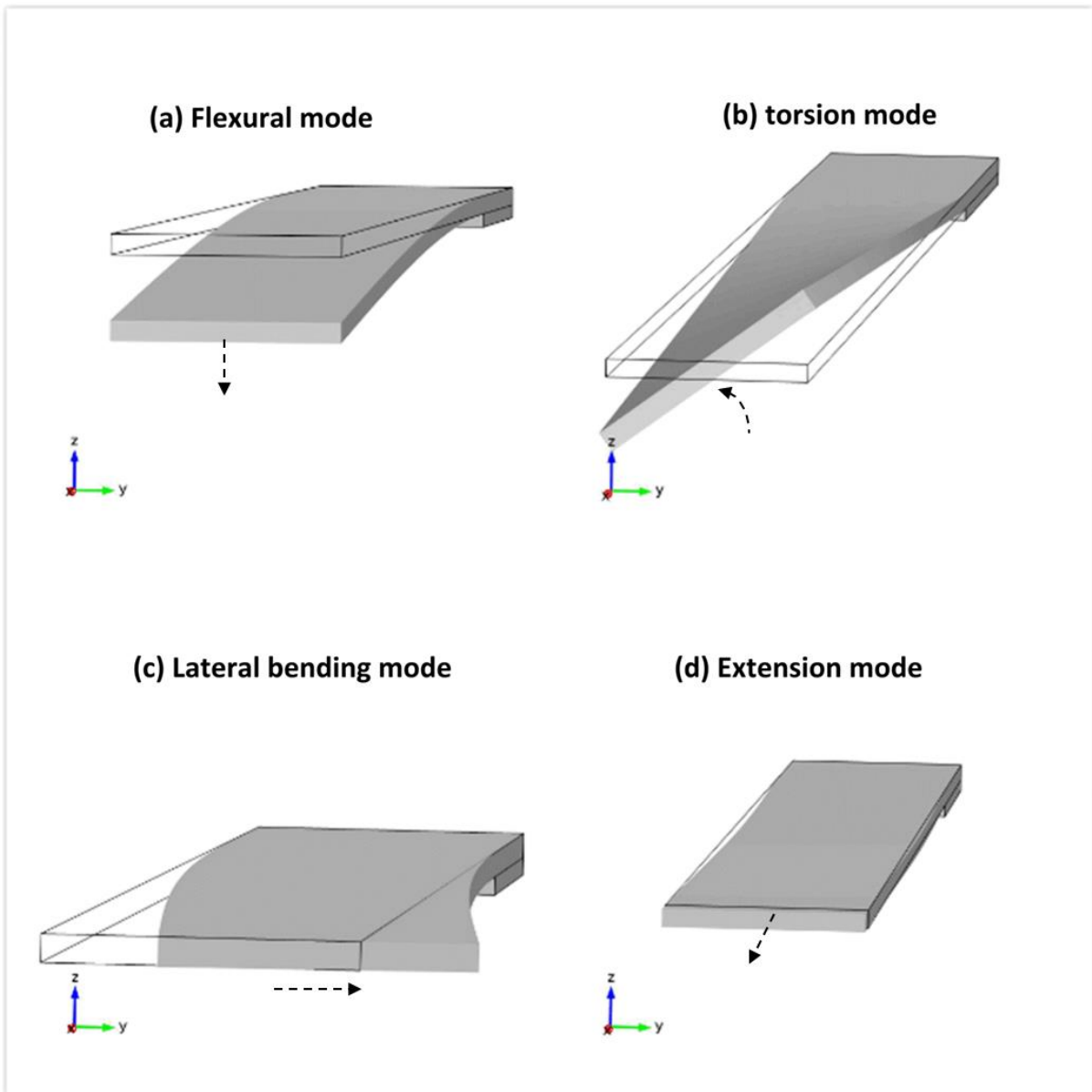


Figure 2.7 Vibration modes of the cantilever

### 2.3 Variants of AFM Imaging techniques

In the aspect regarding the dynamic movement of the cantilever, AFM techniques can be divided into two basic types. One is static mode AFM, the other is dynamic mode AFM. Generally, static mode AFM can be described in a manner such that the tip is pressed onto the sample surface, then the tip is dragged along the surface during the scanning process. The movement of the cantilever can be considered as quasi-static, while the cantilever is

vibrated near to, or at, its first resonant frequency in dynamic AFM mode. Dynamic AFM mode offers benefits compared to static AFM mode, for it has the advantage of obtaining better signal to noise ratio and provides more information concerning the sample's surface with higher resolution (Turner et al., 1997, Dupas et al., 2001, García and Pérez, 2002). To be more specific, contact mode and friction force microscopy (FFM) belong to static mode AFM classifications, while dynamic mode AFM includes tapping mode (TM or intermittent mode), non-contact AFM (NC-AFM), force modulation mode (FMM), atomic force acoustic microscopy (AFAM) mode (or ultrasonic atomic force microscopy, UAFM), torsional resonance (TR) mode, lateral excitation (LE) mode and combined normal and lateral excitation mode.

### **2.3.1 Static mode AFM techniques**

Contact mode AFM is performed by keeping constant contact between tip and sample, whilst, at the same time, the topography is measured. The deflection of the cantilever in the normal direction is obtained by detecting its rotation around the  $y$  axis. The tip-sample interaction force in the normal direction is obtained by multiplying the spring constant of the cantilever and the normal deflection. Contact mode AFM also provides a way to measure the adhesion of the sample by using force distance curve. As for friction force modulation mode, this is a popular method to measure friction. During scanning, friction force modulation mode keeps the normal force constant between the tip and sample. Through measuring the twist angle of the cantilever along the scanning direction, the tip-surface friction force is captured (Marti et al., 1990, Meyer and Amer, 1990).

### **2.3.2 Dynamic mode AFM techniques**

In tapping mode AFM, the cantilever is always vibrated at, or near to, its resonant frequency. The characteristic of this mode is that the tip intermittently contacts the sample during scanning. Moreover, it can provide phase imaging in addition to the usual height image and amplitude image, compared with other AFM techniques. As for non-contact mode AFM, it is sometimes also named frequency modulation AFM (FM-AFM) (Albrecht et al., 1991), where the cantilever is always vibrated at the resonant frequency and the vibration amplitude is maintained constant. Hence, there are two feedback loops in non-contact mode AFM. One

is used to maintain the resonant frequency constant by applying a phase shift of  $90^\circ$  to the vibration signal and then adopt it as a new excitation signal. The other is used to maintain the vibration amplitude constant by changing the amplitude of the excitation signal. During scanning, the tip-sample interaction forces cause the frequency shifts. The topography image is obtained by maintaining the frequency shifts constant in terms of moving the cantilever up or down. There are some advantages of non-contact mode AFM, compared with tapping mode AFM. Non-contact mode AFM can achieve a high quality factor  $Q$ , which can help increase the resolution of image. On the other hand, non-contact mode can even capture images of atomic resolution under small tip-sample separations when it is performed under ultra-high vacuum conditions (Giessibl, 1995, Shin'ichi Kitamura and Masashi Iwatsuki, 1996).

Similar to tapping mode and non-contact mode AFM, vertical bending is also dominant in force modulation microscopy (FMM) and atomic force acoustic microscopy (AFAM). The vibration of the cantilever can be achieved in two ways. One method is to vibrate the cantilever holder, the other technique involves vibrating the base of the sample in the normal direction. During scanning, the tip-sample separation is maintained at a very small distance in order to avoid the tip lifting off the sample surface. In this case, the tip-sample interaction forces can be regarded as being linear (Song and Bhushan, 2008). In force modulation microscopy, the feedback control is turned off in the z-direction. During scanning, the vibration amplitudes of the cantilever reflect the changes in local stiffness. Hence, FMM provides a way to image the elasticity of the sample, especially in the case of soft materials. However, this method does not work so well for hard materials, because hard samples almost do not deform at all. Thus, imaging hard materials may not provide sufficient contrast difference (Maivald et al., 1991, Scott and Bhushan, 2003). On the other hand, AFAM (Rabe and Arnold, 1994, Rabe et al., 1996, Rabe et al., 1998, Rabe et al., 2000, Rabe et al., 2002, Amelio et al., 2001, Hurley et al., 2003, Turner et al., 1997, Turner, 2004) can fill in this gap for imaging hard materials. Here the cantilever is vibrated at ultrasonic frequencies, which can be up to 3MHz. When the cantilever is vibrated at higher order modes, its effective stiffness is improved. Thus, AFAM is able to cause the necessary deformation of hard materials in order to image their elasticity.

The mechanism of torsion resonance (TR) mode (Bhushan and Kasai, 2004, Kasai et al., 2004, Huang and Su, 2004, Reinstädtler et al., 2005a) is different from tapping mode AFM. Two piezos are located on the cantilever holder, which are simultaneously applied with opposite voltages, as shown in Figure 2.8. Under these circumstances, the cantilever is vibrated in a torsional manner. When the tip feels the lateral forces, lateral bending is coupled into torsional resonance mode. On the other hand, the vibration of the cantilever in lateral excitation (LE) mode (Yamanaka and Tomita, 1995, Scherer et al., 1999, Reinstädtler et al., 2005b, Reinstädtler et al., 2003) is caused by the harmonic excitation of the sample. Generally, a piezo actuator is attached beneath the sample holder, which generates lateral vibration. Similar to the TR mode, LE mode is coupled with torsional and lateral bending. Both TR mode and LE mode are widely used to measure surface properties. During scanning, in order to obtain more information about the sample, the tip-sample separation is kept very small. In this case, the stiffness of the cantilever calculated from vertical bending is usually two orders of magnitude smaller than that calculated from lateral and torsional bending. Also, torsional resonance (TR) mode and lateral excitation (LE) mode can guarantee that the deformation mostly stay on the sample. Thus, TR and LE modes are useful for imaging hard materials. According to (Chen and Bhushan, 2005), a phase image captured using TR mode provides more information about the sample than that which is obtained in tapping mode AFM. There are different AFM techniques in existence using the LE mode described above, such as lateral force modulation AFM (LM-AFM), acoustic friction force microscopy and lateral atomic force acoustic microscopy (lateral AFAM). Although they all adopt the lateral excitation technique, the respective excitation frequencies used are different. In LM-AFM, the vibration frequency of the sample is around 16 kHz, while the vibration frequencies in AFFM and lateral AFAM are much larger, and can be as large as 3 MHz. Among these techniques, a measure of the torsional amplitude can be obtained, which is used to measure the friction of the sample.

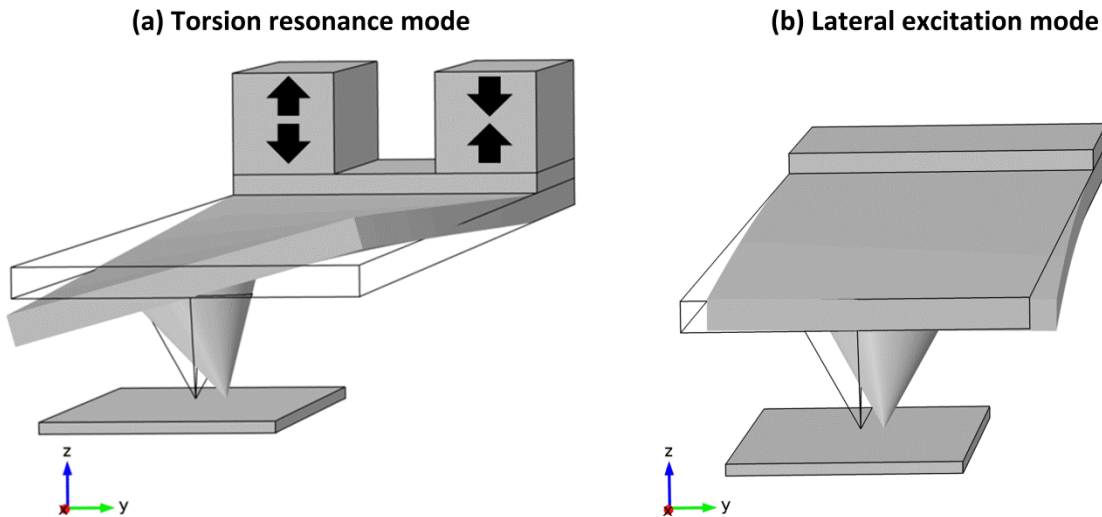


**Figure 2.8 Torsion resonance mode and lateral excitation mode AFM.**

The last AFM mode described here is the combination of flexural mode and LE mode. In other words, the techniques used in AFAM and LM-AFM are coupled together. The cantilever is vibrated in the z direction by the vibration of the sample with a frequency much higher than the first resonant frequency of the vertical bending mode. In the meantime, the sample is simultaneously vibrated laterally with a frequency much lower than the resonant frequency of the lateral bending mode. The advantage of this mode is that it can image the subsurface of the sample (Yamanaka et al., 1994).

## **2.4 Key Components of tapping mode AFM**

### **2.4.1 AFM System**

The key components of a tapping mode AFM system are shown in Figure 2.9. The cantilever is vibrated at, or near to, its resonant frequency. Any interaction forces on the tip would cause the deflection of the cantilever, which is captured by the photodiode detector. Here the setpoint amplitude can be considered as being the key to capturing the image in this AFM mode, which can also be regarded as the tapping amplitude of the cantilever. During scanning, the setpoint amplitude (tapping amplitude) of the cantilever is maintained at a constant level by using a feedback system, which can detect any variations from the target tapping amplitude. When any variation is found, the feedback system sends a signal to the

z-piezo controller to move the cantilever up or down in order to meet the target tapping amplitude. The scanning in the x and y direction is controlled by the x and y piezo actuators. In the following sections, the key components of tapping mode AFM will be introduced individually.

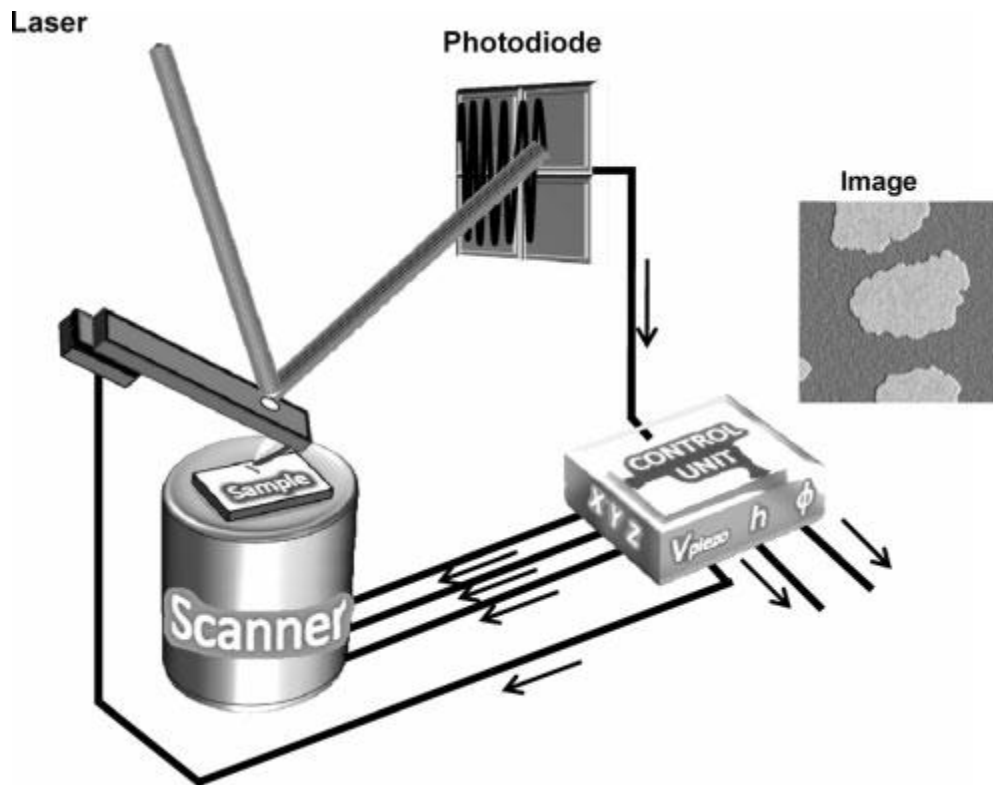


**Figure 2.9 Schematic diagram of the key components of a tapping mode AFM system. Adapted with permission to reproduce this figure from (Garcia, October 2010) has been granted by Wiley Books**

### 2.4.2 Feedback system

In tapping mode AFM, the feedback system is an important part of the system, as shown in Figure 2.10, for it keeps the amplitude constant during the entire scanning process, or when the tip just indents one part of the sample without scanning. A lock-in amplifier is used to detect both the amplitude and the phase of deflection signals. During the measurement process, it compares the difference between the instantaneous amplitude of the cantilever and the setpoint amplitude, which is regarded as an error signal. The error signal is then processed by the proportional integral differential (PID) system, also commonly known as the gain of the system, which outputs a voltage signal to the z piezo which acts to move the

cantilever up or down. The aim of feedback system is to keep the error signal as small as possible. The maximum scanning speed of the microscope depends on how fast the feedback system can adjust the instantaneous amplitude to reach the setpoint amplitude. The range of the acquisition rates is typically between 60 to 500 kHz (Ando et al., 2008).

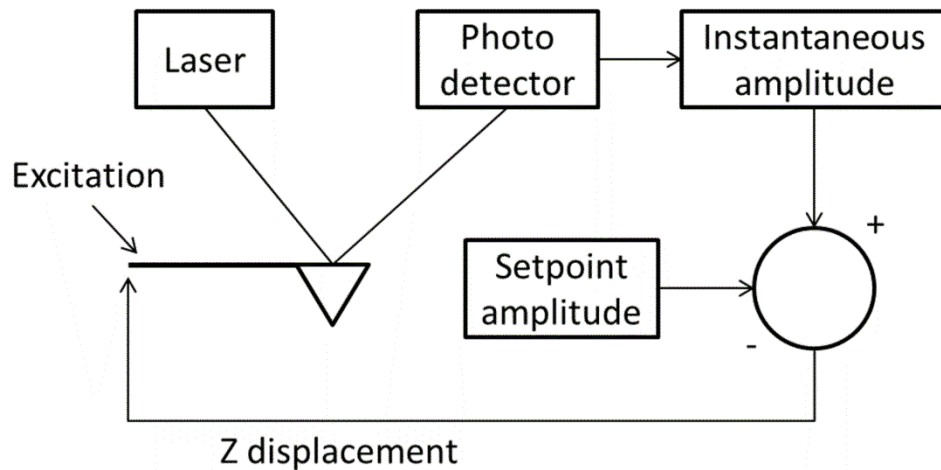


**Figure 2.10 Schematic diagram of feedback system**

### 2.4.3 Optical beam deflection method

The accuracy of the cantilever deflection detection method plays an important role in atomic force microscope. The optical beam deflection method (Alexander et al., 1989) made a great contribution to AFM for its excellent sensitivity and simplicity. Generally, in this method a laser diode launches a light beam onto the back surface of the free end of the cantilever. Any deflection of the cantilever is detected by the photodetector. The photodetector makes it possible to detect the deflection of the cantilever caused by interaction forces in both normal and lateral directions. Thermal noise within the system is the main factor that affects the detection sensitivity. Normally, the system is capable of detecting deflections of the cantilever under 0.01 nm. The optical beam deflection method measures the slope of the vertical deflection of the cantilever instead of the deflection. For a rectangular cantilever, the definition of the cantilever deflection is given with the help of Euler Bernoulli theory, as shown in Equation 2.1:

$$z(x) = \frac{F}{2k} \left[ 3 \left( \frac{x}{L} \right)^2 - \left( \frac{x}{L} \right)^3 \right] \quad (2.1)$$

where  $F$  is the interaction force acting on the tip,  $L$  and  $k$  are the length and spring constant of the cantilever, respectively. From Figure 2.11, it can be seen that the deflection captured by the photo detector is amplified, compared to the cantilever deflection. The relationship between deflection captured by the photo detector  $\Delta A$  and the deflection of cantilever  $\Delta z$  is shown in Equation 2.2:

$$\Delta A \approx 2 \frac{D}{L} \Delta z \quad (2.2)$$

Of course, there are various alternative detection methods, details can be found in (Rugar et al., 1989, Tortonese et al., 1993, Sarioglu and Solgaard, 2008). However, the optical beam deflection method outweighs all other methods in terms of its excellent signal to noise ratio.

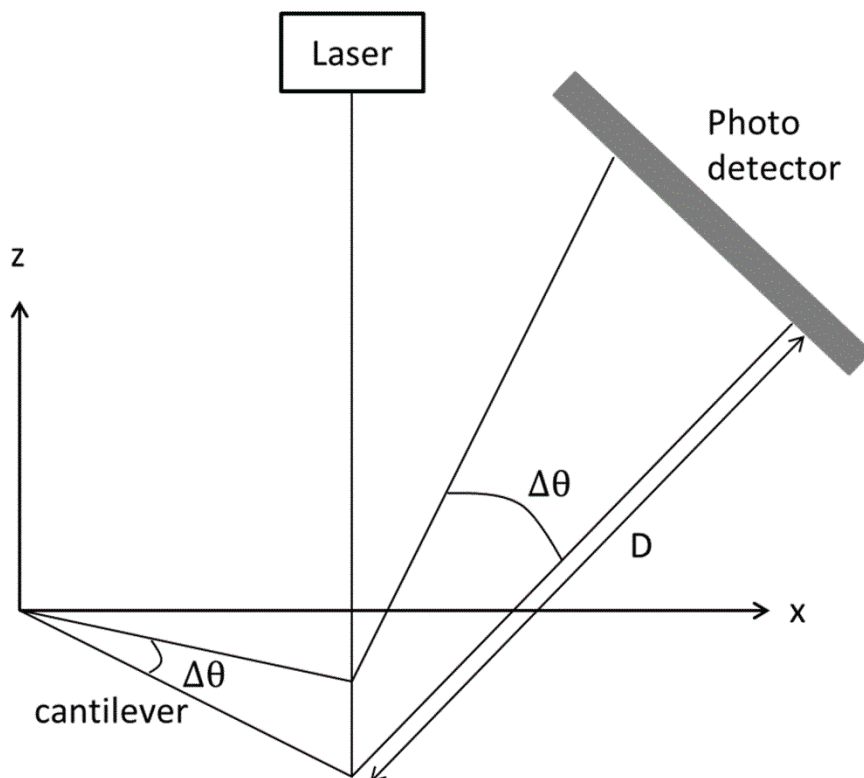


Figure 2.11 Schematic diagram of the Optical Beam Deflection method

### 2.4.3 Piezo-electric actuators

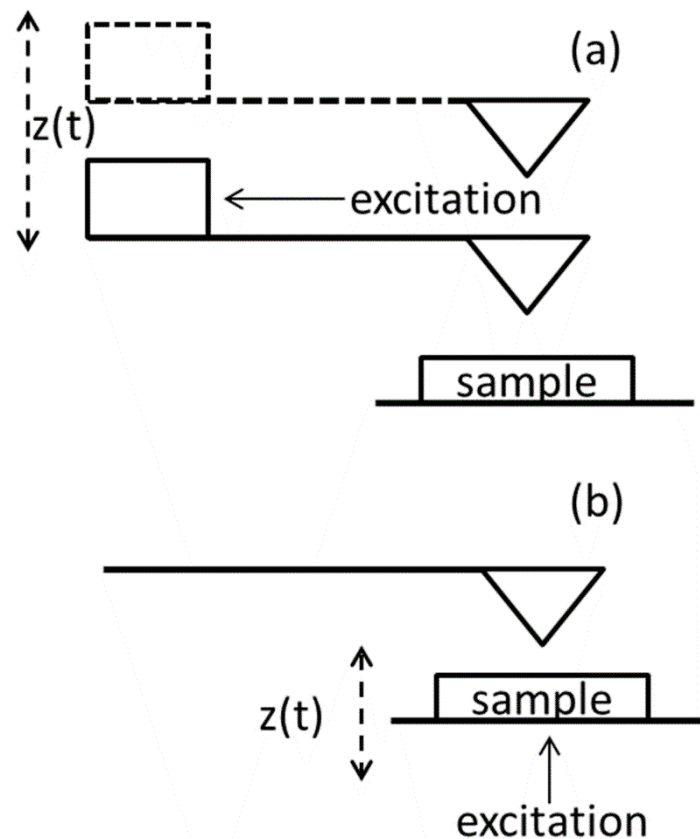


Figure 2.12 (a) acoustic excitation (b) magnetic excitation

In AFM system, piezo-electric actuators are used both to achieve the vibration of the cantilever and also to control the scanning process. To be specific, a Z-piezo moves the cantilever up or down in the Z direction depending upon the feedback system. Also, the Z-piezo acts as an actuator to cause the vibration of the cantilever. In the meantime, the X and Y piezos control the lateral scanning process. Piezo-electric actuators work with the feedback system. When a signal is received from the feedback system, piezos will move the cantilever up or down, then, continue the lateral scanning. There are two kinds of piezo-electric actuators. One consists of all the piezo composed into a single unit, which is placed at the clamped end of the cantilever. The other has the X and Y piezos being separated from the Z-piezo, with the former being located underneath the sample stage. The scanned size of the image can be as large as  $\mu\text{m}^2$  and as small as  $\text{nm}^2$ .

Different methods have been used to activate the vibration of the cantilever, such as acoustic and magnetic excitation, as shown in Figure 2.12. For acoustic method, a piezo is set on the end of the cantilever which is opposite to the tip end. A sinusoidal voltage is applied to the piezo in order to vibrate the cantilever. This method is also adopted by the AFM system, which is the most frequently used method in air or liquid. On the other hand, in the magnetic excitation method, a sinusoidal magnetic force is applied to the sample holder such that a magnetic field is formed to cause the vibration of the cantilever. (Florin et al., 1994, Han et al., 1996).

#### 2.4.4 Cantilever and tip

With the development of the fabrication techniques, it is possible to produce the cantilever and tip into one object. This object can act as a rigid bridge to transfer interaction forces into deflection. As the tip is relatively small compared with the cantilever, the inertial effect is mostly regarded to the mass of cantilever. Figure 2.13 shows a scanning electron microscopy (SEM) image of a rectangular cantilever with a pyramidal shape tip.

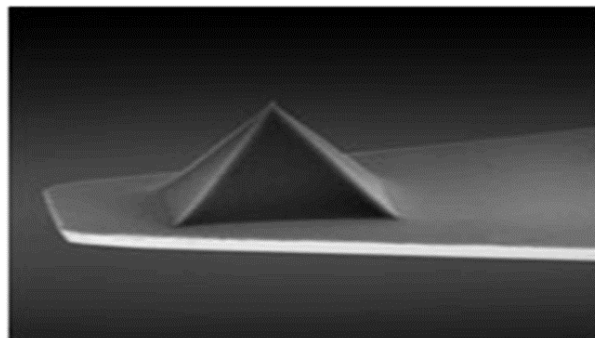


**Figure 2.13 SEM image of an AFM tip. Adapted from (<http://www.nanoandmore.com/AFM-Probe-PNP-TRS.html>)**

Photolithography and etching are the common techniques used to fabricate the cantilevers (Albrecht et al., 1990, Wolter et al., 1991). Silicon and silicon nitride ( $\text{Si}_3\text{N}_4$ ) are the two materials most commonly used to make AFM cantilevers. Nowadays, rectangular and triangular cantilevers are commercially fabricated by the manufacturers, as shown in Figure 2.14. A triangular cantilever is normally used in contact mode AFM for its stability during scanning. However, due to the complexity of the geometry of triangular cantilevers, it is a relatively difficult geometrical form to be used in modelling. Therefore, most of the

analytical descriptions of cantilever dynamics are based upon a rectangular cantilever. Its spring constant, resonant frequency and quality factor are the main properties of a cantilever. The spring constant is particularly significant for force measurement. The spring constant of the cantilever can be as small as 0.06 N/m and as large as 84 N/m, while the resonant frequency can be up to 3600 kHz. The resonant frequency partially reflects the time response of the system, while the quality factor reflects the damping of the system, in other words, it can tell whether the experimental environment is in air, liquid, or in ultra-high vacuum. Generally, the quality factor varies between 1 and 3 in liquids. In air, the quality factor is within the range of a few hundred. However, the quality factor can vary to as much as 10,000.

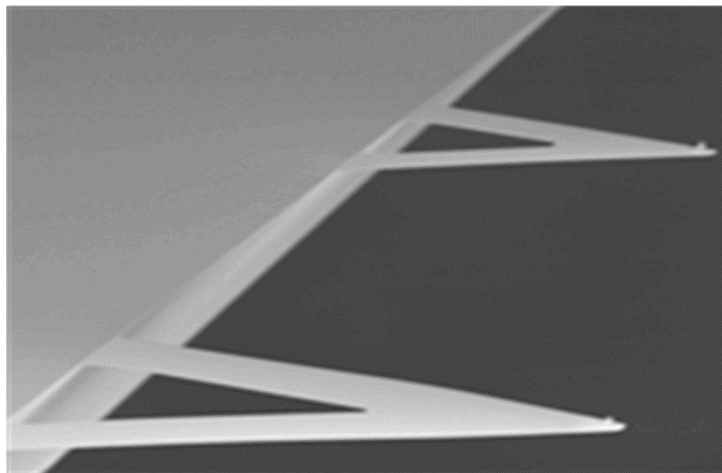


**Figure 2.14 Rectangular and triangular cantilevers. (<http://www.brukerafmprobes.com/p-3693-snl-10.aspx>)**

Some authors have given a definition of the spring constant and resonant frequency for a rectangular cantilever. Equation 2.3 shows that the spring constant is related to the Young's modulus and the dimension of the cantilever (Schäffer, 2005).

$$k = \frac{EWH^3}{4L^3} \quad (2.3)$$

Where E represents the Young's modulus, L, W, H is the length, width and height of the cantilever, respectively. The resonant frequency is expressed as below.

$$f_n = \frac{1}{2\pi} \frac{\kappa_n^2}{\sqrt{12}} \sqrt{\frac{E H}{\rho L^2}} \quad (2.4)$$

Where  $\rho$  represents the mass density,  $\kappa_1$  and  $\kappa_2$  is approximately equal to 1.875 and 4.964, which are the coefficients for the first and second flexural mode, respectively. For higher modes,  $\kappa_n$  refers to the following equation.

$$\kappa_n \approx \pi \left( n - \frac{1}{2} \right), n \geq 3 \quad (2.5)$$

Nowadays, manufacturers can fabricate very sharp tips. The radius of the tip can be as small as 2 nm. The lateral resolution is affected by the radius of the tip and its aspect ratio. Different researchers have investigated how to improve the lateral resolution without compromising too much about the radius of the tip, or its aspect ratio. The fabrication of carbon nanotubes (shown in Figure 2.15) for use as AFM tips makes this possible. Carbon nanotubes not only have a small tip radius, but also a high aspect ratio. Their use also reduces the adhesion between tip and sample. Moreover, they do not easily break when large forces are applied. However, the disadvantage is that it is relatively time consuming to produce the tip and difficult to attach the tip to a silicon cantilever, which has somewhat suppressed the influence of carbon nanotube tip uptake on AFM systems (Cheung et al., 2000, Klinov and Magonov, 2004, Martinez et al., 2005, Snow et al., 2002).

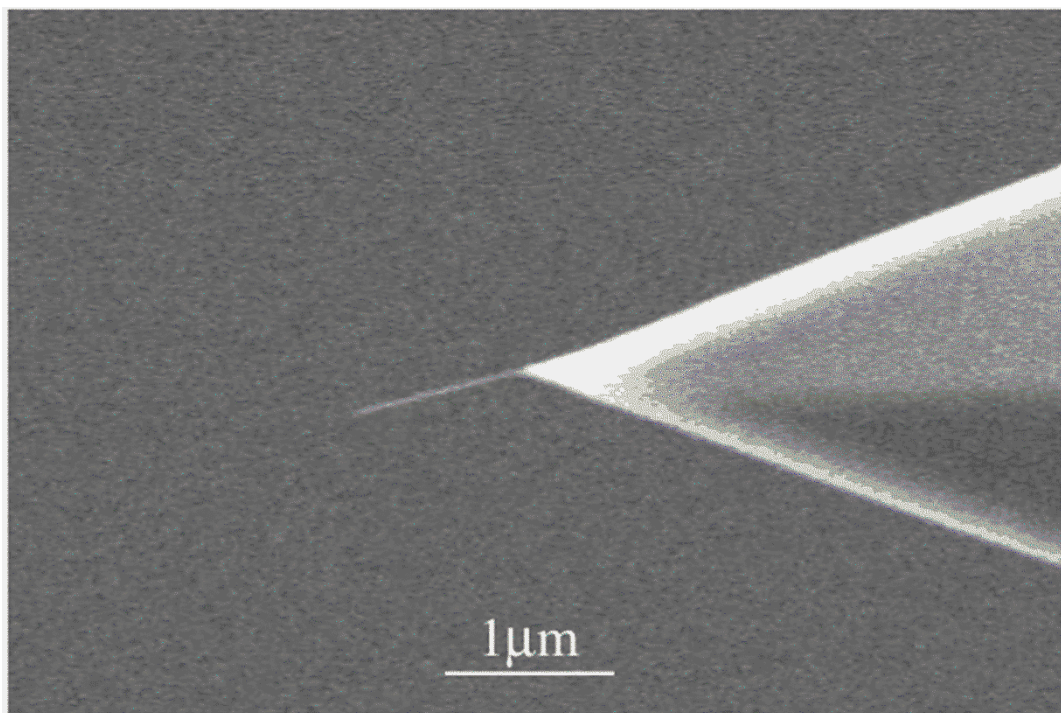


**Figure 2.15 SEM image of a carbon nanotube with a length of 1000nm. Adapted from (Martinez et al., 2005)**

## 2.5 Calibration of the cantilever

It is usually the case that the sensitivity (volts/nm) of the optical detection system may be different after performing many experiments, which would result in inaccurate measurements. Therefore, it is necessary to calibrate the optical sensitivity and spring constant of the cantilever before conducting the AFM experiments. Here, a general description of the optical sensitivity and calibration of the spring constant are given in the following paragraphs.

### 2.5.1 Optical sensitivity

Any deflection of the cantilever is detected by the photodiode detector. Then, the photodiode detector transfers the deflection signal into voltage signal. In order to transform the deflection into units of length, it is necessary to determine the sensitivity of the optical detection system. Generally, the laser spot is aligned on the polished rear surface of the end of the cantilever so that the sum of light reflected onto the photodiode detector is maximized. The procedure of determining the sensitivity is to capture a force-distance curve, which is a measure of the cantilever deflection against the z piezo movement. However, it requires the use of hard sample, because then the deformation of the sample can be neglected. Hence, sample of glass or mica are typically used as the standard calibration sample for optical sensitivity calibration. The force-distance curve shown in Figure 2.16 was produced using a silicon tip upon a glass substrate sample. It shows the cantilever deflection in nanometres against the z piezo movement, in other words, it indicates how the deflection of cantilever changes when the tip moves close to the sample surface. The sensitivity is given under the assumption that the z piezo movement  $\Delta z$  is the same as the deflection of the cantilever:

$$\sigma_s = \frac{\Delta V}{\Delta z} \quad (2.6)$$

where  $\Delta V$  represents the detector signal, while  $\Delta z$  represents the displacement of the z piezo. The detector signal is related to the location of laser spot on the cantilever. Therefore, the length of the cantilever and the laser alignment will affect the detector signal, in other words, the sensitivity (Schäffer, 2005, Schäffer and Fuchs, 2005).

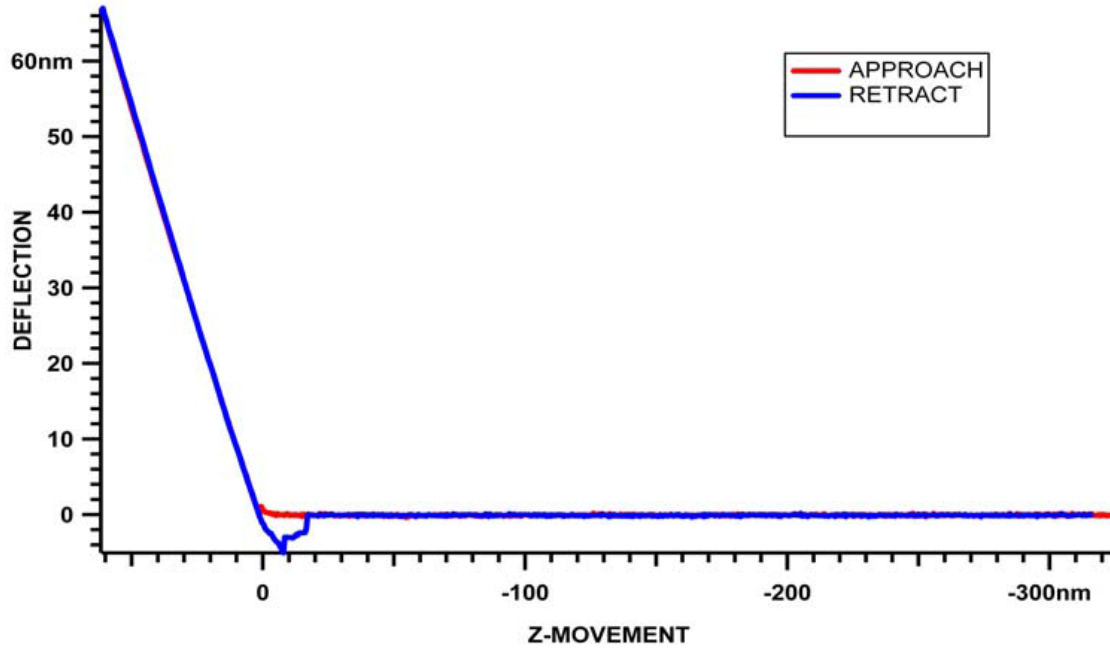


Figure 2.16 force-distance curve

### 2.5.2 Determination of the spring constant

Different methods have been proposed to determine the spring constant, such as the Sader method (Sader et al., 1999) and the thermal noise method (Butt and Jaschke, 1995, Hutter and Bechhoefer, 1993, Walters et al., 1996). Sader and his co-workers found a way to calculate the spring constant of a rectangular cantilever when they studied the fluid dissipation of the dynamic behaviour of the cantilever. In this method, there are few parameters which need to be known in order to determine the spring constant, which is shown in the following equation (Sader et al., 1999):

$$k = 7.524W^2LQ_1\Gamma_i(f_1)f_1^2 \quad (2.7)$$

where  $W$  and  $L$  are the width and the length of the cantilever, respectively.  $f_1$  is the resonant frequency of the first mode.  $\Gamma_i(f_1)$  represents the imaginary part of hydrodynamic function. The hydrodynamic function is related to the Reynolds numbers, which can be expressed as follows:

$$\Gamma(w) = \frac{4i}{Re \ln(-i\sqrt{iRe})} \quad Re \rightarrow 0 \quad (2.8)$$

$$Re = \rho_f \omega b^2 / (4\eta) \quad (2.9)$$

where  $\eta$  is the viscosity of the fluid and  $b$  is the width of the cantilever (Sader et al., 1999).

The ‘thermal noise’ method is commonly used to calibrate the cantilever. Generally, the cantilever is thermally vibrated in its surrounding environment. The spring constant is related to the thermal noise in the deflection signal of the cantilever. In the first thermal noise method, Hutter and Bechhoefer made an assumption that the behaviour of the cantilever resembled that of an ideal spring (Hutter and Bechhoefer, 1993). Later, Butt and Jaschke defined a relationship between the sum of the power of the cantilever deflection and the power against the first resonant frequency (Butt and Jaschke, 1995). The thermal noise method kept on developing by the work of different researchers, the most commonly accepted method was proposed by (Walters et al., 1996). In this method, Walters deduced an analytical expression for the spring constant of the cantilever by applying the equipartition theorem to the cantilever’s potential energy, which is shown in the following equation:

$$\frac{1}{2} k_B T = \frac{1}{2} k \langle x^2 \rangle \quad (2.10)$$

Equation 2.10 can be easily simplified as follows;

$$k = \frac{k_B T}{\langle x^2 \rangle} \quad (2.11)$$

where  $k_B$  represents the Boltzmann’s constant,  $T$  is the temperature, and  $\langle x^2 \rangle$  is the mean square cantilever deflection.  $\langle x^2 \rangle$  can be obtained by integrating the amplitude of the power spectrum shown in Figure 2.17. As the amplitude corresponding to the first resonance is caused by the thermal noise, Walters found a way to avoid low frequency noise and higher harmonics by fitting the power spectrum data near the first resonance by using the following equation:

$$A(\nu) = A_{dc} \frac{\nu_0^2}{\sqrt{(\nu_0^2 - \nu^2)^2 + \frac{\nu_0^2 \nu^2}{Q^2}}} \quad (2.12)$$

where  $A_{dc}$  is the dc amplitude,  $\nu_0$  is the resonant frequency and Q is the quality factor. The data obtained from Equation 2.12 would then be used to calculate the mean square cantilever deflection.

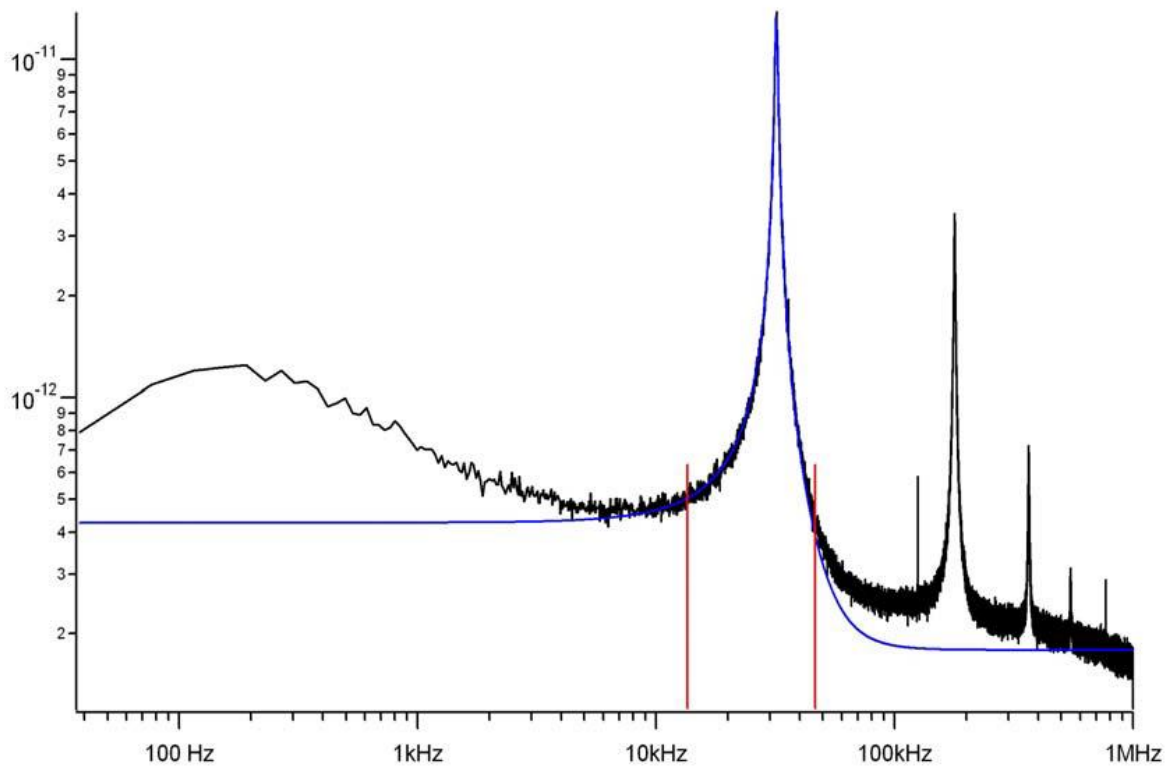


Figure 2.17 power spectrum

### 2.5.3 Damping of AFM system

In AFM, the damping of the system is usually indicated by the quality factor, which usually appears notated as the dimensionless Q factor. Generally, the Q factor is around 100 in normal ambient conditions. While in liquid, the Q factor has a value between 1 and 3. However, the quality factor could be more than 10000 in vacuum.

## 2.6 Summary and Discussions

A brief description has introduced the evolution of the atomic force microscope. Different AFM imaging techniques have also been demonstrated in terms of static mode and dynamic mode. The key components of the AFM system have been described respectively, such as

the feedback system, piezo-electric actuator and cantilever and tip. The theory on how to calibrate the optical sensitivity and spring constant of the cantilever has been briefly discussed.

# Chapter 3

Numerical

Modelling of

Atomic force

Microscope

## Chapter 3 Numerical Modelling of Atomic Force Microscope

In Chapter 3, the development of a point mass model is presented. The 1D beam model and 3D finite element model are also introduced.

### 3.1 Point Mass Analytical Model

#### 3.1.1 The Basic Point Mass Model

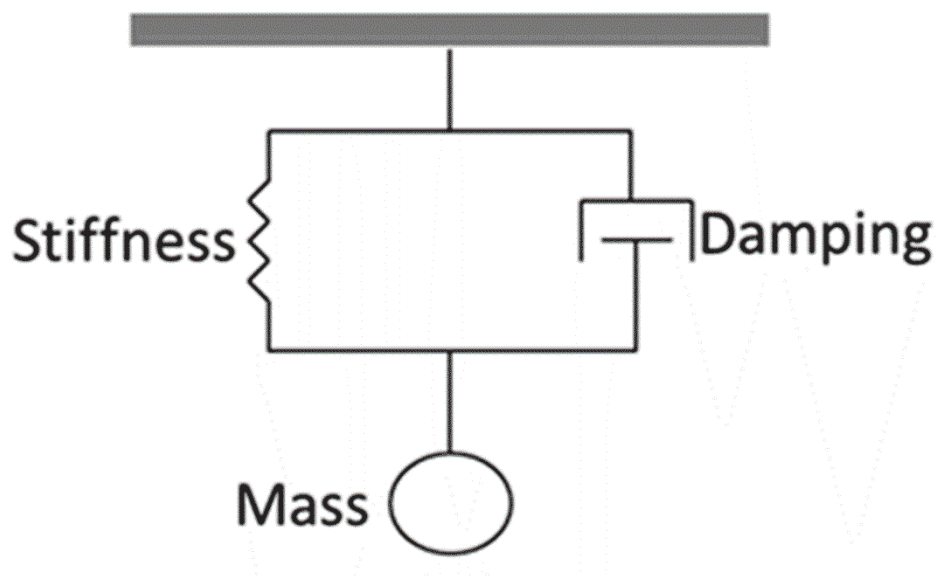


Figure 3.1 Point mass model

Point mass model (Chen et al., 1994, Anczykowski et al., 1996, García and San Paulo, 1999, Paulo and García, 2002, Lozano and Garcia, 2008, Nony et al., 1999, Wang, 1998, Sahin et al., 2007, Schröter et al., 2009) is commonly used to describe the behaviour of tapping mode AFM. In this model, cantilever and tip are represented by a point mass spring, as shown in Figure 3.1. One end of the spring is driven by the external force, while the other end is applied with the tip sample interaction forces. The dynamics of cantilever and tip are more easily understood in terms of a second order differential equation.

$$m\ddot{z} = -kz - \frac{mw_0}{Q}\dot{z} + F_0\cos\omega t + F_{ts}(d) \quad (3.1)$$

where  $k$ ,  $Q$ ,  $w_0$ , and  $w$  are the spring constant, quality factor, resonant frequency and excitation frequency of the cantilever, respectively. While  $m$  represents the mass,  $F_0$  is the amplitude of the excitation force. The last term  $F_{ts}(d)$  is the sum of the tip sample interaction forces, which depends on the instantaneous tip-sample separation  $d$ , in other words, it can also be regarded as time-dependent interaction force. As tapping mode AFM is usually vibrated at, or near to, its first order resonant frequency in flexural mode, the parameters used to describe the equation correspond to the first order flexural mode. When there is no tip-sample interaction, the motion of the cantilever is considered as being 'free vibration'. Equation 3.1 is derived as follows:

$$m\ddot{z} = -kz - \frac{mw_0}{Q}\dot{z} + F_0\cos wt \quad (3.2)$$

This equation also represents a forced and damped harmonic oscillator (Martin et al., 1987). Hence, in order to understand the dynamic behaviour of tapping mode AFM, it is necessary to know about the characteristic of harmonic oscillators. When the excitation frequency ( $w$ ) is much smaller than the resonant frequency ( $w_0$ ), the response of the harmonic oscillator is dominated by the spring constant ( $k$ ). The movement of the oscillator has a sinusoidal relationship with excitation force, which has an amplitude of  $F_0/k$ . On the other hand, if the excitation frequency is much larger than the resonant frequency,  $m \cdot d^2z/dt^2$  is larger than  $kz$ . Hence, under these conditions the response is mostly affected by the mass, in other words, inertial effects are important in this case. In order to solve Equation 3.2, it is necessary to define the damping of the harmonic oscillator. Thus, the damping applied to the harmonic oscillator is related the real tapping mode AFM experiment. As AFM is an under damped system, the damping ratio  $\zeta=1/2Q$  is therefore smaller than 1. Under this condition, the displacement  $z$  is solved as shown in the following equation, which consists of a transient term and a stable term.

$$z = B \exp\left(-\frac{w_0}{2Q}t\right) \cos(w_r t - \beta) + A \cos(wt + \Phi) \quad (3.3)$$

The stable term is similar to the excitation force in terms of having the same resonant frequency, but with a phase lag. The amplitude of the transient term is decreased by a value  $\exp(-N)$ , when the time ( $t$ ) comes across  $N \cdot 2Q/w_0$ , where  $N$  is a constant. The

frequency  $w_r$  of the harmonic oscillator in the transient term is regarded as the new resonant frequency. This new resonant frequency is mainly affected by the damping of the harmonic oscillator, which is shown in the following equation:

$$w_r = w_0 \left(1 - \frac{1}{4Q^2}\right)^{1/2} \quad (3.4)$$

When the AFM experiment is performed in air, the Q factor is over 100. In this case, the new resonant frequency is approximately the same as the excitation frequency. On the other hand, when the experiment is performed in liquid, the Q factor is usually ranging from 1 to 3, which leads to considerably large difference between the new resonant frequency and the excitation frequency. With the help of a Lorentzian expression, the amplitude of the harmonic oscillator is defined as a function of the excitation frequency:

$$A(w) = \frac{F_0/m}{\left[(w_0^2 - w^2) + (ww_0/Q)^2\right]^{1/2}} \quad (3.5)$$

where  $F_0$  represents the amplitude of the driving force,  $w_0$  is the resonant frequency of the cantilever. The amplitude  $A(w)$  reaches its maximum when the excitation frequency is defined as follows:

$$w = w_0 \left(1 - \frac{1}{2Q^2}\right)^{1/2} \quad (3.6)$$

Substituting Equation 3.6 into Equation 3.5, the maximum amplitude  $A_{max}$  is expressed as:

$$A_{max} = \frac{QF_0}{k} \frac{1}{(1 - (1/4Q^2))^{1/2}} \quad (3.7)$$

The expression of phase shift is also developed in the following equation:

$$\tan\Phi = \frac{ww_0/Q}{w_0^2 - w^2} \quad (3.8)$$

Where phase shift  $\Phi$  is defined as the difference of the phase angles between the excitation force and the displacement. When the cantilever is vibrated at its resonant frequency, the phase shift is  $90^\circ$ . Thus, the phase shift of free vibration is  $90^\circ$ , no matter what Q factor is

used. In other words, during free vibration the phase shift is not affected in terms of the damping of the environment.

Above, the dynamic behaviour of tapping mode AFM during free vibration has been described using a harmonic oscillator approach. However, in order to further understand tapping mode AFM, it is necessary to include the tip-sample interaction forces  $F_{ts}$ . A weakly perturbed harmonic oscillator is introduced to the dynamic behaviour of tapping mode AFM during tapping. However, there is a limitation that only small displacements can be applied. The tip-sample interaction forces can be described using the following equation:

$$\mathbf{F}_{ts}(\mathbf{z}) = \mathbf{F}_{ts}(\mathbf{0}) + (d\mathbf{F}_{ts}/d\mathbf{z})\mathbf{z} \quad (3.9)$$

The term  $F_{ts}(0)$  represents the interaction forces on the initial position, where the displacement is zero, while the gradient of the interaction forces ( $dF_{ts}/dz$ ) can be substituted as a spring constant:

$$\mathbf{k}_{ts} = d\mathbf{F}_{ts}/d\mathbf{z} \quad (3.10)$$

The equation of motion of a weakly perturbed harmonic oscillator is formed by substituting Equations 3.9 and 3.10 into Equation 3.1.

$$m\ddot{\mathbf{z}} = -(\mathbf{k} - \mathbf{k}_{ts})\mathbf{z} - \frac{m\omega_0}{Q}\dot{\mathbf{z}} + \mathbf{F}_0\cos\omega t + \mathbf{F}_{ts}(\mathbf{0}) \quad (3.11)$$

The term  $\mathbf{k} - \mathbf{k}_{ts}$  is regarded as being an effective spring constant  $\mathbf{k}_{eff}$ .

$$\mathbf{k}_{eff} = \mathbf{k} - \mathbf{k}_{ts} \quad (3.12)$$

In a harmonic oscillator model, a definition between the resonant frequency and the spring constant of the cantilever can be made, using Equation 3.13:

$$\omega_0 = \sqrt{\mathbf{k}/m} \quad (3.13)$$

Hence, the effective resonant frequency is defined as:

$$\omega_{eff} = \sqrt{\mathbf{k}_{eff}/m} \quad (3.14)$$

The expression for the phase shift can then be derived as:

$$\tan\Phi = \frac{w w_{eff}/Q}{w_{eff}^2 - w^2} \quad (3.15)$$

To sum up, harmonic oscillator is a good method to understand the behaviour of tapping mode AFM, which gives the definition of resonant frequency, amplitude and phase shift. This is the first attempt to describe the mechanism of tapping mode AFM. However, a harmonic oscillator model cannot really match the real experiment, because of its assumptions used to derive the equations above. First, it assumes that the tip-sample interaction force is linear. Second, the interaction forces would cause the frequency shift instead of energy dissipation. Third, the force constant of the interaction force is much smaller than the spring constant of the cantilever. These assumptions are not always true, which are indicated by many experimental results with amplitudes above 1 nm.

### 3.1.2 The Wang Model

Wang (Wang, 1998, Wang, 1999) proposed a different method to describe the behaviour of tapping mode AFM, which is known as the Wang model. Unlike the harmonic oscillator model, the tip-sample interaction forces are defined nonlinearly in terms of elastic force and adhesion force, as shown in Equation 3.15, which are related to the effective Young's modulus  $E^*$ , radius of the tip, indentation  $z - z_0$ , and surface energy  $\gamma$  of the sample.

$$F_{ts} = \frac{4}{3} E^* \sqrt{R} (z - z_0)^{\frac{3}{2}} - 2\pi R \gamma \quad (3.16)$$

The effective Young's modulus is related to the Young's modulus and Poisson's ratio of the tip and sample, as shown in Equation 3.17.

$$E^* = [(1 - \sigma_t^2)/E_t + (1 - \sigma_s^2)/E_s]^{-1} \quad (3.17)$$

where  $\sigma_t, \sigma_s$ , is the Poisson's ratio of the tip and sample respectively, while  $E_t, E_s$  is the Young's modulus of tip and sample. Tapping mode AFM only intermittently contacts the sample in each vibration cycle. In other words, it can be regarded as a nonlinear system. Combined with the Krylov Bogoliubov Mitroposky asymptotic method (Wang, 1998, Wang,

1999), an approximated solution can be obtained. The displacement of the model is expressed as a sinusoidal signal with an excitation frequency  $\omega$ :

$$z = A \cos(\omega t - \Phi) = A \cos \theta \quad (3.18)$$

Based on Equation 3.17, the amplitude and phase shift are also calculated. The amplitude is expressed as a function of the normalized excitation frequency  $\varpi$ :

$$A = \frac{F_0/k}{(1+\varpi)\sqrt{\alpha_{eff}^2 + (\varpi - \varpi_{eff})^2}} \quad (3.19)$$

where  $\varpi = \omega/\omega_0$ , while the effective normalized frequency  $\varpi_{eff}$  is calculated as the integration of the tip-sample interaction forces  $F_{ts}$ :

$$\varpi_{eff}^2 = 1 + \frac{1}{\pi k A} \int_0^{\theta_0} F_{ts}(z) \cos \theta d\theta \quad (3.20)$$

From Equation 3.19, it can be seen that the amplitude  $A$  is only affected by the change of effective normalized frequency  $\varpi_{eff}$  when only elastic force is considered. However, inelastic forces always occur in tapping mode AFM. It may therefore not properly describe the behaviour of tapping mode AFM without considering the inelastic force. The phase shift is expressed as the following equation:

$$\tan \Phi = \frac{\varpi_{eff} - \varpi}{\alpha_{eff}} \quad (3.21)$$

where the effective damping coefficient  $\alpha_{eff}$  is represented using the following equation:

$$\alpha_{eff} = \alpha_0 + \int_0^{\theta_0} \alpha_s \sin^2 \theta d\theta \quad (3.22)$$

where  $\cos \theta_0 = \frac{z_c}{A}$ ,  $\alpha_0$  is the damping of the environment,  $\alpha_s$  is the damping caused by the inelastic interaction forces.

### 3.1.3 The Energy Conservation Model

According to (Paulo and García, 2001, Lozano and Garcia, 2008, Lozano and Garcia, 2009), analytical expressions have been concluded by using the virial theorem method and the energy conservation method. The oscillation amplitude and phase shifts are related to tip-sample interaction forces, energy dissipation and the virial term. The displacement of the tip is defined as:

$$z = A \cos(\omega_0 t - \Phi) \quad (3.23)$$

The energy dissipation is calculated by doing the integration over the tip-sample interaction forces  $F_{ts}$  and velocity of the tip  $\dot{z}(t)$  using Equation 3.23,

$$E_{ts} = \int_0^{T_0} F_{ts}(d) \dot{z}(t) dt = \frac{\pi k A}{Q} (A \sin \Phi - A) \quad (3.24)$$

while the virial is related to both the tip-sample interaction forces  $F_{ts}$  and the displacement of the tip, as shown in Equation 3.22:

$$V_{ts} = \frac{1}{T} \int_0^{T_0} F_{ts}(d) z(t) dt = -\frac{2kA_0}{2Q} A \cos \Phi \quad (3.25)$$

where  $A_0$  represents the free amplitude. The amplitude and phase shift can be calculated using Equations 3.23 and 3.24:

$$A = A_0 \sqrt{(2v)^2 + \left( \frac{1 \pm \sqrt{1 - (4v)^2 - 4\beta/\pi}}{2} \right)^2} \quad (3.26)$$

$$\Phi = \tan^{-1} \frac{1 \pm \sqrt{1 - (4v)^2 - 4\beta/\pi}}{4v} \quad (3.27)$$

From Equations 3.23 and 3.24, it is found that the amplitude and phase shift depend on two factors  $\beta$  and  $v$ . The definitions of these two factors are given below:

$$\beta = QE_{ts}/kA_0 \quad (3.28)$$

$$v = QV_{ts}/kA_0^2 \quad (3.29)$$

where  $\beta$  and  $v$  have the contribution from the non-conservative and conservative forces. Unlike other methods described previously, the amplitude and phase shift are not related to the resonant frequency shift in this method.

### 3.2 1D beam analytical model

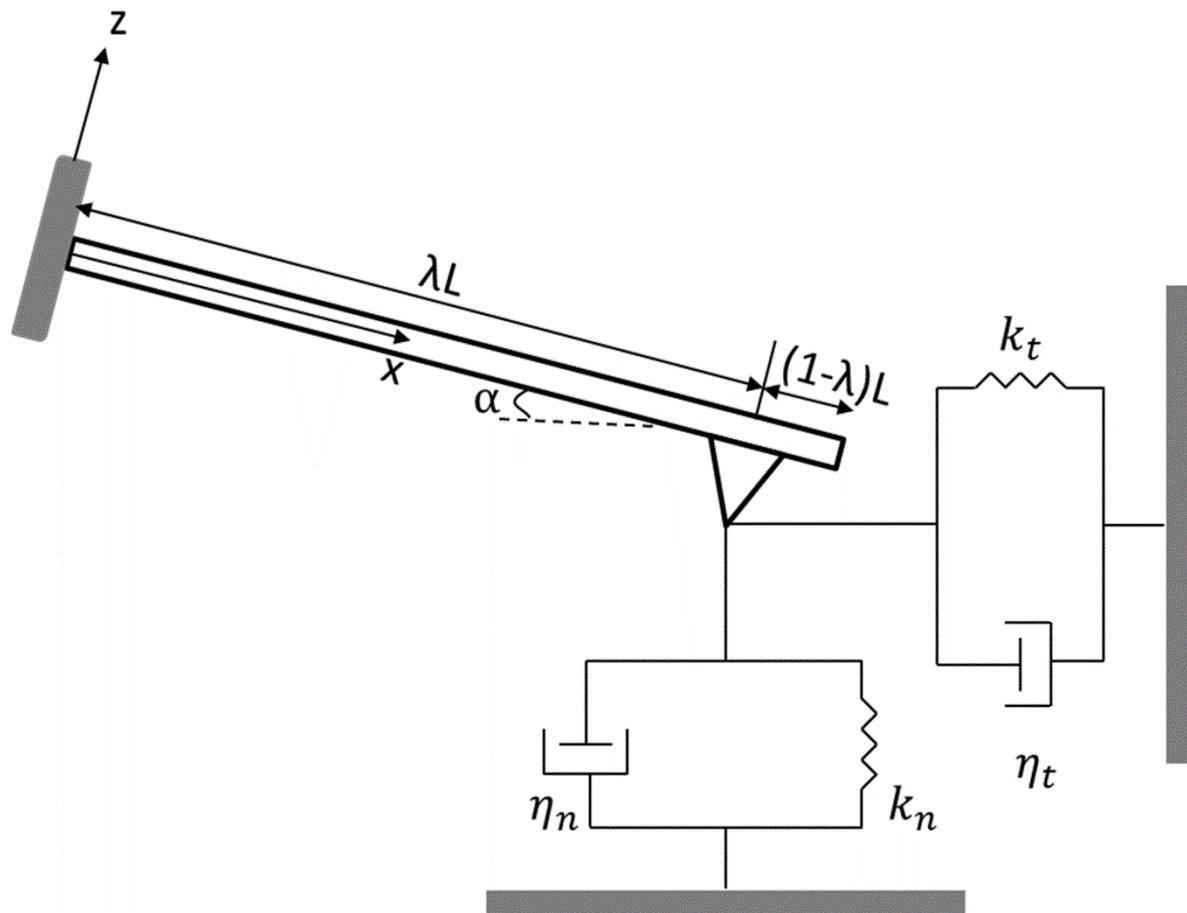


Figure 3.2 1D beam model,  $\lambda$  indicates the location of the tip,  $k_n$ ,  $k_t$  and  $\eta_n, \eta_t$  represent the spring constant and viscosity, respectively, in the normal and tangential directions.

1D beam model is described in Figure 3.2. The motion of the cantilever is represented by the following differential equation (Song and Bhushan, 2008):

$$EI_y \frac{\partial^4 w(x,t)}{\partial x^4} + \rho A \frac{\partial^2 w(x,t)}{\partial t^2} + c_{vb} \frac{\partial w(x,t)}{\partial t} = 0 \quad (3.30)$$

where E,  $\rho$  and A represent the Young's modulus, mass density and cross sectional area, respectively.  $w(x,t)$  is the instantaneous displacement of the cantilever.  $I_y$  represents the moment of inertia about the y axis, which is defined as follows:

$$I_y = bh^3/12 \quad (3.31)$$

where b and h represent the width and height of the beam's cross section. The damping of the cantilever is defined using  $c_{vb}$ , which is expressed as follows:

$$c_{vb} = w\rho A/Q \quad (3.32)$$

where w is the resonant frequency of the flexural mode and Q is the quality factor of the cantilever. The modal analysis is described using the modal shape function  $\Phi_\omega(x)$  ::

$$\Phi_\omega(x) = C_1 e^{-a_{vb}x} + C_2 e^{a_{vb}x} + C_3 e^{-ia_{vb}x} + C_4 e^{ia_{vb}x} \quad (3.33)$$

where  $a_{vb}$  is expressed as follows:

$$a_{vb}^2 = \frac{\rho A}{EI_y} \omega^2 - i \frac{c_{vb}}{EI_y} \omega \quad (3.34)$$

The constants  $C_1$  to  $C_4$  are determined by the boundary conditions of the cantilever. For a freely vibrating cantilever, there are no interaction forces on the tip while the other end of the cantilever is fixed. In this case, the boundary conditions are expressed as:

$$\Phi_\omega|_{x=0} = 0, \Phi'_\omega|_{x=0} = 0, EI_y \Phi''_\omega|_{x=L} = 0, EI_y \Phi'''_\omega|_{x=L} = 0 \quad (3.35)$$

where  $\Phi', \Phi'', \Phi'''$  is the first, second, and third order derivatives of the equation with respect to x, respectively. L represents the length of the cantilever. By substituting Equation 3.33 into Equation 3.35, the resonant frequencies corresponding to different modes can be obtained. In order to avoid a zero solution, the term  $a_{vb}$  is controlled by the following equation:

$$1 + \cos(a_{vb}L) \cosh(a_{vb}L) = 0 \quad (3.36)$$

Linear tip-sample interaction forces can be included into the boundary conditions of the model in terms of  $F_x$  and  $F_z$ , when the vibration of the cantilever is small around its initial position. In this case, one end of the cantilever is still fixed. Hence, there are no displacements and slope at  $x=0$ , which are the same as the boundary conditions previously described at the fixed end of the cantilever. However, the boundary conditions at the tip end will change as follows.

$$\Phi_\omega|_{x=0} = 0, \quad \Phi'_\omega|_{x=0} = 0, \quad EI_y\Phi''_\omega|_{x=L} = F_xL, \quad EI_y\Phi'''_\omega|_{x=L} = -F_z \quad (3.37)$$

where  $l$  represents the height of the tip. When the cantilever is parallel to the sample, the interaction force in the  $z$  direction  $F_z$  can be represented by tip sample interaction forces normal to the sample  $F_n$ , while  $F_x$  can be represented by the interaction force in the lateral direction  $F_t$ .  $F_n$  is expressed as a function of the vertical displacement of the tip:

$$F_n = -(k_n + i\omega\eta_n)\Delta_n \quad (3.38)$$

where  $k_n$  and  $\eta_n$  are the contact stiffness and viscosity in the normal direction, respectively.  $F_{lat}$  is defined as follows:

$$F_t = -(k_{lat} + i\omega\eta_{lat})\Delta_{lat} \quad (3.39)$$

where  $k_{lat}$ ,  $\eta_{lat}$ ,  $\Delta_{lat}$  are the contact stiffness, viscosity and displacement in the lateral direction, respectively. The contact resonant frequencies can be found by substituting Equation 3.30 into Equation 3.34. The instantaneous displacement in the steady state can also be obtained under the following assumption:

$$\omega(x, t) = \Phi_\omega(x)e^{i\Omega t} \quad (3.40)$$

Unlike the point mass model, the 1D beam model can deal with first resonance and higher resonance modes. According to (Rabe et al., 1998), when there is no tip sample interaction forces, both models can properly simulate the first resonance mode. When tip sample interaction forces are included in the model, the 1D beam model can still provide satisfactory results, however, the first resonant frequency provided by the point mass model is too high. The 1D beam model has been used to investigate the stiffness of samples. It was found that higher modes could help in the study of high stiffness samples.

### 3.3 3D numerical model

Unlike the point mass model and the 1D beam model, 3D numerical models (Song and Bhushan, 2006b) are more closely related to the real situation in several different ways, which can be presented in terms of the geometry of the tip and cantilever, the location of the tip on the cantilever and the tilting angle between the tip and sample.

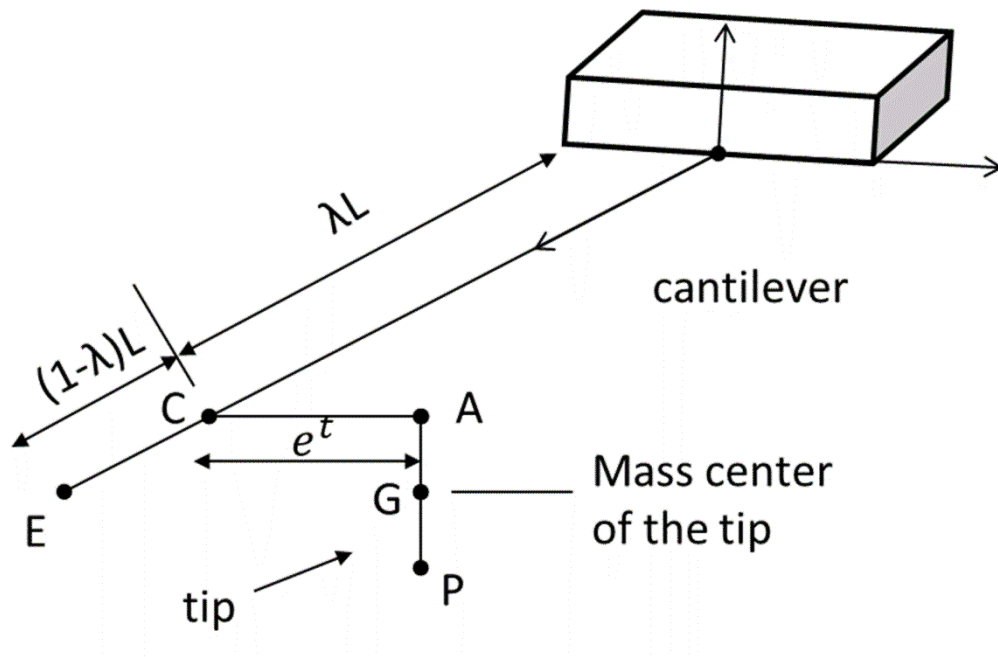


Figure 3.3 Schematic diagram of a 3D finite element model

From Figure 3.3, it can be seen that the location of the tip is indicated by the coordinates of point A. The bottom of the tip is fixed at  $z=0$  in the  $z$  direction, while the coordinates in the  $x$  and  $y$  directions are flexible. The  $x$  coordinate of the tip is proportional to the length of the cantilever  $L$ , which is defined as  $x = \lambda L$ , where  $\lambda$  has a value between 0 and 1, while the  $y$  coordinate is equal to a constant  $e_t$ . This constant determines the distance between point A and point C. If  $e_t = 0$ , the tip exactly locates at point C, which is in the middle of the width of the cantilever. In the 3D numerical model, the cantilever is discretized by 3D beam elements (Song and Bhushan, 2006b). Each 3D beam element contains two nodes, which is shown in Figure 3.4, while each node has six degrees of freedom. Equation 3.38 shows the nodal displacement vector as:

$$\mathbf{d}^e = \{d_{x1}, d_{y1}, d_{z1}, \theta_{x1}, \theta_{y1}, \theta_{z1}, d_{x2}, d_{y2}, d_{z2}, \theta_{x2}, \theta_{y2}, \theta_{z2}\}^T \quad (3.41)$$

where the terms  $d$  and  $\theta$  in the bracket represent the translation displacement and rotation in the  $x$ ,  $y$ ,  $z$  directions, respectively. Besides the nodal displacement vector  $d^e$ , a 3D beam element also contains a nodal force vector  $f^e$ :

$$f^e = \{F_{x1}, F_{y1}, F_{z1}, M_{x1}, M_{y1}, M_{z1}, F_{x2}, F_{y2}, F_{z2}, M_{x2}, M_{y2}, M_{z2}\}^T \quad (3.42)$$

where  $F$  and  $M$  represent the shear force and moment in the  $x$ ,  $y$ ,  $z$  directions, respectively.

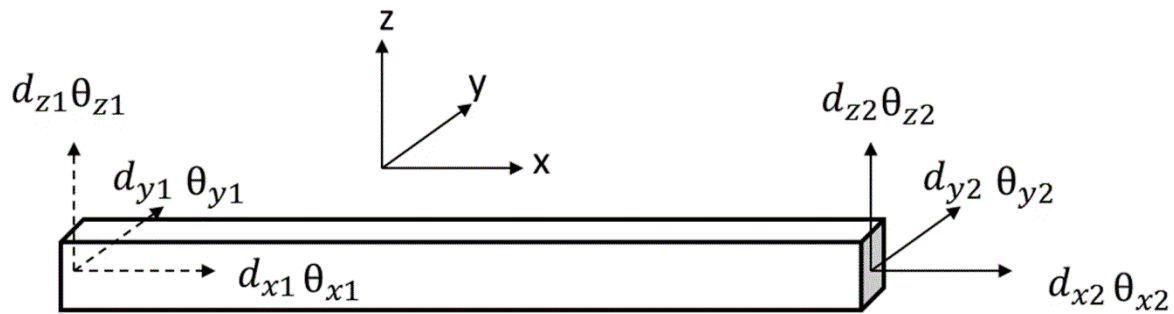


Figure 3.4 3D beam element

The dynamic behaviour of a cantilever system can be generally described using the following equation:

$$M\ddot{d} + C\dot{d} + Kd = F_{ext} + F_{ts} \quad (3.43)$$

where  $M$ ,  $C$ ,  $K$  represent the system mass matrix, damping matrix and stiffness matrix, respectively.  $F_{ext}$  describes the force used to excite the vibration of the cantilever, while  $F_{ts}$  assembles all the tip-sample forces acting on point  $C$ , which is given in the following equation:

$$F_{ts} = G_t^T f_{ts}^C \quad (3.44)$$

where  $G_t$  represents the Kronecker matrix, which contains position information of the nodal displacements acting on point  $C$ . The force vector on point  $C$  is shown in the following equation:

$$f_{ts}^C = \{f_x^C, f_y^C, f_z^C, M_x^C, M_y^C, M_z^C\}^T \quad (3.45)$$

Depend on the tilting angle between the tip and sample, the force acting on point C can be related to the force on the tip using Equation 3.43:

$$\mathbf{f}_{ts}^C = A_{C\alpha} \mathbf{f}_{ts}^\alpha \quad (3.46)$$

where  $\mathbf{f}_{ts}^\alpha = \{f_t, f_{lat}, f_n\}^T$  represents the forces caused by the sample surface in the tangential, lateral and normal directions, respectively.  $A_{C\alpha}$  is a six by three matrix shown as follows:

$$A_{C\alpha} = \begin{bmatrix} \cos \alpha & 0 & -\sin \alpha \\ 0 & 1 & 0 \\ \sin \alpha & 0 & \cos \alpha \\ e_t \sin \alpha & l & e_t \cos \alpha \\ -l \cos \alpha & 0 & l \sin \alpha \\ -e_t \cos \alpha & 0 & e_t \sin \alpha \end{bmatrix} \quad (3.47)$$

where  $\alpha$  is the tilting angle between the tip and sample. When the vibration of the cantilever is small, the tip-sample interaction forces can be treated as being linear. Then, the motion of the cantilever can be rewritten as:

$$\mathbf{M}\ddot{\mathbf{d}} + (\mathbf{C} + \mathbf{C}_{ts})\dot{\mathbf{d}} + (\mathbf{K} + \mathbf{K}_{ts})\mathbf{d} = \mathbf{F}_{ext} + \mathbf{G}_t^T \mathbf{f}_{ts}^\alpha \quad (3.48)$$

where  $\mathbf{C}_{ts}$ ,  $\mathbf{K}_{ts}$  are the effective damping and stiffness caused by the tip-sample interactions, respectively. The term  $\mathbf{f}_{ts}^\alpha$  represents the force vector caused by the movement of the surface of the sample. From the equation, this shows that the tip-sample interaction forces caused by elasticity and viscosity can be understood by adding damping and stiffness matrices to the system. Details of the parameters in the motion of cantilever equation can be found in (Song and Bhushan, 2006b).

### 3.4 Summary and Discussions

The point mass model described by a harmonic oscillator can only properly describe the free vibration of tapping mode AFM. When interaction forces are coupled into the model, the 1D beam model can provide more accurate results in terms of the resonant frequency and the amplitude corresponding to the resonant frequency, compared with those provided by the point mass model. The 1D beam model has been used here to investigate the stiffness of

the sample in fundamental and higher vibration modes. A 3D numerical model is a more advanced model, which can consider the geometrical effects of the tip and the location of the tip. Also, this modelling method gives the capability to be performed either in fundamental mode, or for higher modes. The advantage and disadvantage of different models have been summarized in table 3.1.

**Table 3.1 Advantage and disadvantage of different models**

Model Type	Advantage	Disadvantage
Point mass model	The first model to describe the behaviour of tapping mode AFM, and it can simulate the first resonance free vibration of tapping mode properly.	It assumes that the tip-sample interaction force is linear; the interaction forces would cause the frequency shift instead of energy dissipation, the force constant of the interaction force is much smaller than the spring constant of the cantilever.
The Wang model	Non-linear interaction force is included.	Geometric effect is not considered.
The energy conservation model	Energy dissipation is included.	Geometric effect is not considered.
1D beam model	1D beam model can deal with first resonance and higher resonance modes.	Only linear force is considered.
3D numerical model	It is a 3D model, which considers the geometric effect, takes the non-linear forces into account and is applicable to different vibration modes.	Computational time might be larger.

# Chapter 4

## Tip-Sample

## Interaction

## Force

## Chapter 4 Tip-Sample Interaction Force

During the AFM scanning process there are various forces acting between the tip and the sample. Depending upon the environment that the experiment is being performed in, the interaction forces are different. Generally, the main forces are the van der Waals force, repulsive force, adhesion force and capillary force in air. When the experiment is conducted in liquid, it makes the interaction forces even more complicated. Besides the forces mentioned above, in liquid an electric double layer force and the solvation force are also included.

### 4.1 Van der Waals force

Van der Waals force is caused by the interaction force between atoms, which appears in terms of the dipole interactions between the tip and sample. The net van der Waals force can be obtained by summing up all the dipole interactions. A detailed study of van der Waals forces in AFM has been given by Israelachvili (Israelachvili, 2010) and Butt et al. (Butt et al., 2005). One of the most common expressions of van der Waals force is presented in the following equation.

$$F_{vdW} = -\frac{HR}{6d^2} \quad (4.1)$$

In Equation 4.1, H, R and d are the Hamaker constant, radius of the tip and the instantaneous tip sample separation, respectively. In order to avoid problems in the equation when the value of d approaches zero, an intermolecular distance term  $a_0$  is introduced. When d becomes smaller than  $a_0$ , the van der Waals force is modified as follows.

$$F_{vdW} = -\frac{HR}{6a_0^2} \quad (4.2)$$

Intermolecular distance is related to the Hamaker constant and surface energy  $\gamma$ , as shown in the equation below.

$$a_0 = \sqrt{\frac{H}{24\pi\gamma}} \quad (4.3)$$

A reference value of 0.165 nm is also provided for  $a_0$  in a paper by (Israelachvili, 2010), while the Hamaker constant is of the order of  $10^{-20}$  J (Israelachvili, 2010, Butt et al., 2005). Generally, the van der Waals force between the tip and sample is attractive. However, it may become repulsive depending on the surrounding medium. To be more specific, in ambient, or vacuum, conditions the van der Waals force is attractive when the tip and sample are made of different materials. While the tip and sample are made of the same material, then the van der Waals force is always attractive. It becomes more complicated when the experiment is performed in liquid. In the case of two different materials, whether the van der Waals force is attractive or repulsive here largely relates to the dielectric constant and refractive index (Israelachvili, 2010, Butt et al., 2005).

## 4.2 Capillary force

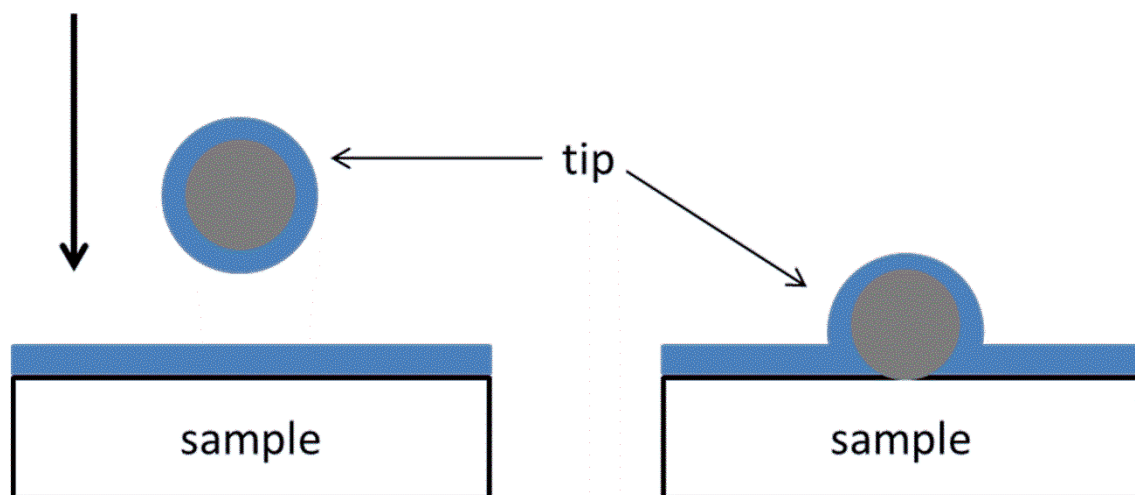


**Figure 4.1** Schematic diagram shows how the water meniscus forms between tip and sample.

When the experiment is performed in air, it is possible to form a water meniscus between the tip and sample, as shown in Figure 4.1, which depends upon the humidity of the environment. In other words, a water meniscus is caused by capillary condensation. Capillary condensation (Casper, 1977) can be described as a thermodynamic process related the radius of the water meniscus and the vapour pressure of the liquid, which can be shown using the Kelvin equation.

$$R_g T \log \frac{P}{P_0} = \frac{\gamma_L V_m}{r_k} \quad (4.4)$$

where  $R_g$ ,  $\gamma_L$ ,  $P$ ,  $P_0$  and  $V_m$  represent the gas constant, surface energy of liquid, vapour pressure and vapour pressure at saturation, respectively. While the relative humidity is described by  $P/P_0$  and  $r_k$  represents the Kelvin radius, as shown in following equation:

$$\frac{1}{r_k} = \frac{1}{r_1} + \frac{1}{r_2} \quad (4.5)$$

where  $r_1$  and  $r_2$  are the principal radii of the water meniscus. Analytical expressions of the capillary force have been obtained by different authors. One suggested that the expression of capillary force for a spherical tip and a flat sample surface is as shown in the following equation (Israelachvili, 2010):

$$F_{cap} = \frac{4\pi R \gamma_L \cos \theta}{1+d/d_0} \quad (4.6)$$

where  $\theta$  represents the contact angle between the liquid and sample surface and  $d_0$  is the initial tip-sample separation. When the instantaneous tip-sample separation ( $d$ ) and contact angle are both zero, the capillary force becomes a maximum, which is shown in the following equation:

$$F_{cap(max)} = 4\pi R \gamma_L \quad (4.7)$$

Other authors (Zitzler et al., 2002) suggested that the capillary force appears at tip-sample separation  $d_{on}$  when the tip approaches the sample, which is shown in the following equation:

$$d_{on} = 2h \quad (4.8)$$

where  $h$  is the thickness of the liquid layer. Also, they found a way to calculate the pull-off distance to break the meniscus when the tip retracts from the sample surface. First, a definition of the volume of the meniscus is given using the following equation:

$$V_m = 4\pi R h^2 + \frac{4}{3}\pi h^3 + 2\pi r^2 h \quad (4.9)$$

where  $R$  is the radius of the tip and  $r$  is the radius of the contact area, as shown in the following equation:

$$r = \sqrt[3]{\frac{3\pi\gamma_L R^2}{E^*}} \quad (4.10)$$

where  $E^*$  is the effective Young's modulus. The tip-sample separation when the tip can pull off from the meniscus is defined as a function of the meniscus volume, under the assumption that the contact angle is zero.

$$d_{off} = V_m^{1/3} - \frac{1}{5R} V_m^{2/3} \quad (4.11)$$

$d_{on}$  is usually smaller than  $d_{off}$  because of the hysteresis caused by the capillary force. In an actual AFM experiment, the typical values of capillary force lies between 1 nN and 100 nN, which is dependent upon the humidity of the experimental environment. However, the effects of the capillary force should be kept as small as possible, for it has nothing to do with the nature of the sample, also it sometimes does significantly affect imaging the sample's surface, because in certain conditions the capillary force may be dominant.

### 4.3 Contact force

Different models have been developed to describe the contact force between the tip and sample. The earliest model was created by Hertz in 1881, now well known as the Hertz model, which only describes the elastic force. The JKR model was proposed by Johnson, Kendall, and Roberts (Johnson et al., 1971), while the DMT model was created by Derjaguin, Muller and Toporov (Derjaguin et al., 1975). These two models are also commonly used to describe the contact deformation in AFM.

#### 4.3.1 Hertz model

The Hertz model defines a relationship between the tip indentation and the contact force, as shown in the following equation (Johnson, 1985):

$$F = \frac{2}{\pi} \frac{E}{(1-\sigma^2)} \tan \alpha \delta^2 \quad (4.12)$$

where  $E$  is the Young's modulus,  $\sigma$  is the Poisson's ratio,  $\alpha$  is the half angle of the conical tip and  $\delta$  is the indentation depth, respectively.

### 4.3.2 DMT model

The DMT model (Derjaguin et al., 1975) is usually better for modelling situations with a relatively small radius of tip and low adhesion forces. In this model, the contact force is considered, as well as adhesion force, which are illustrated in the following equations:

$$F_{adhesion} = -4\pi R\gamma, \quad d < d_0 \quad (4.13)$$

where the adhesion force is related to the radius of tip ( $R$ ) and surface energy ( $\gamma$ ), while the elastic force is expressed in terms of the radius of the tip, effective Young's modulus  $E^*$  and the instantaneous tip-sample separation  $d$ , as shown in the following equations. Here the term  $d_0$  is the initial tip-sample separation.

$$F_{elastic} = \frac{4}{3}E^*\sqrt{R}(-d_0 - d)^{\frac{3}{2}}, \quad d < d_0 \quad (4.14)$$

$$E^* = [(1 - \sigma_t^2)/E_t + (1 - \sigma_s^2)/E_s]^{-1} \quad (4.15)$$

where the effective Young's modulus  $E^*$  is related to the Young's modulus and the Poisson's ratio of the tip and sample. When  $d$  is smaller than  $d_0$ , the tip begins to feel the elastic force and adhesion force. The DMT model also deduces an analytical expression for the contact radius ( $a$ ), as shown in the equation below.

$$a^3 = \frac{3R}{4E^*}(F_{elastic} + F_{adhesion}) \quad (4.16)$$

### 4.3.3 JKR model

The JKR model (Johnson et al., 1971) is used to study contact situations with relatively high adhesion forces and a large radius of tip. For the adhesion force, the form is similar to that of the DMT model.

$$F_{adhesion} = 3\pi R\gamma \quad (4.17)$$

The expression of the elastic force is rather more complicated, which is given in terms of normalized indentation and force.

$$\bar{\delta} = 3(\bar{F} + 2 + 2\sqrt{1 + \bar{F}})^{3/2} - 4(\bar{F} + 2 + 2\sqrt{1 + \bar{F}})^{1/6} \quad (4.18)$$

where  $\bar{\delta} = \delta/\delta_a$  is the normalized indentation and  $\delta_a$  is the pull off separation shown in the following equation.  $\bar{F} = F_{elastic}/F_{adhesion}$  is the normalized applied force.

$$\delta_a = \left(\frac{\pi^2 R \gamma^2}{3E^*}\right)^{1/3} \quad (4.19)$$

Also, the contact radius may be expressed as shown below:

$$a^3 = \frac{3R}{4E^*} \left( F_{elastic} + 2F_{adhesion} + 2\sqrt{F_{elastic}F_{adhesion} + F_{adhesion}^2} \right) \quad (4.20)$$

#### 4.4 Non-conservative forces

Non-conservative force is usually referred to as the force which would cause energy dissipation. Energy dissipation can be caused by different factors, such as the material properties of the sample, like surface energy and viscosity and the surrounding environment, for example the humidity of the ambient air. In an actual AFM experiment it is necessary to consider the energy dissipation, because energy dissipation during the tip sample contact is the reason that actually causes a phase shift. The origin of energy dissipation is generated under two conditions: adhesion energy hysteresis (García et al., 1999) and viscosity force (San Paulo and García, 2001).

Adhesion hysteresis can be caused by both short range and long range attractive interaction forces. The theory is that in order to separate two surfaces, one needs to do more work than bringing the two surfaces together. Here, three different interaction forces are introduced. Adhesion energy hysteresis occurs when the retract surface energy  $\gamma_{retract}$  is different from the approach surface energy  $\gamma_{retract}$ , as the AFM tip approaches and retracts from the sample surface.

$$F_{adhesion} = -4\pi R(\gamma_{retract} - \gamma_{approach}), \quad d < d_0 \quad (4.21)$$

Long range interaction forces occur when there is no contact between the AFM tip and the sample, which are related to the tip-sample separation and a time dependent constant  $\alpha(t)$ , as shown in the following equation:

$$F_l = \frac{\alpha(t)}{d^2} \quad (4.22)$$

Viscosity force is related to the viscosity of the sample material  $\eta$ , radius of the tip  $R$ , indentation and the velocity of the tip. As the velocity changes sign during the approaching and retracting period, the instantaneous viscosity force could be either repulsive or attractive in nature.

$$F_{viscosity} = -\eta\sqrt{R(-d_0 - d)}\dot{d}, \quad d < d_0 \quad (4.23)$$

#### 4.5 Summary and Discussions

Different interaction forces that may occur in actual AFM experiments have been summarised here. Generally, they can be divided into two kinds, namely attractive forces and repulsive forces. The exception is that the viscosity force is the combination of both types. The van der Waals force, contact force, adhesion force and viscosity force will be used in Chapter 7 to define the tip sample interaction forces.

# Chapter 5

# Phase Imaging

## **Chapter 5 Phase Imaging**

In Chapter 5, a general description of phase imaging is introduced. Then, the theory behind phase imaging is demonstrated, along with experimental and numerical modelling results. Analytical models for the phase shift are presented. Interpretation of the phase imaging is given and has been summarized.

### **5.1 General description**

Unlike other image modes, tapping mode AFM not only can measure the topography of the sample, but can also provide a phase image of the sample. Phase imaging was first mentioned in 1995. Virgil Elings presented a new imaging technique based on tapping mode AFM informally. It was said that this could provide high resolution imaging by measuring the phase difference between the actual cantilever deflection and the cantilever driving signal. Although the reasons accounting for the phase shift were not clear, phase imaging was widely used to measure heterogeneous samples.

Phase imaging is a powerful instrument to provide high resolution images of surface properties, which is an extension of tapping mode AFM. When tapping mode AFM is being conducted under a specific set-point amplitude, a phase image is obtained together with the height image. Sometimes, the phase image can provide information that is not shown in the height image. For example, a perfectly flat sample is divided into two regions which have the same height, but different surface properties, as shown in Figure 5.1. The height should show no difference between the two regions if the height measurement is perfectly accurate. However, the phase image can provide different contrast between these two regions.

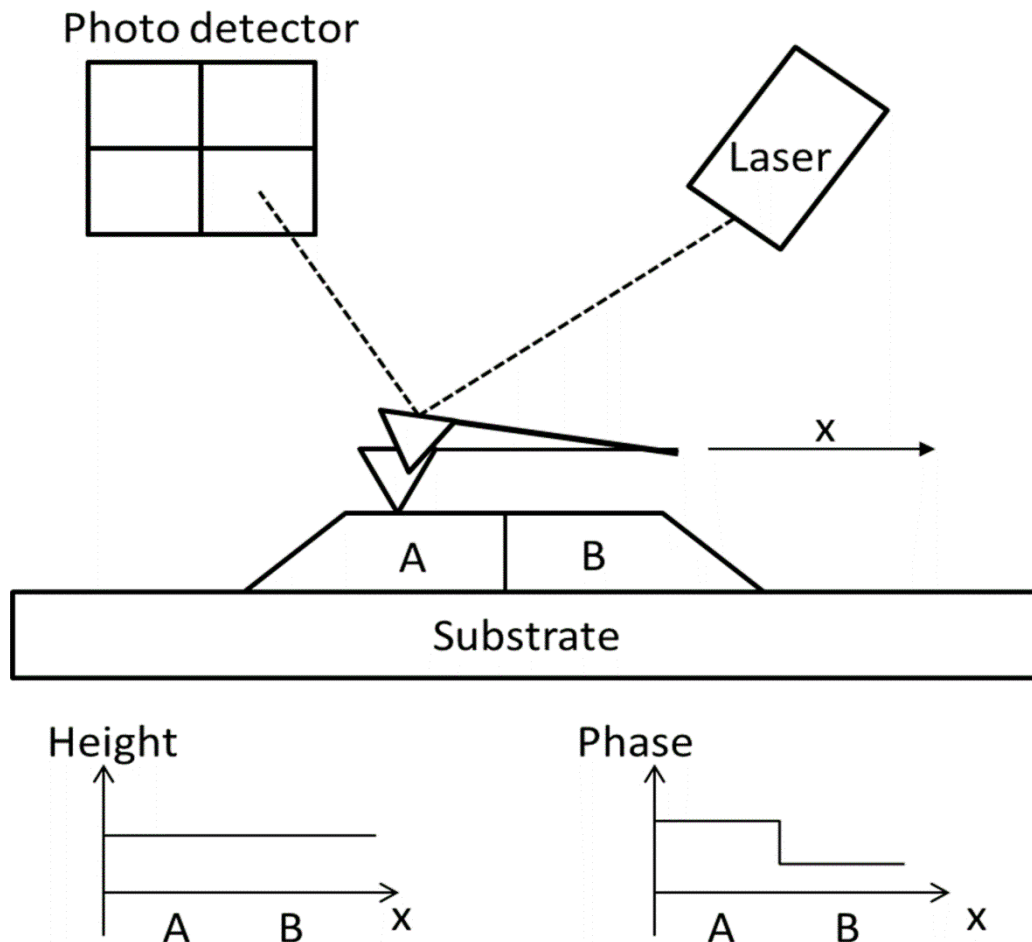


**Figure 5.1 Schematic diagram of height and phase measurement of regions A and B.**

According to (Suo et al., 2006), their experiments showed the advantages of phase imaging. For a biological sample containing some cells buried under capsular material, as shown in Figure 5.2, the height images only describe the morphology of the sample without providing information about the detailed structure of the cells, while the amplitude images reveal the difference between the cells and the surrounding material. Phase images presented here claim to provide better resolution than the other images. The phase images not only clearly show the structure of the cells, with different contrast between the cells and the surrounding material, but they also indicate that phase imaging has the ability to reveal the inner structure, or sub-surface.

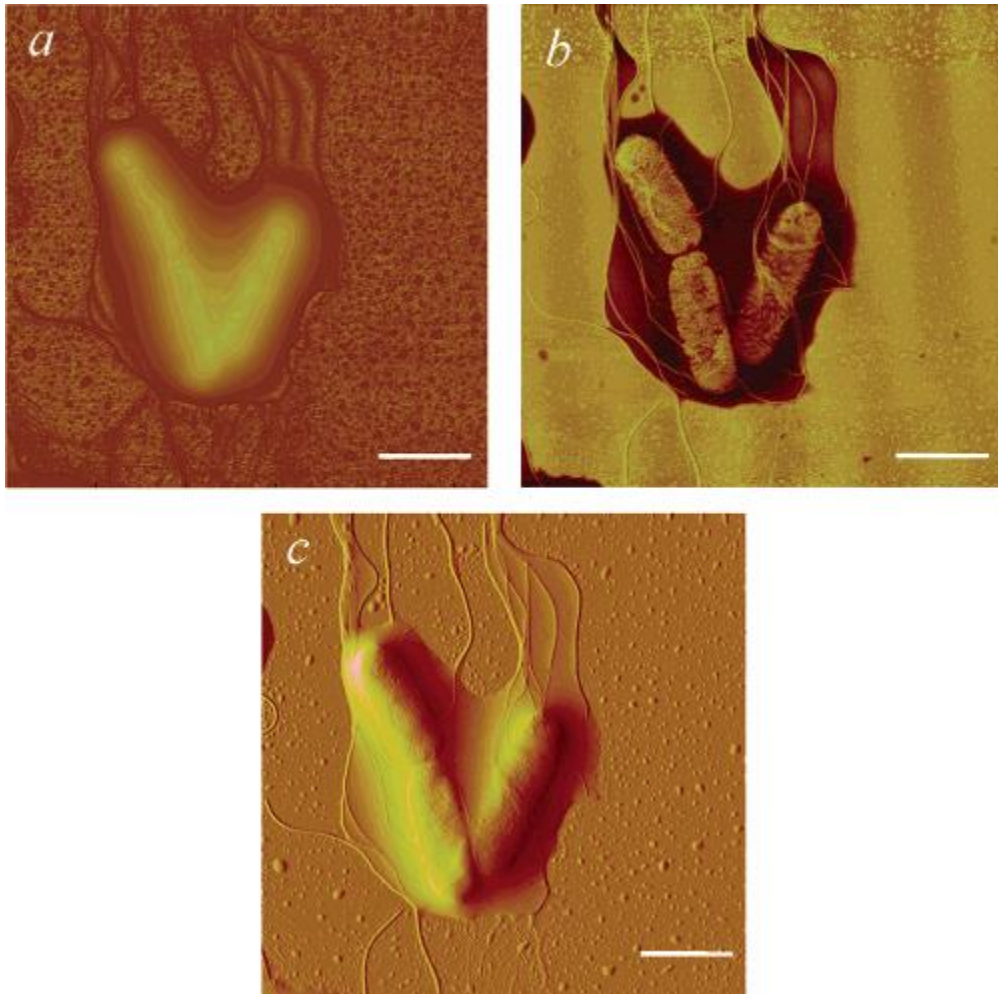


**Figure 5.2 AFM images of three buried cells: (a) Height image, (b) Phase image, (c) Amplitude image, the scale bar corresponds to 2 $\mu$ m. Adapted with permission to reproduce this figure from (Suo et al., 2006) has been granted by American Chemical Society.**

For a hydrogenated diblock copolymer mesophase sample, it has been shown that phase imaging may be advantageous in (Reiter et al., 2001). In Figures 5.3(a) and (b), reproduced from their paper, the figures show the topography image and phase image before crystallization, respectively. The topography image does not provide any detail of the sample structure, while the phase image shows some black 'disk' like pattern. After partial crystallization, shown in Figures 5.3(c) and (d), the topography image still does not show the sample structure. However, the phase image shows the different contrast in terms of black and white spheres, which can help to differentiate the crystalline and the molten PEO micelles. The crystalline micelles are represented in light contrast, which means that the stiffness becomes larger after crystallization.

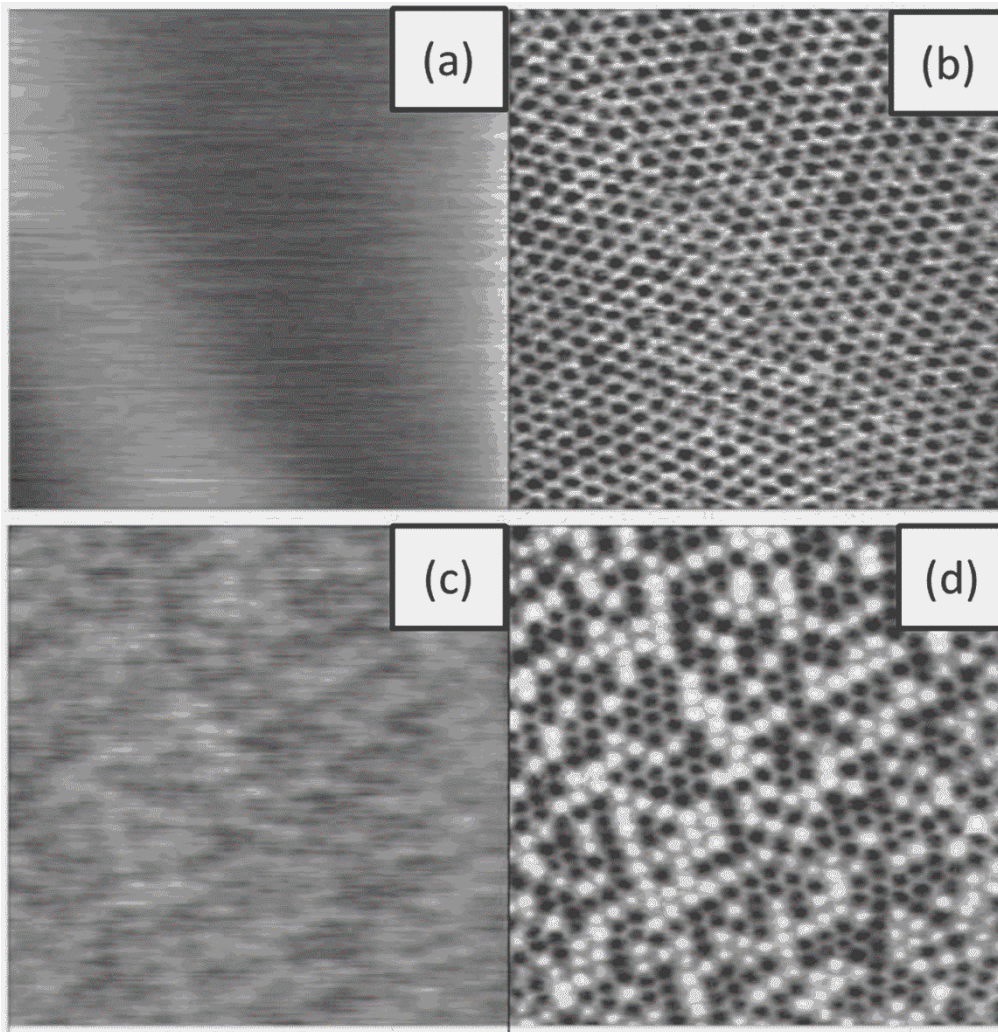


**Figure 5.3** AFM images of hydrogenated diblock copolymer, scanned size: 500nm by 500nm. Adapted with permission to reproduce this figure from (Reiter et al., 2001) has been granted by Physical Review Letters.

With the help with height image and phase image, a three dimensional image can be reconstructed for the sample. The height image is still used to represent the height in the z direction, while the phase image is adopted as the contrast in the x and y directions. The three-dimensional image provides a way to observe the height and variation of sample properties simultaneously (Knoll et al., 2004). Figure 5.3 shows a three dimensional image of parafilm. It can be seen that the phase changes are corresponding to the variation of the height of the film.

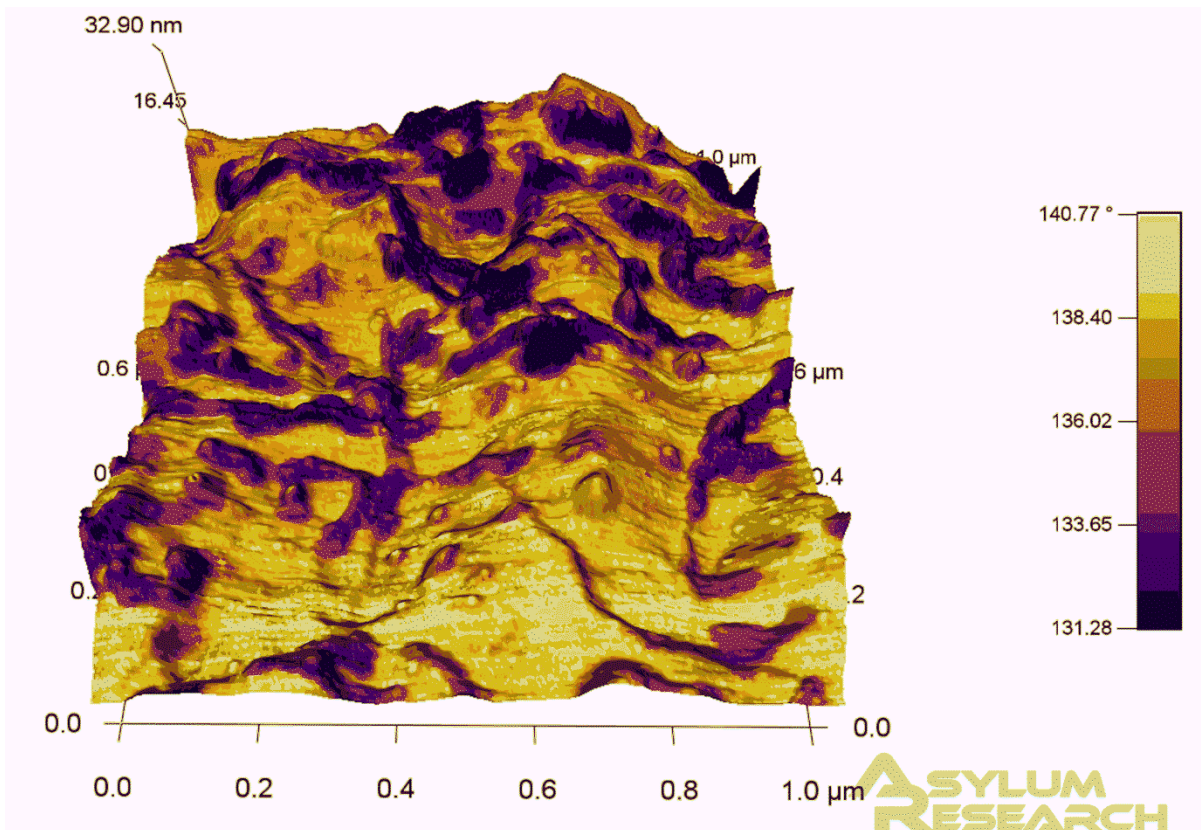


**Figure 5.4 3D image of parafilm reconstructed with height and phase image**

A brief description of the application of phase imaging has been given above. Due to the advantage of phase imaging, tapping mode AFM has been used in many different areas. In terms of the aspect of resolution, tapping mode AFM is able to measure materials ranging from the micrometer to the nanometer scale, and even at the molecular level. On the other hand, in terms of material type, a large range of material has been investigated using tapping mode AFM, such as fibers, polymers, cells, proteins, DNA and so on (Leclère et al., 1996, Brandsch et al., 1997, Suo et al., 2006, Stark et al., 2001, Klinov et al., 2007).

## **5.2 Theory of Phase imaging**

### **5.2.1 Resonance frequency shift theory**

In the initial stages, it was suggested that the change of the local elasticity of the material is the reason that causes a phase contrast in the phase image (Whangbo et al., 1998, Magonov et al., 1997b). Magonov and his co-workers studied how the phase shifts change by varying the repulsive tip-sample interaction forces using tapping mode AFM. They performed

experiments on a polyethylene sample by sweeping around the resonant frequency to observe how the amplitude and phase changes, which is shown in Figure 5.5. It was found that during free vibration, the centre of both amplitude and phase curves correspond to the resonant frequency. In this case, the phase shift is  $90^\circ$ . When the tip moves close to the sample, reaching a setpoint ratio of 0.7 (setpoint ratio = setpoint amplitude/free amplitude), the peak of the amplitude moves to a lower frequency, which leads to the condition that the phase shift against the new resonant frequency becomes larger than  $90^\circ$ . However, when the setpoint ratio reaches a value of 0.2, the repulsive tip-sample interaction forces are enhanced. The peak of the amplitude is wider and shifts to a higher frequency, which result in the condition that the phase shifts are smaller than  $90^\circ$ .

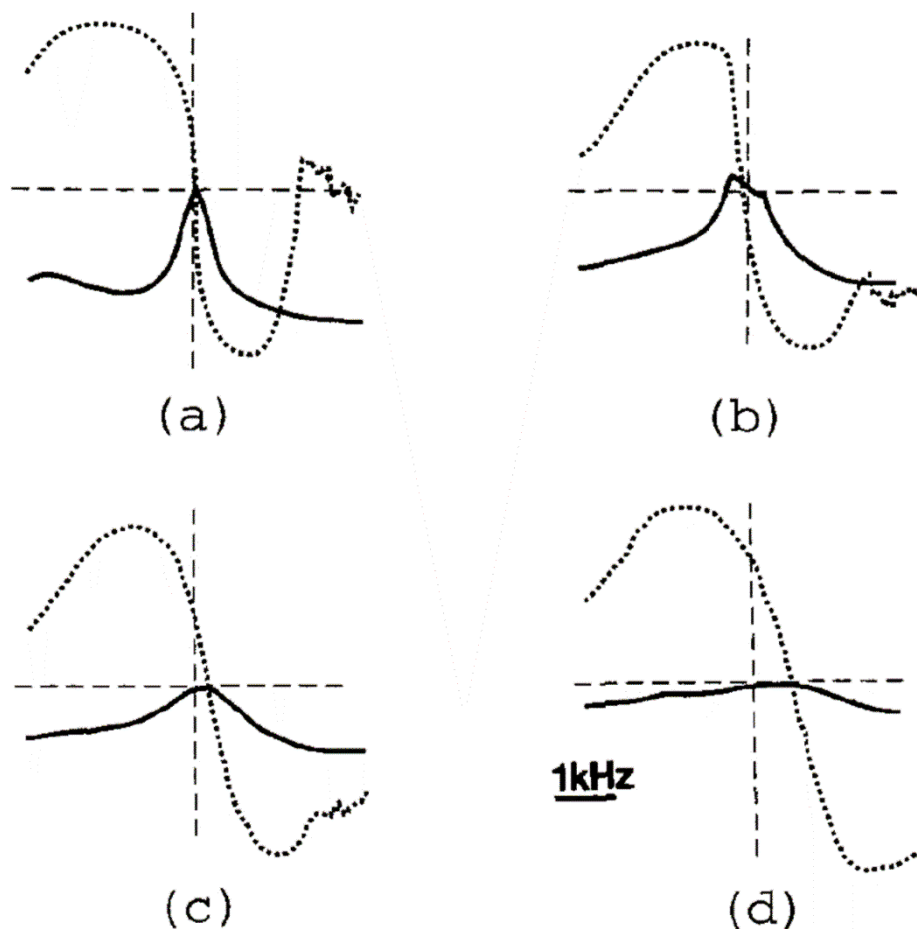


Figure 5.5 AFM experiments are performed on a polyethylene sample. Free vibration amplitude is 20 nm. Amplitude-frequency curve (solid) and phase shift-frequency curve (dash) are shown with different set-point ratios (a) setpoint ratio = 1, (b) setpoint ratio = 0.7, (c) setpoint ratio = 0.5, (d) setpoint ratio = 0.2. Adapted with permission to reproduce this figure from (Magonov et al., 1997b) has been granted by Surface Science.

Phase shifts of both hard and soft materials were investigated (Magonov et al., 1997b). All experiments were performed in air using a Digital Instruments Nanoscope IIIa AFM. Silicon cantilevers were used with a spring constant of 40 N/m and resonant frequency ranging between 150 to 180 kHz. Phase shifts were recorded by changing the setpoint ratio from 0.1 to 1. Different free amplitudes were also studied. From Figure 5.6, it can be seen that the phase shifts of materials whose Young's moduli are larger than 1 GPa, like silicon, glass and mica, share similar trends. The phase shifts gradually increase when the setpoint ratio decreases. As for materials whose Young's moduli are smaller than 1 GPa, the phase shifts are considerably smaller than those of the hard materials when the setpoint ratio ranges from 0.4 to 0.7. However, the phase shifts of soft materials show a sudden increase during hard tapping (when the setpoint ratio is below 0.3), which are larger than the phase shifts of the hard materials. When the free amplitude is below 20nm, the trend of phase shifts is relatively different from that of large free amplitudes ( $\geq 60$  nm). Moreover, the trend could not be obtained repeatedly, which indicates that the tip was affected by the contamination of the surface, such as the liquid layer. Thus, the authors concluded that in order to get a good phase image, it is necessary to adopt a large free amplitude and small setpoint ratio under their experimental conditions.

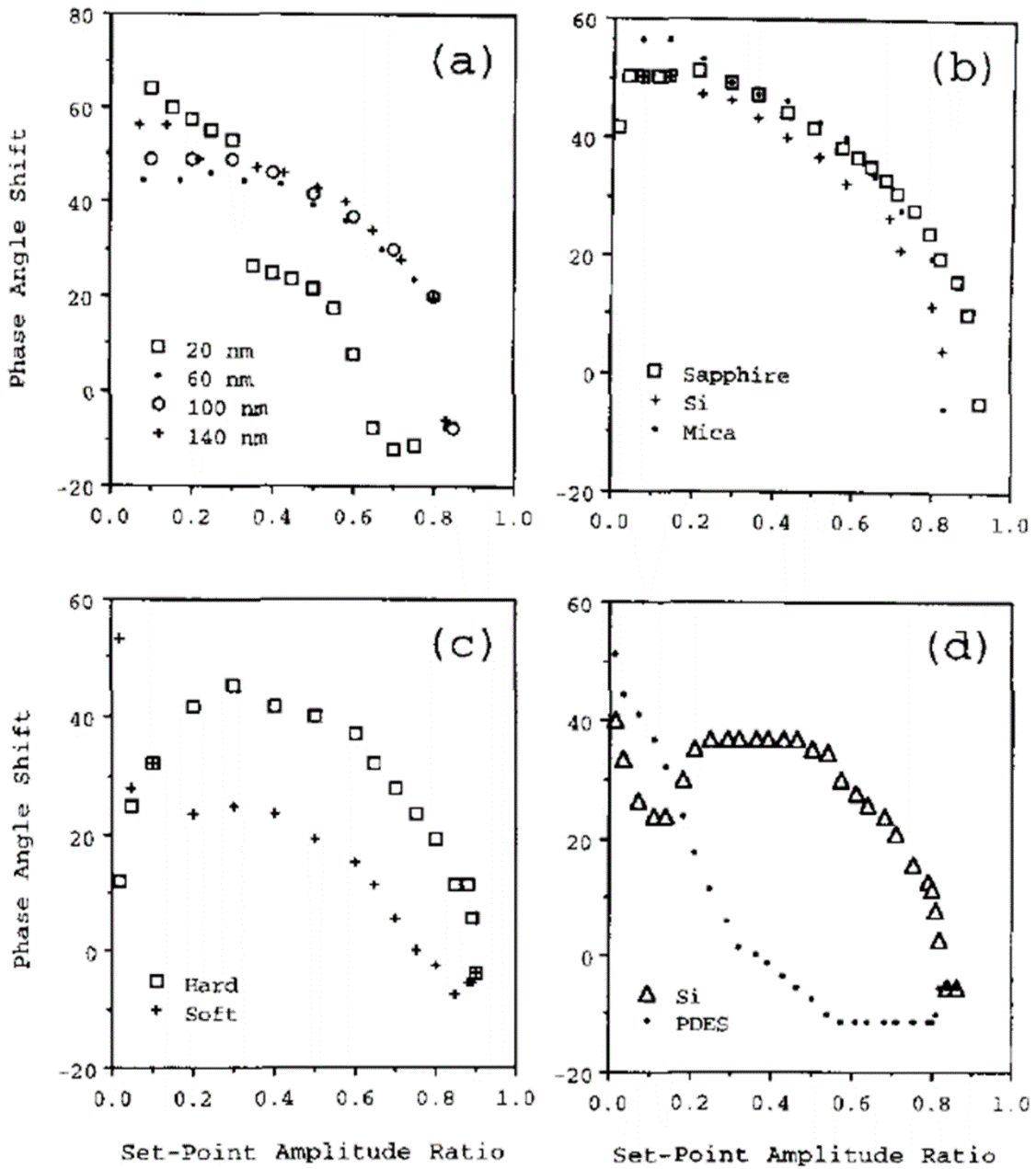


Figure 5.6 Phase shift were recorded against different setpoint ratios with different free vibration amplitudes for materials with different Young's moduli. Adapted with permission to reproduce this figure from (Magonov et al., 1997b) has been granted by Surface Science.

### 5.2.2 Energy dissipation theory

Other researchers thought that energy dissipation during contact between the tip and the sample was the only reason behind the cause of the phase shift (Tamayo and García, 1997).

They performed a numerical simulation to investigate the phase shift. Different materials whose Young's moduli ranged from 0.01 GPa to 100 GPa were tested. It was found that the phase shifts remained the same while only considering the effect of the elastic modulus. However, the behaviour of the phase shifts changed significantly when the effect of viscosity or adhesion energy hysteresis was included, especially for materials with a Young's modulus smaller than 1 GPa. These results are shown in Figures 5.7 and 5.8.

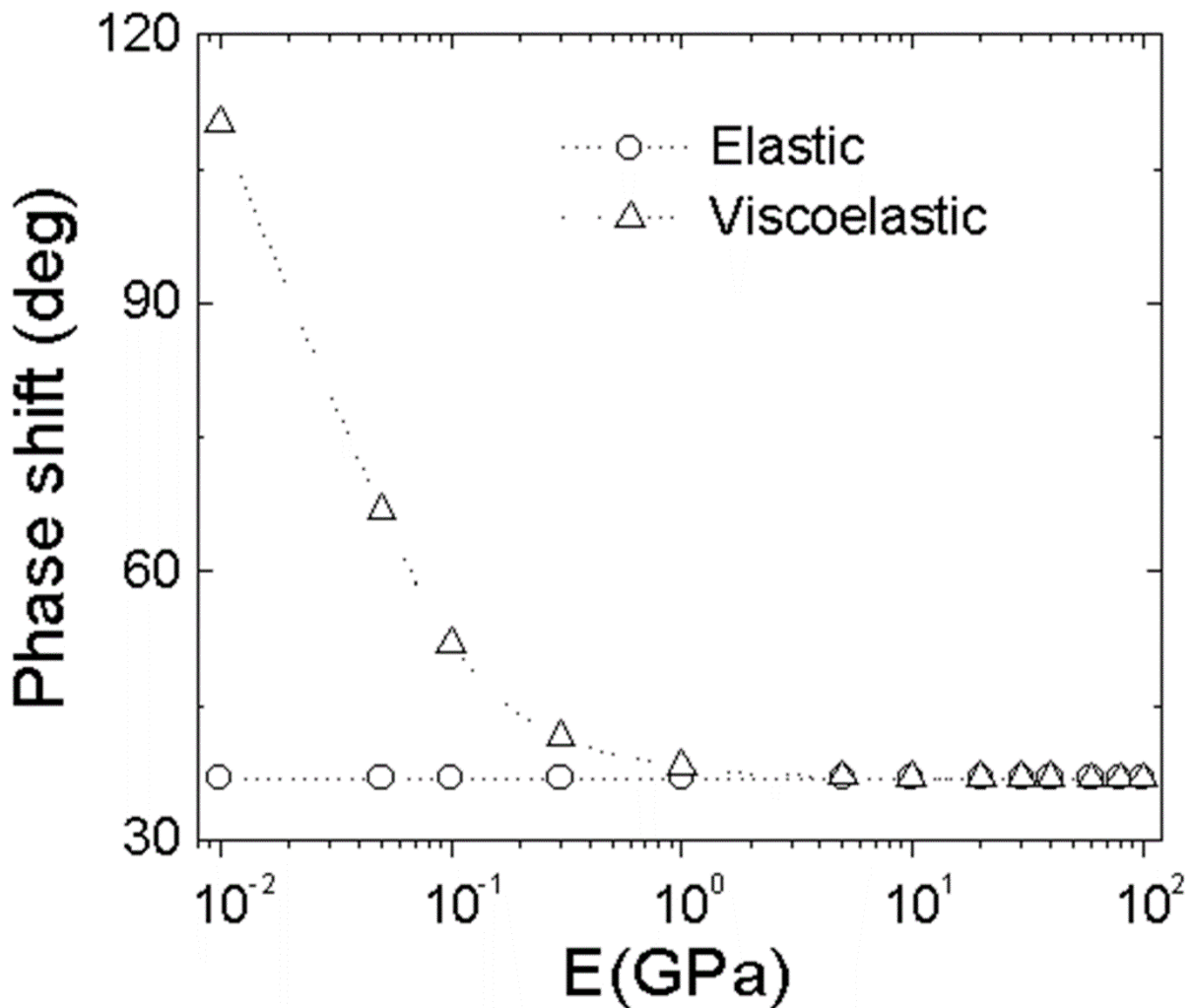


Figure 5.7 Q factor = 500, k = 20N/m, viscosity is 30 Pa\*s. The open circle dash curve shows the phase shifts when only the elastic force is considered, while the open triangle dash curve shows the phase shifts when the viscosity force is coupled with the elastic force. Both phase shifts were obtained under a setpoint ratio = 0.6. Adapted with permission to reproduce this figure from (García et al., 1998) has been granted by Applied Physics A: Materials Science & Processing

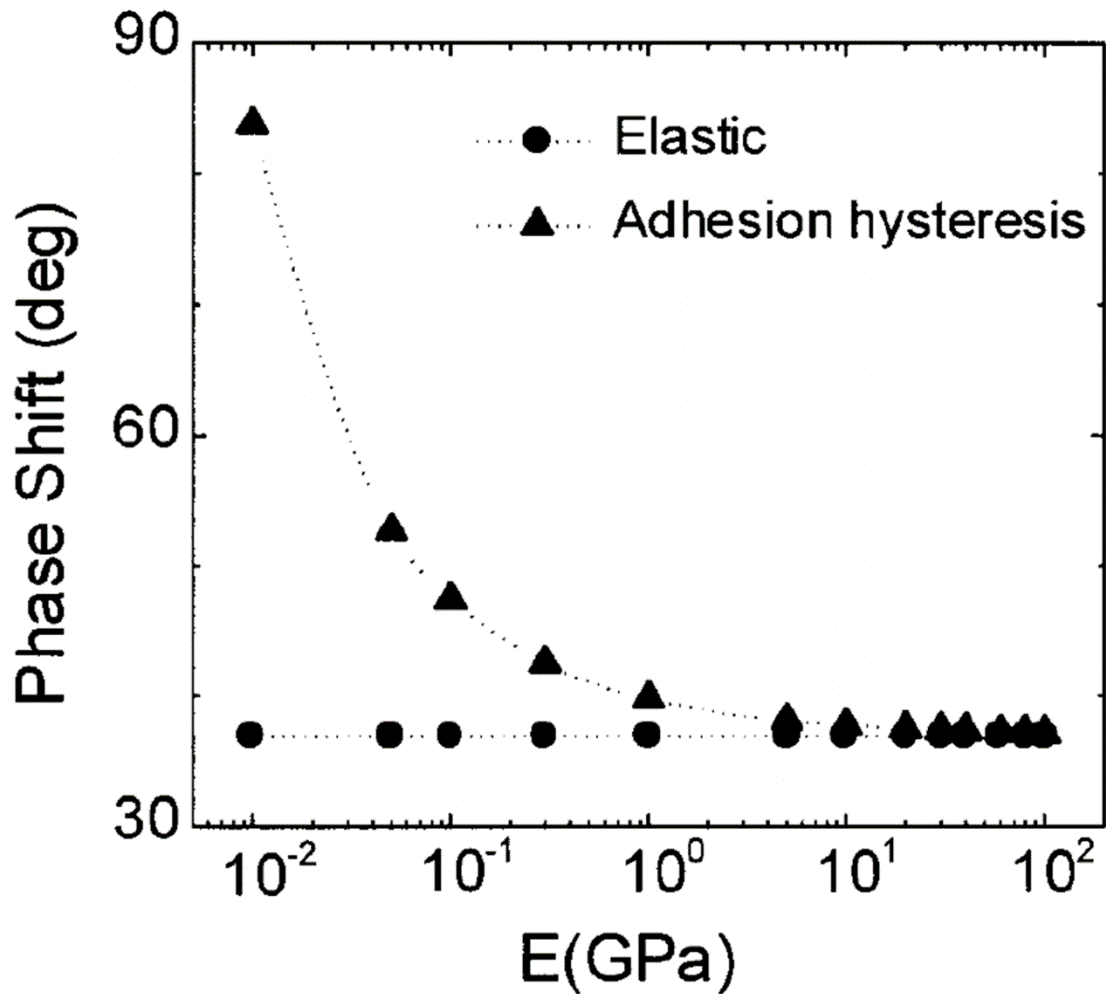


Figure 5.8 Q factor = 500,  $k = 20\text{N/m}$ , approaching surface energy is  $10\text{ mJ/m}^2$ , retracting surface energy is  $60\text{ mJ/m}^2$ . The closed circle dash curve shows the phase shifts when only the elastic force is considered, while the closed triangle dash curve shows the phase shifts when adhesion hysteresis is coupled with the elastic force. Both phase shifts were obtained under a setpoint ratio = 0.6 Adapted with permission to reproduce this figure from (García et al., 1999) has been granted by Surface & Interface Analysis.

### 5.2.3 Analytical models for phase shift

The first approximation to express the phase shift of tapping mode AFM was made by Magonov and his co-workers (Magonov et al., 1997b). They considered the cantilever as a spring. The spring constant is related to the mass and resonant frequency, which is shown as follows:

$$k = m\omega_0^2 \tag{5.1}$$

where  $k$ ,  $m$ ,  $\omega_0$  are the spring constant, mass and resonant frequency of the cantilever, respectively. During free vibration, the phase angle can be expressed as in the following equation:

$$\Phi = \tan^{-1} \frac{m\omega\omega_0}{Q(k-m\omega^2)} \quad (5.2)$$

From the equation above, it can be seen that the phase angle is  $90^\circ$  when the cantilever is vibrated at its resonant frequency. When the tip encounters the tip-sample interaction forces, the spring constant of the cantilever is changed. The effective spring constant is shown as given below:

$$k_{eff} = k + \sigma \quad (5.3)$$

where  $\sigma$  is described as the derivatives of all the forces shown in the following equation:

$$\sigma = \sum_i \frac{\partial F_i}{\partial z} \quad (5.4)$$

where  $z$  is the tip-sample separation. Thus, the phase shifts under different interaction forces can be represented as follows:

$$\Phi = \tan^{-1} \frac{m\omega\omega_0}{Q(k+\sigma-m\omega^2)} \quad (5.5)$$

When  $\sigma$  is much smaller in magnitude than the spring constant  $k$ , the phase angle at the resonant frequency can be derived as follows:

$$\Phi_0 = \tan^{-1} \frac{k}{Q\sigma} \quad (5.6)$$

Thus, the phase shift can be calculated as being the difference of the phase angles between free vibration and vibration under the tip-sample interaction forces, which is shown as follows:

$$\Delta\Phi_0 = \frac{\pi}{2} - \tan^{-1} \frac{k}{Q\sigma} \approx \frac{Q\sigma}{k} \quad (5.7)$$

The sign of the phase shift determines the characteristic of the sum of the tip-sample interaction forces. When the phase shift is negative, it indicates that the overall tip-sample interaction force is attractive. Vice versa, when the phase shift is positive, the overall tip-sample interaction force is repulsive.

Later, another analytical expression was deduced for phase shift using a point mass model when experimentation is performed under a high quality factor (García et al., 1999). When the cantilever is vibrated in the stable state, the displacement of the cantilever can be presented using the following equation:

$$\mathbf{z} = \mathbf{z}_0 + A \cos(\omega t - \Phi) \quad (5.8)$$

In order to maintain the amplitude of the cantilever constant during the stable state, the energy provided by the excitation signal in each cycle has to be equal to the dissipated energies in each cycle caused by the damping of the environment and the tip-sample interaction forces, which is shown in the following equation:

$$E_{exc} = E_{med} + E_{dis} \quad (5.9)$$

where  $E_{exc}$  is the energy supplied by the excitation signal, which is defined as:

$$E_{exc} = \oint F_0 \cos(\omega t) \frac{dz}{dt} dt = \frac{\pi k A_0 A(\omega) \sin \Phi}{Q} \quad (5.10)$$

$E_{med}$  shown in the following equation represents the energy dissipated by the damping of the environment.

$$E_{med} = \oint \left( \frac{m\omega_0}{Q} \frac{dz}{dt} \right) \frac{dz}{dt} dt = \frac{\pi k A^2 \omega}{Q \omega_0} \quad (5.11)$$

As for the energy dissipated by the tip-sample interaction forces, it is expressed as:

$$E_{dis} = \oint (F_{ts}) \frac{dz}{dt} dt \quad (5.12)$$

Hence, the relationship between the phase shift and the energy can be derived as:

$$\sin \Phi = \frac{A\omega}{A_0\omega_0} \left( 1 + \frac{E_{dis}}{E_{med}} \right) \quad (5.13)$$

It can be seen that the phase shift depends on the tapping amplitude  $A$  (which is also named the setpoint amplitude) and the dissipated energy  $E_{dis}$  by the interaction forces. As the setpoint amplitude is always maintained constant during the operation of an AFM experiment, it can be concluded that the contribution from the setpoint amplitude to the phase shift can be neglected. In other words, for two materials that have the same surface conditions, but different stiffnesses, in order to maintain the setpoint amplitude, the piezo needs to move the cantilever up or down. At the same time, the stiffness of two materials is not a significant factor, which can be demonstrated more clearly using the following equation:

$$A = z_1 + \delta_1 = z_2 + \delta_2 \quad (5.14)$$

For example, assume that material 1 is harder than material 2. Thus, the indentation  $\delta_1$  is smaller than  $\delta_2$ . However, the setpoint amplitude  $A$  needs to be the same value. Thus, the only solution is to change the tip-sample separation  $z_1$  and  $z_2$ . Hence, if these two materials are imaged using tapping mode AFM, the phase images will not tell any difference between the two materials. However, this case is under the ideal situations, as it is difficult to find some materials with different stiffness, but which dissipate the same amount of energy. To sum up, under certain circumstances, a conclusion can be drawn from the above equations that the phase shift does not depend on the stiffness of the material, but only the energy dissipation, which is related to surface conditions, like adhesion, viscosity and so on. According to (Bar et al., 1999, Tamayo and García, 1998), the equation has been validated by experiments performed on different materials, such as polydimethylsiloxane, graphite and purple membranes.

Later, a new expression of phase shift was derived from Equation 5.13 by using the virial theorem (San Paulo and García, 2001, Paulo and García, 2001) shown as follows:

$$\cos \Phi = \frac{2Q}{kAA_0} \left[ \frac{\langle F_{ts} \rangle^2}{k} - \langle F_{ts} z \rangle + \frac{1}{2} k A^2 \left( 1 - \frac{\omega^2}{\omega_0^2} \right) \right] \quad (5.15)$$

When the cantilever is vibrated at its resonant frequency, the above equation can be deduced as follows if the average value of the deflection  $z$  is much smaller than the vibration amplitude  $A$ .

$$\cos \Phi = \frac{2Q\langle F_{tsz} \rangle}{kAA_0} \quad (5.16)$$

On the other hand, the expression for the displacement of the cantilever needs to be modified when the experiment is performed with a low quality factor (Garcia et al., 2007, Tamayo, 1999). Here the displacement of the cantilever is no longer based on the first resonant mode, because the tip-sample interaction forces activate higher harmonics and modes. For quality factor smaller than 5, the displacement of the cantilever is defined as:

$$\mathbf{z} = \mathbf{z}_0 + \sum_{n=1}^{\infty} \mathbf{A}_n \cos(n\omega t - \Phi_n) \quad (5.17)$$

where  $n$  represents the order of the harmonic and mode, and  $A_n$  is the corresponding amplitude. Substituting the above equation into Equation 5.9, the phase shift related to higher modes can be obtained as follows:

$$\sin \Phi_1 = \sum_{n=1}^{\infty} \frac{n^2 A_n^2 \omega}{A_0 A_1 \omega_0} \left( 1 + \frac{E_{dis}}{E_{med}} \right) \quad (5.18)$$

The above equation shows the phase shift when higher harmonics are involved. In this case, the term  $A_n/A_1$  which is related to the elastic contribution from the stiffness of the material can be separated from the term related to the energy dissipation. Thus, when higher harmonics are involved, phase shifts are related to the elasticity and energy dissipation of the materials of the sample.

As mentioned above, energy dissipation is the reason for causing a phase shift. Vice versa, energy dissipation can be described as a function of the setpoint amplitude and vibration frequency, which is shown in the following equation:

$$E_{dis} = \frac{\pi k A^2}{Q} \left( \frac{A_0}{A} \sin \Phi - \frac{\omega}{\omega_0} \right) \quad (5.19)$$

where  $Q$ ,  $A_0$  and  $\omega_0$  represent quality factor, free vibration amplitude and resonant frequency, respectively. On the other hand, the above equation can also be transformed to describe the average power dissipated during the tip-sample interactions:

$$\langle P_{dis} \rangle = \frac{k A^2 \omega}{2Q} \left( \frac{A_0}{A} \sin \Phi - \frac{\omega}{\omega_0} \right) \quad (5.20)$$

According to (Cleveland et al., 1998, Martínez and García, 2006, Garcia et al., 2006), the dissipated energy and power shown in the equations above are useful for measuring dissipation at the nanoscale. During high resolution AFM experiments, in each vibration cycle, there is around 0.5 to 50 eV energy dissipated. In other words, during the contact between tip and sample, there is approximately 0.008 to 0.8 pW of power lost. For example, if the resolution is 2nm, it can be calculated that the energy dissipated in each bond is within the range between 0.0001 to 0.1 eV. The energy lost in each bond is not large enough to break the bonds of most materials. Thus, phase imaging can be applied to most materials due to its non-invasive characteristics.

### **5.3 Interpretation of phase imaging**

Since the development of AFM techniques, they have been widely used in different fields. Although high resolution images have been obtained, many researchers were still trying to understand these images. Motomatsu and his coworkers studied the triblock copolymer consisting of polystyrene, polyethylene and polybutylene. Experiments were performed using triangular silicon nitride cantilevers under contact mode AFM. The spring constant of the cantilever was 0.1 N/m, and the tip had a pyramid shape with a radius of about 20nm. They thought that the height image of AFM indicated the hard and soft composition of the sample. Also, a conclusion was drawn that higher areas in the height image indicated the polystyrene component (Motomatsu et al., 1997). However, Dijk and his groupmate had an opposite opinion that higher areas should indicate softer composition of material (van den Berg et al., 1994).

Phase imaging was used by McLean and Sauer (McLean and Sauer, 1997) to investigate the attribution of materials. They scanned a triblock copolymer sample using Nanoscope IIIa AFM with a long cantilever of 125um. Tip radii ranging from 5-10nm were also adopted. The resonant frequency of the cantilever was around 300 kHz. Experiments were performed under high, moderate and light tapping forces, respectively. For high and moderate tapping, phase shifts were in the range between 16-22°, while the phase shifts were around 7-11° for light tapping. Interesting behaviour was seen in the height image. They found that higher areas in the height image represented harder materials during moderate tapping. As for hard tapping, the contrast of the height image reversed, resulting in lower areas indicating

harder materials. It was found that the phase shifts relied upon the composition of the materials instead of the height. According to (Magonov et al., 1997a, García et al., 1998), a PDES polymer was studied using tapping mode AFM. Because PDES is a soft material with high viscosity, it is easily damaged during the scanning conducted in contact mode AFM. PDES was placed on a silicon substrate. Experiments were performed with a long silicon cantilever whose first resonant frequency was between 250 and 300 kHz. Phase image revealed the lamellar structure of the polymer sample. The structure was observed better in the mesomorphic state than in the amorphous state, because the sample was stiffer. Also, the lamellar structure was represented by the brighter area of the phase image. In this case, the contrast of the phase image could help to differentiate the stiffness of the PDES sample.

Whangbo and his co-workers (Bar et al., 1997) were trying to investigate the factors affecting the height and phase image in tapping mode AFM. In that work polyethene-co-styrene (PES) and poly(2,6-dimethyl-1,4-phenylene oxide) (PPO) were blended together as a test sample. Silicon cantilevers with spring constant ranging from 13 to 70 N/m were used. Images were captured in air using a Nanoscope III AFM microscope. Contrast of the height and phase images were studied under different free vibration amplitudes and setpoint ratios (setpoint ratio = setpoint amplitude/ free vibration amplitude). Free vibration is defined when the tip is far away from the sample, where interaction forces on the tip can be neglected. Setpoint ratio can be regarded as being a variable to control how the amplitude damps. On the other hand, it can also to some extent indicate the distance between tip and sample. Experiments were carried out using a relatively low free vibration amplitude of 15nm. It was found that the composition of the polymer was not revealed in the height images, while the phase images showed some structure represented by dark contrast during light tapping. As setpoint amplitude was decreased, the difference between the polymer structures and its surrounding material was seen in both the height and phase images. Resolution of the images could be improved when the setpoint amplitude was further decreased, which separated the polymer structure (darker area) from the surrounding material (brighter area). Further experiments were performed using free vibration amplitudes of 45nm and 75nm, respectively. With the increased free vibration amplitude, the polymer structure was able to be seen in the height images even under light tapping. During moderate tapping, structures of the polymer were represented by brighter areas in

the phase images, while the height image no longer provided information about the structures. For hard tapping, both the height and phase images revealed the polymer structure in terms of a darker contrast. For some reason, the contrast of phase image reversed between moderate tapping and hard tapping modes. When the free vibration amplitude was further increased to 75nm, the polymer structure could be visualized in both the height and phase images under different tapping conditions. Also, the contrast reversed in both the height and phase images between moderate and hard tapping modes. In this case, it is difficult to relate the contrast of the various images to different compositions of the sample materials. This problem could be solved by implementing force-distance curve measurement. It has been found that the harder the sample material, then the stiffer the slope of the curve is.

#### **5.4 Summary and Discussions**

This chapter summarizes research into phase imaging carried out by various different authors. People have been trying to understand and investigate the phase information available in tapping mode AFM in terms of experimentation and numerical simulations. At the beginning, the phase shift was considered to be related to the elasticity of the sample. Later, it was found that the phase shift was related to the energy dissipation due to the contact between tip and sample. Different analytical expressions have also been developed to describe various phase imaging scenarios and these have been presented and discussed in this chapter.

# Chapter 6

A Real Contact Model

Based on Finite

Element Modelling of

Tapping Mode AFM

## Chapter 6 A Real Contact Model Based on Finite Element Modelling of Tapping Mode AFM

### 6.1 A Real Contact Model

The first attempt in this research programme to build a real contact model was performed by using the commercial finite element software COMSOL Multiphysics. The contact model consists of a cantilever, a tip and a sample. The cantilever and tip are made of Silicon Nitride, whose Young's modulus and Poisson's ratio are 250 GPa and 0.23 respectively. The cantilever has dimensions of 100  $\mu\text{m}$  in length, 40  $\mu\text{m}$  in width and 0.6  $\mu\text{m}$  in thickness. The tip's height is 3.5  $\mu\text{m}$  and the tip's surface is a flat square surface with a length of 10 nm. The sample is made of silicon, whose Young's modulus and Poisson's ratio are 170 GPa and 0.28 respectively, which has dimensions of 500 nm in length, 500 nm in width and 200 nm in thickness. The geometry of the contact model is shown in Figure 6.1.

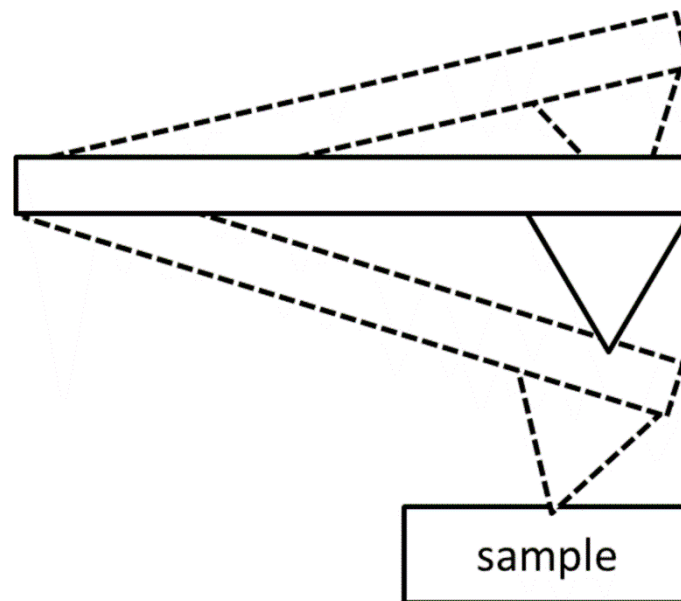


**Figure 6.1** Schematic diagram of the side view of the geometry of 3D real contact model.

As the tip's surface area is only 10nm by 10nm, the contact area between the tip and the sample is very small. Therefore, the mesh on the tip and sample needs to be very small as well. The maximum element size for the tip surface model is 4.5 nm, while the maximum element size for the sample surface is 2nm. In order to avoid large computational times,

only the mesh of a circular area on the sample surface (which is indicated in blue) is refined, where the maximum element size is 2nm, which is shown in Figure 6.2.

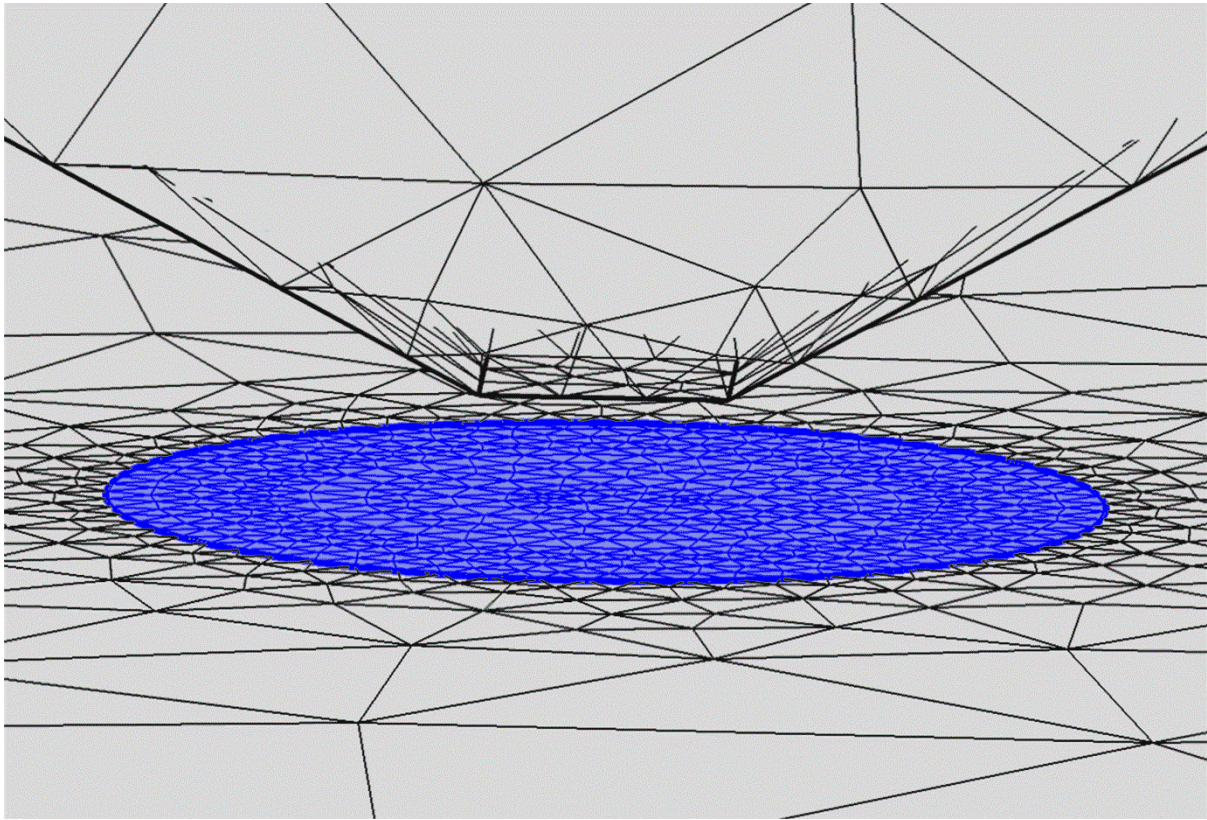


**Figure 6.2 Refined mesh on the sample surface, which is indicated as a blue circle.**

The complete mesh of the whole model contains 13072 domain elements, 4622 boundary elements, and 392 edge elements. The boundary conditions are shown in Figure 6.3. One end of the cantilever is a fixed constraint, and the bottom of the sample is also a fixed constraint, both of which are indicated by the arrows in Figure 6.3. In order to cause sinusoidal vibration of the cantilever, a time dependent sinusoidal force is applied to the edge of the other end of the cantilever shown in Figure 6.4, which is expressed by the following equation:

$$\text{Edge load} = \sin(2 * \pi * f * t) * 1e^{-8} \quad (6.1)$$

where  $f$  is the first resonant frequency of the cantilever,  $t$  represents time and  $1e^{-8}$  is the amplitude of the edge load. In this study, the resonant frequency is 82,424 Hz.

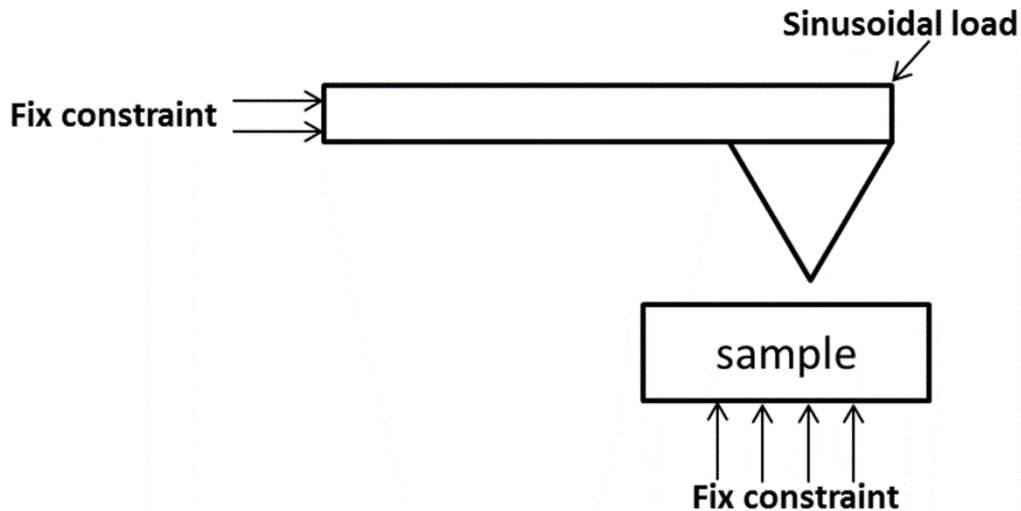


Figure 6.3 Boundary conditions are shown on the side view of the schematic diagram of 3D geometry contact model.

## 6.2 Preliminary Results

Based on the boundary conditions presented in Section 6.1, a time dependent study was carried out to investigate the dynamic displacement response of the cantilever. The initial tip-sample separation is 5nm. Only one cycle of the vibration is performed in the simulation. In other words, the time length set for the simulation study is  $1.22e^{-5}$  (1/f). However, the actual computational time here required almost 19 hours to obtain one cycle of the cantilever vibration using a PC with an Interl(R) Core(TM) i7-2600 CPU and memory of 12GB, which could be due to the complication of contact analysis. Figure 6.4 shows the dynamic displacement response of the cantilever. It can be seen that the tip contacts the sample surface, then bounces back and contacts the surface once again. During the contact period, the maximum stress on the sample can reach to 9.7 GPa as shown in Figure 6.5.

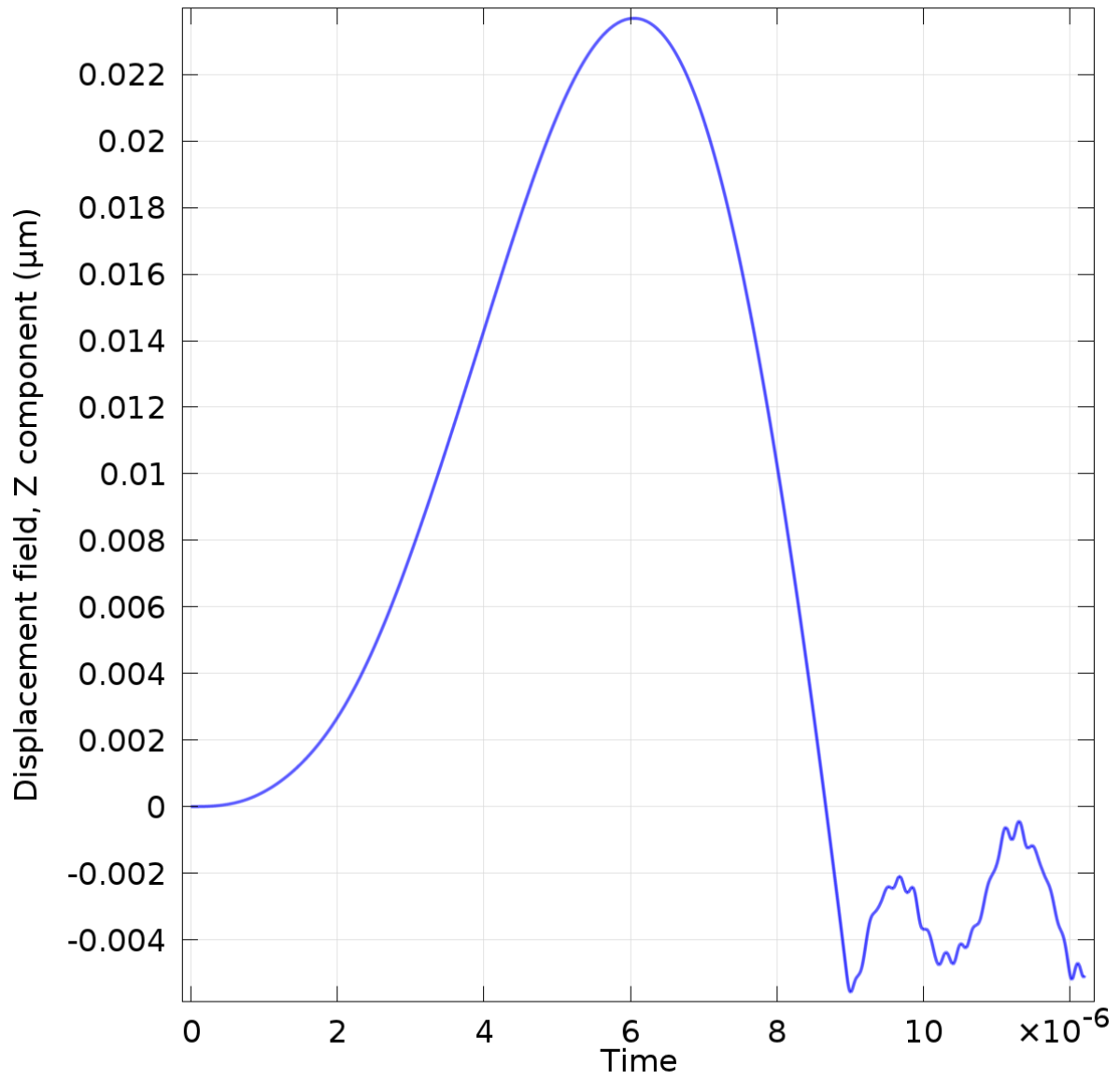


Figure 6.4 Dynamic displacement response of the cantilever for one cycle ( $1.22e^{-5}$  s), unit of time: s.

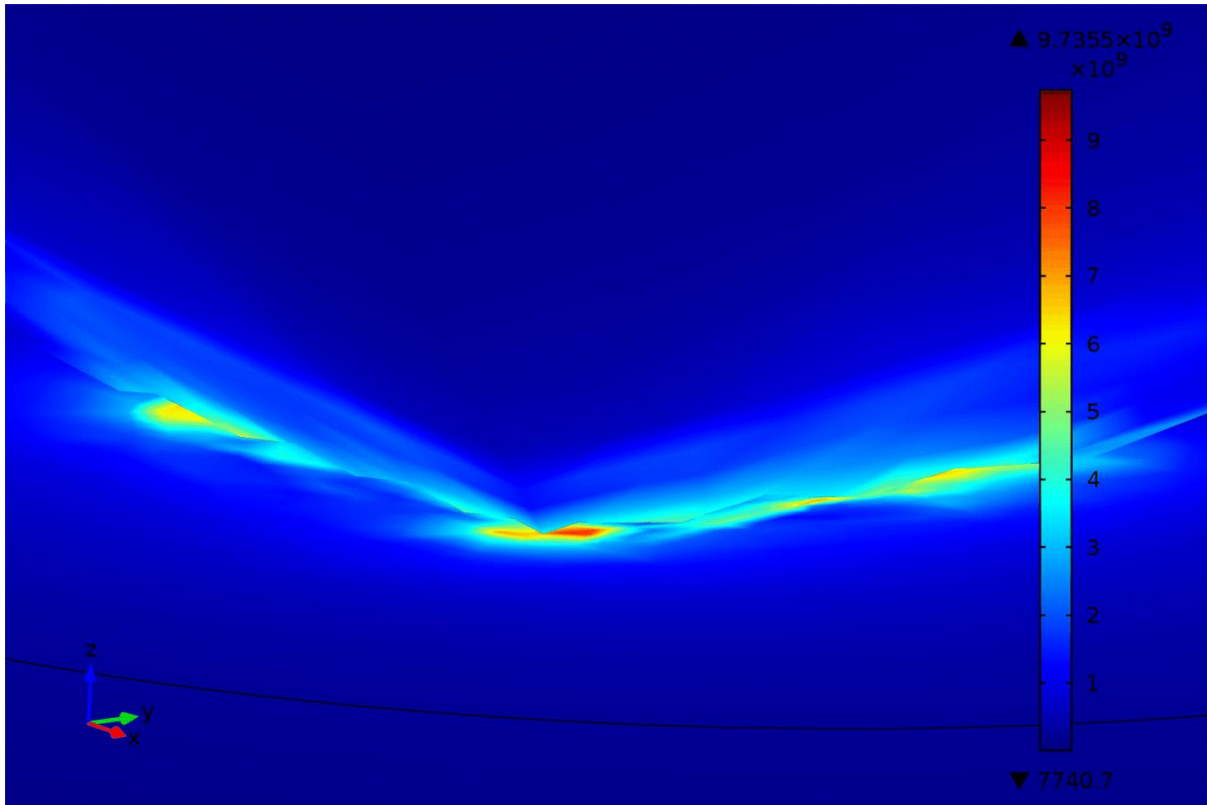


Figure 6.5 Stress on the tip and sample, the unit of the colour bar is Pa.

### 6.3 Summary and Discussions

Although the simulation manages to model the real contact between the tip and the sample and provides a preliminary result for the dynamic displacement response of the cantilever, the computational time is very high. During the tapping period, the displacement of the cantilever may take hundreds of cycles to become stable. Also, the stress can possibly lead to the instability of the simulation. Wrong prediction for the next time step during contact can result in large stress, which prevents the convergence of the simulation. Hence, with a computational load of nearly 19 hours per cycle, it seems unrealistic to carry out the study using this real contact model.

# Chapter 7

A Simplified 3D  
Model Based Finite  
Element Modelling of  
Tapping Mode AFM

## Chapter 7 A Simplified 3D Model Based Finite Element Modelling of Tapping Mode AFM

In Chapter 7, a simplified 3D finite element model is presented to simulate tapping mode AFM. The geometric model and material properties of the cantilever and tip are introduced. The boundary conditions of the simulation are also described. The difference between the computer simulation model and a real AFM system is illustrated. Verification of the mesh model, modal analysis and damping analysis are demonstrated in this chapter as well. The aim of this chapter is to introduce the simulation setup and discussion of the model.

### 7.1 The geometric model and material properties

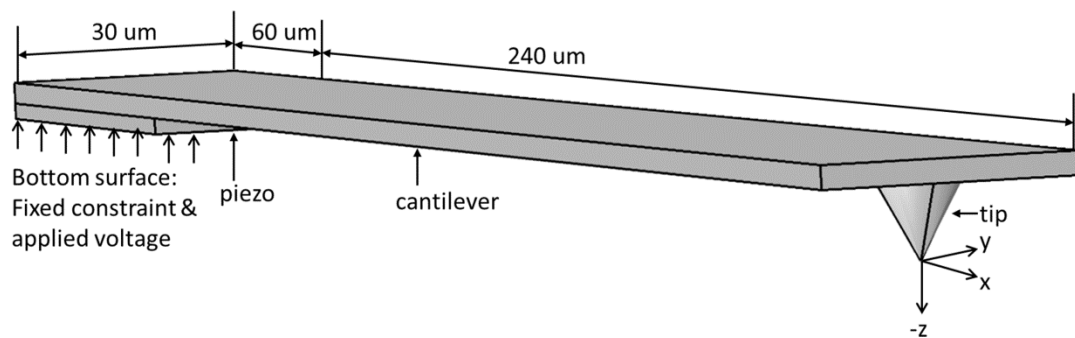
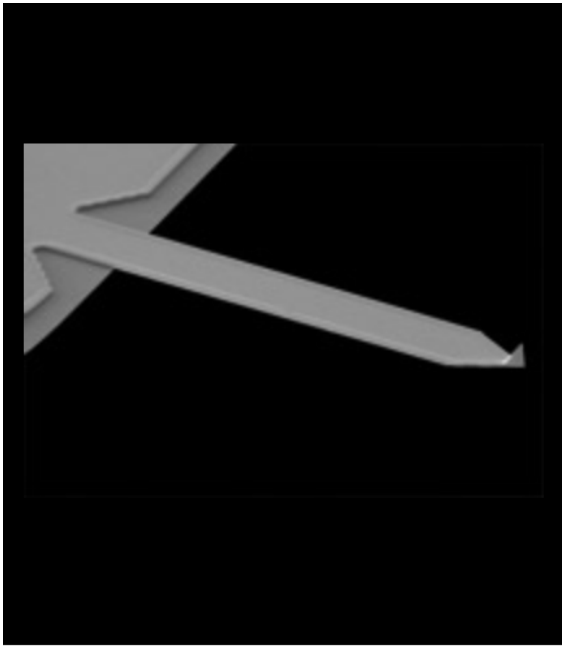


Figure 7.1 Geometric model

Commercial finite element software named COMSOL Multiphysics was used here as a tool to simulate the behaviour of the tapping mode AFM instrument. This software builds the geometrical model of a rectangular silicon cantilever with the following dimensions as used in the simulation, 240 μm length, 30 μm width, 2.7 μm thickness and with a silicon tip radius of 9nm, which has a conical shape and flat tip surface.

	<b>Lever</b>	<b>1</b>
	<b>Spring k (N/m)</b>	2 (0.5 - 4.4)
	<b>Freq (kHz)</b>	70 (50 - 90)
	<b>Length (μm)</b>	240 (230 - 250)
	<b>Width (μm)</b>	30 (28 - 32)
	<b>Thickness (μm)</b>	2.7 (1.7 - 3.7)
	<b>Shape</b>	rectangular
	<b>Material</b>	Silicon
	<b>Reflex Coating (nm)</b>	Al (100)

**Figure 7.2 SEM image of cantilever and tip (<http://www.asylumresearch.com/Probe/AC240TS>)**

The cantilever dimensions are the same as those of the Olympus model AC240TS cantilever type shown in Figure 7.2, which is typically of one used in AFM experiments.

The Young's modulus and Poisson ratio of the cantilever and tip are 170 GPa and 0.28, respectively. A simulated piezo actuator with dimensions of 60 μm length, 30 μm width and 2 μm thickness is virtually attached to the simulated cantilever. The geometric model is shown in Figure 7.1.

## 7.2 Boundary conditions

A fixed constraint is applied to the bottom surface of the piezo actuator. A sinusoidal voltage is subsequently applied to the piezo actuator in order to vibrate the cantilever vertically. The selection of the frequency of the applied voltage is around the first resonant frequency of the flexural mode, because the first order resonant frequency in the flexural mode has a major impact upon the phase shift in tapping mode AFM. It is generally accepted that the phase shift in free vibration mode is  $90^{\circ}$  when the cantilever is vibrated at its first order resonant frequency. If the driving frequency is below the first order resonant frequency, then the phase shift will be smaller than  $90^{\circ}$ . Otherwise, the phase shift will be

larger than  $90^\circ$ . The phase shift changes rapidly around the resonant frequency. Thus, the cantilever is usually vibrated at, or near to, its first order resonant frequency.

In this proposed simulation model, there is no test sample. The tip-sample interaction is simulated by applying interaction forces to the AFM cantilever tip in the Z-axis, as is shown in Figure 7.1. The interaction forces including the elastic force, adhesion force, viscosity force, and the van der Waals force between the tip and the sample are defined in the simulation by the equations described in Chapter 4. The tip-sample contact position is determined by the tip-sample separation as illustrated by the horizontal line in Figure 7.3. Moreover, in order to include adhesion energy hysteresis, the contact region is divided into two parts. The difference between the approaching surface energy in region I and the retracting surface energy in region II would lead to energy dissipation, which is representative of the real world situation that occurs during experiments with an actual AFM instrument.

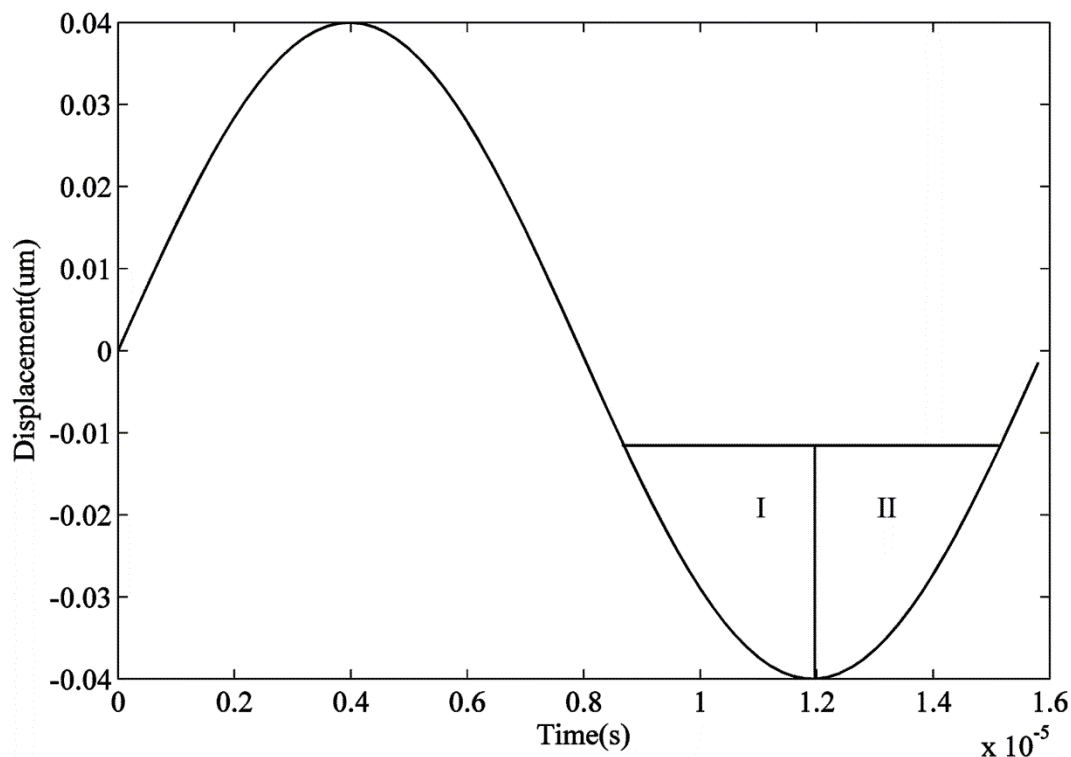


**Figure 7.3 Illustration of tip-sample contact area. I: the approaching contact region; II: the retracting contact region.**

Notice that the Q factor has a significant impact on the dynamic vibration of the cantilever. The Q factor also indicates the experimental environment. Generally, the Q factor in air is in between 100 to 200. In liquid, the Q factor is usually ranging from 1 to 3. The Q factor is related the damping ratio  $\zeta$  as is shown in Equation 7.1.

$$Q = 1/2\zeta \quad (7.1)$$

Where the damping ratio  $\zeta$  is one of the factors used to determine the damping coefficients, as Rayleigh damping (Liu and Gorman, 1995) is used to define the damping of the model. In other words, the Q factor has its own contribution in terms of determining the damping of the model. The definition of Rayleigh damping is shown in Equation 7.2.

$$C = \eta M + \delta K \quad (7.2)$$

Where C, M, K represents the matrices of the damping, mass and stiffness, respectively. The term  $\eta$  is the damping coefficient of the mass matrix, while  $\delta$  is the damping coefficient of the stiffness matrix. It is obvious that these two damping coefficients are important factors within Rayleigh damping. The damping coefficients are related the damping ratio  $\zeta$  and the angular resonant frequencies  $w_i$  ( $2\pi f_i$ ) and  $w_j$  ( $2\pi f_j$ ) of the cantilever, as shown in Equations 7.3 and 7.4. The selection of the resonant frequencies determines the damping response of the system. In this study, the cantilever is vibrated at its first order flexural mode, thus we have chosen the first order and second order resonant frequencies of the cantilever's flexural mode for  $w_i$  and  $w_j$  respectively.

$$\delta = \frac{2\zeta}{w_i + w_j} \quad (7.3)$$

$$\eta = w_i w_j \delta \quad (7.4)$$

### **7.3 Difference between the finite element model and the real tapping mode AFM system**

In a real AFM system, when tapping mode imaging is carried out, it is necessary to determine a set-point, which is the stable amplitude of the tapping cantilever, in order to obtain the phase image. When the cantilever moves from one X-Y position to the next X-Y

position during the mechanical scanning process, the vibration amplitude will change due to the height difference between the two consecutive positions upon the sample's surface. During the tapping process, the feedback mechanism would send a signal to the piezo actuator, which causes the cantilever to move upwards, or downwards, along the Z-axis until the stable amplitude reaches the pre-determined set-point. The choice of set-point has a significant impact upon the quality of the phase images that are produced (Wang et al., 2003). It was found that the phase images could reproduce detailed structure of the sample when the set-point was fixed at around half of the free vibration amplitude. When the set-point was fixed at a value that is close to the free vibration amplitude, then the phase images could reveal no sample structure at all. The set-point not only depends upon the tip-sample separation, but also upon the level of indentation of the tip into the sample. The indentation level depends on the material properties of the test sample. In a real AFM experiment, the tip-sample separation is not actually measured.

In the proposed FEA method, the tip-sample separation is set, instead of the set-point, to study the dynamic behaviour of the cantilever during the tapping process. Also, in the simulation there are no scanners to move the cantilever in the x and y directions. In other words, the cantilever stays at the initial position during the entire tapping process. The intention of this study instead focuses on observation of the dynamic behaviour of the cantilever rather than on the imaging process.

## **7.4 Mesh**

Meshing can be regarded as an art, but not purely science. Finer meshing should lead to better accuracy. One can mesh the model with very fine elements, on the other hand, the computation time here will be very long indeed. Hence, it is necessary to cope with these kinds of issues. The simulation time should be relatively short, but not at the price of significantly losing accuracy. In this model, a triangular mesh is applied to the tip surface, i.e. the bottom side of the cantilever. Then, a swept mesh is applied to mesh through the tip, cantilever and piezo. Finer mesh is used upon the tip surface because this is where instantaneous forces appear. The maximum element size upon the tip surface is 10 nm. As for the cantilever and piezo surfaces, here a coarser mesh is applied, where the maximum

element size is 4  $\mu\text{m}$ . The complete mesh model is shown in Figure 7.4, which consists of a total of 3540 domain elements, 3680 boundary elements, and 498 edge elements.

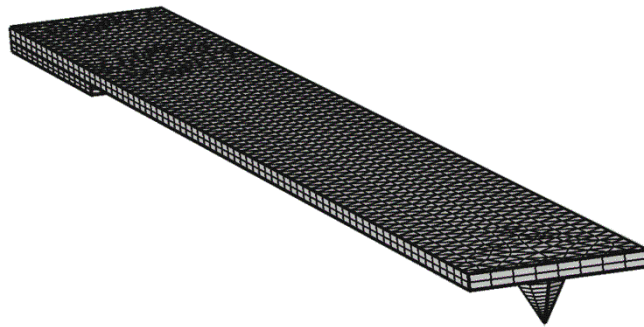


Figure 7.4 Mesh model

## 7.5 Study types of the simulation

Different simulation studies can be performed in Comsol Mutiphysics. Generally, there are eigenfrequency study, frequency domain study, stationary study and time-dependent study modes available.

### 7.5.1 Eigenfrequency study

An Eigenfrequency study is usually used to find out the eigenfrequency of an object by solving Equation 7.5.

$$\Phi_{\omega}(x) = C_1 e^{-a_{vb}x} + C_2 e^{a_{vb}x} + C_3 e^{-ia_{vb}x} + C_4 e^{ia_{vb}x} \quad (7.5)$$

where  $a_{vb}^2 = \frac{\rho A}{EI_y} \omega^2 - i \frac{c_{vb}}{EI_y} \omega$ , E,  $\rho$ , A and  $I_y$  represent the Young's modulus, mass density and cross sectional area, the moment of inertia about the y axis, respectively.  $C_1, C_2, C_3, C_4$  are determined by the boundary conditions. It is necessary to apply a fixed constraint on the object to limit the number of vibration modes in different directions, which has been

described in Section 7.2. The default number of eigenfrequencies is 6, as shown in Figure 7.5. A user can choose the number of eigenfrequencies to be solved. After selecting the number of eigenfrequencies to be solved, the simulation is ready to run. When the simulation is solved, it will output the eigenfrequencies, where each frequency corresponds to one vibration mode. Details of the results of eigenfrequency study will be demonstrated in Section 7.7.

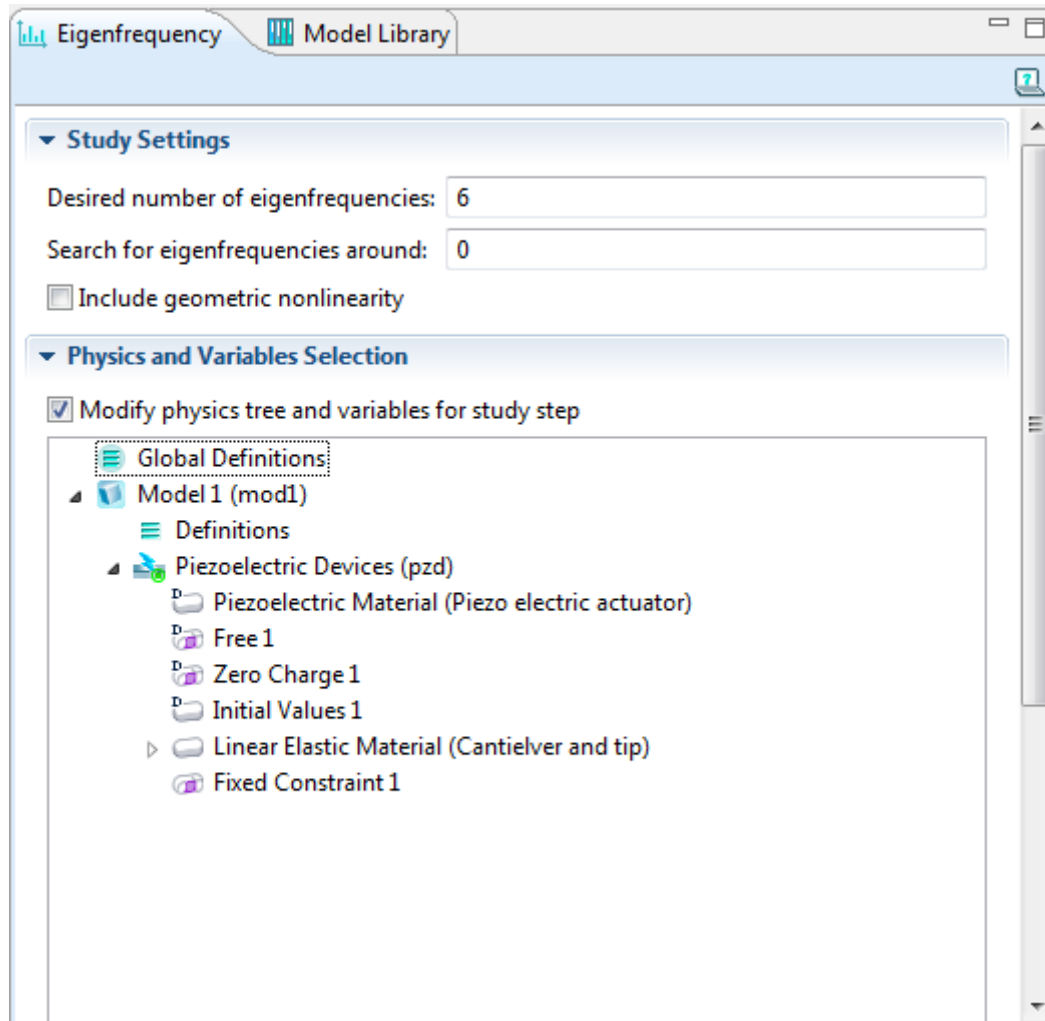


Figure 7.5 User interface of Eigenfrequency study

### 7.5.2 Frequency domain study

A Frequency domain study can be used to observe the frequency response of an object from harmonic loads. The equations in frequency domain study are time dependent, which will be described in later section, but noting that a harmonic excitation of the displacement field  $u$  has a time dependence of the form as shown in Equation 7.6.

$$\mathbf{u} = \mathbf{u}e^{i\omega t} \quad (7.6)$$

where  $w$  represents the angular frequency. A load is usually applied on the object. The simulation can be solved after selecting the frequency range shown in Figure 7.6. The interval of the frequency range determines the accuracy of the simulation. Smaller intervals will lead to larger computational times. The results of this study will be shown in Section 7.6.

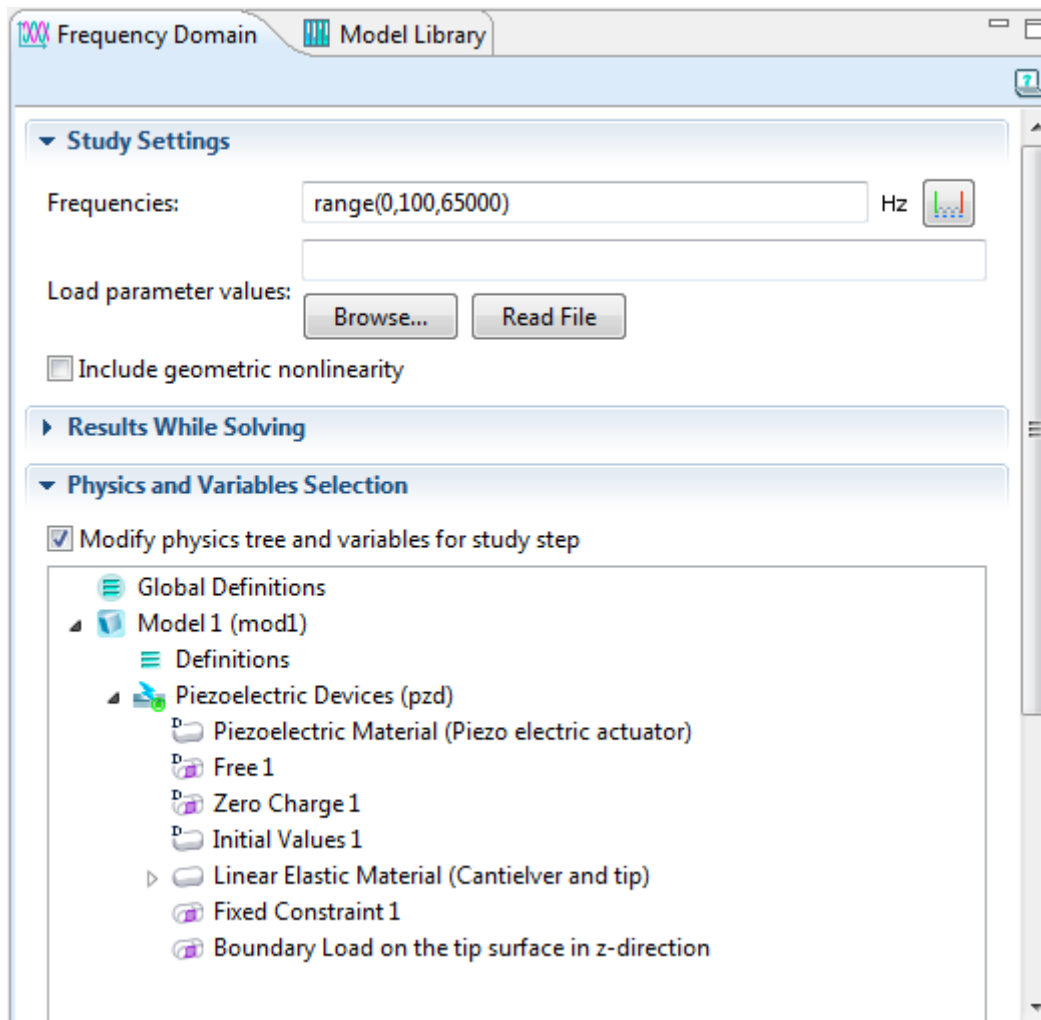


**Figure 7.6 User interface of Frequency domain study**

### 7.5.3 Stationary study

A Stationary study is used when the inertial effect of the object is not that important, in other words, the simulation is solved without considering the mass of the object. In this thesis, no simulation will be performed using stationary study mode.

### 7.5.4 Time-dependent study

A Time-dependent study deals with problems which depend on time. Also, the inertial effect of an object is considered. The simulation results for the dynamic behaviour of tapping

mode AFM will be obtained by carrying out a time-dependent study, which are obtained by solving the Equation 7.7.

$$M\ddot{u} + C\dot{u} + Ku = F_{ts}(u, \dot{u}) \quad (7.7)$$

where  $M$ ,  $C$ ,  $K$  is the mass matrices, damping matrices and stiffness matrices, respectively.  $F_{ts}$  is the tip sample interaction force. Once the boundary conditions of the model are set, the next step is to set the time range shown in Figure 7.7 for outputting the results when the simulation is complete. It must be borne in mind that the time-dependent solver may not solve the simulation by taking the time interval  $4e^{-7}$ (s) set in the time range. However, the time step taken by the time-dependent solver can be manually set so that it can match that of the output, which is shown in Figure 7.8. In order to solve the simulation efficiently, the time step taken by the solver has to be chosen carefully. If the time step is too large, the simulation may not converge. On the other hand, if the time step is too small, the computational time will be too long. The simulation results from time-dependent study will be discussed in Chapter 8.

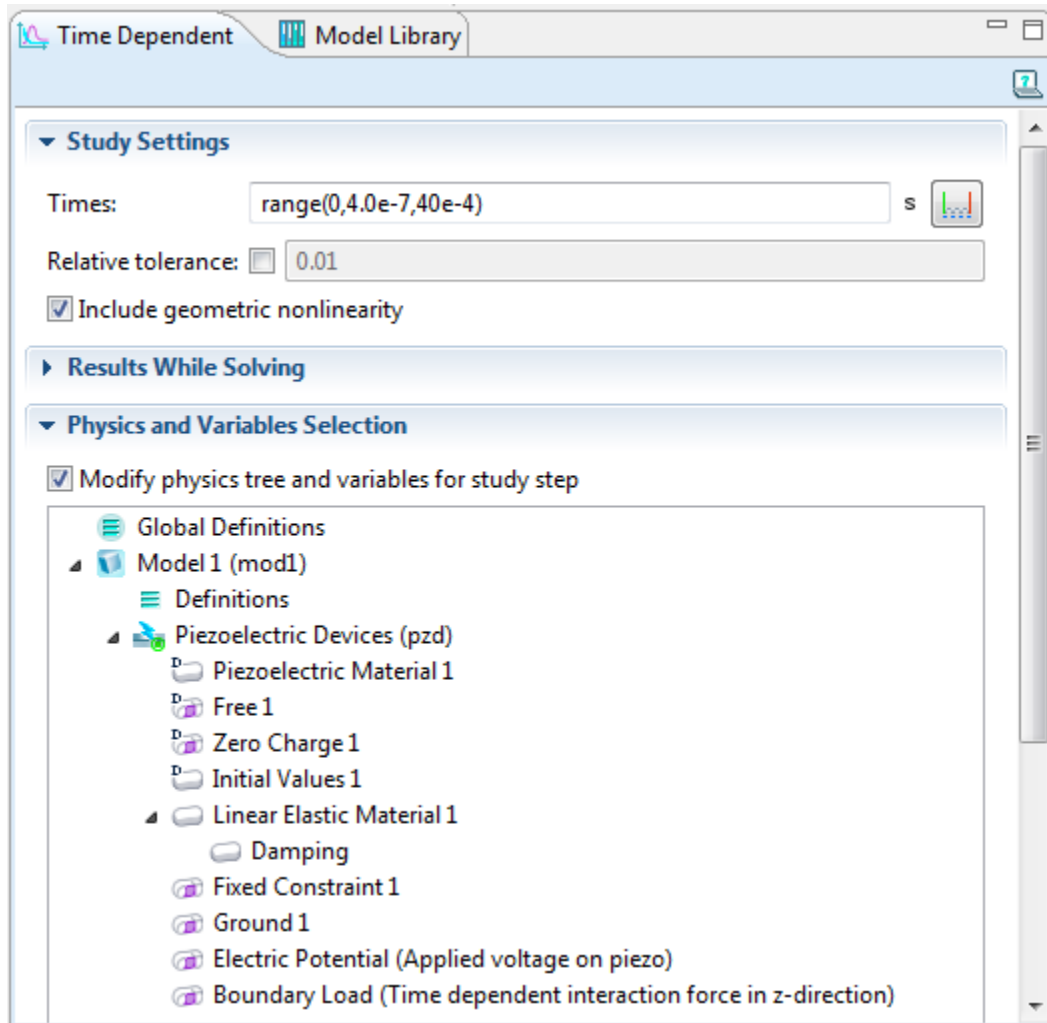


Figure 7.7 User interface of Time-dependent study

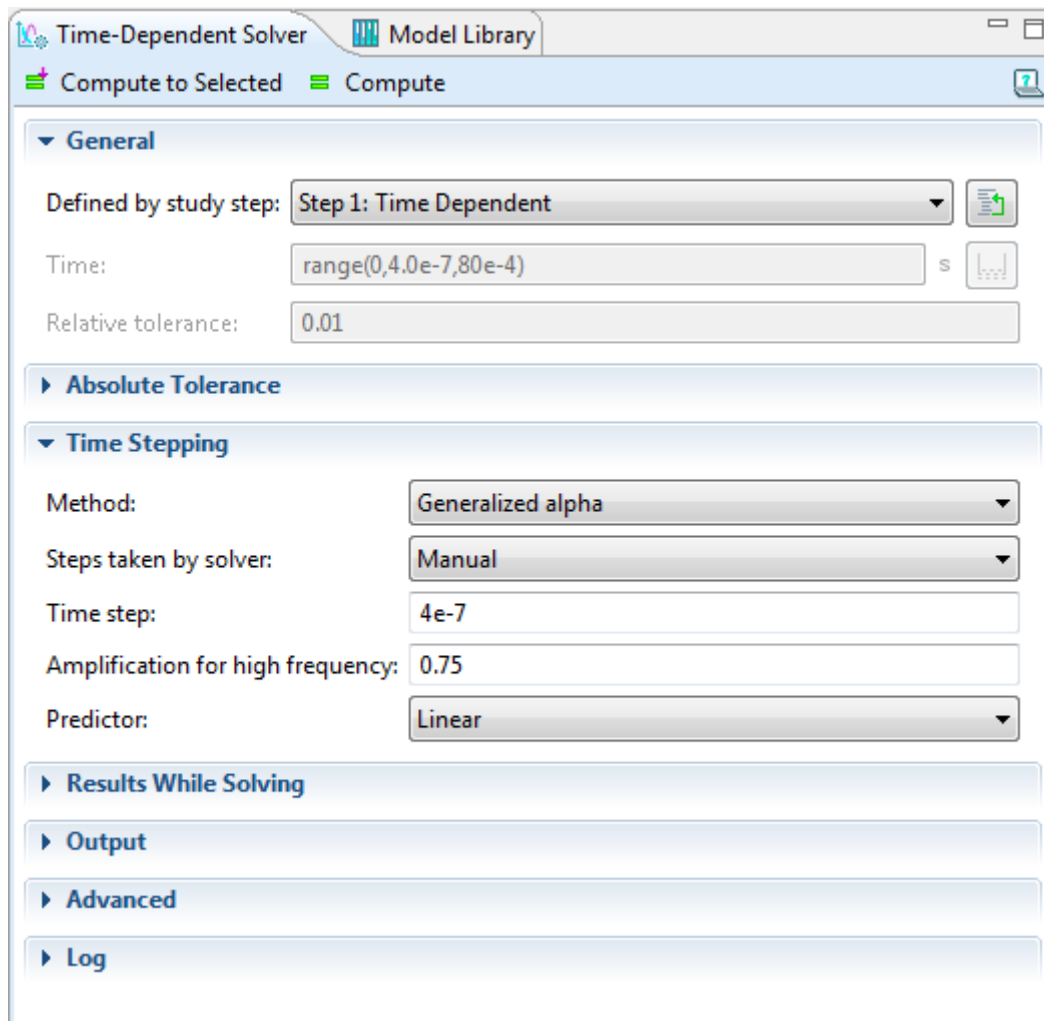
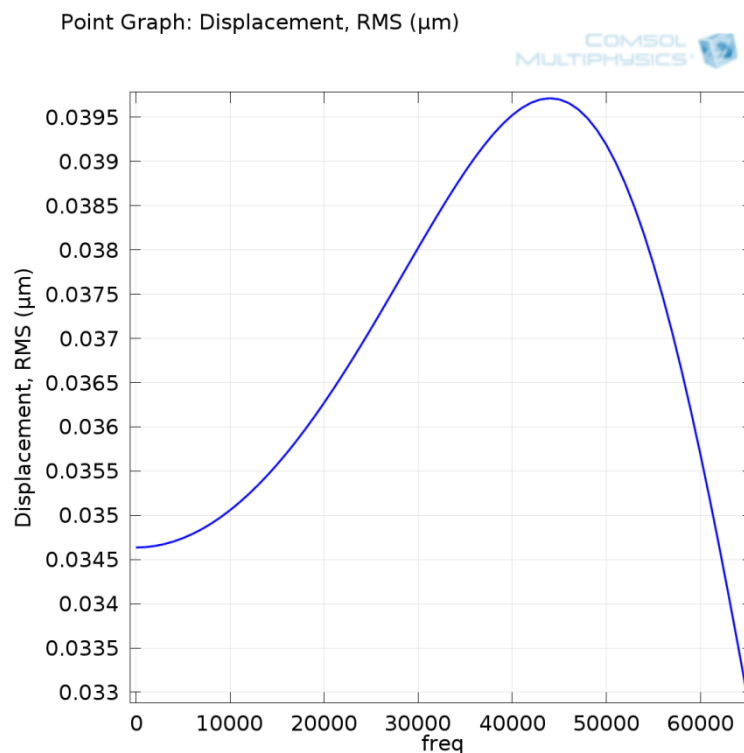


Figure 7.8 User interface of Time-dependent solver

## 7.6 Discussions of the FEA model

It is still an open question as to whether the current mesh is adequate. Hence, it is necessary to see whether this model matches the real physical phenomena encountered in a real AFM instrument. An easy way to check the model is to monitor the displacement of the cantilever under free vibration by changing the excitation frequency of the voltage signal. As mentioned above, the cantilever is usually vibrated at, or near to, its first order resonant frequency of flexural mode. Hence, by changing the excitation frequency, it should be able to find out the peak of the displacement of the cantilever corresponding to the resonant frequency that is largest among all the other excitation frequencies. In order to perform a quick check, large damping is applied because then the cantilever can reach its stable state more quickly. The effect of the damping will be discussed later on Section 7.8. Hence, a

quality factor of 1 is chosen for simulation. First, a frequency domain study is performed to find the resonant frequency under the current damping conditions, which is shown in Figure 7.9. It can be seen that the resonant frequency should be around 44000 Hz. Then a time dependent study is carried out to evaluate the displacement signal while the frequency of the applied voltage signal is swept between 40000 Hz and 60000 Hz. Figure 7.10 shows the displacement signals against different excitation frequencies. It seems to be difficult to differentiate the amplitude difference between each signal. Hence, post processing has been applied to the displacement signal to obtain the amplitudes. Figure 7.11 shows the amplitudes against different excitation frequencies. It can be seen that the amplitude against 46000 Hz is largest. The amplitudes around this frequency are gradually decreasing. The simulation results produce the same phenomenon which is consistent with the real physics. Therefore, the model should be able to provide relatively accurate results.



**Figure 7.9 Frequency response of the cantilever when  $Q = 1$ , unit of frequency is Hz.**

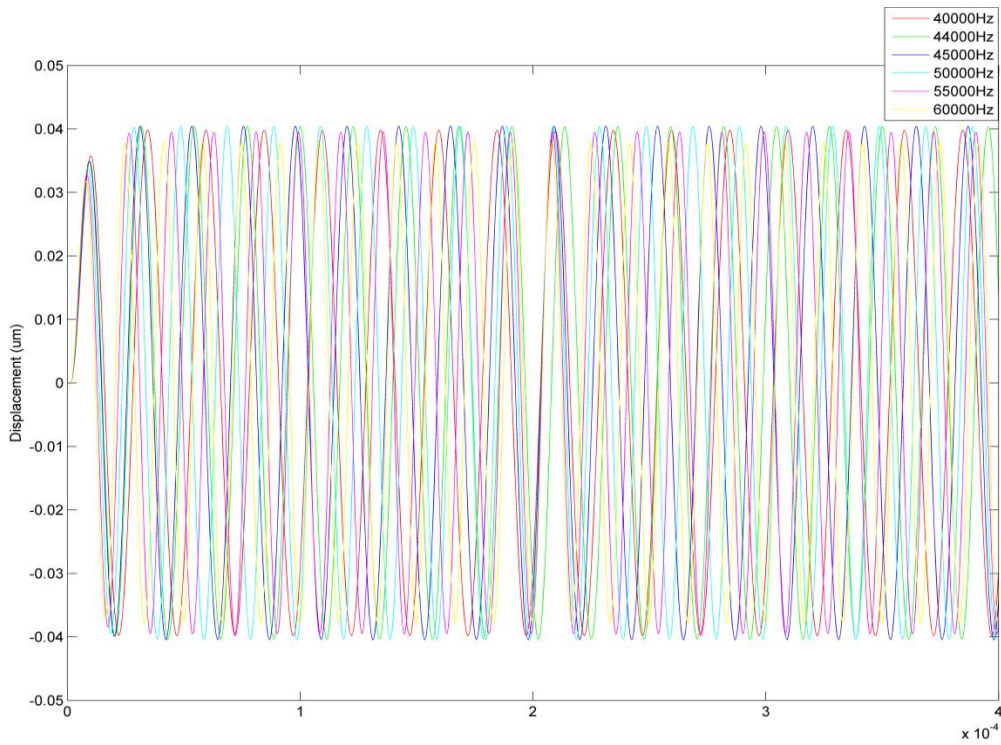


**Figure 7.10 Displacement of the cantilever against different vibration frequencies.**

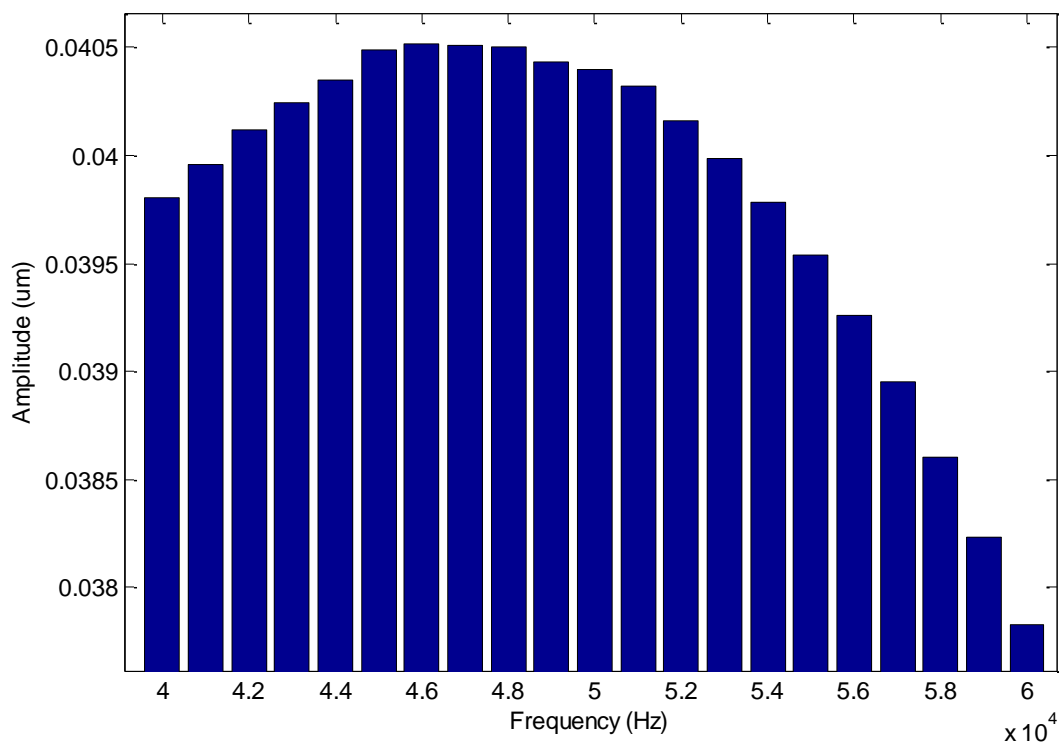


**Figure 7.11 Amplitude of the cantilever against different vibration frequencies**

## 7.7 Modal analysis of the cantilever

Modal analysis has been carried out to study the cantilever vibration modes by using the eigenfrequency study in COMSOL Multiphysics. An eigenfrequency study is used to find the natural frequencies of an object. In the eigenfrequency study, only fixed constraint is applied, which is shown in Figure 7.1. Table 7.1, 7.2, 7.3 show the results of natural frequencies of different vibration modes, where the resonant frequency of the first order flexural mode is 62,920 Hz. Different vibration modes are also shown in Figures 7.12, 7.13, 7.14, 7.15, such as the flexural modes, lateral bending modes, torsion modes and extension mode.

**Table 7.1 Different orders of natural frequencies of flexural mode**

Flexural mode	1 <sup>st</sup>	2 <sup>nd</sup>	3 <sup>rd</sup>	4 <sup>th</sup>
Resonant frequency (kHz)	62.92	396.44	1114.87	2193

**Table 7.2 Different orders of natural frequencies of torsion mode**

Torsion mode	1 <sup>st</sup>	2 <sup>nd</sup>	3 <sup>rd</sup>	4 <sup>th</sup>
Resonant frequency (kHz)	991.71	2999.66	5088.39	7301.64

**Table 7.3 Different orders of natural frequencies of lateral mode and extension mode**

Vibration mode	1 <sup>st</sup> Lateral mode	2 <sup>nd</sup> Lateral mode	1 <sup>st</sup> Extension mode
Resonant frequency (kHz)	664.27	3947.18	8593.8

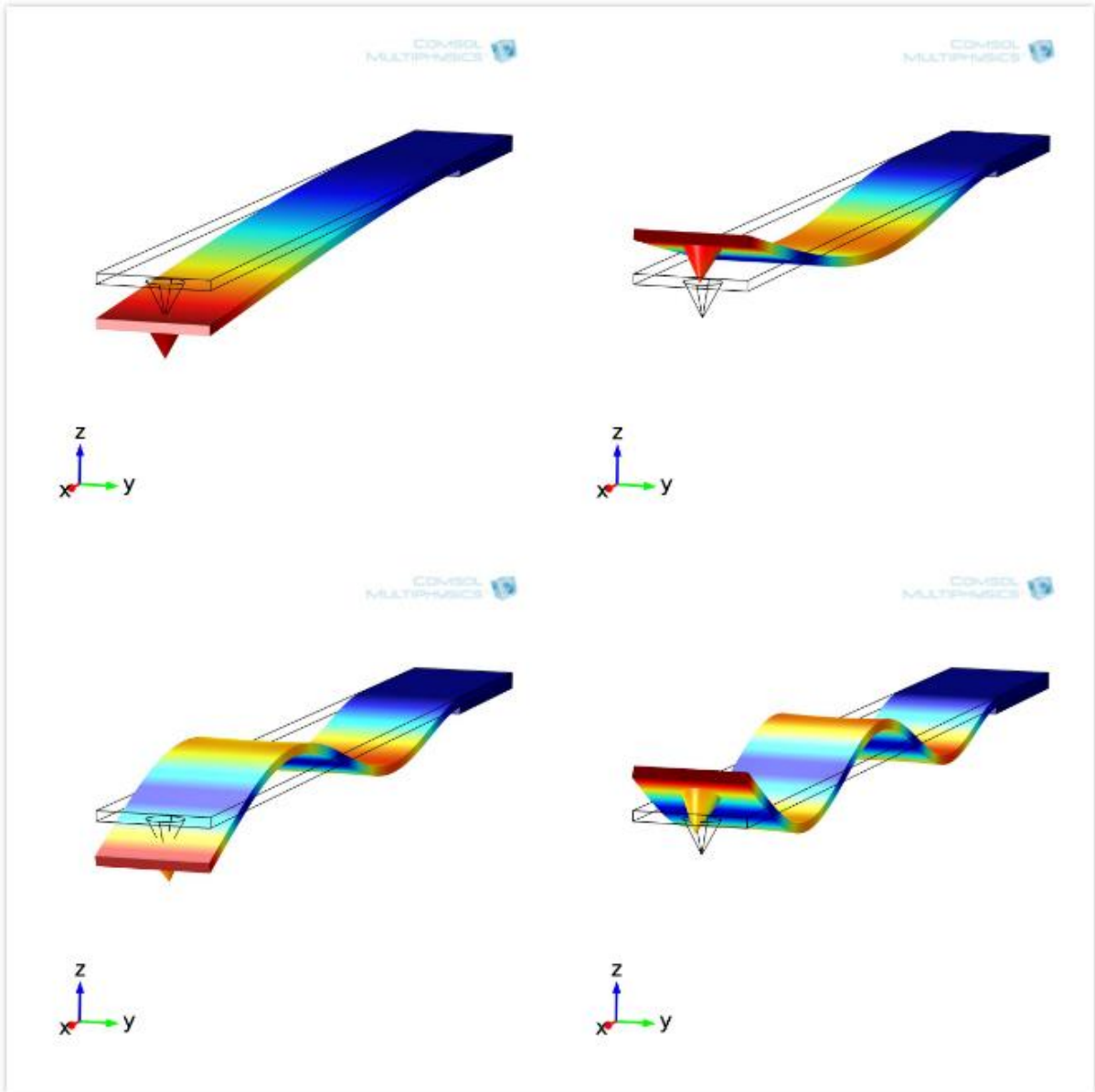


Figure 7.12 Flexural modes (a) first order, (b) second order, (c) third order, (d) fourth order

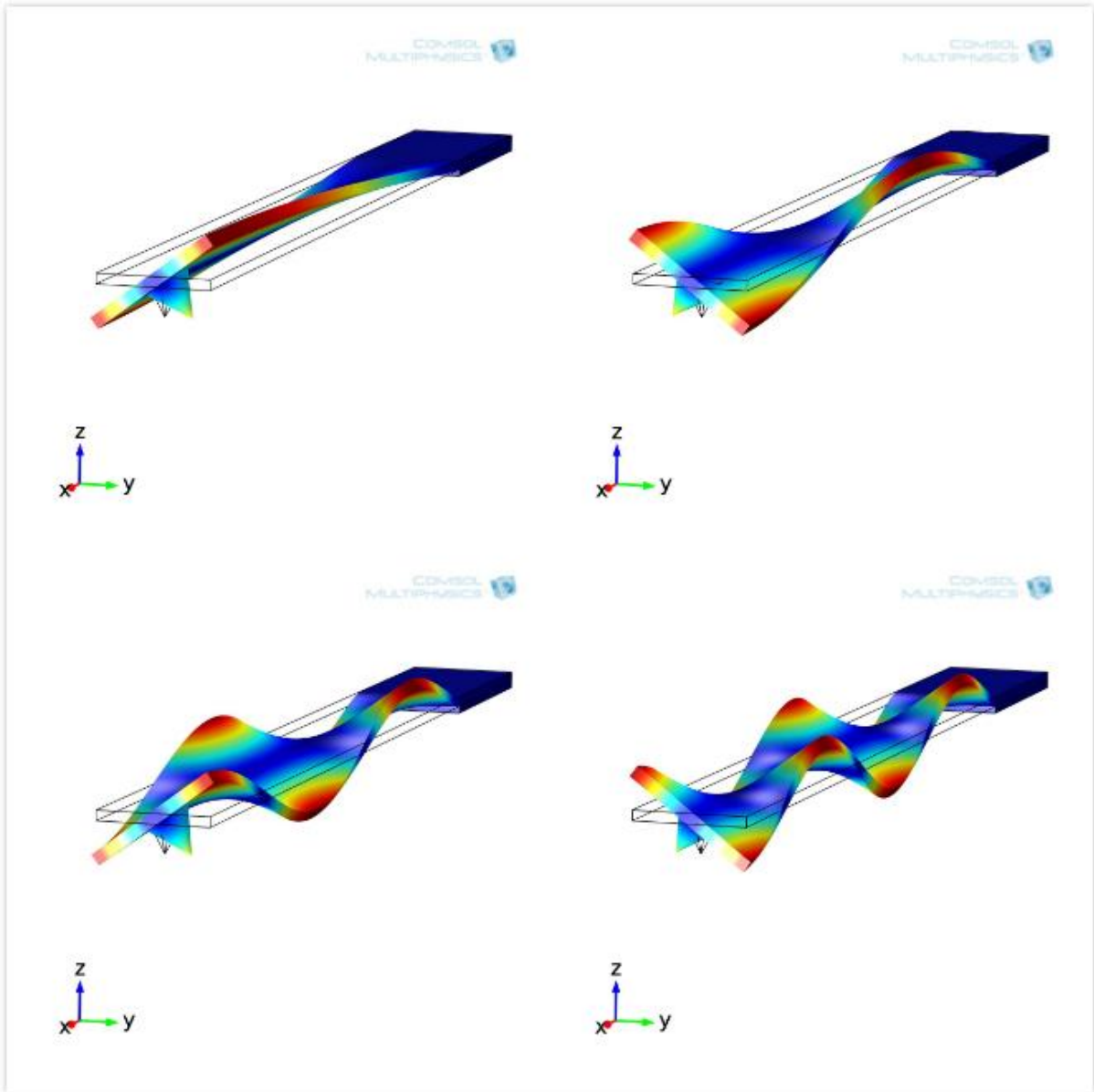


Figure 7.13 Torsion modes (a) first order, (b) second order, (c) third order, (d) fourth order

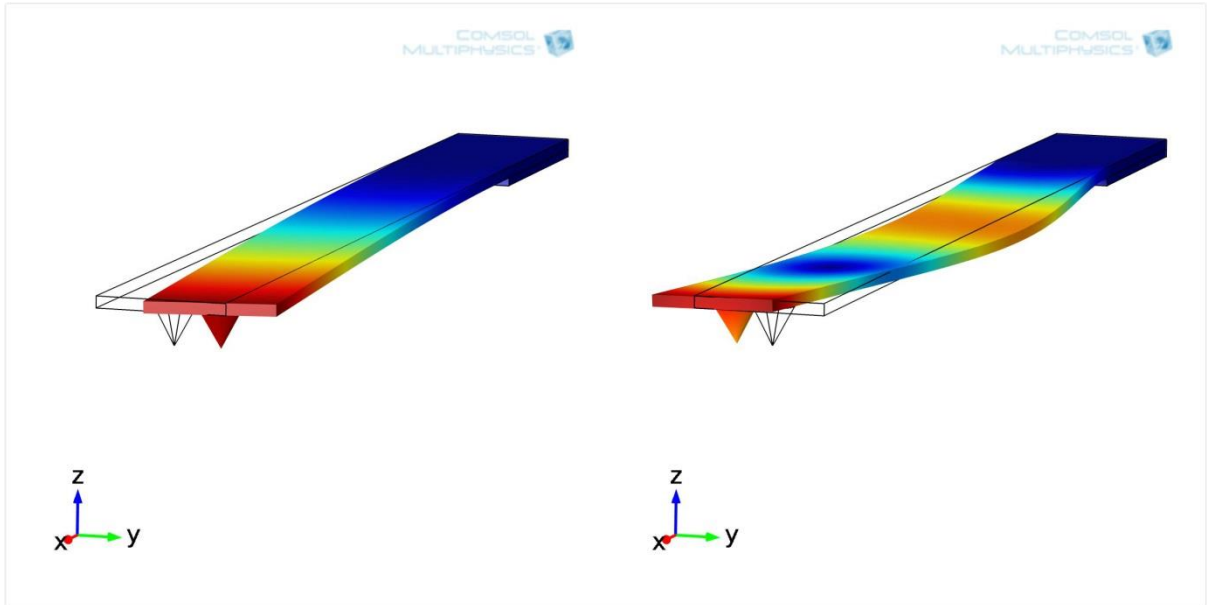


Figure 7.14 Lateral modes: (a) first order, (b) second order.

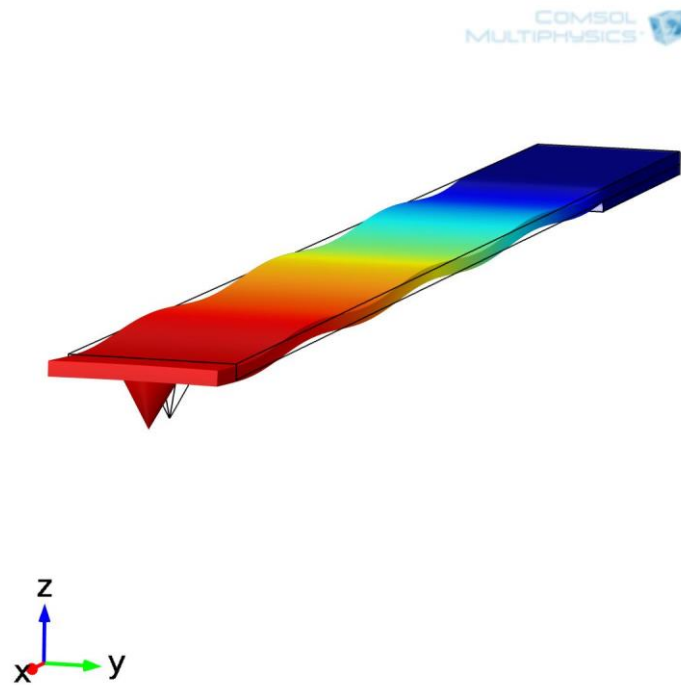


Figure 7.15 First order extension mode

## 7.8 Damping analysis of the cantilever

Modal analysis as described above provides the resonant frequencies of different vibration modes without the damping effects. However, in reality damping always exists. This study only focuses on tapping mode AFM. Hence, the damping of the model depends on the resonance of the first and second order flexural modes and the quality factor  $Q$ . As the natural resonant frequencies are fixed, which are computed from the modal analysis above, it can be said that, in other words, the quality factor controls the damping of the model. Generally, the  $Q$  factor in air varies from 100 to 200. In liquid, the  $Q$  factor usually ranges from 1 to 3. A frequency domain study is used to evaluate how the damping affects the resonant frequency of the model. Here, quality factors of 100 and 1, and also no damping at all are considered. In the frequency domain study, a fixed constraint is applied. Also, in order to activate only the frequency of the flexural mode, a static force is loaded on the tip surface in the  $z$  direction. From Figure 7.16, it can be seen that the quality factor has a large impact upon the resonant frequency. When the quality factor is 1, the resonant frequency is damped to around 45,000 Hz. On the other hand, when quality factor is 100, the resonant frequency is very close to the natural resonant frequency of 62,920 Hz.

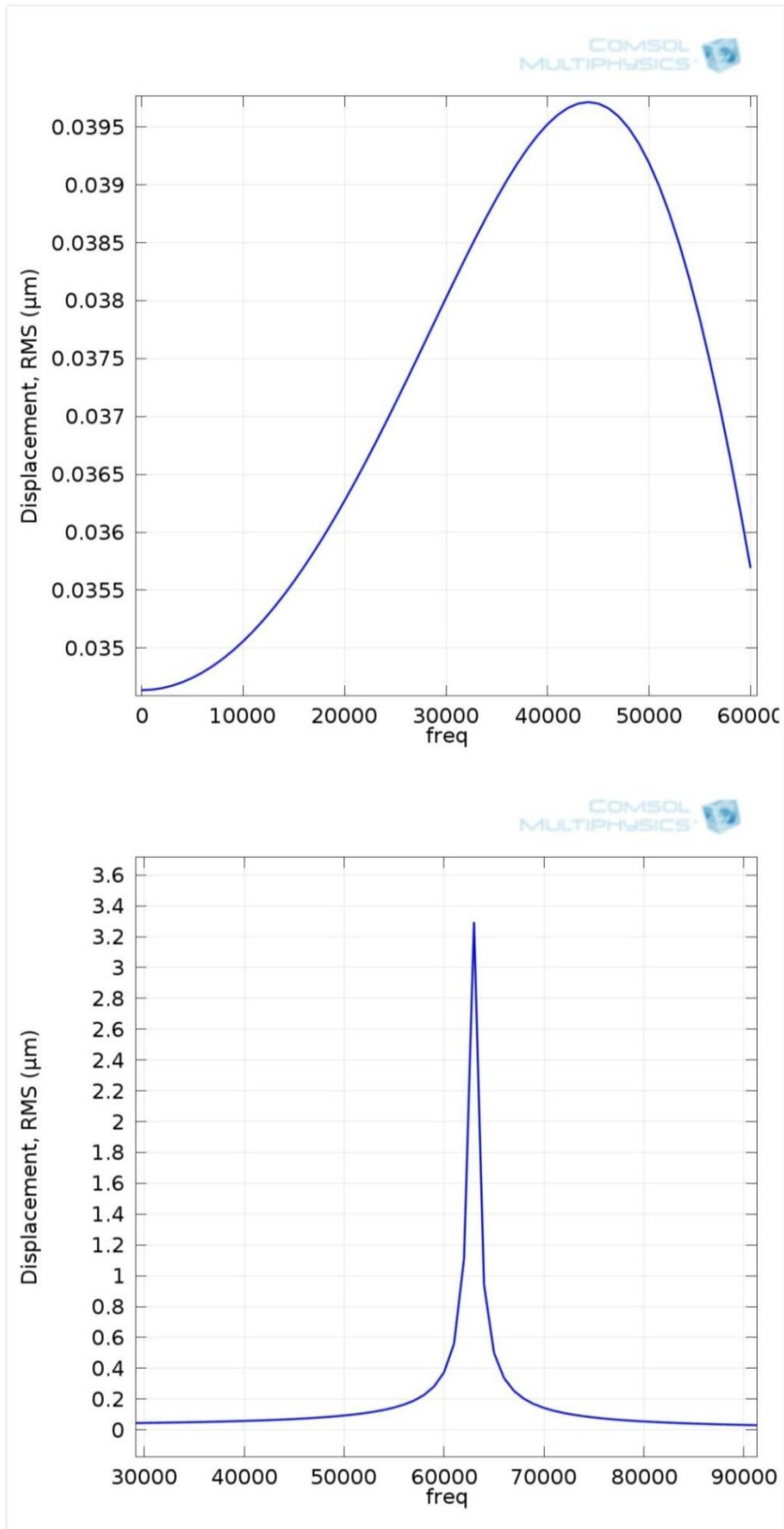


Figure 7.16 Frequency response of the cantilever for different degrees of damping: (a)  $Q = 1$ , (b)  $Q = 100$ , unit of frequency is Hz.

## 7.9 Summary and Discussions

The simulation results obtained from different types of simulation have been presented in this thesis. Also, the simplified model shown here can significantly decrease the computational time, because there is no sample included. Instead of a real contact between the tip and sample, the interaction forces applied upon the tip surface are represented using the equations shown in Chapter 4, such as elastic force, adhesion force, viscosity force and van der Waals force. The shape of the cantilever and tip is not exactly the same as the real product, but is a reasonable approximation. In order to avoid the complexity of the simulation, a normal rectangular geometry is used as the cantilever and a conical tip with a flat surface is used to represent the AFM tip. Different vibration modes have been shown by carrying out a modal analysis, such as the flexural mode, torsional mode, lateral mode and extension mode.

# Chapter 8

Dynamic Behaviour

Analysis of Tapping

Mode AFM

## **Chapter 8 Dynamic Behaviour Analysis of Tapping Mode AFM**

In Chapter 8, the simulation results for the dynamic behaviour of tapping mode AFM are presented in terms of the dynamic cantilever displacement response under free vibration and for different interaction forces. Phase shifts, stable amplitude, transition time and instantaneous frequency can be analysed through the dynamic displacement of the cantilever. The aim here is to analyse the dynamic behaviour of tapping mode AFM and find out how the phase shifts are affected by the different interaction forces.

### **8.1 Dynamic Behaviour of the Cantilever under Free Vibration**

#### **8.1.1 Simulation setup**

Free vibration is defined when there is no tip-sample interaction during the vibration process. In this case, only fixed constraint and sinusoidal voltage are applied to the simulation model. The frequencies determined from the frequency domain study under different damping conditions are selected as the excitation frequencies of the voltage signal. A time dependent study has been carried out to investigate the cantilever displacement behaviour under different damping conditions.

#### **8.1.2 Simulation results**

It can be seen that it takes more than 1 ms for the displacement signal to become stable under relatively low damping conditions ( $Q=100$ ), as shown in Figure 8.1, while the displacement signal becomes stable after one cycle vibration in Figure 8.2. Damping does not only affect the time over which the displacement signal becomes stable, but also the amplitude of the displacement signal. In order to reach the free vibration amplitude of 40nm, shown in Figure 8.2, the voltage applied to the virtual piezo actuator has to be increased significantly to 1.6V, while only 0.1V is applied to piezo actuator to obtain the results shown in Figure 8.1.

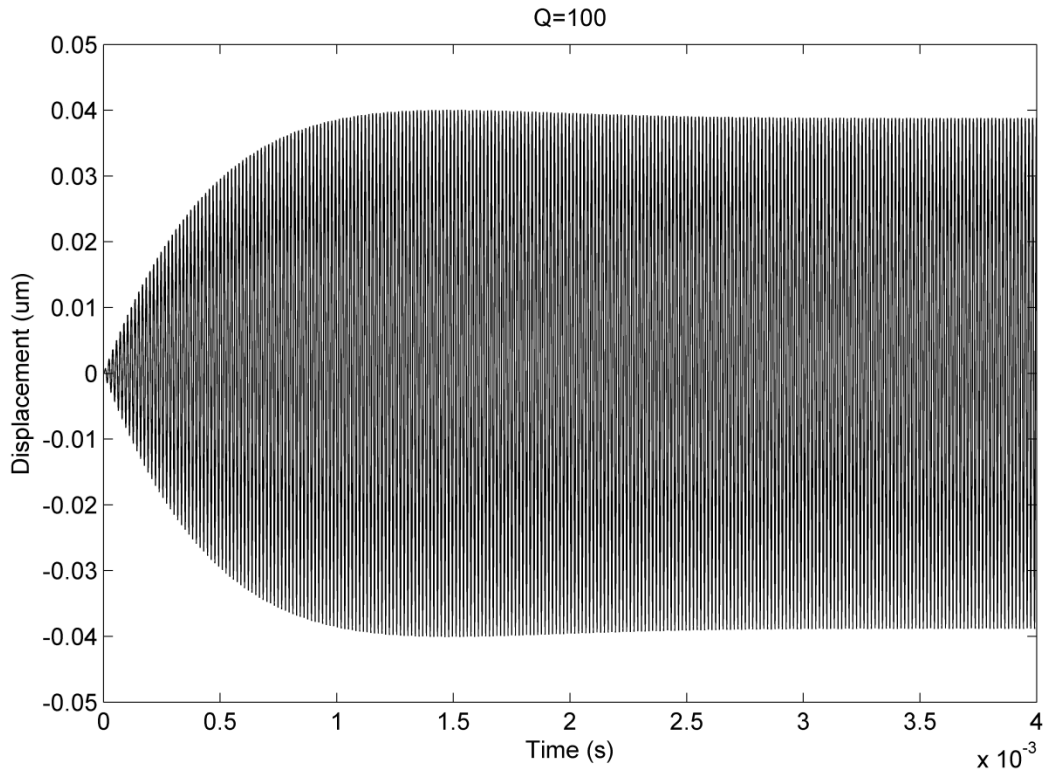


**Figure 8.1 Displacement of cantilever when Q = 100.**

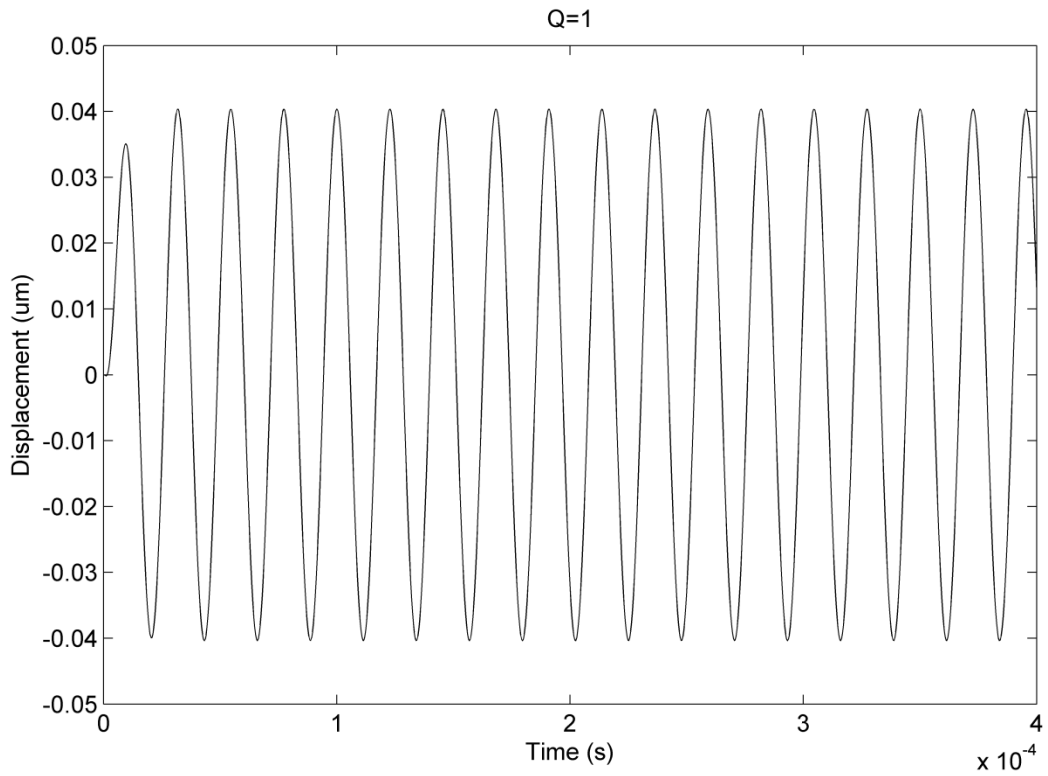


**Figure 8.2 Displacement of cantilever when Q = 1.**

## 8.2 Dynamic Behaviour Analysis of the cantilever under tip-sample interaction

### 8.2.1 Simulation setup

Different damping conditions were applied into the simulation model, in terms of the quality factor being set at  $Q=100$  and  $Q=5$ , respectively. In both simulations, the free vibration amplitude of the cantilever was 40nm. The same elastic force with a Young's modulus of 1GPa and a Poisson's ratio of 0.4 respectively was applied to the simulated AFM tip's surface.

### 8.2.2 Dynamic displacement response of a cantilever

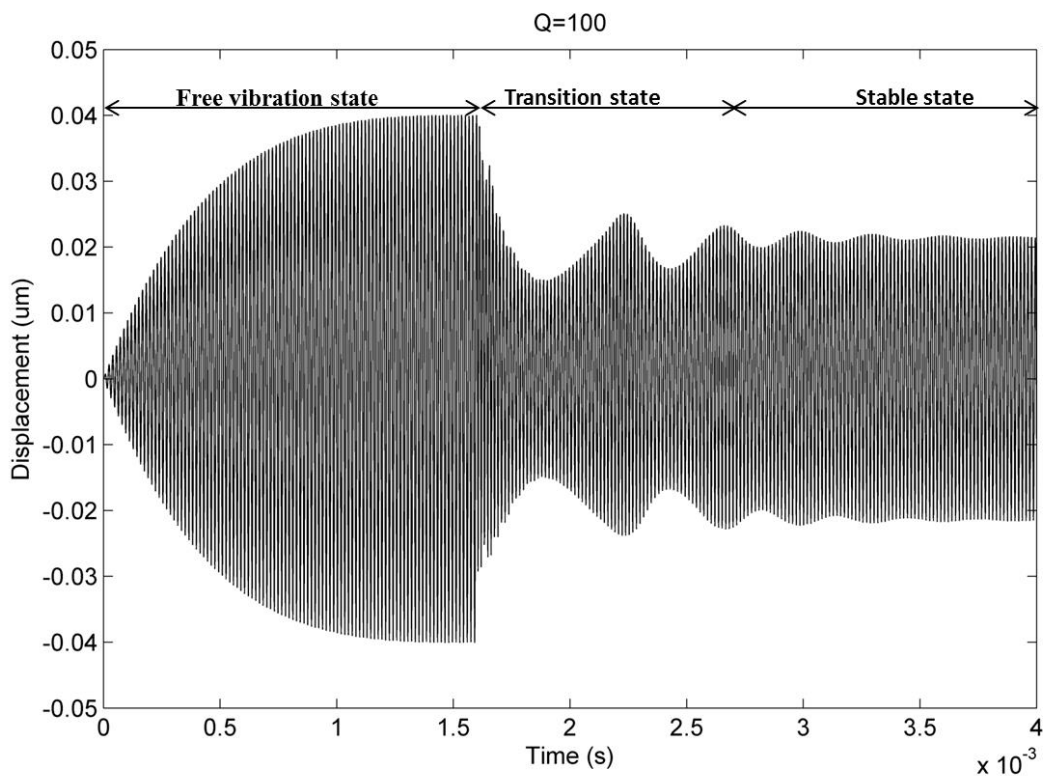
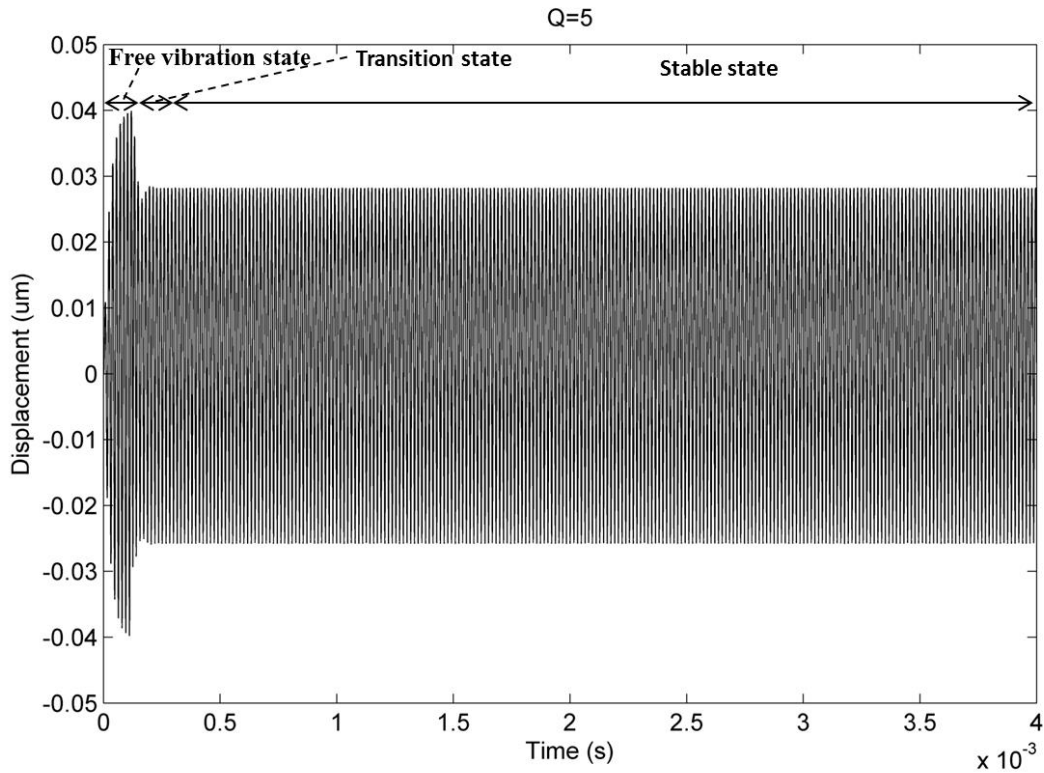


Figure 8.3 The simulated dynamic displacement response of a cantilever during tapping mode imaging, when only considering the elastic force. Free vibration amplitude  $Amp_{free} = 40\text{nm}$ , tip-sample separation  $d_0 = 20\text{nm}$ ,  $Q=100$ . Test sample material: Young's modulus of the test sample 1GPa, Poisson's ratio of the test sample 0.4.



**Figure 8.4** The simulated dynamic displacement response of a cantilever during tapping mode imaging, when only considering the elastic force. Free vibration amplitude  $A_{mpfree} = 40\text{nm}$ , tip-sample separation  $d_0 = 20\text{nm}$ ,  $Q=1$ . Test sample material: Young's modulus of the test sample  $1\text{GPa}$ , Poisson's ratio of the test sample  $0.4$ .

Figure 8.3 shows a dynamic displacement response of the cantilever tapping a test sample. In the simulation, the cantilever starts from free vibration and then interacts with a test sample. From Figure 8.3, it can be seen that the dynamic vibration of the cantilever can be divided into three states: free vibration, a transition state, and the stable state. As mentioned above, the tip-sample interaction is simulated by applying different interaction forces between the tip and sample. The dynamic displacement response is obtained by only considering the elastic force using the following parameters: resonant frequency of  $62,920\text{Hz}$ , free vibration amplitude of  $40\text{nm}$ , initial tip-sample separation,  $d_0$ , of  $20\text{nm}$ , Young's modulus of the test sample of  $1\text{GPa}$ , a Poisson's ratio of the test sample of  $0.4$ , and a  $Q$  factor of  $100$ . Figure 8.4 shows the dynamic cantilever displacement response that is obtained by changing only the  $Q$  factor to a value of  $1$ , compared to the previously used value of  $Q = 100$ , that was shown in Figure 8.3 and keeping all other parameters the same as

those used in Figure 8.3. From Figure 8.3 and 8.4, it can be seen that a bigger Q factor leads to a longer transition state.

### **8.3 Phase shift analysis**

The dynamic vibration of the cantilever is affected by different interaction forces. Moreover, it can be seen that these interaction forces are affected by many factors, including tip-sample separation, radius of the tip, Young's modulus, surface energy and the viscosity of the sample. In other words, all of these factors may make some contributions to the phase shifts that comprise the phase image. Although many studies have been attempted to interpret the AFM phase images (Liu and Gorman, 1995, Magonov et al., 1997b, Chen et al., 2002, Tamayo and García, 1997, García et al., 1999, García et al., 1998, San Paulo and García, 2001), it still remains as a particularly challenging issue. Therefore further research is carried out in this thesis to gain better understanding and interpretation of the phase shift, by analysing the dynamic displacement response of the cantilever under different interaction forces and for different test materials, through a finite element analysis approach.

#### **8.3.1 Phase shift extraction from the dynamic displacement response of the cantilever**

Phase shift is interpreted as being the phase lag between the driving voltage signal and the actual displacement response of the cantilever. A Fourier transform is first applied to the displacement response signal. Power spectrum and phase vs frequency curves are then obtained, which are shown in Figure 8.5 and Figure 8.6, respectively. Firstly, the frequency corresponding to the maximum power in the power spectrum is established, which indicates the first resonant frequency. Secondly, the phase angle that corresponds to this frequency is determined. The same method is subsequently applied to the voltage signal, rather than the displacement response signal. The difference between the phase angle of the displacement response signal and that of the voltage signal is then defined as representing the phase shift. This method for calculating the phase shift has been employed in all of the following results.

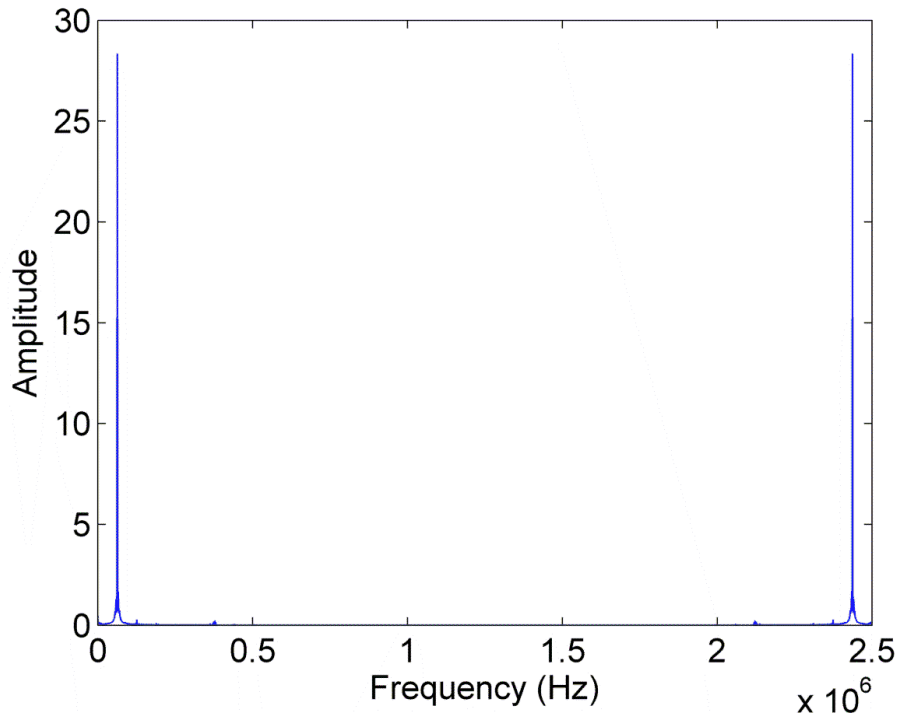


Figure 8.5 Power spectrum of the displacement signal.

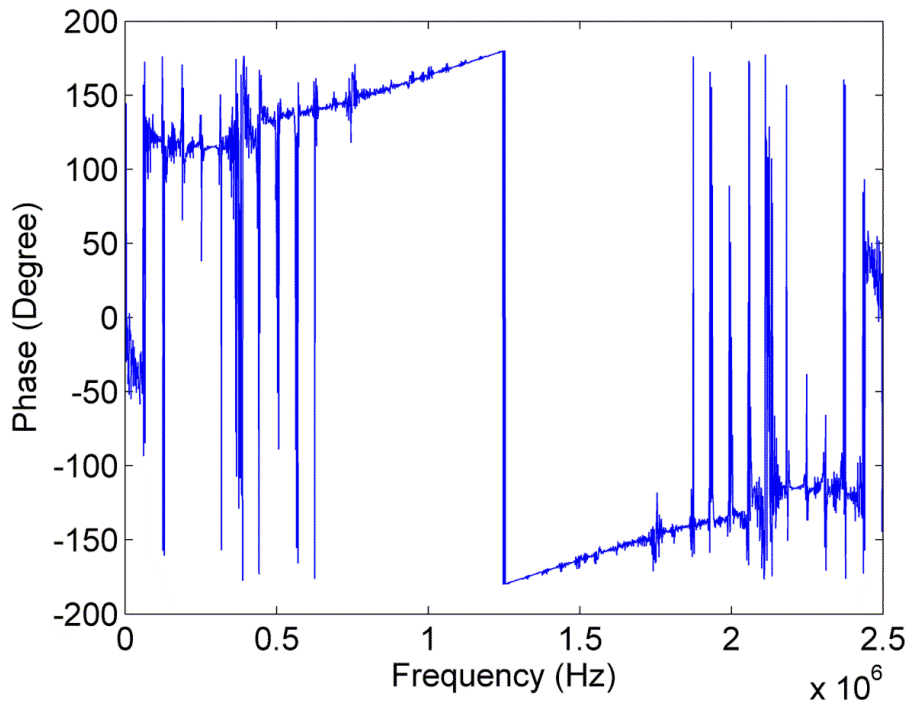
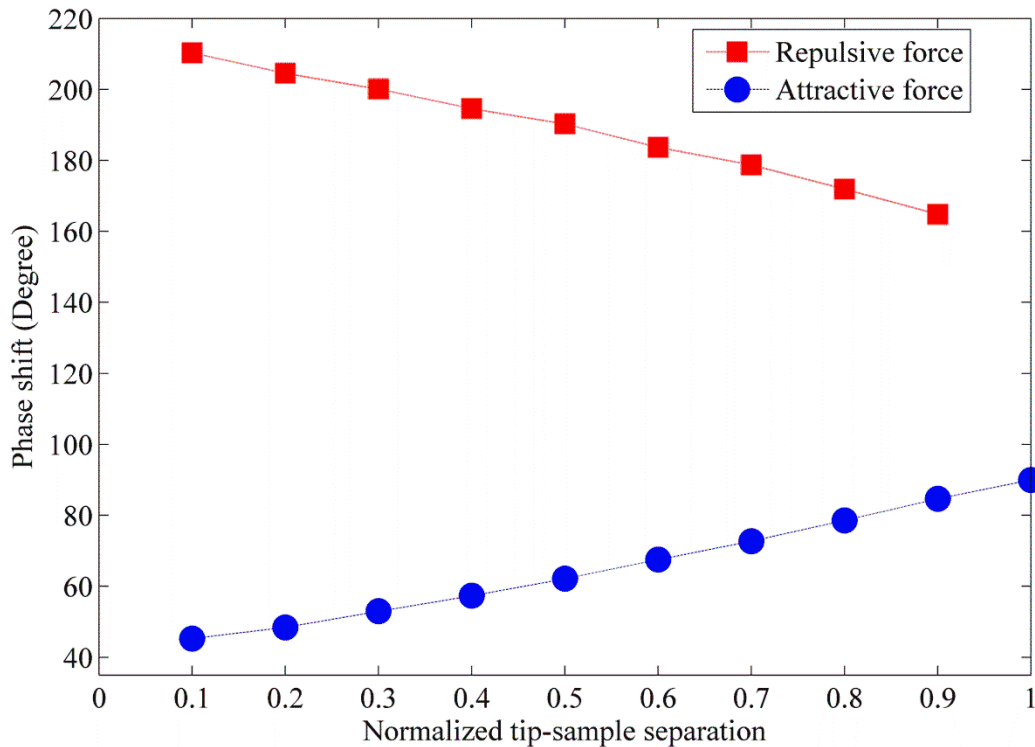


Figure 8.6 Phase versus frequency obtained by doing FFT to the displacement signal of the cantilever.

### 8.3.2 Phase shift analysis

#### 1) Effect of repulsive force and attractive force on phase shift



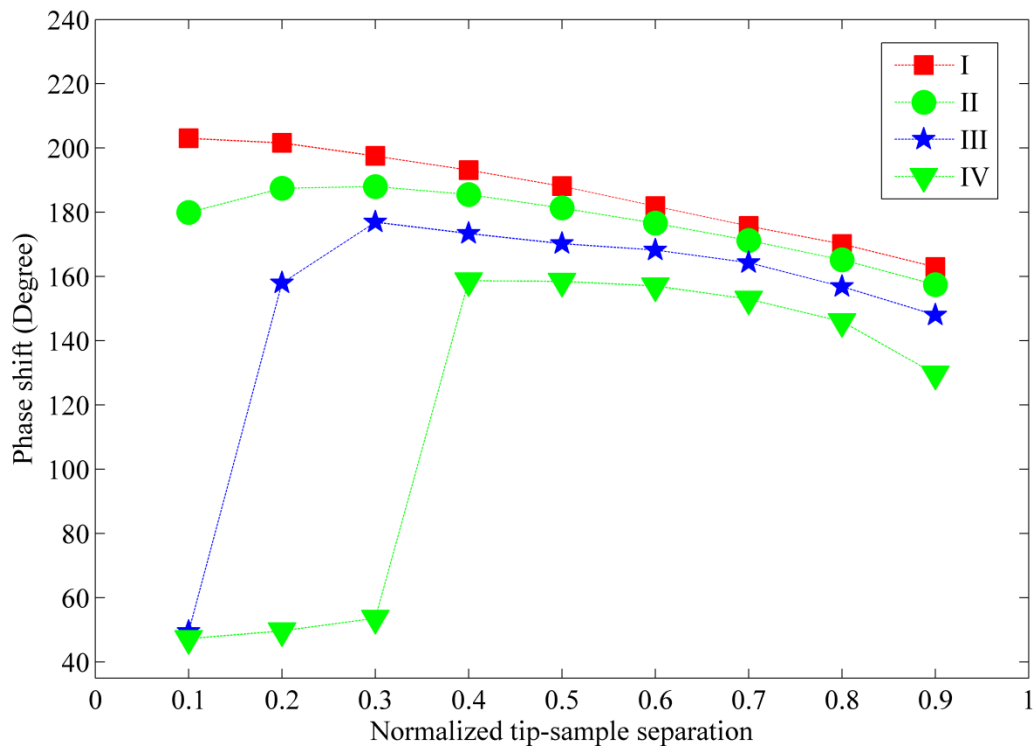
**Figure 8.7** The trend of phase shifts when only elastic force (Square) or adhesion force (Circle) is applied to the cantilever tip.

Figure 8.7 shows the behaviour of phase shifts when only the elastic force, or adhesion force, is applied to the tip surface in the Z-axis. The elastic force is defined here with a Young's modulus of 1GPa and a Poisson's ratio of 0.4, by using Equation 4.14. In addition identical approaching and retracting surface energies of 30 mJ/m<sup>2</sup> are used here to define the adhesion force. Notice that an offset is added into the phase shifts here to make the phase shift of the cantilever at free vibration equal to 90°. This operation is always used in the real phase images produced by an actual tapping mode AFM system and so it is reproduced here and applied throughout the thesis. The tip-sample separation  $d_0$  is normalized to the cantilever's free vibration amplitude  $Amp_{free}$ :

$$d_{0n} = \frac{d_0}{Amp_{free}} \quad (8.1)$$

The normalized tip-sample separation  $d_{0n}$  is used to analyse the simulation results in this thesis. The phase shifts increase linearly as the tip-sample separation decreases (i.e., the tip becomes closer to the sample) when only repulsive force is considered (red square). On the other hand, the phase shifts decrease linearly as the tip-sample separation decreases when only attractive force is considered (blue circle). It is worth noting that the elastic force is a purely repulsive force and that the adhesion force is a purely attractive force. From Figure 8.7, it can also be seen that the phase shifts are below  $90^\circ$  in the attractive regime, while the phase shifts are above  $90^\circ$  in the repulsive regime.

## 2) Effect of adhesion hysteresis on phase shift



**Figure 8.8 Phase shifts under elastic force and with different levels of adhesion energy hysteresis. The surface energy  $\gamma_{\text{approach}}$  is  $30\text{mJ/m}^2$ ; The  $\gamma_{\text{retract}}$  is respectively,  $35\text{mJ/m}^2$  (I),  $60\text{mJ/m}^2$  (II),  $90\text{mJ/m}^2$  (III), and  $120\text{mJ/m}^2$  (IV).**

Figure 8.8 shows the phase shifts under different levels of adhesion hysteresis, coupled with the elastic force, which are applied to the cantilever tip in the Z-axis. The elastic force is defined here with a Young's modulus of 1GPa and a Poisson's ratio of 0.4, by using

Equation 4.14. In curves I, II, III, IV, the approach surface energy  $\gamma_{\text{approach}}$  is  $30\text{mJ/m}^2$ , while the corresponding retract surface energies  $\gamma_{\text{retract}}$  are  $35\text{mJ/m}^2$ ,  $60\text{mJ/m}^2$ ,  $90\text{mJ/m}^2$  and  $120\text{mJ/m}^2$ , respectively. From Figure 8.8, it can be seen that the adhesion energy hysteresis decreases the phase shift significantly. For curves I and II, both are in the repulsive regime for all the tip-sample separations, but the phase shifts show a decreasing trend when the tip approaches the sample. When the level of hysteresis further increases, as in curve III, this shows a transition from the repulsive regime to the attractive regime as the tip-sample separation becomes close to 0.1. It can be seen that in curve III the phase shift at a normalised tip-sample separation of 0.1 is below  $90^\circ$ . This behaviour is more obvious when the level of hysteresis is further increased, as shown in curve IV. The transition from the repulsive regime into the attractive regime as the tip approaches the sample is due to the two opposite contributions to the phase shifts by the repulsive and attractive forces, as can be clearly seen in Figure 8.7.

### 3) Effect of van der Waals force on phase shift

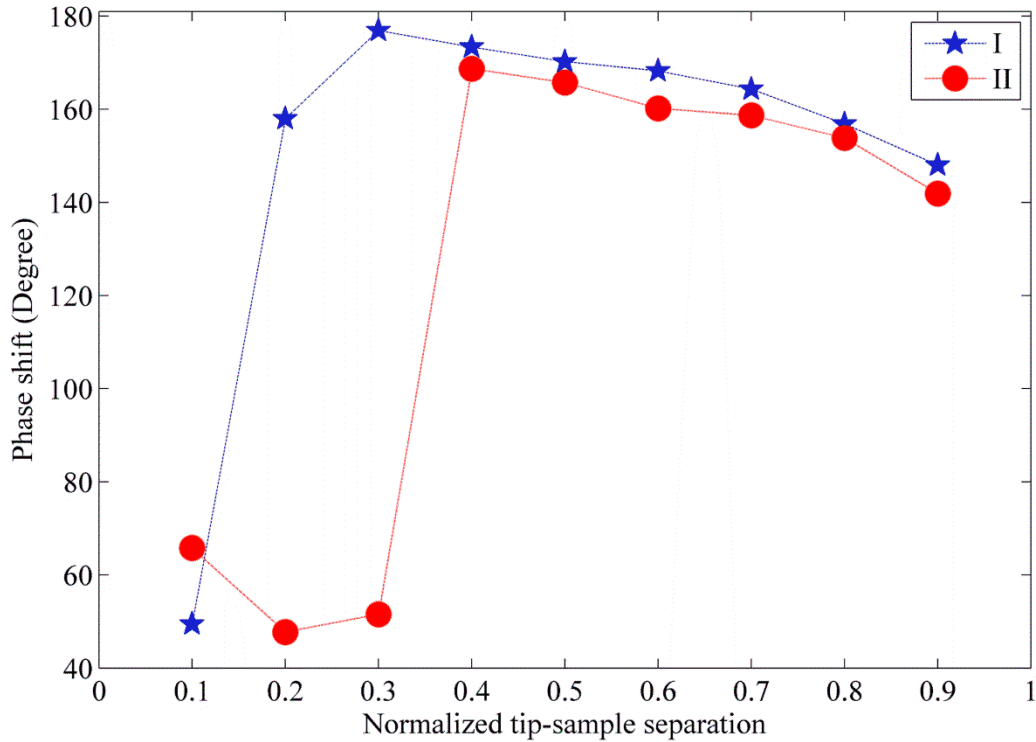


**Figure 8.9** Phase shifts under elastic force with a Young's modulus of 1GPa and Poisson's ratio of 0.4 coupled with I: adhesion hysteresis; II: adhesion hysteresis and van der Waals force. The  $\gamma_{\text{approach}}$  surface energy is  $30\text{mJ/m}^2$ , the  $\gamma_{\text{retract}}$  is  $90\text{mJ/m}^2$ , the Hamaker constant is  $6e^{-20}$  J.

In order to verify whether modelling other attractive interaction forces has the ability to decrease the level of phase shift, the van der Waals force was also added into the simulation. The results are shown in Figure 8.9. In Figure 8.9, curve I is adopted from curve III in Figure 8.8. Based on curve I, van der Waals force is further added by using Equations 4.1-4.3 to produce curve II, where the Hamaker constant is  $6e^{-20}$  J and the surface energy  $\gamma$  is  $30\text{mJ/m}^2$ . From Figure 8.9, it can be seen that the addition of the van der Waals force further decreases the phase shift. The transition from the repulsive regime to the attractive regime moves towards larger tip-sample separations. While curve I approaches the attractive regime at a normalized tip-sample separation of 0.1, curve II approaches the attractive regime at a normalized tip-sample separation of 0.3, which once again

demonstrates the contribution made by the repulsive and attractive forces, as shown in Figure 8.7.

#### 4) Effect of viscosity force on phase shift

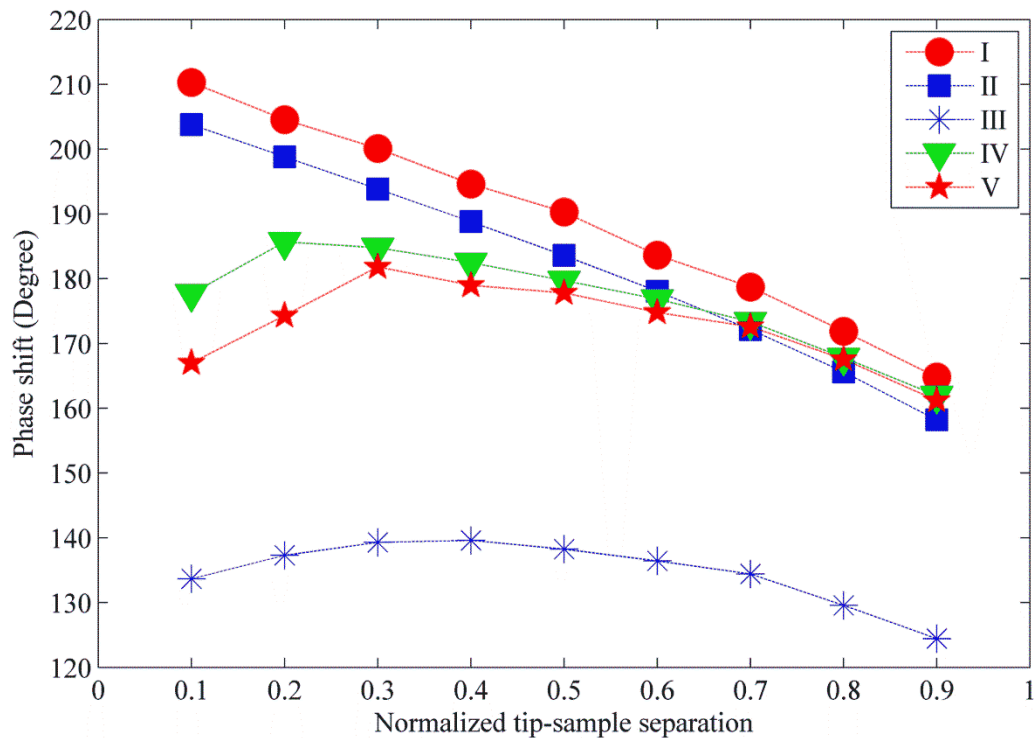


**Figure 8.10 Phase shifts under elastic force and for different viscosity forces. I: elastic force only; II: elastic force + low viscosity force. III: low viscosity force only; IV: elastic force + high viscosity force. V: high viscosity force only.**

Figure 8.10 shows the simulated behaviour of the cantilever phase shifts when elastic and viscosity forces are applied to the cantilever tip in the Z-axis. The elastic force is defined here with a Young's modulus of 1GPa and a Poisson's ratio of 0.4, by using Equation 4.14. The low viscosity force is calculated based on a viscosity of 500Pa\*s by using Equation 4.23, while the high viscosity force is calculated based on a viscosity of 5000Pa\*s. For curve I, only the elastic force is applied to the cantilever tip. For curve II, a low viscosity force and the elastic force are both applied to the tip. Comparing curves I and II, it can be seen that the added viscosity forces cause around 6° of phase shift at every tip-sample separation. Curves III and V show the phase shifts when only the viscosity force is applied. From curves III and

V, when we have only viscosity force applied, it can be seen that the phase shifts both decrease when the tip approaches the sample. Curve IV, shows a situation where a high viscosity force and the same elastic force that was used previously are both applied to the tip. From Figure 8.10, it can be seen that curve IV has a similar trend to curve III, which indicates that here the viscosity force is dominant. As the viscosity force consists of both a repulsive force and an attractive force, when the elastic force is included in the simulation, as shown in curve IV, the overall force becomes repulsive and thus the phase shifts are all above  $90^\circ$ .

From Figures 8.8 and 8.10, it can be observed that a phase image obtained using a small tip-sample separation provides more information on the sample features, such as the elasticity, viscosity and adhesion of material, because at normalized tip-sample separations ranging from 0.1 to 0.3, the phase shifts under different interaction forces can be differentiated.

#### 5) Effect of elastic force on phase shift

The results shown above have been produced using the same elastic force with a Young's modulus of 1 GPa and a Poisson's ratio of 0.4. In order to investigate how phase shifts change under different elastic forces, simulations were also performed by changing the Young's modulus value to 5 GPa. The results are presented in Figure 8.11.

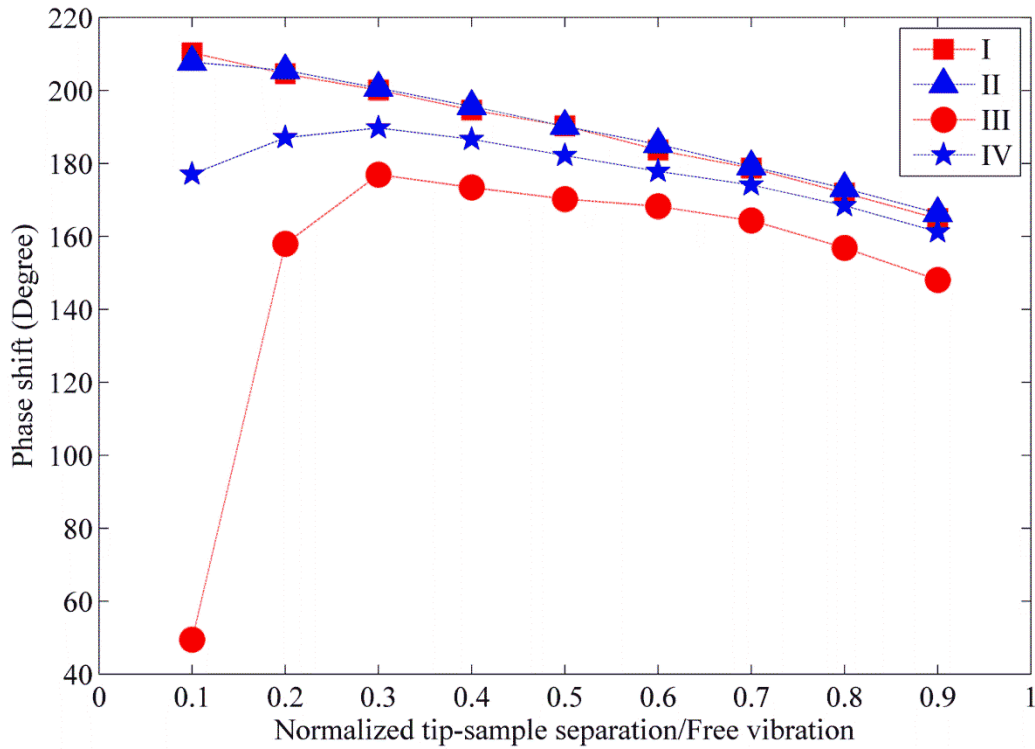


**Figure 8.11** Phase shifts of I: only elastic force with a Young's modulus of 1GPa and Poisson's ratio of 0.4; II: only elastic force with a Young's modulus of 5GPa and Poisson's ratio of 0.4; III , IV are based on I and II, respectively, with the same adhesion hysteresis, where the  $\gamma_{\text{approach}}$  surface energy is 30mJ/m<sup>2</sup> and the  $\gamma_{\text{retract}}$  is 90mJ/m<sup>2</sup>.

In curves I and II of Figure 8.11, only elastic force is considered on the cantilever tip's surface in the Z-axis, with two different Young's moduli of 1GPa and 5GPa, respectively, and Poisson's ratios of 0.4. It can be seen from Figure 8.11 that these two curves almost overlap each other. Thus, this indicates that the phase shifts are not sensitive to a change of Young's modulus in the case of purely elastic force existing. Curves III and IV show the behaviour of the phase shifts when adhesion hysteresis is coupled into curves I and II, where the approaching surface energy  $\gamma_{\text{approach}}$  is 30mJ/m<sup>2</sup> and the  $\gamma_{\text{retract}}$  is 90mJ/m<sup>2</sup>. Curve IV is under the repulsive regime at all tip sample separations, because the strength of the elastic force is dominant. From curves III and IV, it is observed that the elastic force does affect the phase shifts in the case of combined forces applied to the tips, which always happens in real AFM experiments.

## 8.4 Transition time analysis

As mentioned in Section 8.3, the phase shifts in tapping mode AFM are obtained from the stable state of the cantilever vibration. When the cantilever moves to a particular X-Y position during mechanical scanning, the cantilever needs to reach a new stable state due to the tip-sample separation changes caused by the surface topography of the test sample. The transition time taken to move from a free vibration state to a stable state, as shown in Figure 8.3, limits the AFM's scanning speed. Therefore, an investigation of the transition times under different conditions, such as different tip-sample interaction forces and different tip-sample separations, can provide guidance on the selection of the optimal scanning speeds to be used in tapping mode AFM imaging.

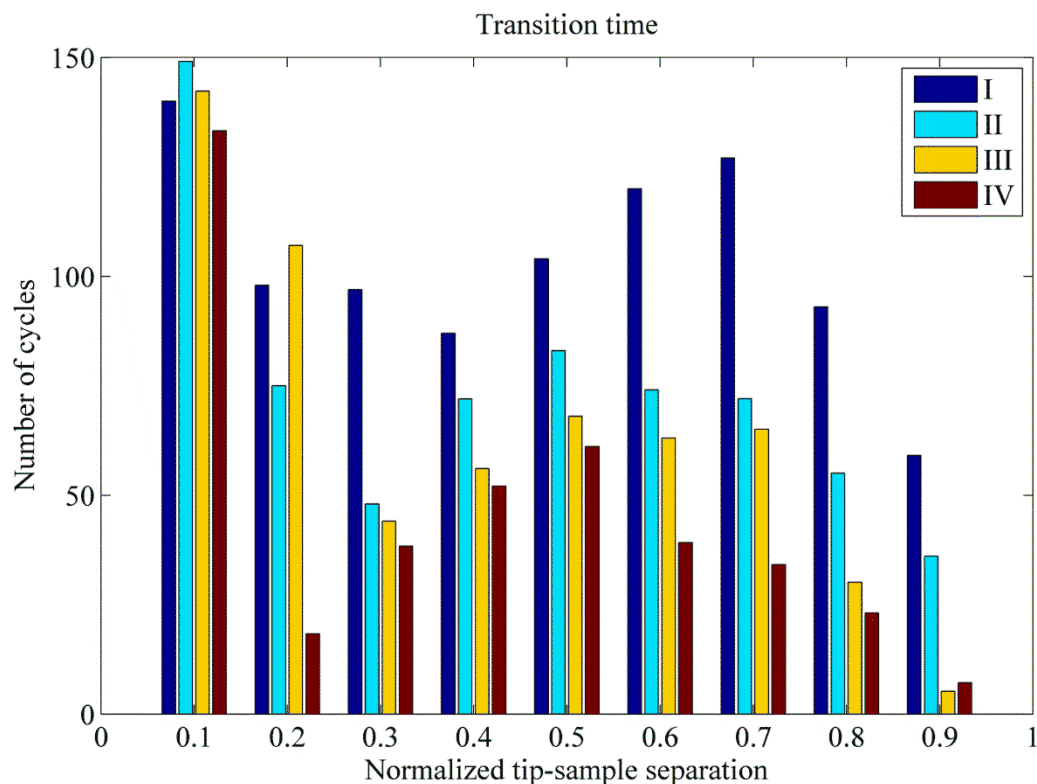


**Figure 8.12** Transition time: I. purely elastic force. II, III, IV. elastic force and different levels of adhesion hysteresis. For II, III and IV, the  $\gamma_{\text{approach}}$  is  $30\text{mJ/m}^2$ ; The  $\gamma_{\text{retract}}$  is,  $35\text{mJ/m}^2$  (II),  $60\text{mJ/m}^2$  (III),  $90\text{mJ/m}^2$  (IV) respectively.

Figure 8.12 shows the transition time calculated from the simulated dynamic displacement responses used to obtain the phase shifts presented in Figure 8.8. Since a driving sinusoidal voltage with a frequency of 62,920Hz is applied to the virtual piezo actuator to vibrate the cantilever, the period of the driving voltage is  $1.5893e-5$  seconds. In Figure 8.12, the transition time is expressed as a number of cycles which is based on the period of this driving voltage. The transition time is the vibration time of the transition state which is marked in the dynamic displacement response in Figure 8.3.

From Figure 8.12, it can be seen that the transition time is relatively short at normalized tip-sample separations of around 0.2 or 0.9. However, either case may result in losing the contribution from the elasticity or adhesion of the material as shown in Figure 8.8. At a normalized tip-sample separation of 0.2, the phase shifts are below  $90^0$ , which indicate attractive forces are dominant. On the other hand, repulsive force is dominant at normalized tip-sample separation of 0.9. Thus, in order to capture a phase image with the contributions from both elasticity and adhesion, we may need to compromise the scanning speed by choosing a normalized tip-sample separation of around 0.4, because the phase shifts are about to change from the repulsive regime to the attractive regime, as shown in Figure 8.8, which contain the contributions from the repulsive force and attractive force.

## 8.5 Stable amplitude analysis

From the dynamic displacement responses, as shown in Figure 8.3, the amplitude of the cantilever vibration in the stable state can be extracted. The stable state is defined in this thesis, for the convenience of the analysis, as being the case when the difference of the amplitude between a current vibration cycle and the previous vibration cycle is smaller than a value of 1nm. The stable amplitude is calculated from the displacement signal below zero, shown in Figure 8.3, which is affected by various interaction forces, such the elastic force, adhesion force and viscosity force. Figure 8.13 shows the stable amplitudes calculated from the simulated dynamic displacement responses, where dataset I is only considering the elastic force (with a Young's modulus of 1GPa and a Poisson's ratio of 0.4), dataset II couples the elastic force used in dataset I with adhesion hysteresis, whose  $\gamma_{\text{approach}}$  surface energy is  $30\text{mJ/m}^2$  and  $\gamma_{\text{retract}}$  is  $90\text{mJ/m}^2$ . The reference bars shown in Figure 8.13 represent initial the tip-sample separation. Generally, the stable amplitudes should be larger than the

reference bars. Otherwise, the tip does not actually contact the sample. As the tip-sample separation decreases, the stable amplitudes decrease correspondingly. One exception occurs when the normalised tip-sample separation is at a value of 0.1 in dataset II. This is due to the fact that the tip is bouncing on and off the sample's surface, as shown in Figure 8.14. In other words, the tip is in contact with the sample intermittently even in the contact region.

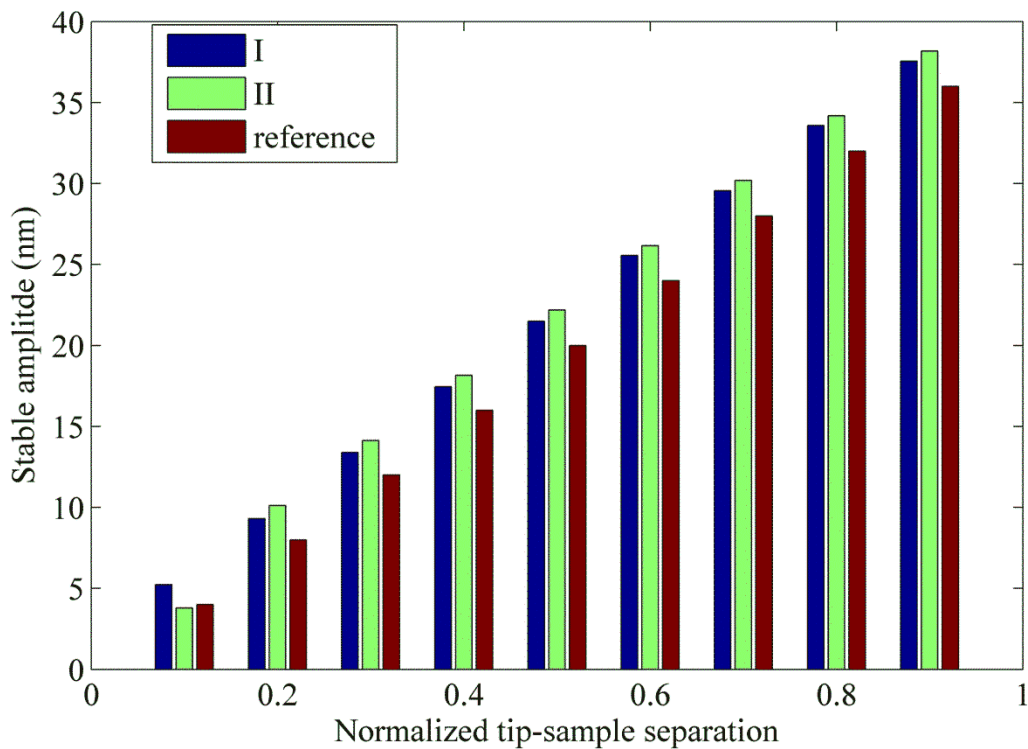


**Figure 8.13 Stable amplitude under I: purely elastic force, II: elastic force and adhesion hysteresis.**

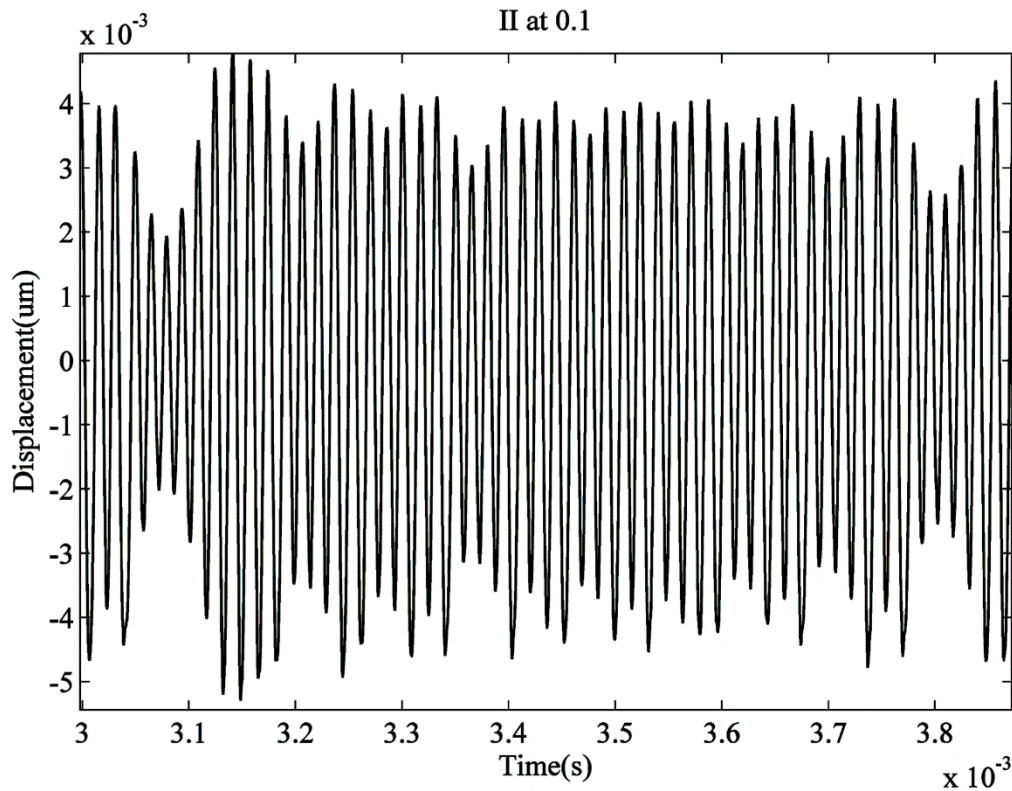


**Figure 8.14 Dynamic displacement response of the cantilever during the steady state.  $Q=100$ , free vibration amplitude  $A_{\text{free}} = 40\text{nm}$ , tip sample separation  $d_0 = 4\text{nm}$ . Young's modulus =  $1\text{GPa}$ , Poisson's ratio =  $0.4$ .  $\gamma_{\text{approach}} = 30\text{mJ/m}^2$ ,  $\gamma_{\text{retract}}=90\text{mJ/m}^2$ . Elastic force has been coupled with adhesion hysteresis to produce this result.**

The reason that the tip is bouncing on and off the surface in the figure above could be due to the adhesion force. It may be a good idea to see whether enhancing the strength of the adhesion force would make this bouncing effect more obvious. Figure 8.15 shows the results of stable amplitude, where data set I couples elastic force of a Young's modulus of  $1\text{GPa}$  and a Poisson's ratio of  $0.4$ , with adhesion hysteresis, whose  $\gamma_{\text{approach}}$  surface energy is  $100\text{mJ/m}^2$  and  $\gamma_{\text{retract}}$  is  $150\text{mJ/m}^2$ . As for data set II, same elastic force is applied, but the hysteresis effect is increased by changing the retract surface energy  $\gamma_{\text{retract}}$  to  $200\text{mJ/m}^2$ . It is found that a large adhesion force with large hysteresis leads to the bouncing effect becoming more obvious, which can be seen in data set II, where all the values are smaller than the reference bar.

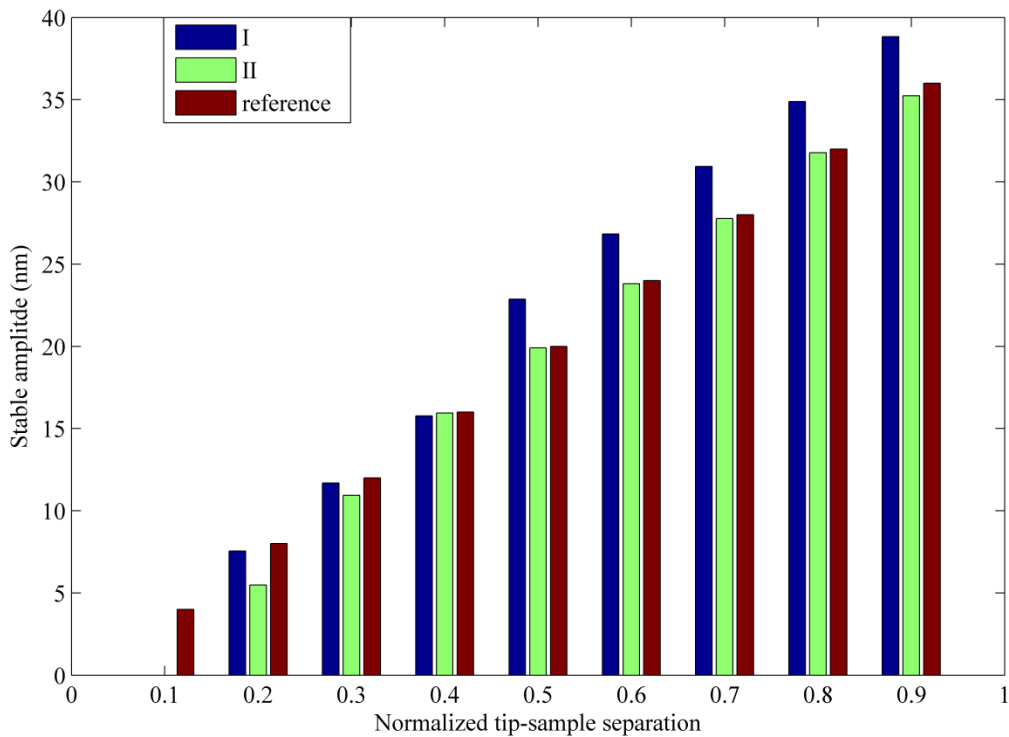


**Figure 8.15 Stable amplitudes of elastic force couples with I:  $\gamma_{\text{approach}} = 100\text{mJ/m}^2$ ,  $\gamma_{\text{retract}}=150\text{mJ/m}^2$ , II:  $\gamma_{\text{approach}} = 100\text{mJ/m}^2$ ,  $\gamma_{\text{retract}}=200\text{mJ/m}^2$**

Figure 8.16 shows the stable amplitudes when viscosity force is coupled with elastic force. The elastic force is defined here with a Young's modulus of 1GPa and a Poisson's ratio of 0.4. The viscosity force is calculated based on a viscosity of 500Pa\*s and 5000Pa\*s, respectively, in both data set I and data set II. It can be seen that both the stable amplitudes in data set I and II are larger than the reference bar, which indicates that the tip does not bounce off the surface during the contact period.

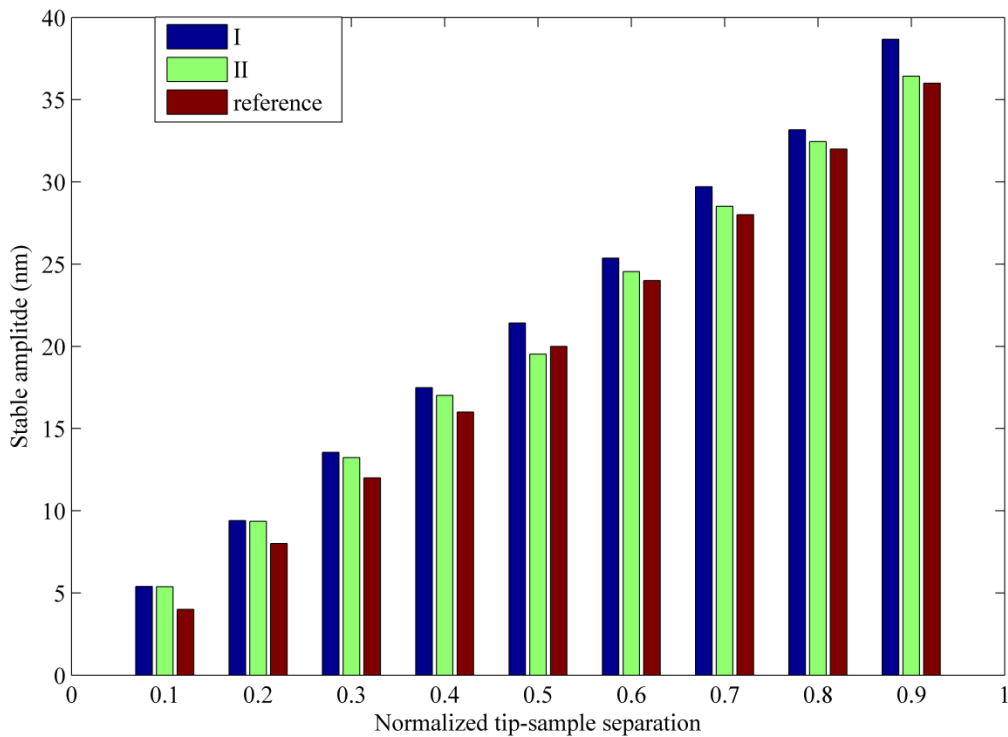


**Figure 8.16** Stable amplitudes of elastic force couples with viscosity force I: 500 Pa\*s, II: 5000 Pa\*s

## 8.8 Instantaneous frequency

Phase shifts are due to shifts in the cantilever's resonant frequency. Without any tip-sample interactions, the phase shift corresponding to the resonant frequency would be  $90^\circ$ . It was found that the phase shift would become smaller than  $90^\circ$  for small tip-sample separations, while the resonant frequency of the cantilever would shift to higher frequencies. For relatively large tip-sample separations, the phase shift would be larger than  $90^\circ$ , while the resonant frequency would shift to lower frequencies (Magonov et al., 1997b). Figure 8.17 shows the vibration periods of each vibration cycle in a simulated dynamic displacement response signal. The simulated dynamic displacement response signal is obtained under the following conditions: Young's modulus of 1GPa and Poisson's ratio of 0.4, approach surface energy  $\gamma_{\text{approach}}$  is  $30\text{mJ/m}^2$ , and retract surface energies  $\gamma_{\text{retract}}$  are  $90\text{mJ/m}^2$ . The vibration period is computed through a zero crossing method. The vibration period change in a cycle is equivalent to the frequency change in that cycle. From Figure 8.17, it can be seen that the period decreases during the transition state. The vibration period is the same both in the

free vibration state and at the stable state. The relationship between this dynamic behaviour and the phase shift is worthy of further study in the future.

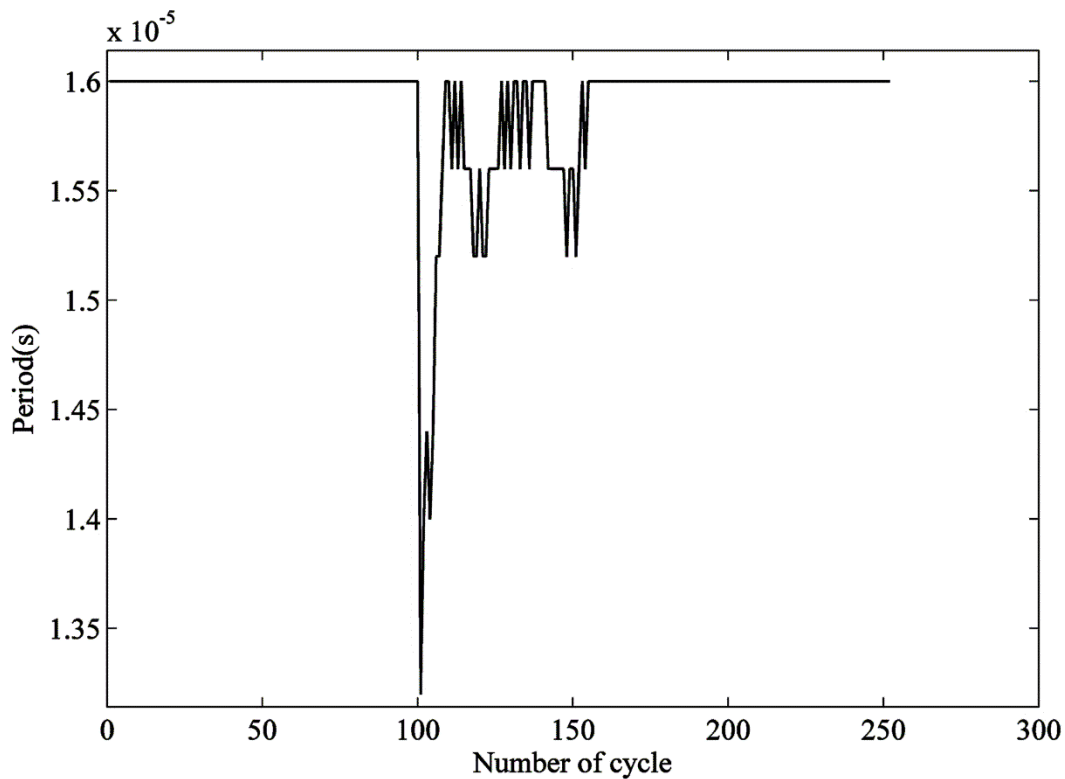


**Figure 8.17** Vibration periods,  $Q=100$ , free vibration amplitude  $Amp_{free}= 40nm$ , tip-sample separation  $d_0= 20nm$ . Young's modulus =  $1GPa$ , Poisson's ratio =  $0.4$ .  $\gamma_{approach} = 30mJ/m^2$ ,  $\gamma_{retract} = 90mJ/m^2$ . Elastic force has been coupled with adhesion hysteresis to produce this result.

## 8.9 Summary and Discussions

The dynamic displacements of the cantilever have been shown under different damping conditions in this chapter. It was found that the transition of the displacement of the cantilever from free vibration to the tapping period is shorter both in free vibration analysis and the analysis when the tip sample interaction force is applied. Also, it was discovered that while the attractive forces have the ability to decrease the phase shift, on the other hand, repulsive forces can increase the phase shift. The transition in the phase shifts curve indicates the repulsive and attractive regimes. The transition time analysis that has been presented may provide an idea of how to optimise high speed imaging in tapping mode AFM, provided that the adhesion force dominates the tip sample interaction force.

# Chapter 9

AFM

Experimentation

## **Chapter 9 AFM Experimentation**

Chapter 9 gives a brief description of the equipment used in the AFM system. The procedure of calibration of the system, force curve analysis and imaging is also presented. The aim is to demonstrate how to carry out an AFM experiment and hence to support the computer simulation results.

### **9.1 Equipment**

In this thesis, experiments were carried out using a Molecular Force Probe-3D (MFP-3D) atomic force microscope (Asylum Research, Santa Barbara, CA) with software written in IGOR pro (Wavemetrics, USA). The maximum scanning range in the x and y directions is 90  $\mu\text{m}$ , while the movement of the z-piezo is up to 16  $\mu\text{m}$ . In order to avoid problems due to external noise, the MFP-3D-IO was first mounted upon a TS-150 active vibration isolation table (HWL Scientific instruments GmbH, Germany), both of which were located inside an acoustic isolation enclosure (IGAM mbH, Germany). The whole AFM system setup is shown in Figure 9.1. Silicon cantilevers (Olympus model AC240TS) were used with nominal manufacturer values for length, width, thickness and tip radius of 240 $\mu\text{m}$ , 30 $\mu\text{m}$ , 2.7 $\mu\text{m}$  and 9nm respectively. The resonant frequency and spring constant (k) of the cantilevers were measured at approximately 72 kHz and 2N/m, respectively. The procedure of how to determine the resonant frequency and spring constant of the cantilever will be demonstrated in Section 9.3.



**Figure 9.1** The whole AFM system setup.

## 9.2 Preparation of samples

For the experimental work three relatively soft samples, polyurethane (PU), polyvinyl chloride (PVC) and parafilm were used. The polymer was supplied by Biomer Technology Ltd in a liquid form. To develop the polymer, the polyurethane solution was first poured into a glass petri dish and swirled until the polyurethane solution had contacted the edges of the glass dish. The polyurethane was then cured in an oven at 60°C for 2 hours. The PVC was purchased commercially in the form of cling wrap. The parafilm was also purchased commercially in the form of a plastic film with a paper backing. To prepare the samples so as to be ready for AFM measurements the PU, PVC and parafilm were placed on a glass microscope slide.

### 9.3 Cantilever calibration

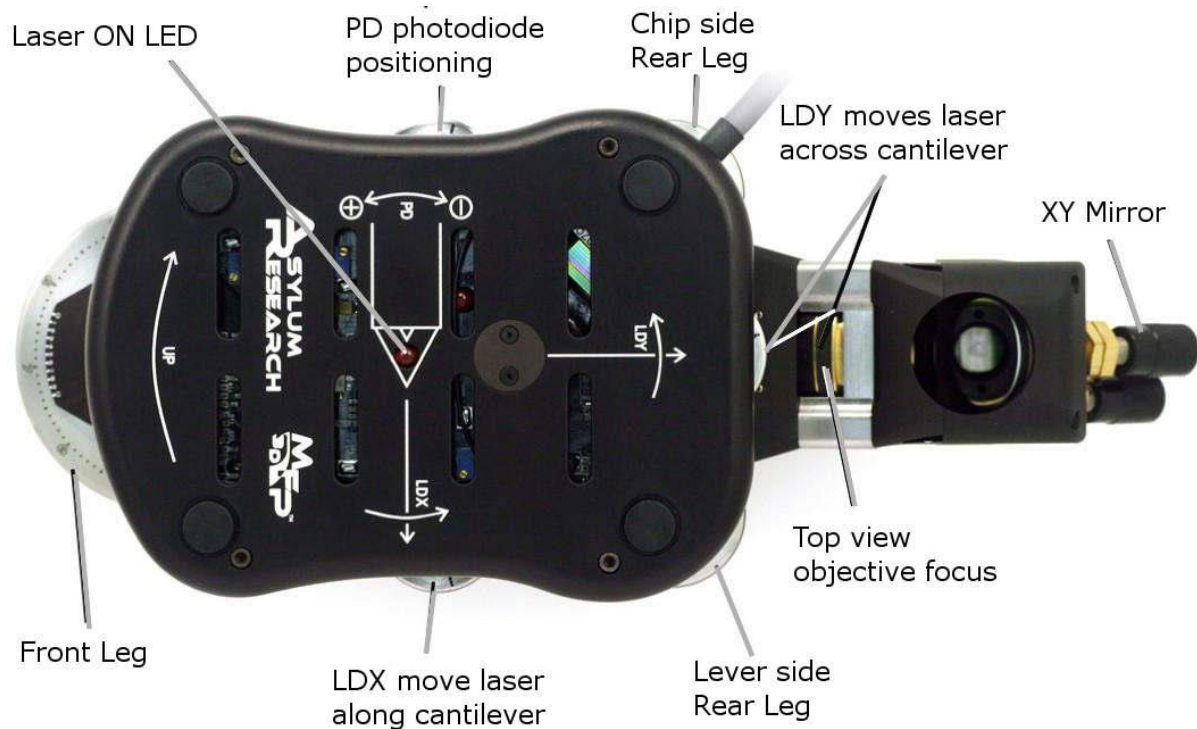


Figure 9.2 Top view of the AFM

Before experiments were carried out the cantilever was first calibrated. This was achieved by characterising the inverse optical lever sensitivity (*Invol*s), which is software driven for the MFP3D AFM system and is described in (Meyer and Amer, 1988). Generally, the sum shown in Figure 9.3 needs to be adjusted to a maximum by moving the laser along and across the cantilever, using thumbwheels LDX and LDY as indicated in Figure 9.2. For example, the value of the 'Sum' shown in Figure 9.3 here has reached its maximum value. The next step is to adjust the deflection to zero by using the photodiode positioning. When the first two steps are completed, the cantilever can be automatically tuned by pressing the 'Auto Tune' button, shown in Figure 9.4. After the cantilever is tuned, it will show the resonant frequency of the cantilever and the phase shift at the resonant frequency, which is demonstrated in Figure 9.5. The procedure of the calibration of the spring constant is simple. Just choose the cantilever type and press the 'GetRealCalibration' icon, which is shown in Figure 9.6. Calibration of the spring constant helps to measure the real spring constant of the cantilever, which is 2.08 N/m in this experiment. Also, it can determine that an

amplitude of 1 volt, as recorded by the photodetector, is equal to a cantilever displacement distance of 43.6nm.

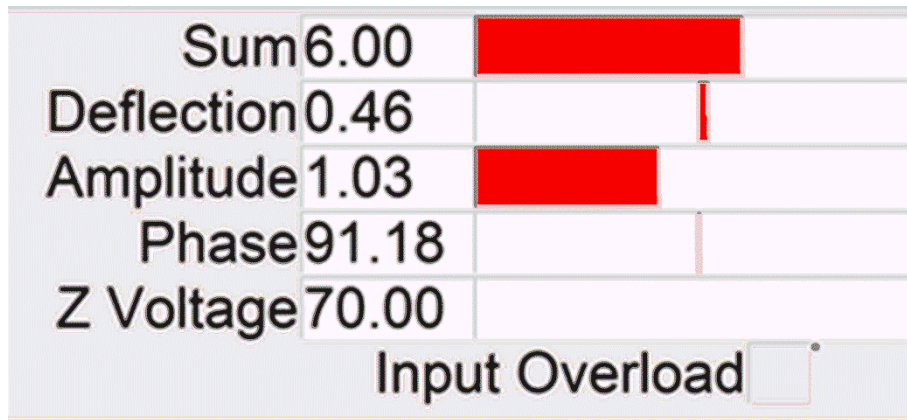


Figure 9.3 Sum and deflection meter.



Figure 9.4 The tune tab in the master channel

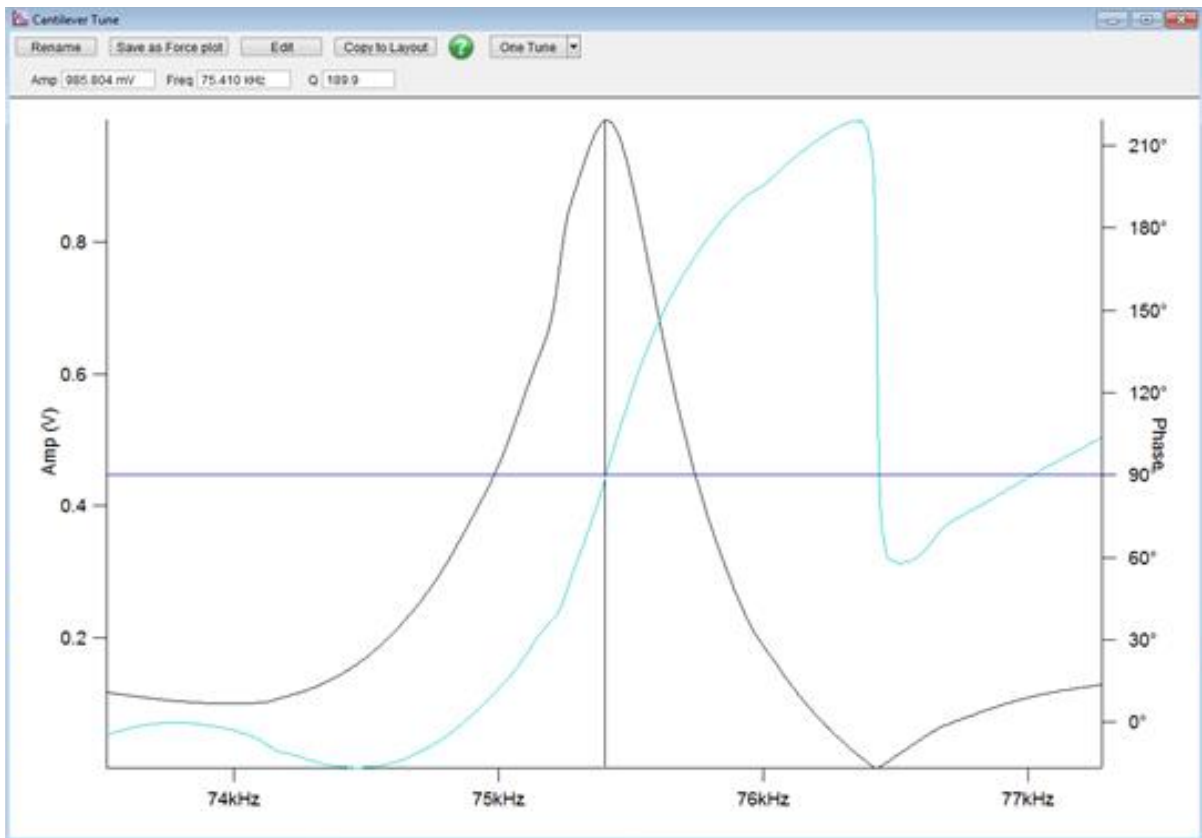


Figure 9.5 Tune graph shows the resonant frequency of the cantilever and the phase shift at resonant frequency.

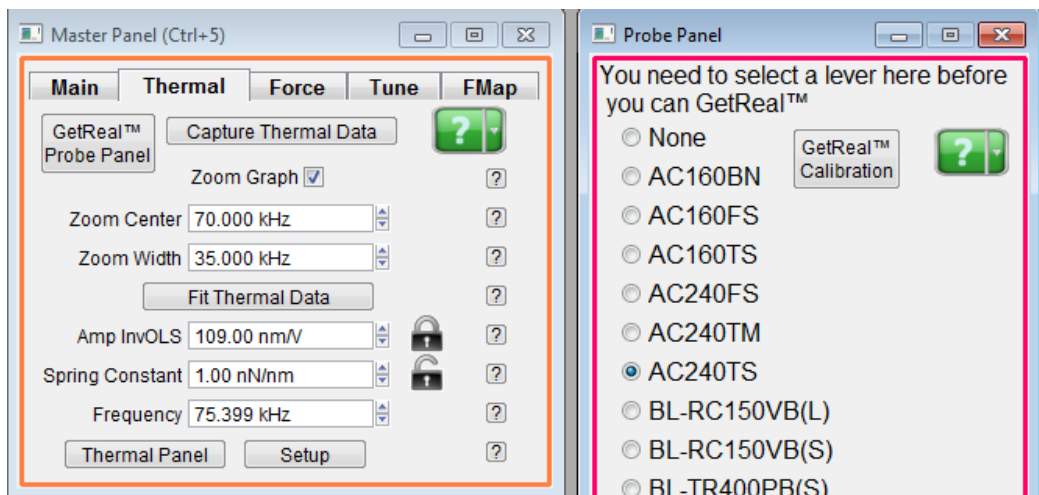


Figure 9.6 The user interface of calibration of the spring constant.

## 9.4 Force curve analysis

After calibration of the inverse optical lever sensitivity and the spring constant these are indicated to the user as having being calibrated by the appearance of solid green filled circles on the user panel (see Figure 9.7), which means that the system is now ready to perform measurements. Force curve measurement was subsequently performed using contact mode AFM. The force curve can be captured by pressing the 'Single Force' button shown in the force panel. The force curves captured here represent how the deflection changes when the tip is moving close to and then retracted from the sample. The aim is to investigate the adhesion of sample materials. Figures 9.8 to 9.11 show the force curves of different samples. Figure 9.8 shows the force curve of a glass substrate. It can be seen that the trace and retrace curve almost overlap each other, which indicates that the adhesion of the glass sample is very small. As for other samples shown in Figures 9.8 to 9.11, it was found that the adhesion of parafilm is largest compared to that of PU and PVC. Hence, the force curve measurements provide a basic idea about the surface condition of the samples.

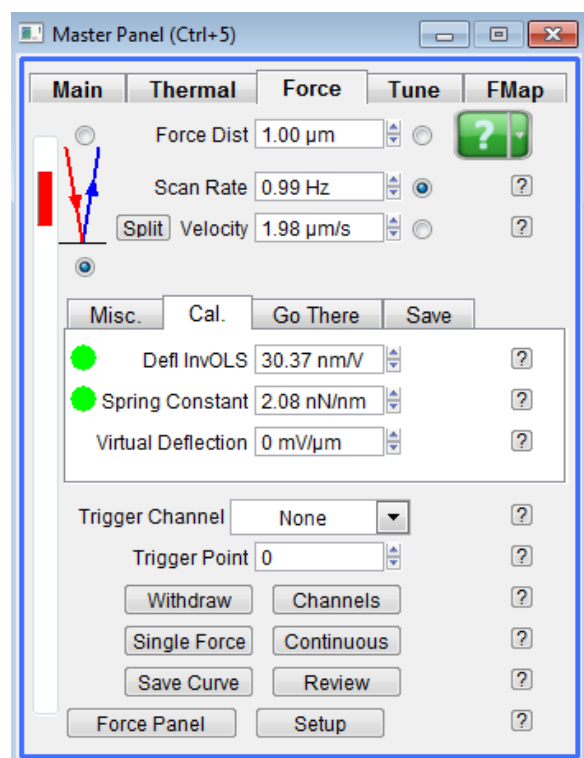
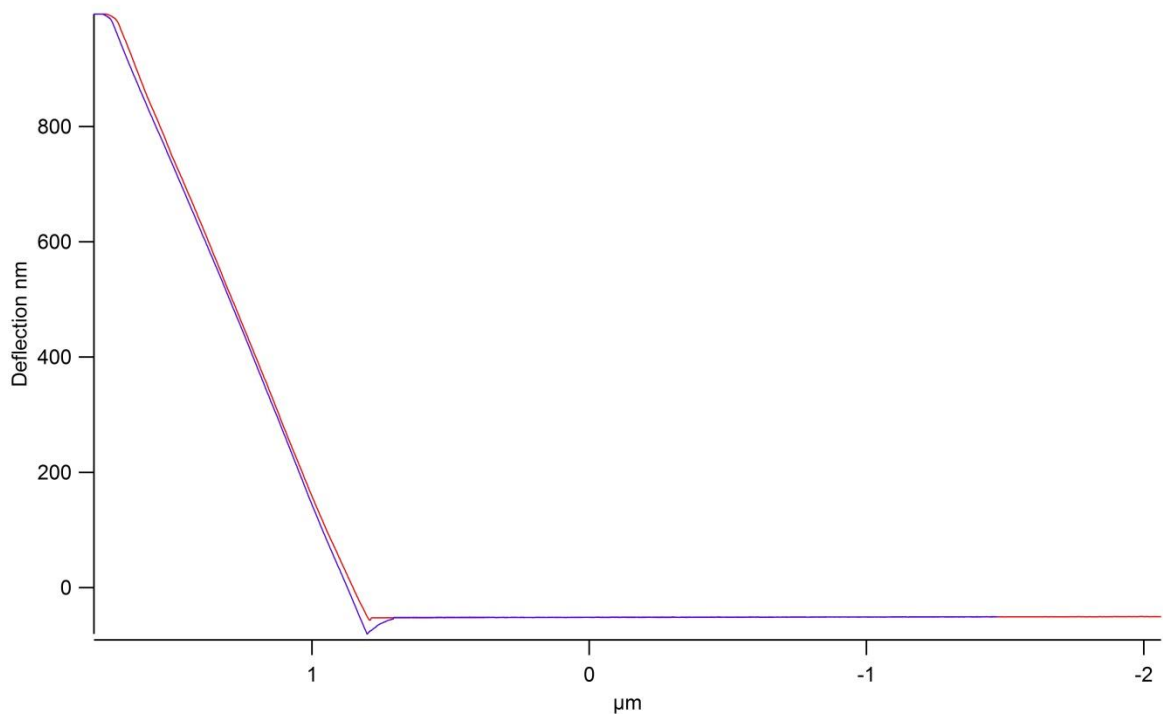
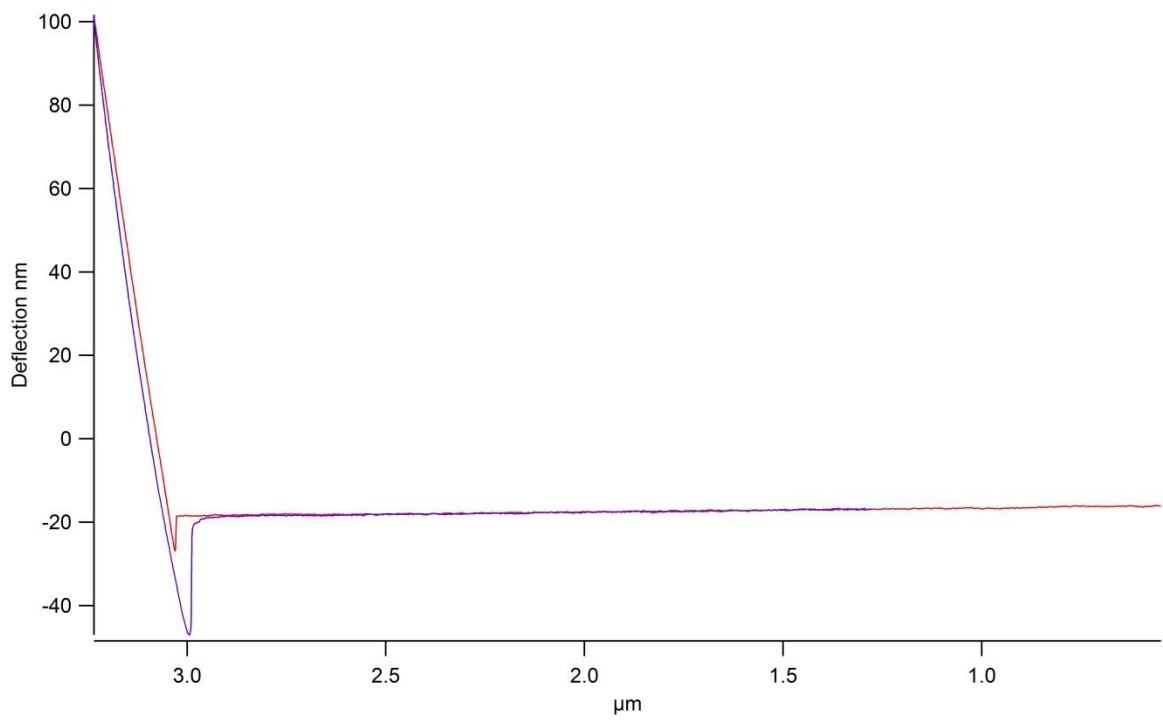


Figure 9.7 Force panel in the AFM software.



**Figure 9.8 Force curve of a glass substrate**



**Figure 9.9 Force curve of PU**

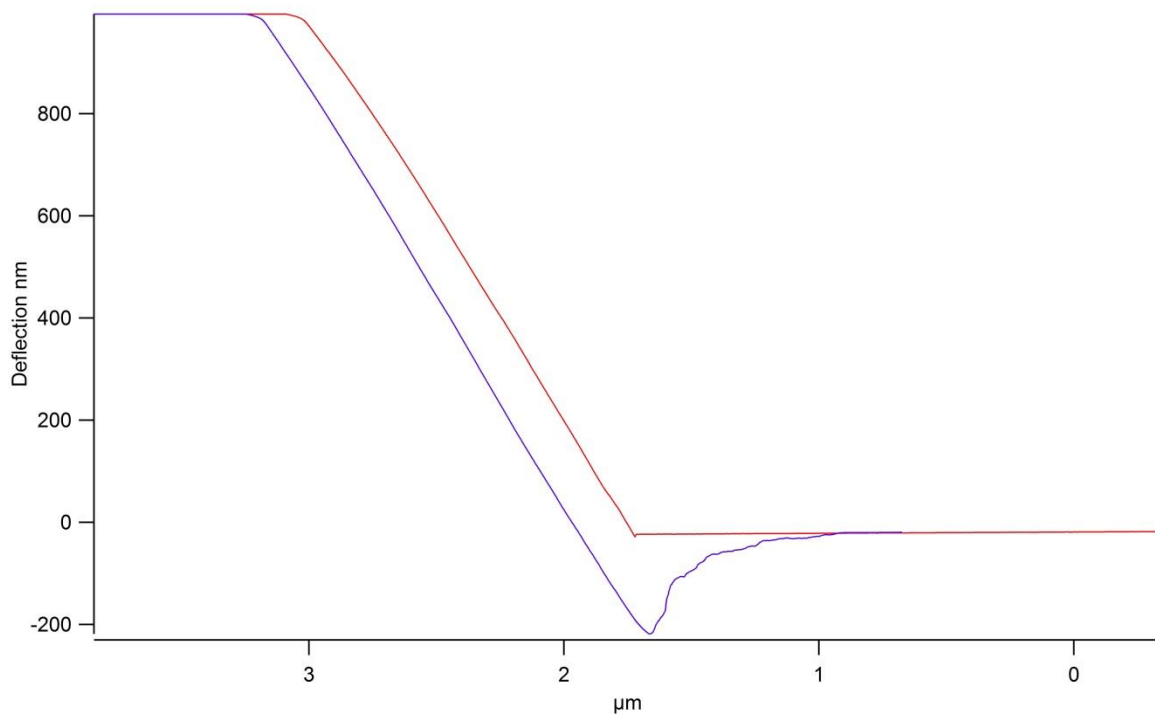


**Figure 9.10 Force curve of parafilm**

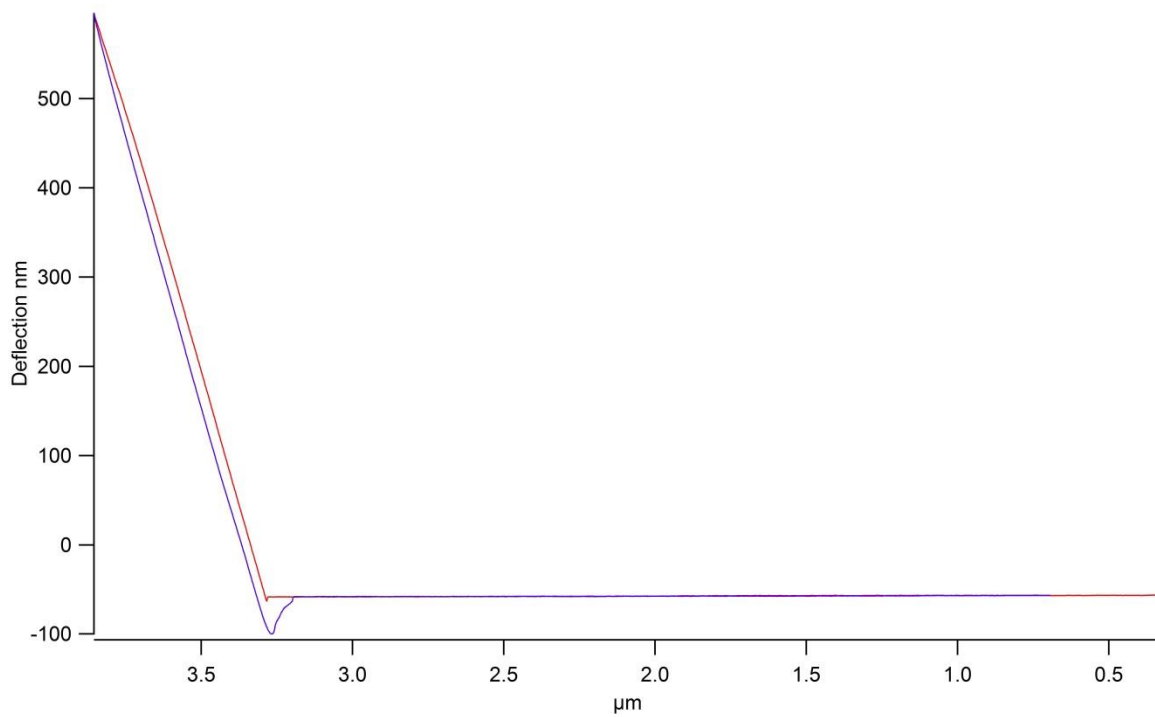


**Figure 9.11 Force curve of PVC**

## 9.5 AFM imaging

Imaging of the sample was then performed using tapping mode AFM. PU, PVC and parafilm whose Young's moduli ranging from 0.1 GPa to 4 GPa were used as the test samples here. The scanning size of the sample was chosen as  $5\mu\text{m}$  by  $5\mu\text{m}$  to gain an overview of the sample structure. The target amplitude which could be regarded as the free vibration amplitude of the cantilever was set to 1 Volt. Images were captured by changing the setpoint amplitude from 900 mV to 100 mV. Generally, one just needs to choose the scan size and setpoint amplitude and press the 'Do scan' button, shown in Figure 9.12, to scan one image.

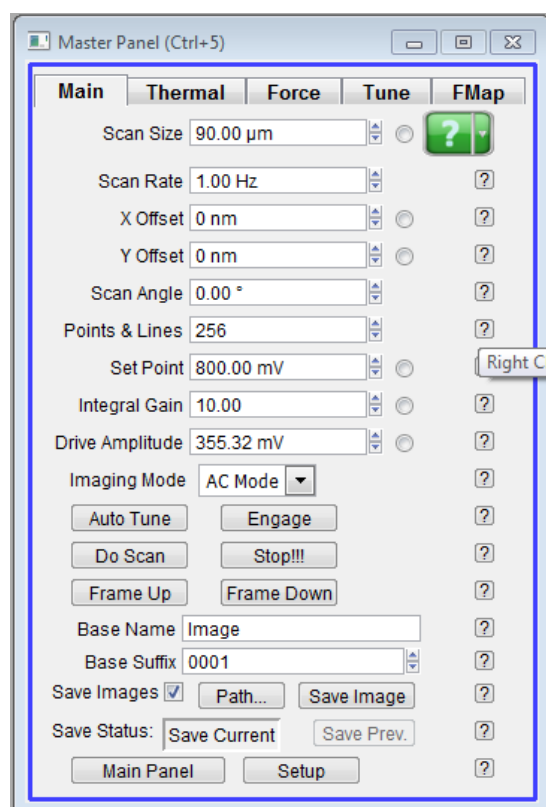


**Figure 9.12** Main panel in the AFM software

Phase images, amplitude images and height images of PU were then captured under light tapping (setpoint amplitudes: 700mV to 900mV), mediate tapping (setpoint amplitudes: 400mV to 600mV) and hard tapping conditions (setpoint amplitudes: 100mV to 300mV), respectively, as shown in Figure 9.13 (a-c).

It can be seen from Figure 9.13 that the PU sample is relatively flat, which is indicated in the height images which show that the maximum height difference is about 20 nm. However, the phase images do not seem to offer significantly more information than the other images. The reason could probably be due to the nature of the PU, which does not contain much internal structure. Figure 9.14 shows the images for parafilm, which adopt the same setting parameters that were used to produce Figure 9.13. It is immediately obvious that parafilm has more internal structure than PU. Under light tapping in Figure 9.14(a), the phase image is quite similar to the amplitude image. However, when the setpoint amplitude is changed to 200 mV, this reveals the advantage of phase imaging. In Figure 9.14(c), the internal structures of parafilm are separated in terms of dark and white pixels in the phase image, while the amplitude image remains the same.

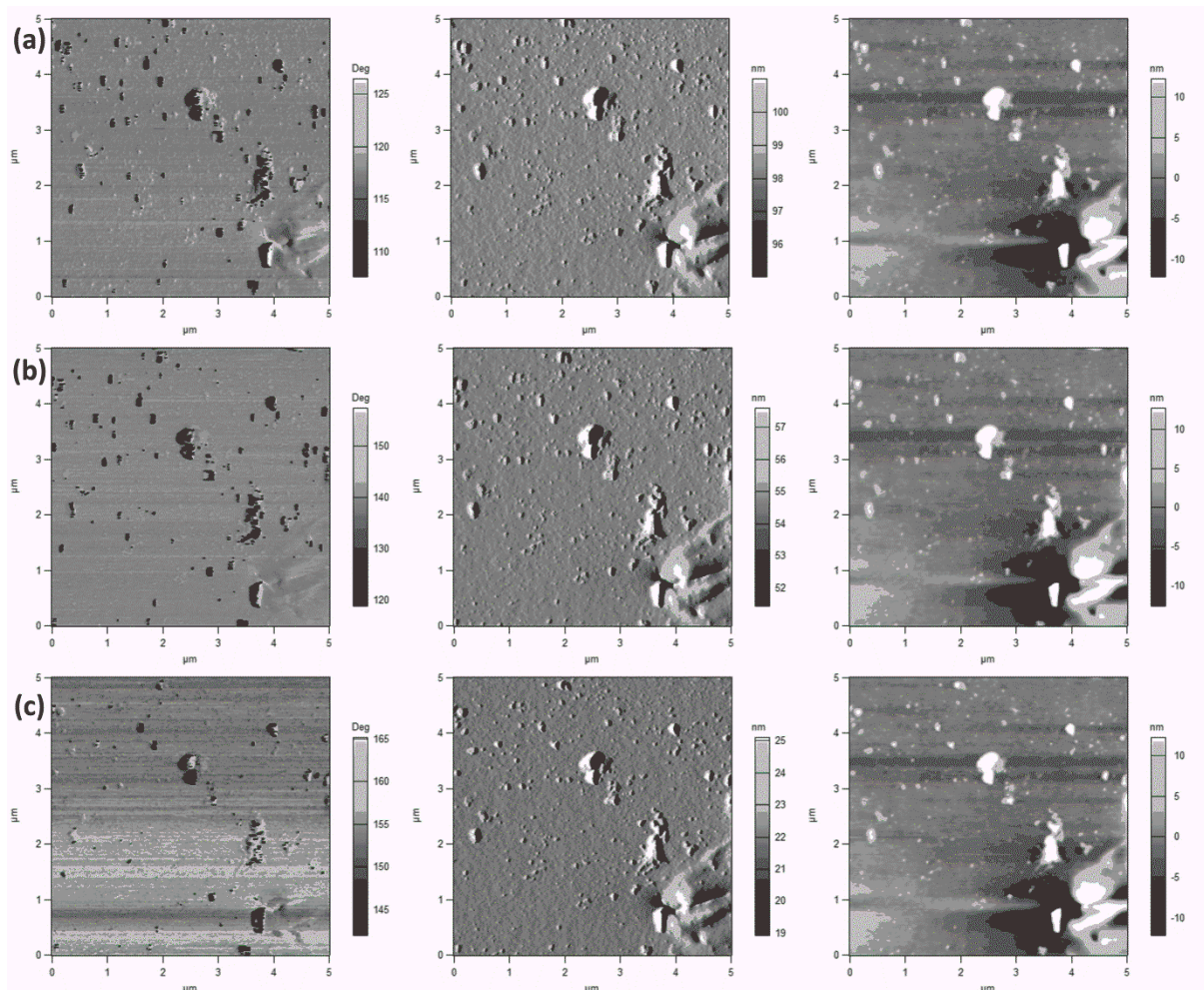


**Figure 9.13** Phase image, amplitude image, height image for a PU sample in each row: (a) setpoint amplitude: 900 mV, (b) setpoint amplitude: 500 mV, (c) setpoint amplitude: 200 mV.

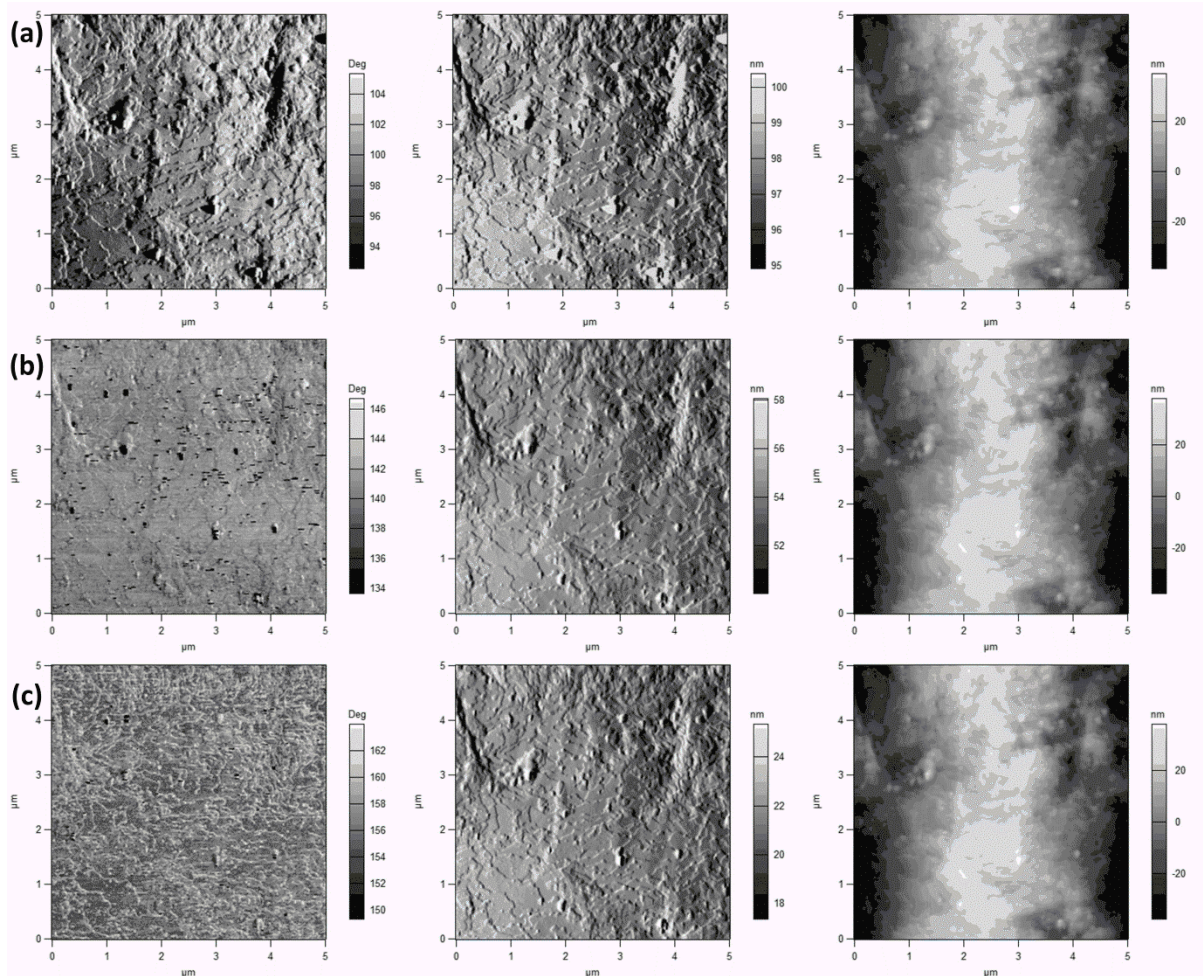


**Figure 9.14** Phase image (left column), amplitude image (middle column), height image (right column) of a parafilm sample, with each row representing: (a) setpoint amplitude: 900 mV, (b) setpoint amplitude: 500 mV, (c) setpoint amplitude: 200 mV.

Further experiments were performed whether or not to observe the internal structures of parafilm more clearly by choosing a smaller scanned size. The scanned size of the sample was changed to  $1.5\mu\text{m}$  by  $1.5\mu\text{m}$ . Again, there is no significant difference in contrast of the phase image and the amplitude image under light tapping conditions, as shown in Figure 9.15(a). When the setpoint amplitude is changed to 500 mV, the phase image separates the internal structure of the parafilm sample in terms of the dark contrast shown in Figure 9.15(b).

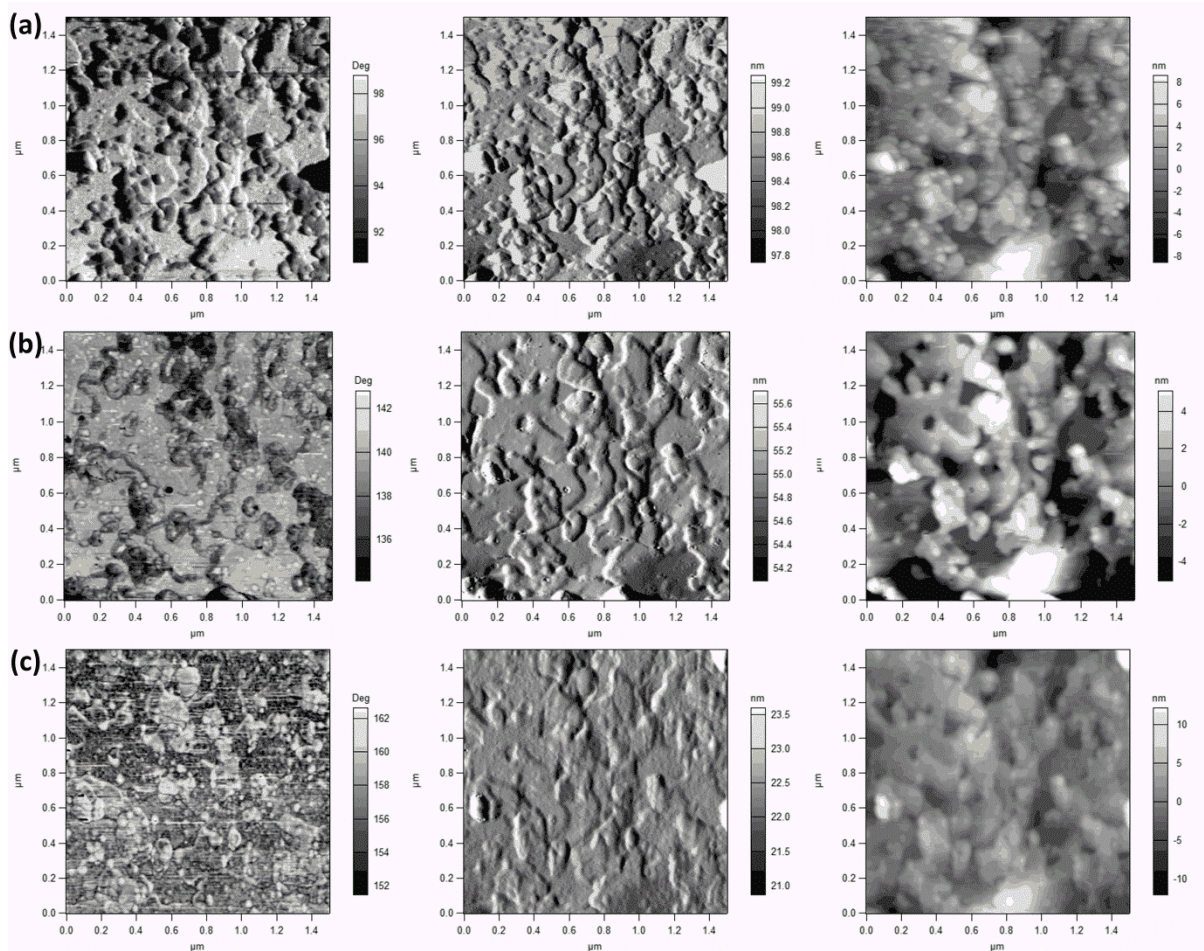


**Figure 9.15** Phase image, amplitude image, height image of parafilm in each row: (a) setpoint amplitude: 900 mV, (b) setpoint amplitude: 500 mV, (c) setpoint amplitude: 200 mV. (1.5 $\mu$ m\*1.5 $\mu$ m)

## 9.6 Measurement of phase shift

### 9.6.1 Indirect phase shift measurement

In order to calculate the phase shift of the experiment data by adopting the same method to extract the phase shift from the simulated displacement data using FFT as mentioned in Section 8.31, an Agilent Technologies DSO1004A oscilloscope was used to capture the deflection of the cantilever by connecting the deflection output of the AFM controller. However, due to the limitations of the oscilloscope, only 10,240 data points could be captured in one go. Hence, the time dependent deflection curves captured here represent signals that have already entered the main tapping period and so they have missed the transition period. Figure 9.16 shows one data set for the deflection signal captured using

this oscilloscope. Ten data sets were obtained in the experiment. By performing an FFT upon the deflection signals, one can plot the phase shifts against different setpoint ratios. However, the phase shifts obtained using this method deviate from the phase shifts shown in the sum and deflection meter for some unknown reason. Hence, it was considered to be better to read the phase shift value directly from the sum and deflection meter, which is shown in the next section.

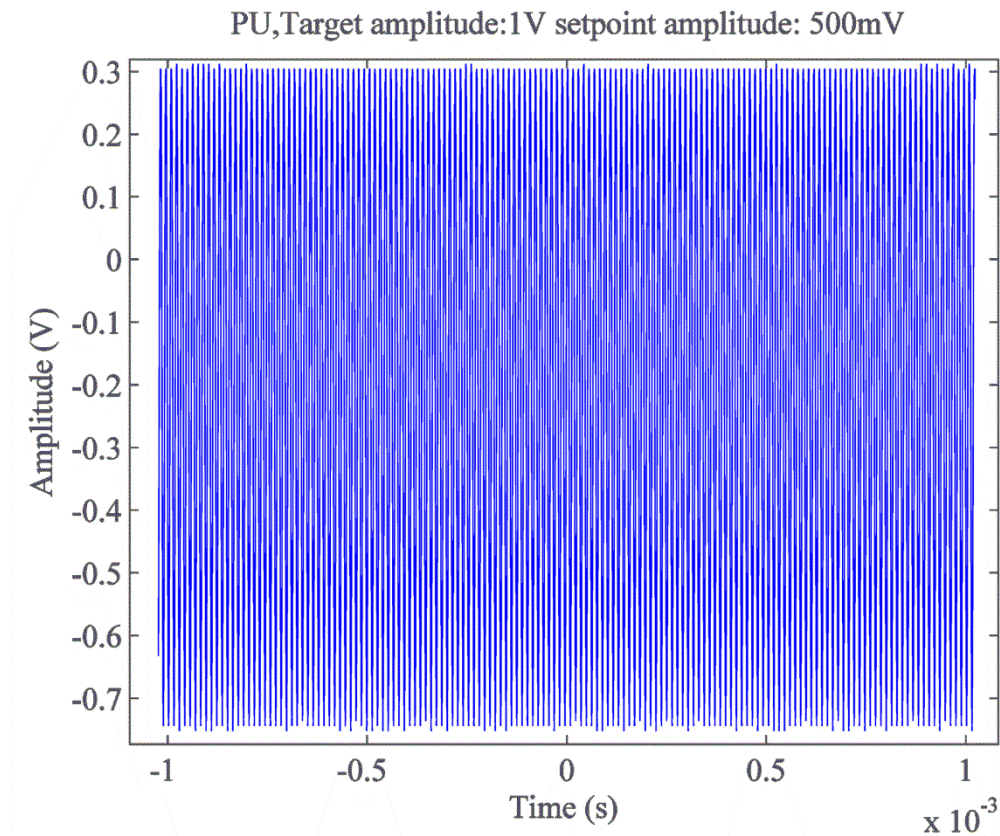


**Figure 9.16 Deflection signal of cantilever captured using oscilloscope from the real AFM instrument during experimentation: setpoint amplitude of 500mV, Q=134.8, resonant frequency= 74504 Hz.**

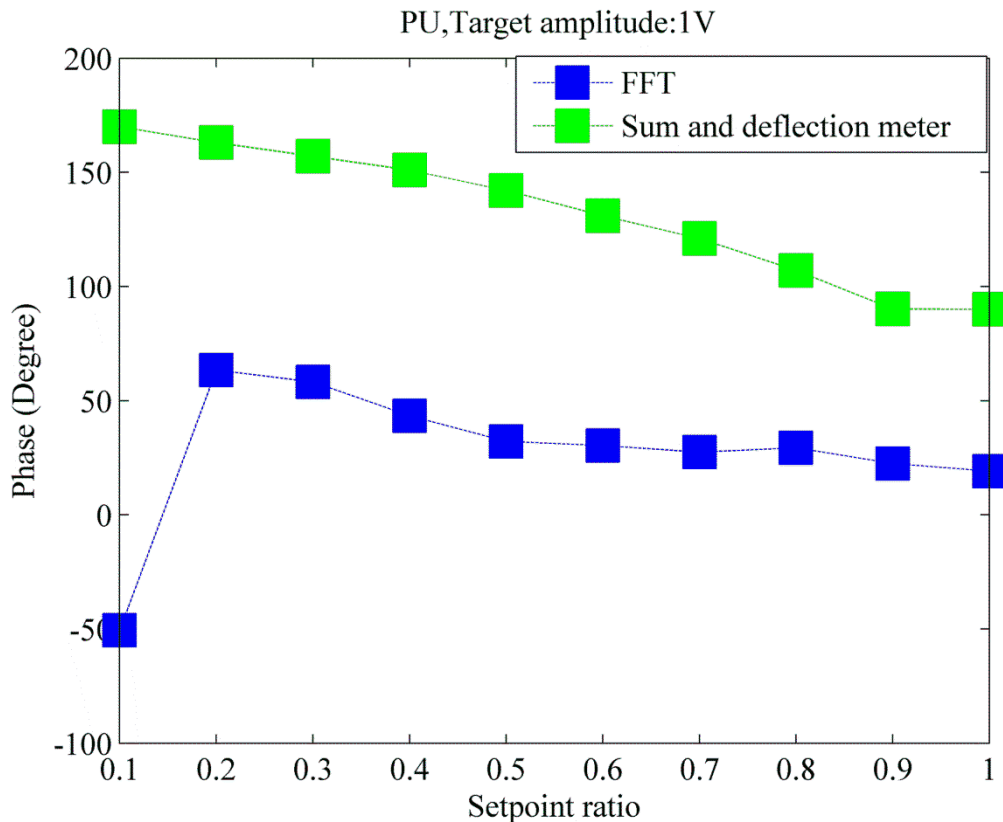


**Figure 9.17** Phase shifts which were obtained using an FFT of the deflection signals and from the sum and deflection meter.

### 9.6.2 Direct phase shift measurement

For these AFM measurements the cantilever was driven at its fundamental frequency (approx.72kHz) and ramped down until the setpoint amplitude was reached. Phase shifts were recorded by changing the setpoint ratio (setpoint ratio = setpoint amplitude/free amplitude). The phase shifts were recorded from set-point amplitudes varying from 900mV to 100mV representing light to hard tapping regimes respectively. Data was recorded using the AFM software and analysed using Matlab. Efforts were also made to capture the cantilever displacement response signal. For polyurethane (PU) and polyvinyl chloride (PVC), the phase shifts shown are in the repulsive regime, as indicated in by phase shifts  $>90^\circ$  in Figure 9.18. The phase shifts gradually increase when the tip sample separation decreases, which has a similar trend to that of the simulation results. One exception is found that the phase shift at setpoint ratio 0.1 is smaller than  $90^\circ$ , which could be due to the attractive forces. This once again supports the simulation results.

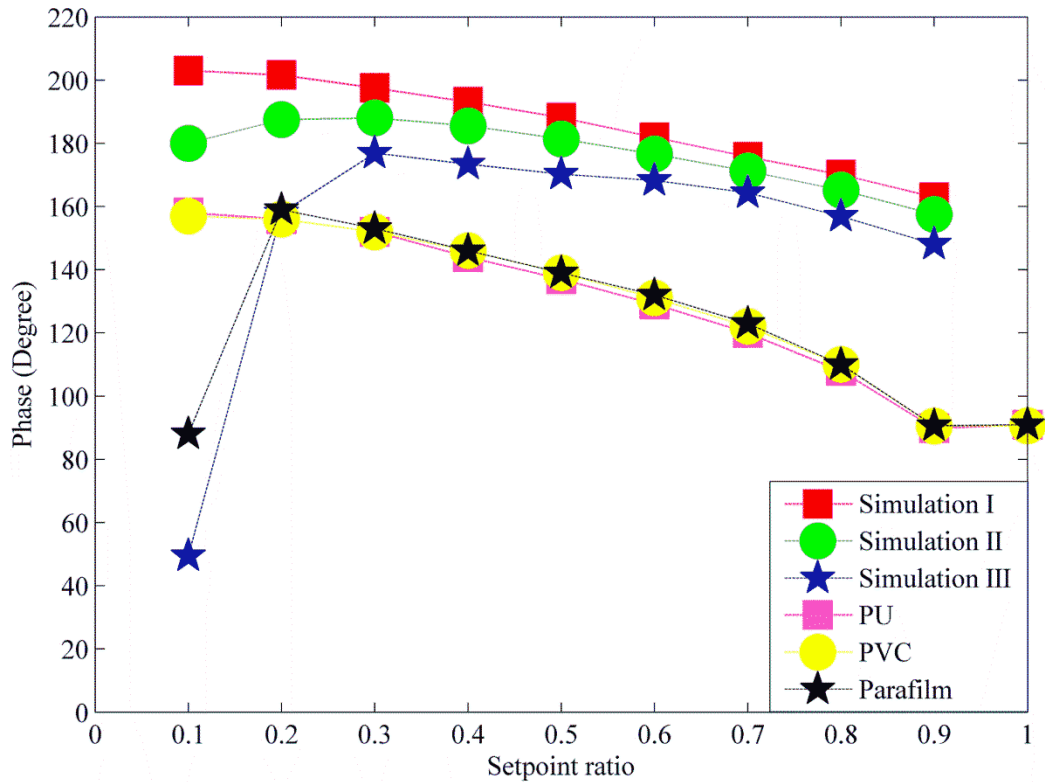


**Figure 9.18 Comparison of the phase shifts recoded against different setpoint ratios for PVC, PU and Parafilm with the simulation results.**

### 9.7 Summary and Discussions

Calibration of the system provides the basis for the accuracy of the experimental results. Force curve analysis gives a basic idea of the adhesion properties of the various different samples. Phase images, amplitude images and height images were all obtained under different setpoint amplitudes for PU and parafilm. It is hard to differentiate between the various AFM image modalities of the PU samples captured under low tapping, mediate tapping and hard tapping conditions. As for parafilm, the phase image captured under mediate tapping conditions can separate the internal structures in terms of bright and dark contrast areas. However, there is no physical evidence indicating which interaction force changes the phase contrast. The phase shifts directly obtained from the AFM share similar

trends with the simulation results, although the actual values of the phase shift are different. Efforts have also been made to capture the cantilever deflection signal. At the moment, it is not possible to record the deflection signal from free vibration to the tapping period due to the limitations of the oscilloscope that is available. These aspects are worthy of further investigation in future research work.

# Chapter 10

# Conclusions

## Chapter 10 Conclusions

### 10.1 Conclusions

A real contact 3D finite element model has been proposed to simulate the tapping mode AFM. Preliminary results were obtained. It was found that the tip bounces on and off the sample.

In the real contact 3D finite element model, the stress during contact was too high reaching the ultimate strength of the material, which could lead to the instability of the simulation.

The disadvantage of the real contact 3D model was that the computational time is very high with a computational load of nearly 19 hours for one cycle cantilever vibration. Hence, it seems unrealistic to carry out the study using this real contact model. The conclusions drawn from the real contact 3D model can be referred to Chapter 6.

Hence, a simplified 3D finite element model has been proposed to simulate the behaviour of tapping mode AFM. The computational time was significantly improved. It only took one hour and a half to obtain 250 cycles vibration.

Cantilever displacement was obtained under free vibration and contact vibration. It was found that damping has a significant effect on the stabilization of cantilever displacement. The smaller the Q factor, the quicker the displacement signal becomes stable.

The phase shift has been studied by analysing the cantilever displacement under different tip-sample interaction forces. It was found that the phase shifts are larger than  $90^\circ$  when repulsive forces are dominant. On the other hand, the phase shifts are smaller than  $90^\circ$  when only the attractive forces are dominant.

The phase shift is not very sensitive to the elastic forces in terms of different Young's moduli. However, the attractive force has the ability to decrease the value of the phase shifts when coupled with elastic force.

The source of the attractive forces may come from adhesion force and viscosity force. The adhesion hysteresis has the impact to divide the phase shifts into repulsive and attractive

regions. On the other hand, the phase shifts caused by the viscosity force remain in the repulsive.

Besides the phase shift, the transition time was also extracted from the cantilever displacement signal. The transition time can be an indicator that can help optimize the scanning speed in real AFM experiments.

Moreover, stable amplitudes were extracted from the cantilever displacement signal. It was found out that the tip may not contact the sample even it was under the tapping period. Also, the instantaneous frequency of each vibration cycle was calculated.

The simplified model proposed in this thesis can be used as a tool to investigate other AFM techniques. All the conclusions corresponding to the simplified 3D finite element model can be referred to Chapter 7 and 8.

From the experiment results in Chapter 9, it was found that force curve analysis gives a basic idea of the adhesion properties of the various different samples.

Phase images, amplitude images and height images were all obtained under different setpoint amplitudes for PU and parafilm. It is hard to differentiate between the various AFM image modalities of the PU samples captured under low tapping, mediate tapping and hard tapping conditions. As for parafilm, the phase image captured under mediate tapping conditions can separate the internal structures in terms of bright and dark contrast areas. However, there is no physical evidence indicating which interaction force changes the phase contrast.

Phase shifts were obtained indirectly by doing a FFT to the deflection signal captured by an oscilloscope. However, the phase shifts calculated using this method deviates from the direct phase shift output from AFM system. Also, it was not possible to record the deflection signal from free vibration to the tapping period.

The phase shifts directly obtained from the AFM share similar trends with the simulation results, although the actual values of the phase shift are different. Hence, experiments have been performed to support the computer simulation results.

The proposed method illustrated in this thesis provides a potential tool that can be used to interpret AFM phase images. How to use these dynamic behaviours to quantitatively interpret phase images still requires further study.

## **10.2 Further work**

An AFM is a very complex instrument. In this thesis, only the impact of the test samples reflected by the interaction forces on the dynamic behaviour of the cantilever was investigated using a simplified 3D finite element model. As the tip sample interaction forces are defined using mathematical expressions, it is hard to tell whether or not the geometry and material property of cantilever and tip have large influence on the simulation results. Hence, the impact of the shape, size and material properties of the AFM cantilever and tip upon the cantilever's dynamic behaviour will require to be studied in the future to aid in gaining a more complete understanding of tapping mode AFM. Generally, a quantitative analysis will be carried out. For example, simulations will be performed with different tip shape, such as cone, pyramid and sphere tip, but with same tip radius and same kind of material. Simulation results will be summarized and compared along with different tip shape. One may find out what kind of tip shape will be useful for tapping mode AFM.

Also, further investigation into interaction forces in the x and y directions should be considered, as only interaction forces in the z direction have been discussed here. The results help us to understand the vibration mechanism of the cantilever under tip-sample interactions and may enable optimisation of system parameters to increase the quality of AFM phase images.

The methods described in this thesis also open up an approach by which it is possible to investigate the dynamic behaviour of AFM cantilevers operating under higher vibration modes, for example the second flexural mode. Based on the simplified 3D finite element model, torsion mode AFM could also be studied by modifying the piezo activation.

Moreover, as the simulation of real 3D contact model was time consuming and might not be stable, some modification may be applied into the simplified 3D finite element model. The idea is that the simulation is firstly performed using the simplified 3D finite element model,

so that the cantilever displacement will reach its steady state in free vibration. By adopting the data from the first simulation, a continual simulation may be performed. However, a tangible sample is added into the continual simulation. Of course, this modification will require more computational time and power than just running the simplified 3D model, but the advantage is that this model will more closely resemble a real AFM system. It should therefore be able to provide more meaningful results.

When all the work mentioned above is successfully done, one may consider adding a feedback system and x and y scanner into the simulation to perfectly resemble the real tapping mode AFM system. The difficulty would be another software is needed to monitor process the simulation data instantaneously and feedback to the simulation software. The advantage is that it will be exactly like the real tapping mode AFM system. However, this may only be done when the computational power is significantly increased.

From the experimental point of view, it would be a good idea to use a better oscilloscope to capture the entire cantilever deflection from the free vibration period right through to full contact vibration. Then the same method that was used to process the simulation displacement can be applied to the cantilever deflection data in order to calculate the phase shifts, which may provide more consistent results between experiment and simulation.

## References

- ALBRECHT, T. R., AKAMINE, S., CARVER, T. E. & QUATE, C. F. 1990. Microfabrication of cantilever styli for the atomic force microscope. *Journal of Vacuum Science & Technology A*, 8, 3386-3396.
- ALBRECHT, T. R., GRÜTTER, P., HORNE, D. & RUGAR, D. 1991. Frequency modulation detection using high - Q cantilevers for enhanced force microscope sensitivity. *Journal of Applied Physics*, 69, 668-673.
- ALEXANDER, S., HELLEMANS, L., MARTI, O., SCHNEIR, J., ELINGS, V., HANSMA, P. K., LONGMIRE, M. & GURLEY, J. 1989. An atomic - resolution atomic - force microscope implemented using an optical lever. *Journal of Applied Physics*, 65, 164-167.
- AMELIO, S., GOLDADE, A. V., RABE, U., SCHERER, V., BHUSHAN, B. & ARNOLD, W. 2001. Measurements of elastic properties of ultra-thin diamond-like carbon coatings using atomic force acoustic microscopy. *Thin Solid Films*, 392, 75-84.
- ANCZYKOWSKI, B., KRÜGER, D. & FUCHS, H. 1996. Cantilever dynamics in quasinoncontact force microscopy: Spectroscopic aspects. *Physical Review B*, 53, 15485-15488.
- ANDO, T., UCHIHASHI, T. & FUKUMA, T. 2008. High-speed atomic force microscopy for nano-visualization of dynamic biomolecular processes. *Progress in Surface Science*, 83, 337-437.
- ANSELMETTI, D., LUTHI, R., MEYER, E., RICHMOND, T., DREIER, M., FROMMER, J. E. & GUNTHERODT, H.-J. 1994. Attractive-mode imaging of biological materials with dynamic force microscopy. *Nanotechnology*, 5, 87.
- BAR, G., DELINEAU, L., BRANDSCH, R., BRUCH, M. & WHANGBO, M.-H. 1999. Importance of the indentation depth in tapping-mode atomic force microscopy study of compliant materials. *Applied Physics Letters*, 75, 4198-4200.
- BAR, G., THOMANN, Y., BRANDSCH, R., CANTOW, H. J. & WHANGBO, M. H. 1997. Factors Affecting the Height and Phase Images in Tapping Mode Atomic Force Microscopy. Study of Phase-Separated Polymer Blends of Poly(ethene-co-styrene) and Poly(2,6-dimethyl-1,4-phenylene oxide). *Langmuir*, 13, 3807-3812.
- BHUSHAN, B. & KASAI, T. 2004. A surface topography-independent friction measurement technique using torsional resonance mode in an AFM. *Nanotechnology*, 15, 923.
- BINNIG, G., QUATE, C. F. & GERBER, C. 1986. Atomic Force Microscope. *Physical Review Letters*, 56, 930-933.
- BINNIG, G. & ROHRER, H. 1983. Scanning tunneling microscopy. *Surface Science*, 126, 236-244.
- BINNIG, G., ROHRER, H., GERBER, C. & WEIBEL, E. 1982. Surface Studies by Scanning Tunneling Microscopy. *Physical Review Letters*, 49, 57-61.
- BRANDSCH, R., BAR, G. & WHANGBO, M. H. 1997. On the Factors Affecting the Contrast of Height and Phase Images in Tapping Mode Atomic Force Microscopy. *Langmuir*, 13, 6349-6353.
- BUTT, H.-J., CAPPELLA, B. & KAPPL, M. 2005. Force measurements with the atomic force microscope: Technique, interpretation and applications. *Surface Science Reports*, 59, 1-152.
- BUTT, H.-J. & JASCHKE, M. 1995. Calculation of thermal noise in atomic force microscopy. *Nanotechnology*, 6, 1.
- CASPER, J. M. 1977. Physical chemistry of surfaces (3rd Ed.), Arthur W. Adamson, Wiley-Interscience, New York, 1976, 698 pp. \$24.95. *Journal of Polymer Science: Polymer Letters Edition*, 15, 632-633.
- CHEN, J., WORKMAN, R. K., SARID, D. & HOPER, R. 1994. Numerical simulations of a scanning force microscope with a large-amplitude vibrating cantilever. *Nanotechnology*, 5, 199.
- CHEN, N. & BHUSHAN, B. 2005. Morphological, nanomechanical and cellular structural characterization of human hair and conditioner distribution using torsional resonance mode with an atomic force microscope. *Journal of Microscopy*, 220, 96-112.

- CHEN, X., ROBERTS, C. J., ZHANG, J., DAVIES, M. C. & TENDLER, S. J. B. 2002. Phase contrast and attraction–repulsion transition in tapping mode atomic force microscopy. *Surface Science*, 519, L593-L598.
- CHEUNG, C. L., HAFNER, J. H. & LIEBER, C. M. 2000. Carbon nanotube atomic force microscopy tips: Direct growth by chemical vapor deposition and application to high-resolution imaging. *Proceedings of the National Academy of Sciences*, 97, 3809-3813.
- CLEVELAND, J. P., ANCZYKOWSKI, B., SCHMID, A. E. & ELINGS, V. B. 1998. Energy dissipation in tapping-mode atomic force microscopy. *Applied Physics Letters*, 72, 2613-2615.
- DERJAGUIN, B. V., MULLER, V. M. & TOPOROV, Y. P. 1975. Effect of contact deformations on the adhesion of particles. *Journal of Colloid and Interface Science*, 53, 314-326.
- DUPAS, E., GREMAUD, G., KULIK, A. & LOUBET, J.-L. 2001. High-frequency mechanical spectroscopy with an atomic force microscope. *Review of Scientific Instruments*, 72, 3891-3897.
- FLORIN, E. L., RADMACHER, M., FLECK, B. & GAUB, H. E. 1994. Atomic force microscope with magnetic force modulation. *Review of Scientific Instruments*, 65, 639-643.
- FRITZ, M., RADMACHER, M., CLEVELAND, J. P., ALLERSMA, M. W., STEWART, R. J., GIESELMANN, R., JANMEY, P., SCHMIDT, C. F. & HANSMA, P. K. 1995. Imaging Globular and Filamentous Proteins in Physiological Buffer Solutions with Tapping Mode Atomic Force Microscopy. *Langmuir*, 11, 3529-3535.
- FUKUI, K.-I., ONISHI, H. & IWASAWA, Y. 1997. Imaging of individual formate ions adsorbed on TiO<sub>2</sub>(110) surface by non-contact atomic force microscopy. *Chemical Physics Letters*, 280, 296-301.
- GARCIA, R. October 2010. Amplitude Modulation Atomic Force Microscopy. 193.
- GARCIA, R., GÓMEZ, C., MARTINEZ, N., PATIL, S., DIETZ, C. & MAGERLE, R. 2006. Identification of Nanoscale Dissipation Processes by Dynamic Atomic Force Microscopy. *Physical Review Letters*, 97.
- GARCIA, R., MAGERLE, R. & PEREZ, R. 2007. Nanoscale compositional mapping with gentle forces. *Nat Mater*, 6, 405-411.
- GARCÍA, R. & PÉREZ, R. 2002. Dynamic atomic force microscopy methods. *Surface Science Reports*, 47, 197-301.
- GARCÍA, R. & SAN PAULO, A. 1999. Attractive and repulsive tip-sample interaction regimes in tapping-mode atomic force microscopy. *Physical Review B*, 60, 4961-4967.
- GARCÍA, R. & SAN PAULO, A. 2000. Dynamics of a vibrating tip near or in intermittent contact with a surface. *Physical Review B*, 61, R13381-R13384.
- GARCÍA, R., SAN PAULO, A. & TAMAYO, J. 1999. Phase contrast and surface energy hysteresis in tapping mode scanning force microscopy. *Surface and Interface Analysis*, 316, 312-316.
- GARCÍA, R., TAMAYO, J., CALLEJA, M. & GARCÍA, F. 1998. Phase contrast in tapping-mode scanning force microscopy. *Applied Physics A*, 66, S309-S312.
- GIESSIBL, F. J. 1995. Atomic Resolution of the Silicon (111)-(7x7) Surface by Atomic Force Microscopy. *Science*, 267, 68-71.
- HAN, W., LINDSAY, S. M. & JING, T. 1996. A magnetically driven oscillating probe microscope for operation in liquids. *Applied Physics Letters*, 69, 4111-4113.
- HANSMA, P. K., CLEVELAND, J. P., RADMACHER, M., WALTERS, D. A., HILLNER, P. E., BEZANILLA, M., FRITZ, M., VIE, D., HANSMA, H. G., PRATER, C. B., MASSIE, J., FUKUNAGA, L., GURLEY, J. & ELINGS, V. 1994. Tapping mode atomic force microscopy in liquids. *Applied Physics Letters*, 64, 1738-1740.
- [HTTP://EN.WIKIPEDIA.ORG/WIKI/SCANNING\\_TUNNELING\\_MICROSCOPE.](http://en.wikipedia.org/wiki/Scanning_Tunneling_Microscope)
- [HTTP://WWW.ASYLUMRESEARCH.COM/PROBE/AC240TS](http://www.asylumresearch.com/probe/ac240ts), O.
- [HTTP://WWW.BRUKERAFMPROBES.COM/P-3411-DTT10.ASPX.](http://www.brukerafmpobes.com/p-3411-dtt10.aspx)
- [HTTP://WWW.BRUKERAFMPROBES.COM/P-3693-SNL-10.ASPX.](http://www.brukerafmpobes.com/p-3693-snl-10.aspx)
- [HTTP://WWW.NANOANDMORE.COM/AFM-PROBE-PNP-TRS.HTML.](http://www.nanoandmore.com/afm-probe-pnp-trs.html)

- HUANG, L. & SU, C. 2004. A torsional resonance mode AFM for in-plane tip surface interactions. *Ultramicroscopy*, 100, 277-285.
- HURLEY, D. C., SHEN, K., JENNETT, N. M. & TURNER, J. A. 2003. Atomic force acoustic microscopy methods to determine thin-film elastic properties. *Journal of Applied Physics*, 94, 2347-2354.
- HUTTER, J. L. & BECHHOEFER, J. 1993. Calibration of atomic - force microscope tips. *Review of Scientific Instruments*, 64, 1868-1873.
- ISRAELACHVILI, J. 2010. *Intermolecular and Surface Forces, Third Edition*, Academic Press.
- JALILI, N. & LAXMINARAYANA, K. 2004. A review of atomic force microscopy imaging systems: application to molecular metrology and biological sciences. *Mechatronics*, 14, 907-945.
- JOHNSON, K. L. 1985. *Contact Mechanics*, Cambridge University Press.
- JOHNSON, K. L., KENDALL, K. & ROBERTS, A. D. 1971. *Surface Energy and the Contact of Elastic Solids*.
- KASAI, T., BHUSHAN, B., HUANG, L. & SU, C. 2004. Topography and phase imaging using the torsional resonance mode. *Nanotechnology*, 15, 731.
- KLINOV, D., DWIR, B., KAPON, E., BOROVOK, N., MOLOTSKY, T. & KOTLYAR, A. 2007. High-resolution atomic force microscopy of duplex and triplex DNA molecules. *Nanotechnology*, 18, 225102.
- KLINOV, D. & MAGONOV, S. 2004. True molecular resolution in tapping-mode atomic force microscopy with high-resolution probes. *Applied Physics Letters*, 84, 2697-2699.
- KNOLL, A., MAGERLE, R. & KRAUSCH, G. 2004. Phase behavior in thin films of cylinder-forming ABA block copolymers: Experiments. *The Journal of Chemical Physics*, 120, 1105-1116.
- KÜHLE, A., SO/RENSEN, A. H. & BOHR, J. 1997. Role of attractive forces in tapping tip force microscopy. *Journal of Applied Physics*, 81, 6562-6569.
- LECLÈRE, P., LAZZARONI, R., BRÉDAS, J. L., YU, J. M., DUBOIS, P. & JÉRÔME, R. 1996. Microdomain Morphology Analysis of Block Copolymers by Atomic Force Microscopy with Phase Detection Imaging. *Langmuir*, 12, 4317-4320.
- LEUBA, S. H., YANG, G., ROBERT, C., SAMORI, B., VAN HOLDE, K., ZLATANOVA, J. & BUSTAMANTE, C. 1994. Three-dimensional structure of extended chromatin fibers as revealed by tapping-mode scanning force microscopy. *Proceedings of the National Academy of Sciences*, 91, 11621-11625.
- LIU, M. & GORMAN, D. G. 1995. Formulation of Rayleigh damping and its extensions. *Computers & Structures*, 57, 277-285.
- LOZANO, J. R. & GARCIA, R. 2008. Theory of Multifrequency Atomic Force Microscopy. *Physical Review Letters*, 100, 076102.
- LOZANO, J. R. & GARCIA, R. 2009. Theory of phase spectroscopy in bimodal atomic force microscopy. *Physical Review B*, 79, 014110.
- LYUBCHENKO, Y. L. & SHLYAKHTENKO, L. S. 1997. Visualization of supercoiled DNA with atomic force microscopy in situ. *Proceedings of the National Academy of Sciences*, 94, 496-501.
- MAGONOV, S. N., ELINGS, V. & PAPKOV, V. S. 1997a. AFM study of thermotropic structural transitions in poly(diethylsiloxane). *Polymer*, 38, 297-307.
- MAGONOV, S. N., ELINGS, V. & WHANGBO, M. H. 1997b. Phase imaging and stiffness in tapping-mode atomic force microscopy. *Surface Science*, 375, L385-L391.
- MAGONOV, S. N. & RENEKER, D. H. 1997. CHARACTERIZATION OF POLYMER SURFACES WITH ATOMIC FORCE MICROSCOPY. *Annual Review of Materials Science*, 27, 175-222.
- MAIVALD, P., BUTT, H. J., GOULD, S. A. C., PRATER, C. B., DRAKE, B., GURLEY, J. A., ELINGS, V. B. & HANSMA, P. K. 1991. Using force modulation to image surface elasticities with the atomic force microscope. *Nanotechnology*, 2, 103.
- MARTI, O., COLCHERO, J. & MLYNEK, J. 1990. Combined scanning force and friction microscopy of mica. *Nanotechnology*, 1, 141.
- MARTIN, Y. & WICKRAMASINGHE, H. K. 1987. Magnetic imaging by "force microscopy" with 1000 Å resolution. *Applied Physics Letters*, 50, 1455-1457.
- MARTIN, Y., WILLIAMS, C. C. & WICKRAMASINGHE, H. K. 1987. Atomic force microscope - force mapping and profiling on a sub 100 - Å scale. *Journal of Applied Physics*, 61, 4723-4729.

- MARTINEZ, J., YUZVINSKY, T. D., FENNIMORE, A. M., ZETTL, A., GARCÍA, R. & BUSTAMANTE, C. 2005. Length control and sharpening of atomic force microscope carbon nanotube tips assisted by an electron beam. *Nanotechnology*, 16, 2493.
- MARTÍNEZ, N. F. & GARCÍA, R. 2006. Measuring phase shifts and energy dissipation with amplitude modulation atomic force microscopy. *Nanotechnology*, 17, S167.
- MARTÍNEZ, N. F., LOZANO, J. R., HERRUZO, E. T., GARCIA, F., RICHTER, C., SULZBACH, T. & GARCIA, R. 2008. Bimodal atomic force microscopy imaging of isolated antibodies in air and liquids. *Nanotechnology*, 19, 384011.
- MCLEAN, R. S. & SAUER, B. B. 1997. Tapping-Mode AFM Studies Using Phase Detection for Resolution of Nanophases in Segmented Polyurethanes and Other Block Copolymers. *Macromolecules*, 30, 8314-8317.
- MEYER, G. & AMER, N. M. 1988. Novel optical approach to atomic force microscopy. *Applied Physics Letters*, 53, 1045-1047.
- MEYER, G. & AMER, N. M. 1990. Simultaneous measurement of lateral and normal forces with an optical - beam - deflection atomic force microscope. *Applied Physics Letters*, 57, 2089-2091.
- MÖLLER, C., ALLEN, M., ELINGS, V., ENGEL, A. & MÜLLER, D. J. 1999. Tapping-Mode Atomic Force Microscopy Produces Faithful High-Resolution Images of Protein Surfaces. *Biophysical Journal*, 77, 1150-1158.
- MOTOMATSU, M., MIZUTANI, W. & TOKUMOTO, H. 1997. Microphase domains of poly(styrene-block-ethylene/butylene-block-styrene) triblock copolymers studied by atomic force microscopy. *Polymer*, 38, 1779-1785.
- NONNENMACHER, M., O'BOYLE, M. P. & WICKRAMASINGHE, H. K. 1991. Kelvin probe force microscopy. *Applied Physics Letters*, 58, 2921-2923.
- NONY, L., BOISGARD, R. & AIMÉ, J. P. 1999. Nonlinear dynamical properties of an oscillating tip-cantilever system in the tapping mode. *The Journal of Chemical Physics*, 111, 1615-1627.
- PAULO, Á. S. & GARCÍA, R. 2001. Tip-surface forces, amplitude, and energy dissipation in amplitude-modulation (tapping mode) force microscopy. *Physical Review B*, 64, 193411.
- PAULO, Á. S. & GARCÍA, R. 2002. Unifying theory of tapping-mode atomic-force microscopy. *Physical Review B*, 66, 041406.
- PUTMAN, C. A. J., VAN DER WERF, K. O., DE GROOTH, B. G., VAN HULST, N. F. & GREVE, J. 1994. Tapping mode atomic force microscopy in liquid. *Applied Physics Letters*, 64, 2454-2456.
- RABE, U., AMELIO, S., KESTER, E., SCHERER, V., HIRSEKORN, S. & ARNOLD, W. 2000. Quantitative determination of contact stiffness using atomic force acoustic microscopy. *Ultrasonics*, 38, 430-437.
- RABE, U., AMELIO, S., KOPYCINSKA, M., HIRSEKORN, S., KEMPF, M., GÖKEN, M. & ARNOLD, W. 2002. Imaging and measurement of local mechanical material properties by atomic force acoustic microscopy. *Surface and Interface Analysis*, 33, 65-70.
- RABE, U. & ARNOLD, W. 1994. Acoustic microscopy by atomic force microscopy. *Applied Physics Letters*, 64, 1493-1495.
- RABE, U., JANSER, K. & ARNOLD, W. 1996. Vibrations of free and surface - coupled atomic force microscope cantilevers: Theory and experiment. *Review of Scientific Instruments*, 67, 3281-3293.
- RABE, U., TURNER, J. & ARNOLD, W. 1998. Analysis of the high-frequency response of atomic force microscope cantilevers. *Applied Physics A*, 66, S277-S282.
- RADMACHER, M., FRITZ, M., HANSMA, H. & HANSMA, P. 1994. Direct observation of enzyme activity with the atomic force microscope. *Science*, 265, 1577-1579.
- REINSTÄDTLER, M., KASAI, T., RABE, U., BHUSHAN, B. & ARNOLD, W. 2005a. Imaging and measurement of elasticity and friction using the TRmode. *Journal of Physics D: Applied Physics*, 38, R269.

- REINSTÄDTLER, M., RABE, U., GOLDADE, A., BHUSHAN, B. & ARNOLD, W. 2005b. Investigating ultra-thin lubricant layers using resonant friction force microscopy. *Tribology International*, 38, 533-541.
- REINSTÄDTLER, M., RABE, U., SCHERER, V., HARTMANN, U., GOLDADE, A., BHUSHAN, B. & ARNOLD, W. 2003. On the nanoscale measurement of friction using atomic-force microscope cantilever torsional resonances. *Applied Physics Letters*, 82, 2604-2606.
- REITER, G., CASTELEIN, G., SOMMER, J.-U., RÖTTELE, A. & THURN-ALBRECHT, T. 2001. Direct Visualization of Random Crystallization and Melting in Arrays of Nanometer-Size Polymer Crystals. *Physical Review Letters*, 87, 226101.
- RIVETTI, C., GUTHOLD, M. & BUSTAMANTE, C. 1996. Scanning Force Microscopy of DNA Deposited onto Mica: Equilibration versus Kinetic Trapping Studied by Statistical Polymer Chain Analysis. *Journal of Molecular Biology*, 264, 919-932.
- RODRÍGUEZ, T. R. & GARCÍA, R. 2002. Tip motion in amplitude modulation (tapping-mode) atomic-force microscopy: Comparison between continuous and point-mass models. *Applied Physics Letters*, 80, 1646-1648.
- RODRÍGUEZ, T. R. & GARCÍA, R. 2004. Compositional mapping of surfaces in atomic force microscopy by excitation of the second normal mode of the microcantilever. *Applied Physics Letters*, 84, 449-451.
- RUGAR, D., MAMIN, H. J. & GUETHNER, P. 1989. Improved fiber - optic interferometer for atomic force microscopy. *Applied Physics Letters*, 55, 2588-2590.
- SADER, J. E., CHON, J. W. M. & MULVANEY, P. 1999. Calibration of rectangular atomic force microscope cantilevers. *Review of Scientific Instruments*, 70, 3967-3969.
- SAHIN, O., MAGONOV, S., SU, C., QUATE, C. F. & SOLGAARD, O. 2007. An atomic force microscope tip designed to measure time-varying nanomechanical forces. *Nat Nano*, 2, 507-514.
- SAHIN, O., QUATE, C. F., SOLGAARD, O. & ATALAR, A. 2004. Resonant harmonic response in tapping-mode atomic force microscopy. *Physical Review B*, 69, 165416.
- SAN PAULO, A. & GARCÍA, R. 2001. Amplitude, deformation and phase shift in amplitude modulation atomic force microscopy: a numerical study for compliant materials. *Surface Science*, 471, 71-79.
- SARIOGLU, A. F. & SOLGAARD, O. 2008. Cantilevers with integrated sensor for time-resolved force measurement in tapping-mode atomic force microscopy. *Applied Physics Letters*, 93, -.
- SCHÄFFER, T. E. 2005. Calculation of thermal noise in an atomic force microscope with a finite optical spot size. *Nanotechnology*, 16, 664.
- SCHÄFFER, T. E. & FUCHS, H. 2005. Optimized detection of normal vibration modes of atomic force microscope cantilevers with the optical beam deflection method. *Journal of Applied Physics*, 97, -.
- SCHERER, V., ARNOLD, W. & BHUSHAN, B. 1999. Lateral force microscopy using acoustic friction force microscopy. *Surface and Interface Analysis*, 27, 578-587.
- SCHRÖTER, K., PETZOLD, A., HENZE, T. & THURN-ALBRECHT, T. 2009. Quantitative Analysis of Scanning Force Microscopy Data Using Harmonic Models. *Macromolecules*, 42, 1114-1124.
- SCOTT, W. W. & BHUSHAN, B. 2003. Use of phase imaging in atomic force microscopy for measurement of viscoelastic contrast in polymer nanocomposites and molecularly thick lubricant films. *Ultramicroscopy*, 97, 151-169.
- SEBASTIAN, A., SALAPAKA, M. V., CHEN, D. J. & CLEVELAND, J. P. 2001. Harmonic and power balance tools for tapping-mode atomic force microscope. *Journal of Applied Physics*, 89, 6473-6480.
- SHIN'ICHI KITAMURA & MASASHI IWATSUKI 1996. Observation of Silicon Surfaces Using Ultrahigh-Vacuum Noncontact Atomic Force Microscopy. *Japanese Journal of Applied Physics*, 35, L668.
- SNOW, E. S., CAMPBELL, P. M. & NOVAK, J. P. 2002. Single-wall carbon nanotube atomic force microscope probes. *Applied Physics Letters*, 80, 2002-2004.
- SONG, Y. & BHUSHAN, B. 2006a. Simulation of dynamic modes of atomic force microscopy using a 3D finite element model. *Ultramicroscopy*, 106, 847-873.

- SONG, Y. & BHUSHAN, B. 2006b. Simulation of dynamic modes of atomic force microscopy using a 3D finite element model. *Ultramicroscopy*, 106, 847-873.
- SONG, Y. & BHUSHAN, B. 2008. Atomic force microscopy dynamic modes: modeling and applications. *Journal of Physics: Condensed Matter*, 20, 225012.
- SPATZ, J. P., SHEIKO, S. & MÖLLER, M. 1996. Ion-Stabilized Block Copolymer Micelles: Film Formation and Intermicellar Interaction. *Macromolecules*, 29, 3220-3226.
- STARK, M., MÖLLER, C., MÜLLER, D. J. & GUCKENBERGER, R. 2001. From Images to Interactions: High-Resolution Phase Imaging in Tapping-Mode Atomic Force Microscopy. *Biophysical Journal*, 80, 3009-3018.
- STARK, M., STARK, R. W., HECKL, W. M. & GUCKENBERGER, R. 2002. Inverting dynamic force microscopy: From signals to time-resolved interaction forces. *Proceedings of the National Academy of Sciences*, 99, 8473-8478.
- STARK, R. W. & HECKL, W. M. 2000. Fourier transformed atomic force microscopy: tapping mode atomic force microscopy beyond the Hookian approximation. *Surface Science*, 457, 219-228.
- SUGAWARA, Y., UEYAMA, H., UCHIHASHI, T., OHTA, M., MORITA, S., SUZUKI, M. & MISHIMA, S. 1997. True atomic resolution imaging with noncontact atomic force microscopy. *Applied Surface Science*, 113-114, 364-370.
- SUO, Z., YANG, X., AVCI, R., KELLERMAN, L., PASCUAL, D. W., FRIES, M. & STEELE, A. 2006. HEPES-Stabilized Encapsulation of Salmonella typhimurium. *Langmuir*, 23, 1365-1374.
- TAMAYO, J. 1999. Energy dissipation in tapping-mode scanning force microscopy with low quality factors. *Applied Physics Letters*, 75, 3569-3571.
- TAMAYO, J. & GARCÍA, R. 1997. Effects of elastic and inelastic interactions on phase contrast images in tapping-mode scanning force microscopy. *Applied Physics Letters*, 71, 2394-2396.
- TAMAYO, J. & GARCÍA, R. 1998. Relationship between phase shift and energy dissipation in tapping-mode scanning force microscopy. *Applied Physics Letters*, 73, 2926-2928.
- TERRIS, B. D., STERN, J. E., RUGAR, D. & MAMIN, H. J. 1989. Contact electrification using force microscopy. *Physical Review Letters*, 63, 2669-2672.
- TORTONESE, M., BARRETT, R. C. & QUATE, C. F. 1993. Atomic resolution with an atomic force microscope using piezoresistive detection. *Applied Physics Letters*, 62, 834-836.
- TURNER, J. A. 2004. Non-linear vibrations of a beam with cantilever-Hertzian contact boundary conditions. *Journal of Sound and Vibration*, 275, 177-191.
- TURNER, J. A., HIRSEKORN, S., RABE, U. & ARNOLD, W. 1997. High-frequency response of atomic-force microscope cantilevers. *Journal of Applied Physics*, 82, 966-979.
- VAN DEN BERG, R., DE GROOT, H., VAN DIJK, M. A. & DENLEY, D. R. 1994. Atomic force microscopy of thin triblock copolymer films. *Polymer*, 35, 5778-5781.
- VIANI, M. B., SCHÄFFER, T. E., PALOCZI, G. T., PIETRASANTA, L. I., SMITH, B. L., THOMPSON, J. B., RICHTER, M., RIEF, M., GAUB, H. E., PLAXCO, K. W., CLELAND, A. N., HANSMA, H. G. & HANSMA, P. K. 1999. Fast imaging and fast force spectroscopy of single biopolymers with a new atomic force microscope designed for small cantilevers. *Review of Scientific Instruments*, 70, 4300-4303.
- WALTERS, D. A., CLEVELAND, J. P., THOMSON, N. H., HANSMA, P. K., WENDMAN, M. A., GURLEY, G. & ELINGS, V. 1996. Short cantilevers for atomic force microscopy. *Review of Scientific Instruments*, 67, 3583-3590.
- WANG, L. 1998. Analytical descriptions of the tapping-mode atomic force microscopy response. *Applied Physics Letters*, 73, 3781-3783.
- WANG, L. 1999. The role of damping in phase imaging in tapping mode atomic force microscopy. *Surface Science*, 429, 178-185.
- WANG, Y., SONG, R., LI, Y. & SHEN, J. 2003. Understanding tapping-mode atomic force microscopy data on the surface of soft block copolymers. *Surface Science*, 530, 136-148.
- WHANGBO, M.-H., BAR, G. & BRANDSCH, R. 1998. Description of phase imaging in tapping mode atomic force microscopy by harmonic approximation. *Surface Science*, 411, L794-L801.

- WOLTER, O., BAYER, T. & GRESCHNER, J. 1991. Micromachined silicon sensors for scanning force microscopy. *Journal of Vacuum Science & Technology B*, 9, 1353-1357.
- YAMANAKA, K., OGISO, H. & KOLOSOV, O. 1994. Ultrasonic force microscopy for nanometer resolution subsurface imaging. *Applied Physics Letters*, 64, 178-180.
- YAMANAKA, K. & TOMITA, E. 1995. Lateral Force Modulation Atomic Force Microscope for Selective Imaging of Friction Forces. *Japanese Journal of Applied Physics*, 34, 2879.
- ZHONG, Q., INNIS, D., KJOLLER, K. & ELINGS, V. B. 1993. Fractured polymer/silica fiber surface studied by tapping mode atomic force microscopy. *Surface Science*, 290, L688-L692.
- ZITZLER, L., HERMINGHAUS, S. & MUGELE, F. 2002. Capillary forces in tapping mode atomic force microscopy. *Physical Review B: Condensed matter and materials physics*, 66, 155436.

## Appendix

Matlab code:

### 1) Calculation of phase shift

This code is used to extract the phase shift from the displacement signal stored in a csv file by using FFT. The phase shift obtained here has been converted into unit of degree. Also, power spectrum of the displacement signal can be obtained.

```
clear
load Q100_69290Hz_30to120_40nmto36nm_1GPa_disp.csv
x1=Q100_69290Hz_30to120_40nmto36nm_1GPa_disp(7502:end,2);
%x=x-mean(x);
y1 = fft(x1);
m1 = abs(y1);
p1 = (angle(y1));
f1 = (0:length(y1)-1)*2.5e6/length(y1);
plot(f1,m1,'r')
plot(f1,p1*180/pi,'r')
n= find((m1>max(m1)-1e-9)&(m1<max(m1)+1e-9))
if n==1
    n= 1+find((m1(2:end)>max(m1(2:end))-1e-9)&(m1(2:end)<max(m1(2:end))+1e-9))
    f1(n)
end
f1(n)
phase=p1(min(n))*180/pi
```

### 2) Calculation of transition time and stable amplitude

This code is first used to determine the stable amplitude of the displacement signal. After the stable amplitude is determined, transition time between the free vibration displacement signal and the stable state can be obtained.

```

clear;close

load Q100_69290Hz_30to120_40nmto36nm_1GPa_disp.csv

data = Q100_69290Hz_30to120_40nmto36nm_1GPa_disp;

x=data(:,2);

t=data(:,1);

z=[];

c=[];

y=[];

% find the peaks in the signal

for i=2:length(x)-1

    if x(i-1)<x(i)&& x(i)>x(i+1)&& x(i)>0

        z(end+1)=i;

    end

end

peak=x(z);

tpeak=t(z);

figure

subplot(2,2,1)

plot(tpeak,peak,'s--')

xlabel('Time of each peak')

ylabel('Peak values(um)')

title('All the peaks in one displacement signal')

for i=2:length(peak)-1

    if peak(i-1)<peak(i)&& peak(i)>peak(i+1)

        z(end+1)=i;

    end

end

maxpeak= peak(z);

for j=2:length(peak)-1

    if peak(j-1)>peak(j)&& peak(j)<peak(j+1)

```

```

        y(end+1)=j;
    end
end
minpeak = peak(y);
subplot(2,2,2)
plot(maxpeak,'rs--')
hold on
plot(minpeak,'s--')
xlabel('Time of each peak')
ylabel('Peak values(um)')
title('Differentiate Maxpeaks and Minpeaks')
legend('maxpeak','minpeak')
% obtain the same length of maxpeak and minpeak
% find the difference between maxpeak and minpeak
if length(maxpeak)~=length(minpeak)
    'dimension of matrix is different'
    maxpeak = maxpeak(1:min(length(maxpeak),length(minpeak)));
    minpeak = minpeak(1:min(length(maxpeak),length(minpeak)));
end
peakdiff= maxpeak - minpeak;
subplot(2,2,3)
plot(peakdiff,'s--')
xlabel('Numbers')
ylabel('Difference of maxpeak and minpeak(um)')
title('Difference between maxpeaks and minpeaks')
%find the peak values of peakdiff
%calculate the stable time from the last index of peak value
[pks,locs]= findpeaks(peakdiff)
subplot(2,2,4)
plot(locs,pks,'s--')

```

```

m = find(pks>1e-3)
n = find(peakdiff(locs(max(m)):end)<=1e-3)
index = min(n)+locs(max(m))-1
index_stable = find(peak==(maxpeak(index)))
%double t_stable
t_stable = tpeak(index_stable)
amp_stable = maxpeak(index)
amplitude_stable= mean(peak(index_stable:end))

```

### 3) Calculate the instantaneous frequency

This code is to calculate the instantaneous frequency in each vibration cycle of the displacement signal by using a zero crossing method.

```

clear
load Q100_69290Hz_30to90_40nmto20nm_1GPa_elastic_adhesion_disp.csv
x=Q100_69290Hz_30to90_40nmto20nm_1GPa_elastic_adhesion_disp(:,2);
t=Q100_69290Hz_30to90_40nmto20nm_1GPa_elastic_adhesion_disp(:,1);
z=[];
c=[];
for i=1:length(x)-1
if x(i)<0&&x(i+1)>0
z(end+1)=i;
end
end
t=t(z);
for j=2:length(t)
c(j-1)=t(j)-t(j-1);
end
plot(c,'gs--') % T: vibration period
figure
plot(1./c,'rs--')% instantaneous frequency

```